CNWRA 93-02S

NRC HIGH-LEVEL RADIOACTIVE WASTE RESEARCH AT CNWRA JULY—DECEMBER 1993

Prepared for

Nuclear Regulatory Commission
Contract NRC-02-93-005

Prepared by

Center for Nuclear Waste Regulatory Analyses
San Antonio, Texas

February 1994

CNWRA 93-02S

NRC HIGH-LEVEL RADIOACTIVE WASTE RESEARCH AT CNWRA JULY—DECEMBER 1993

Prepared for

Nuclear Regulatory Commission
Contract NRC-02-93-005

Prepared by

Center for Nuclear Waste Regulatory Analyses
San Antonio, Texas

February 1994

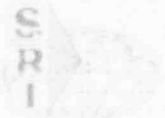

CNWRA 93-02S

NRC HIGH-LEVEL RADIOACTIVE WASTE RESEARCH AT CNWRA JULY–DECEMBER 1993

Prepared for

Nuclear Regulatory Commission
Contract NRC-02-93-005

Contributors

M.P. Ahola, R.G. Baca, A.H. Chowdhury, C.B. Connor, G.A. Cragnolino, F.T. Dodge, D.S. Dunn, A. Ghosh, R.T. Green, B.E. Hili, S.M. Hsiung, V. Kapoor, R.D. Manteufel, S. McDuffie, S. Mohanty, W.M. Murphy, R.T. Pabalan, E.C. Pearcy, N. Sridhar, G.L. Stirewalt, S.A. Stothoff, D.R. Turner, G.W. Wittmeyer, S.R. Young

Edited by

Budhi Sagar

Center for Nuclear Waste Regulatory Analyses
San Antonio, Texas

February 1994

(THIS PAGE INTENTIONALLY LEFT BLANK)

PREVIOUS REPORTS IN SERIES

Number	Name	Date Issued
CNWRA 90-01Q	First Quarterly Research Report for 1990 January 1–March 30	May 1990
CNWRA 90-02Q	Second Quarterly Research Report for 1990 April 1–June 30	August 1990
CNWRA 90-03Q	Third Quarterly Research Report for 1990 July 1–September 30	November 1990
NUREG/CR-5817 Volume 1 CNWRA 90-01A	Report on Research Activities for Calendar Year 1990	December 1991
CNWRA 91-01Q	First Quarterly Research Report for 1991 January 1–March 30	May 1991
CNWRA 91-02Q	Second Quarterly Research Report for 1991 April 1–June 30	August 1991
CNWRA 91-03Q	Third Quarterly Research Report for 1991 July 1–September 30	November 1991
NUREG/CR-5817 Volume 2 CNWRA 91-01A	NRC High-Level Radioactive Waste Research at CNWRA Calendar Year 1991	May 1993
NUREG/CR-5817 Volume 3, No. 1 CNWRA 92-01S	NRC High-Level Radioactive Waste Research at CNWRA January–June 1992	May 1993
NUREG/CR-5817 Volume 3, No. 2 CNWRA 92-02S	NRC High-Level Radioactive Waste Research at CNWRA July–December 1992	July 1993
CNWRA 93-01S	NRC High-Level Radioactive Waste Research at CNWRA January–June 1993	August 1993

(THIS PAGE INTENTIONALLY LEFT BLANK)

PREFACE

The Center for Nuclear Waste Regulatory Analyses (CNWRA), a Federally Funded Research and Development Center (FFRDC), conducts research on behalf of the U.S. Nuclear Regulatory Commission (NRC). The NRC-funded research at the CNWRA is focused on activities related to the NRC responsibilities defined under the Nuclear Waste Policy Act (NWPA), as amended. Progress for the period of July 1, 1993 to December 31, 1993 on 10 of 12 research projects that are currently active is described in this report. Two research projects not reported here are the Stochastic Analysis of Flow and Transport, and Unsaturated Mass Transport, both of which are scheduled for completion in March 1994. Topical reports on these two projects are in preparation. For a brief summary of the work in the reporting period, the reader is referred to the Executive Summary beginning on page 1-1.

In addition to disseminating research results through publications in appropriate open literature (e.g., CNWRA topical reports, NRC documents, and journals) and at technical meetings, workshops, and symposia; the CNWRA produces these research reports twice yearly. See page iii for a list of previous reports in this series.

Each chapter in this semi-annual report summarizes the progress made in a particular research project and is authored by the researchers in that project. Since readers of this report may be interested only in a particular topic, each chapter is self-contained and can be read without reference to other chapters. Coverage in the semi-annual reports is limited to only the key aspects of progress made; greater detail is provided in topical reports that are produced during the course of the research or at its conclusion, as appropriate. The editor of this report ensures that each chapter is reviewed for its technical and programmatic content and that some uniformity as to the depth of descriptions is maintained across the various chapters.

The NRC evaluates its research needs continually as the research progresses. The research needs are based on user needs identified jointly by the NRC Offices of Nuclear Material Safety and Safeguards (NMSS) and Nuclear Regulatory Research (RES). Generally, the NMSS is the user in the sense that its staff applies the research results to strengthen its reviews of the submittals by the U.S. Department of Energy (DOE), including the License Application for the first High-Level Nuclear Waste (HLW) Repository. In their turn, the user needs are based on Key Technical Uncertainties (KTUs) that are identified during the process of developing strategies and methods for determining compliance with the applicable regulations—in this case, 10 CFR Part 60. Thus, the research is directed toward evaluation of the KTUs.

(THIS PAGE INTENTIONALLY LEFT BLANK)

CONTENTS

CONTENTS (cont'd)

CONTENTS (cont'd)

CONTENTS (cont'd)

CONTENTS (cont'd)

(THIS PAGE INTENTIONALLY LEFT BLANK)

FIGURES

FIGURES (cont'd)

FIGURES (cont'd)

FIGURES (cont'd)

TABLES

(THIS PAGE INTENTIONALLY LEFT BLANK)

ACKNOWLEDGMENTS

This report was prepared to document work performed by the Center for Nuclear Waste Regulatory Analyses (CNWRA) for the U.S. Nuclear Regulatory Commission (NRC) under Contract NRC-02-93-005. The activities reported herein were performed on behalf of the NRC Office of Nuclear Regulatory Research (RES), Division of Regulatory Applications. The report is an independent product of the CNWRA and does not necessarily reflect the views or regulatory position of the NRC.

Active support from several people during the production of this report is thankfully acknowledged. First and foremost, this report is possible only because of the wholehearted cooperation from the principal investigators and researchers within each project who kept to the tight schedule of the editor. Technical reviewers—R.G. Baca, D.A. Ferrill, C.J. Freitas, V. Kapoor, P.C. Lichtner, H.L. McKague, W.M. Murphy, P.K. Nair, E.C. Pearcy, J.L. Russell, and S.A. Stothoff—provided substantive comments that materially improved the quality of the report. Programmatic reviews were performed by W.C. Patrick and the editor. Able secretarial support was provided by E.F. Cantu, B.P. Caudle, L.F. Gutierrez, M.A. Gruhlke, B.L. Garcia, C. Garcia, F.A. Masterson, A. Ramos, and R.A. Sanchez. Southwest Research Institute (SwRI) Publications Services staff provided illustration, editorial, and format adherence support.

Finally, the valued interaction with NRC project officers—G.F. Birchard, L.A. Kovach, T.J. McCartin, M.B. McNeil, T.J. Nicholson, J. Philip, and J.D. Randall—is gratefully acknowledged.

QUALITY OF DATA, ANALYSES AND CODE DEVELOPMENT

DATA: Sources of data are referenced in each chapter. CNWRA-generated laboratory and field data contained in this report meet quality assurance requirements described in the CNWRA Quality Assurance Manual. For all other data, their respective sources should be consulted for determining their level of quality assurance.

ANALYSES AND CODES: Scientific/engineering computer codes used in analyses contained in this report are: VTOUGH (Chapter 2), UDEC (Chapter 3), FITEQL and MINTEQA2 (Chapter 6), and ARC/INFO Geographic Information System (GIS) (Chapters 8 through 11). Only the computer code UDEC is presently controlled under the CNWRA Software Configuration Procedure TOP-018.

(THIS PAGE INTENTIONALLY LEFT BLANK)

1 EXECUTIVE SUMMARY

1.1 INTRODUCTION

Progress from July 1 to December 31, 1993, on 10 of 12 research projects underway at the Center for Nuclear Waste Regulatory Analyses (CNWRA) is discussed in this report. All 12 projects are sponsored by the U.S. Nuclear Regulatory Commission (NRC) to fulfill its mandate under the Nuclear Waste Policy Act (NWPA), as amended. In this regard, it is important to recognize that the NRC regulatory responsibilities are distinct from those of the U.S. Department of Energy (DOE), which is responsible for siting, constructing, and operating a repository for the disposal of high-level nuclear waste (HLW). The DOE has undertaken the development and implementation of a broad range of techniques and methods to obtain information and produce analyses necessary to determine site suitability, design the engineered portions of the repository, and complete a license application. In fulfilling its responsibilities for assuring the radiological health and safety of the public, the NRC conducts confirmatory and exploratory (also referred to as anticipatory) research to:

- Develop the licensing tools and technical bases necessary to judge the adequacy of the DOE license application
- Ensure a sufficient independent understanding of the basic physical processes taking place at the proposed geologic repository site
- Maintain an independent, but limited, confirmatory research capability to be used in evaluating DOE prelicensing and license application submittals

Figure 1-1 depicts the basic relation between NRC research program and licensing needs. Regulations applicable to the licensing of a HLW repository (primarily 10 CFR Part 60) are translated into regulatory requirements, each of which must be met before the NRC staff can recommend the issuance of a license. Strategies and methods for determining if DOE demonstration of compliance with the regulatory requirements is acceptable are currently being developed and documented in the NRC License Application Review Plan (LARP). Key technical uncertainties (KTUs) are defined based on the risk to compliance determination. Evaluation and reduction of the KTUs are the primary objectives of the research undertaken by the NRC. Each chapter of this report outlines the specific KTUs being addressed by the research described in that chapter.

Each of the research projects discussed herein is being conducted in accordance with approved Research Project Plans, which were developed consistent with the NRC statement-of-work. These plans are the vehicle for establishing the objectives, technical approach, justification, and funding for each of the studies. They also describe the interrelationships among the various projects, which provide a sound basis for integrating research results. Because the plans primarily address planning and management matters, they are not discussed further in this report (with the exception of stating project objectives).

This document provides an executive summary that covers, in capsule form, the progress of each research project over the past 6 months. The executive summary is followed by Chapters 2 through 11, representing each of the 10 currently active research projects. Project objectives and a report of research activities and results (as appropriate) to date are given in each chapter. Progress toward fulfillment of identified research needs and development of particular regulatory products is addressed

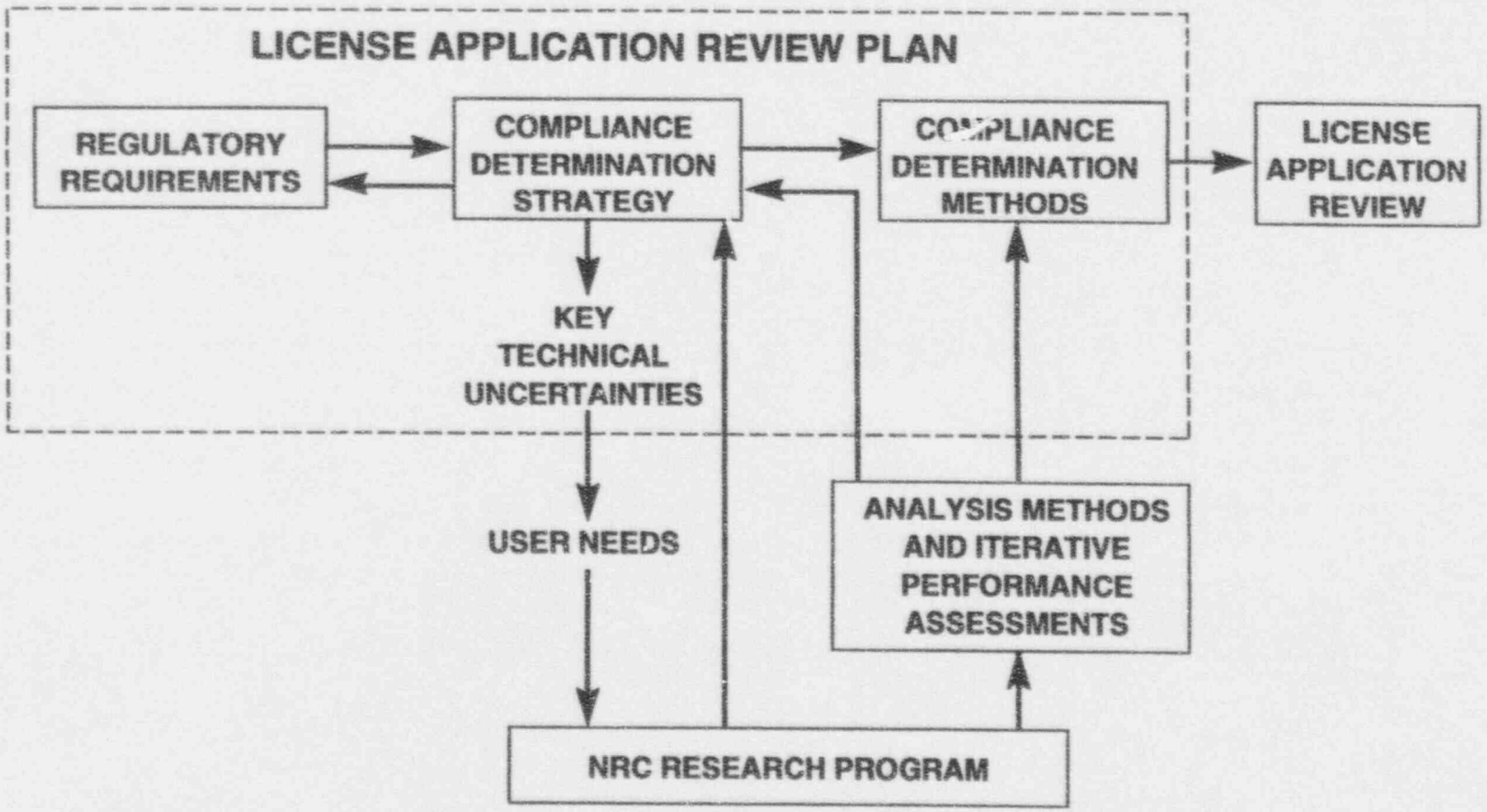

Figure 1-1. Relationship of NRC HLW Research Program to licensing needs

in cases where such progress has been significant. In addition, commentary is provided on anticipated progress for each project in the ensuing 6-month period. Two research projects not reported are: (i) Stochastic Analysis of Flow and Transport, and (ii) Unsaturated Mass Transport. These projects will be concluded in March 1994, and their findings will be reported in separate topical reports.

1.2 THERMOHYDROLOGY

The objective of the Thermohydrology Research Project is to understand thermohydrologic mechanisms as they affect the overall performance of a geologic high-level waste (HLW) repository and the performance of the multiple barrier system. Redistribution of moisture in response to the heat-generating waste emplaced in partially saturated medium is the primary process studied in this project.

Information developed within the Thermohydrology Research Project will be used to support specific portions of the LARP. Results gained from this research project will provide practical experience and knowledge applicable to the review of descriptions of the individual systems and characteristics of the site (Sections 3.1.1, 3.1.2, 3.1.3, and 3.1.5). Similarly, these studies will provide an information base for the development of portions of the LARP relating to both favorable and potentially adverse thermohydrological conditions (Sections 3.2.2.1, 3.2.2.2, 3.2.2.3, 3.2.2.4, 3.2.3.1, 3.2.3.2, 3.2.3.4, 3.2.3.5, and 3.2.3.7). The Thermohydrology Research Project provides an opportunity to assess the interaction of the thermal impact of the HLW upon water present in the repository environment. This knowledge will be critical in the development and support of Section 2.3, Assessment of compliance with the groundwater travel time (GWTT) performance objective; Section 2.4, Effectiveness of natural barriers against the release of radioactive material to the environment; and Section 2.1, Description of engineered systems and components that provide a barrier between the waste and the geologic setting.

Laboratory-scale experiments and analyses have been designed and conducted for the investigation of moisture redistribution. Information gained from the conduct of past experiments has aided in the formulation of subsequent experiments with more narrowly focused objectives. Recent experiments have been designed to address those mechanisms that dominate processes such as advection- and buoyancy-driven water vapor transport and the preferential flow of fluids. An objective of these experiments is to identify simplified mathematical models that satisfactorily describe the dominant mechanisms that contribute to the transport of air, water, and heat.

Presented in this report is a reanalysis of dimensionless terms useful in evaluating the relative importance of factors affecting the movement of water, air, and heat through partially saturated fractured, porous media. This analysis can be useful in evaluating the nature of moisture redistribution caused by different heat loads. The issue of different heat loads imposed by alternate waste package densities within the repository has been raised with the prospect of an extended-dry repository. The analysis indicates that the relative importance of the driving mechanisms of liquids and gases, in particular water vapor, may be judged by a newly defined advection number which, can be interpreted as the ratio of the nonbuoyancy-induced pressure gradient to the buoyancy-induced pressure gradient. For advection numbers much greater than one, the fluid would generally flow in the direction of decreasing pressure, while for advection numbers much less than one, a circulatory motion will tend to develop.

A cylindrically shaped, laboratory-scale experiment has been designed and constructed at the CNWRA. The purpose of this experiment is to investigate the redistribution of moisture in the presence of a gas pressure gradient. Gas pressure gradients are expected to contribute significantly to moisture

redistribution, particularly under higher heat load conditions. Numerical simulations indicated that a permeability of less than 10^{-16} m^2 would be needed to generate significant gas pressure in the experiment. Associated with this task is a preliminary evaluation of a field study proposed by the U.S. Department of Energy (DOE). This study, the proposed Fran Ridge large block heater test, provides an opportunity to assess whether dimensional analysis and the identification of dominant mechanisms at the laboratory scale are also valid at a larger scale. Conclusions regarding this validity have yet to be reached.

The nature of the liquid and gas flow regimes for the large block test and the cylinder test has been characterized using a pressure-buoyancy analytical model and simulated numerically. Regimes in which either buoyancy-driven or advection-driven gas flows were predicted were consistent with and supported by the numerical simulations. Results from these analyses and simulations are reported in this document.

1.3 SEISMIC ROCK MECHANICS

Long-term deterioration of vertical emplacement boreholes and emplacement drifts (if in-drift emplacement is considered) and potentially enhanced near-field fluid flow resulting from the coupled processes are among the important concerns for safe high-level nuclear waste (HLW) disposal (Rojstaczer and Wolf, 1992; Wood et al., 1985; Hsiung et al., 1992; Kemeny and Cook, 1990; Hofmann, 1993; Waller, 1966; Muir-Wood and King, 1993). Repetitive seismic loads and thermal loads generated by decay of the emplaced waste are among the factors that could potentially cause rock degradation or change near-field flow patterns due to joint normal and shear deformations. Evidence in the literature (Rojstaczer and Wolf, 1992; Wood et al., 1985; Waller, 1966, Muir-Wood and King, 1993) indicates that the most likely serious effect of earthquakes on hydrology is changes in fracture permeability.

A key technical uncertainty (KTU) that has been identified, which could pose a high risk of noncompliance with the performance objectives of 10 CFR Part 60, is the ability to predict the long-term effects of repetitive seismic and thermal conditions on the degradation of emplacement drifts and boreholes that may have implications on the performance of the Engineered Barrier Systems (EBS), retrievability of waste, and long-term waste isolation, especially if some of these openings are left unfilled at closure. The objective of the Seismic Rock Mechanics Research Project is to conduct laboratory and field studies and theoretical analyses to develop techniques that could be used to predict the response of near-field rock mass at the proposed repository at the Yucca Mountain site when it is subjected to repetitive seismic and long-term temperature conditions. The techniques developed and the knowledge gained in this project are being used to support the development and implementation of portions of the License Application Review Plan (LARP) and prelicensing activities. The results of ongoing activities in Tasks 2, 3, and 9 are reported herein.

Task 2 included a comprehensive laboratory characterization of rock-joint behavior to obtain a better understanding of joint behavior under dynamic loading conditions and to develop a complete data set that can be used for evaluation of existing rock-joint models in Task 3. Observations of the laboratory experimental results on single-jointed rock specimens from the Apache Leap Site, Arizona, under cyclic pseudostatic, harmonic, and earthquake shear loading conditions have identified two important distinct features for a joint during shearing. The first finding is that the shear strength upon reverse shearing is less than that for forward shearing. The second is that the joint dilation resulting from forward shearing recovers during reverse shearing. Reverse shearing behavior is important because it can result from expected earthquake or thermal loading conditions. Failure to consider these two features of joint behavior

in underground structural design and performance analysis could result in (i) an overestimation of the stability of emplacement drifts and emplacement boreholes, and (ii) prediction of an incorrect pattern of near-field flow (including preferential pathways for water and gas).

Within the range of variation of the test input velocity or frequency, no noticeable effect of the input frequency on the peak joint shear strength and the joint shear strength for the reverse shearing was observed. Consequently, it is possible to ignore the effect of shearing velocity variations in evaluating joint behavior.

Task 3 includes two types of qualification studies on rock-joint models/computer codes. In the first phase, a few currently available computer codes were selected and evaluated against four benchmark problems that have closed-form solutions. Codes with an acceptable performance were candidates for the second phase of the qualification studies, in which the dynamic response of well-designed and executed laboratory experiments on single-joint rock specimens were to be analyzed. Among the five codes evaluated in the first phase study, UDEC and 3DEC were able to reproduce the analytical solutions of all four benchmark problems and the UDEC code was selected for the second phase study. In the second phase study, the constitutive equations of the Mohr-Coulomb, Barton-Bandis, and Continuously-Yielding models were evaluated explicitly to assess the ability of these models for joint behavior prediction. This evaluation was followed by assessment of the numerical implementation of these three models in the UDEC code by modeling the cyclic pseudostatic and dynamic tests on single-jointed Apache Leap tuff joints. None of the three rock-joint models was found to be able to simulate satisfactorily the joint shear experimental behavior during reverse shearing in which the shear strength is smaller than that at the end of the forward shearing. As observed from the laboratory cyclic pseudostatic and dynamic test results, this difference could be large depending upon joint profiles.

All three models assume an increasing nature of joint dilation (that is, the dilation does not decrease for either direction of shear). This assumption is not consistent with the joint dilation behavior observed in the laboratory. Laboratory results showed that a joint tends to recover from the forward shearing dilation during reverse shearing with a certain amount of hysteresis between the dilation and dilation-recovery curves. The dilation recovery can be complete. The implementation of these three models in the UDEC code closely follows the constitutive equations. Consequently, none of the three rock-joint models implemented in the UDEC code satisfactorily simulates the joint shear and dilation behaviors as observed from the laboratory cyclic pseudostatic and dynamic test results that appear to show different mechanisms between forward and reverse shearing. Furthermore, it has been found that the joint dilation in the Barton-Bandis joint model has not been implemented properly in the UDEC code.

Task 9 during the second half of 1993 included the **DE**velopment of **CO**upled models and their **VAL**idation against **EX**periments (DECOVALEX) Phase II modeling. The Near-Field Repository Model (BMT3), one of two problems for this phase, was analyzed by the NAC-CNWRA team during this period using the UDEC computer code. Due to the complexity in the specified fracture geometry for the BMT3 problem, simplifications had to be made in the UDEC analysis. Two different UDEC models were run, each having a different extent of fracturing included in the model. The results of the two analyses show that the mechanical response does not vary much between the two models, indicating that the much simpler model would likely suffice for the mechanical analysis. The hydrologic response was more sensitive to the degree or extent of fractures included in the UDEC model, resulting in larger variations in flow rates between the two models. A preliminary comparison of the UDEC results with those obtained by two other research teams is given, however, further discussion among the teams is needed in order to clarify the reasons for any discrepancies.

1.4 INTEGRATED WASTE PACKAGE EXPERIMENTS

The NRC regulation 10 CFR 60.113 requires waste packages to provide substantially complete containment of radionuclides for a minimum period of 300 to 1,000 yr. As stated in the License Application Review Plan (LARP) 5.4, Sections 2.2.2 and 2.2.3, the Key Technical Uncertainties (KTUs) in the assessment of Engineered Barrier System (EBS) compliance with performance objectives include the prediction of environmental effects on the performance of waste packages and the EBS, and the extrapolation of short-term laboratory and prototype test results to predict long-term performance of EBS components. The goal of the Integrated Waste Package Experiments (IWPE) program is to provide a critical evaluation of the information available for assessment of compliance with regulatory requirements pertaining to the EBS by a suitable combination of literature surveys and critical experiments. Because the current waste package concept relies on a thin-walled metal container, most of the current effort in the IWPE program is focused on the degradation modes of candidate container materials. To achieve its objectives, the IWPE program is divided into six tasks: Task 1—Corrosion, Task 2—Stress corrosion cracking, Task 3—Thermal stability of materials, Task 4—Microbially influenced corrosion, Task 5—Other degradation modes, and Task 6—General reporting. The results of ongoing activities in Tasks 1 and 2 are reported in Chapter 4.

The general approach to long-term life prediction of container materials subject to localized corrosion conditions is pointed out along with the role of experimental investigations. Two of the parameters used in this approach are the initiation and repassivation potentials for localized corrosion. In performance assessment (PA) calculations, experimentally determined repassivation potentials are used to predict the occurrence of localized corrosion of waste package containers. These empirical parameters are then justified by more detailed models separate from the PA codes. Experimental investigations of the mechanistic aspects of the repassivation potential to verify model predictions and aid detailed model development were performed in this reporting period. To understand the mechanisms of repassivation of a pit or crevice, the chemical changes within the pit/crevice as a function of external potential need to be studied.

The experimental results reported in this section are compared with the predictions of a crevice corrosion model, TWITCH (Walton and Kalandros, 1992), developed as part of the Engineered Barrier System Performance Assessment Codes (EBSPAC) (Sridhar, et al., 1993). The crevice corrosion model, similar to many such models in the literature, assumes that the pH inside the crevice becomes lower and the chloride concentration higher until a critical concentration is reached, which results in the initiation of active crevice corrosion due to the destabilization of the protective passive film on the metal surface. The experimental results, however, indicate that the change in pH and chloride concentration inside a crevice lags behind the increase in corrosion of the crevice. Further, the model does not predict any effect of externally applied potential on crevice corrosion, since a potential-independent current is assumed. In contrast, experiments indicate that a higher externally applied potential results in faster changes in crevice chemistry. These basic discrepancies between the model and experiments are speculated to be due to several causes, including the dissolution of secondary particles in the alloy such as manganese sulfides and the rough nature of the metallic surfaces. The roughness results in variable crevice gap. Crevice corrosion may initiate in regions of extremely small gaps by the mechanism proposed by the models, but needs a high enough potential to propagate into adjoining areas. Since a reasonably large volume of solution is required for the microelectrodes used in these experiments to detect changes in solution composition, whereas local changes in current density can be detected more sensitively, a lag time between the two events may be expected. Another interesting result is that, upon repassivation, the

changes in solution composition back to the original values are much more sluggish than changes in the corrosion rate. This observation suggests that the mechanism of repassivation in deep pits or crevices is related to variations in the corrosion potential of the metal inside the crevice rather than changes in solution composition. These results point to directions for future modifications in the model for crevice corrosion so that the repassivation potential can be predicted.

The applicability of critical potentials of localized corrosion for predicting stress corrosion cracking (SCC) is being explored using slow strain rate and constant-deflection tests on type 316L stainless steel and alloy 825. The results generated thus far are consistent with the assumption that in chloride-containing solutions SCC is initiated above a critical potential related to the repassivation potential for localized corrosion. Stress corrosion cracking of type 316L stainless steel was induced in slow strain rate tests by concentrated chloride solutions (>9.1 moles/kg water) and at lower chloride concentrations by the presence of thiosulfate. However, no SCC was observed with that technique at chloride concentrations lower than 6 moles/kg water, even in the presence of thiosulfate. On the other hand, SCC was observed on type 316L stainless steel, but not in alloy 825, using U-bend specimens in constant-deflection tests conducted in more dilute solutions containing thiosulfate. It was noted that the susceptibility to localized corrosion and cracking is more pronounced in areas of the specimens in which a liquid film is formed on their surfaces above the vapor/solution interface. As expected, alloy 825 was found to be far more resistant to SCC than type 316L stainless steel. The need to study crevice conditions and concentration processes at the vapor/liquid interface leading to the initiation of cracks is emphasized.

1.5 GEOCHEMICAL ANALOGS

The Geochemical Natural Analog Research Project was initiated to develop a better understanding of the usefulness and limitations of natural analog studies when employed to support a license application for a high-level waste (HLW) repository and to provide fundamental data on the long-term behavior of HLW within a repository environment. Field and literature data were used to select two sites for analog research: the Nopal I uranium deposit in the Peña Blanca district, Chihuahua, Mexico, and the Akrotiri archaeologic site on Thera (Santorini), Greece. This report describes recent results from the Akrotiri site.

Study at the Akrotiri analog is focused on elemental transport from metallic artifacts into silicic tuffs; these artifacts were buried for 3,600 yr under conditions comparable to those anticipated for the proposed Yucca Mountain repository. Samples have been collected of corrosion products from bronze artifacts discovered in room Delta 3 of the Akrotiri excavation. Mineralogic analyses of these corrosion products show them to be composed largely of cuprite (Cu_2O) and paratacamite [$Cu_2(OH)_3Cl$]. Chemical analyses of corrosion products show compositions dominated by Cu and Cl with minor Fe, Ti, and Ag.

Field measurements of current hydraulic properties and interpretations of past hydrologic conditions have placed constraints on these factors. Field measurements were conducted of moisture content, matric potential, saturated hydraulic conductivity, sorptivity, and unsaturated hydraulic conductivity of both the Minoan tuff through which infiltrating waters flowed to the anthropogenic horizon at Akrotiri and the underlying Cape Riva tuff, into which trace metals from the artifacts have been transported. An intermittent stream is interpreted to have been significant to the infiltration of water into room Delta 3. Based on observations of local topography, the size of the drainage basin feeding the stream has been estimated at 0.5 km^2. Using historical meteorologic data, constraints have been placed on conditions likely to produce intermittent flow through the stream. Field observations of locally present

alluvial deposits suggest that deposition of this material was probably synchronous with Minoan volcanism rather than associated with subsequent fluvial activity in the stream valley.

1.6 SORPTION MODELING FOR HIGH-LEVEL WASTE PERFORMANCE ASSESSMENT

Performance Assessment (PA) models traditionally use a purely empirical approach to represent contaminant sorption on geologic materials. These models are unable to account for the effects of changes in solution and solid chemistry on sorption processes. Surface complexation models (SCMs) have been developed and used to quantitatively account for these changes in modeling the complex behavior observed in experimental studies of the sorption of toxic species such as Zn^{2+}, Cd^{2+}, Pb^{2+}, and CrO_4^{2-} on simple (hydr)oxides. Recent studies have begun to provide similar sorption data for radionuclides, particularly the actinides, and the extension of SCM methods to radioelement systems and more complex multioxides such as clays and zeolites is a necessary step in applying developing mechanistic approaches to sorption modeling for performance assessment at Yucca Mountain (YM).

The research presented here builds on work done earlier in Task 2, using parameters developed for the relatively simple Diffuse Layer (DLM) surface complexation model to characterize a number of simple (hydr)oxides. Using experimental data from Task 3, the DLM is able to reproduce the observed effects of surface-area/solution-volume ratio on uranium(6+) sorption on α-alumina assuming a single surface complex of XOH_2-$(UO_2)_2CO_3(OH)_3^0$. The DLM was also applied to the sorption of uranium(6+) on kaolinite and clinoptilolite and neptunium(5+) sorption on biotite by assuming stoichiometric proportions of silanol ($SiOH^0$) and aluminol ($AlOH^0$) sites at the mineral surface. In all cases, the fit is reasonably good, but more than one type of surface complex is required to reproduce the observed sorption behavior. Similar results for different postulated surface complexes illustrate one limitation of the SCM approach. However, independent evidence from spectroscopic investigations may be able to further limit the focus to a relatively few possible complexes formed at the surface. Although SCMs present an idealized mineral/water interface and are not strictly mechanistic at the atomic level, they do have a sound theoretical basis and employ physically and chemically reasonable representations of the mineral surface. Because of this theoretical basis, these models are able to account for changes in system chemistry in a quantitative way that purely empirical approaches cannot.

To develop an understanding of radionuclide sorption processes and the important physical and chemical parameters that affect sorption behavior in the YM environment, experiments are being conducted to investigate the sorption behavior of uranium on geologic media. During the second half of 1993, experiments were completed to determine the possible effects of pH, uranium concentration, and ionic strength on the sorption of uranium(6+) on clinoptilolite, which is the predominant zeolite mineral occurring underneath YM, Nevada. In addition, because surface adsorption is the predominant mechanism for uranium sorption and because the ratio of fluid-volume to mineral-surface-area can vary significantly along a fluid flow-path, experiments were also conducted to determine the effect of solid-surface-area to solution-volume ratio on uranium(6+) sorption. The latter experiments, which used α-alumina as the sorbent phase, also provided information on possible differences in uranium sorption behavior on different types of minerals.

The results showed that uranium sorption on both clinoptilolite and α-alumina is strongly dependent on pH. The amount of uranium sorbed increases sharply at pH values above about 4.0 (adsorption edge) and decreases sharply at pH values above about 6.5 (desorption edge). It reaches a

maximum value at pH ~ 6.3. Experiments at various initial ΣU using clinoptilolite showed that the %U sorbed increases with decreasing initial ΣU, although the relative increase in %U sorbed is smaller at lower ΣU. Data from the reverse experiments indicated that the uranium sorption reactions are reversible. Sorption studies using α-alumina and variable sorbent-surface-area/solution-volume ratio demonstrated that, at constant pH, the total uranium sorbed increases as the surface-area-to-volume ratio increases, although the increase is not directly proportional to the surface areas of the α-alumina powders. The adsorption and desorption edges at higher surface-area/solution-volume ratios enclose those at lower ratios, that is, at a fixed volume of solution, the adsorption edge shifts to more acidic pH with increasing surface area of α-alumina, whereas the desorption edge shifts to more alkaline pH. A similar shift in adsorption/desorption edges with increasing surface area was reported by Tripathi (1984) for uranium(6+) sorption on the iron oxide mineral goethite.

Results of control experiments, which were designed to quantify the amount of uranium lost from solution due to sorption onto fluorinated ethylene propylene (FEP) Teflon® container walls, showed that significant amounts of uranium are lost to the container, particularly at low initial ΣU. Container sorption is strongly dependent on solution pH and reaches a maximum at pH values between 5.0 and 6.0. The pH at which maximum container sorption occurs shifts to more acidic conditions with decreasing initial ΣU. These results demonstrate that sorption and retardation experiments must be well-constrained with respect to experimental artifacts, such as container losses, in order to get meaningful results.

A comparison of uranium sorption on clinoptilolite results in a 0.1 or 1.0 m $NaNO_3$ matrix showed that an increase in ionic strength decreased both the overall sorption and container sorption. However, after correcting for container losses, the data indicated that the relative amounts of uranium sorbed on clinoptilolite did not significantly change with the change in ionic strength.

Results of these laboratory experiments provide an understanding of the important parameters that control the sorption behavior of uranium. Because of the strong dependence on pH and sorbent-surface-area/solution-volume ratio, modeling of sorption processes will likely require that changes in groundwater chemistry and in rock/fluid ratio be appropriately accounted for in performance assessment calculations if retardation by sorption processes is included. The similarity in the pH dependence of uranium sorption on clinoptilolite and α-alumina is important. It may help identify simplified approaches to modeling sorption and thus help in the development of Compliance Determination Methods (CDMs) relevant to the Key Technical Uncertainties (KTUs) identified in Section 6.1 of the LARP and in developing conceptual models related to the PA Research Project and the Iterative Performance Assessment (IPA) Phase 3. The information derived from the laboratory experiments may also help interpret data on uranium distribution and migration at the Peña Blanca field site of the Geochemical Natural Analog Research Project.

1.7 PERFORMANCE ASSESSMENT RESEARCH

The primary programmatic objectives of this project are threefold. The first objective is to provide modeling technology that will benefit the U.S. Nuclear Regulatory Commission (NRC) Iterative Performance Assessment (IPA) activity and the development of methodologies that will be used in compliance determination methods (CDMs). A second, and equally important, objective is to address key technical uncertainties (KTUs) associated with conceptual models, mathematical models, model parameters, future system states (i.e., disruptive scenarios), and model validation. The third objective is to provide the technical basis for formulating guidance to the U.S. Department of Energy (DOE) in the

specific areas of PA modeling approaches and validation strategies. Research conducted under the Performance Assessment (PA) Research Project is divided among three major tasks: Task 1—Conceptual model development, Task 2—Computational model development, and Task 3—Model evaluation. In this reporting period, a strong emphasis was given to Task 1, which includes research on hydrologic conceptual models and disruptive event scenarios. Research on disruptive event scenarios was given the highest priority. At a lower level priority, research was performed on: (i) Analysis of hydrologic data from the Peña Blanca site (Task 1), (ii) Evaluation of a new computational technique for flow and transport modeling (Task 2),; and (iii) Model validation exercise using the INTRAVAL data set for Yucca Mountain (Task 3).

Work on disruptive event scenarios (i.e., future system states) was given high priority in accordance with technical direction from the NRC project officer. Disruptive event scenarios are an important element of the NRC IPA exercises and provide the basis for estimating how well the geologic repository may perform under combinations of adverse events and processes. In this reporting period, the major portion of staff effort was devoted to two related activities: (i) an independent review and critique of the four IPA disruptive event scenario types; and (ii) a state-of-the-art review of the scenario-selection approaches. The first activity produced a detailed letter report containing recommendations for improvement of the current IPA scenario models and modules. These recommendations are expected to be incorporated into the NRC/CNWRA plan for the IPA Phase 3 exercise. The second activity produced a technical report (Bonano and Baca, 1994), which will be issued concurrent with this document. The report shows that many countries are using approaches very similar to the NRC/Sandia National Laboratories (SNL) scenario methodology used in IPA. Only the United Kingdom is utilizing a truly distinct approach that is based on environmental simulation. The report identifies a number of open generic issues in scenario analysis such as the validity of estimates of probability of occurrence, lack of uniqueness or completeness of scenarios, as well as the role of expert judgment in these issues. The subject document is expected to contribute to the formulation of guidance on disruptive scenarios. Research on conceptual models of flow and transport in fractured-porous tuff was also performed jointly with the Geochemical Analog of Contaminant Transport in Unsaturated Rock Research Project, however a discussion of progress will be included in the next reporting period.

Limited work was performed on identifying advanced computational methods that can reduce the current computational constraints of the IPA total-system PA code, total performance assessment (TPA), and of the various codes used in both auxiliary analyses and subsystem PAs. The experience gained in the recently completed IPA Phase 2 exercise, for example, has shown that the TPA requires an extremely long execution time (e.g., 160 hr on a Cray X/MP supercomputer), which is almost cost prohibitive. It was also found that some of the detailed codes for flow and transport modeling not only required long execution times and large memory, but also, in certain instances, encountered numerical instabilities. In an effort to identify more efficient, accurate, and robust computational techniques, an initial evaluation was performed of a new computational method referred to as the method of contours. This method appears to have a unique capability to accommodate the hyperbolic behavior of the governing equations.

In the previous reporting period, work was initiated on the INTRAVAL model validation exercise using the Yucca Mountain test case. The validation exercise, as posed to the INTRAVAL modelers, was to use rock-hydraulic property data, detailed microstratigraphic data, and measured saturation profiles in near-surface boreholes and then to predict the saturation profile at a yet-to-be-drilled borehole. For this exercise, a conceptual model of the hydrostratigraphic setting was formulated. Initially, general finite-difference and finite-element computer codes were applied to model the unsaturated flow

in a one-dimensional (1D) column. Because of numerical problems encountered (i.e., long computer execution times and nonconvergent results), a simple 1D, steady-state flow code was developed. The code was applied using a composite fracture-matrix formulation for the unsaturated hydraulic conductivity function. The model application and comparison with field data were completed. The steady-state model results, although indicating reasonable agreement with the field data, suggest that measured water contents by themselves reveal little about the nature of infiltration processes. This observation is supported by the fact that disparate conceptual models can produce calculated moisture profiles that are very reasonable matches to the field data.

1.8 VOLCANIC SYSTEMS

Characterization of the frequency and nature of past volcanic events in the Yucca Mountain region (YMR), and assessment of the probability and consequences of future volcanism, are critical aspects of prelicensing scientific investigations. The technical objectives of the Volcanic Systems of the Basin and Range Research Project are to: (i) assess the probability of continued magmatic activity in the YMR, (ii) develop models that better predict the interaction between geologic structure and volcanism in this tectonic setting, and (iii) develop scenarios for the impact of volcanism on the candidate Yucca Mountain repository. These studies will provide prelicensing guidance to the U.S. Department of Energy (DOE) and are critical to license application review, as evidenced in specific sections of the License Application Review Plan (LARP) (Section 3.2.1.9, Evidence of igneous activity as a potentially adverse condition; Section 3.2.2.7, Impact of volcanism on groundwater movement; and Section 6.1, Assessment of compliance with the requirement for cumulative releases of radioactive materials). The Volcanic System of the Basin and Range Research Project has been designed to assess the probability of future volcanism in the YMR, taking into account the range of activity and structural controls on activity that are an inherent part of western Great Basin volcanism.

During the last six months, work has concentrated on assessing geochronological methods used to date Quaternary and Neogene basaltic rocks in the YMR. This assessment presents overviews of the general principles for dating techniques used in the YMR, discussions on the limitations and uncertainties associated with these techniques, and an evaluation of dates produced by these techniques for basaltic rocks of the YMR (Hill et al., 1993). It was found that to evaluate the precision of a series of dates adequately, nonaveraged data must be presented because reported averages usually do not account for large precision errors. Available geologic, geochemical, and geochronological data for four Western Great Basin volcanic fields have been compiled and entered into the CNWRA geographic information system (GIS). These data are used to test the hypothesis of Crowe et al. (1993) that basaltic volcanoes of the Basin and Range province tend to form at low elevations in alluvial basins. It was found that Crowe et al. hypothesis was not valid. Probability model development included incorporation and evaluation of volcano age uncertainties into models and publication of initial probability models (Connor and Hill, 1993). A more detailed examination of spatially nonhomogeneous Poisson probability models for volcanic eruption is in final peer review for publication in Geophysical Research Letters.

1.9 TECTONICS PROCESSES

The objectives of the Tectonics Research Project are: (i) to compile and integrate tectonic data for the central Basin and Range and Yucca Mountain (YM) regions, and (ii) to develop and assess models of tectonic processes. The purpose of the project is to evaluate the adequacy of existing data, methods, and models for demonstrating and determining compliance with regulatory requirements. Of particular

concern is the adequacy of existing and anticipated data for quantitatively assessing compliance with waste-isolation performance objectives. A Geographic Information System (GIS) is being used to compile data from disparate sources into an integrated management, review, and analysis environment. Significant technical accomplishments to date consist of: (i) development of digital terrain models of the YM and central Basin and Range regions; (ii) production of integrated maps of Quaternary faults, Quaternary basaltic volcanic fields, and historic earthquake seismicity; and (iii) compilation of an initial database of geodetically measured regional strain and geologically determined slip rates for individual fault systems. Data and references compiled by Tectonics Research project staff have been used to develop Compliance Determination Strategies (CDSs) on Structural Deformation [License Application Review Plan (LARP) No. 3.2.1.5], Evidence of Igneous Activity (LARP No. 3.2.1.9), and Structural Deformation and Groundwater (LARP No. 3.2.2.8). Digital terrain and boundary data, and visualization methods developed for tectonics research are also being used in the regional hydrogeology research project.

Significant technical accomplishments since the last report include: (i) digitization of a substantially more detailed Quaternary fault coverage in the Tectonics Research Geographic Information System (TecResGIS) and improved correlation with large earthquakes, (ii) field work to assist in conducting U.S. Nuclear Regulatory Commission (NRC)/California Institute of Technology (CalTech) Global Positioning Satellite (GPS) survey in the YM region, and (iii) completion of a literature review on geochronological methods used to determine slip history of faulting.

Detailed maps of Quaternary fault traces have been digitized and coregistered with the current catalog of earthquake hypocenters. The resultant map provides improved regional correlation of earthquakes with discrete ground-rupturing fault segments. The map also distinctly shows areas where mapping of Quaternary fault traces is inadequate. Regional correlations of earthquakes, Quaternary faults, Holocene faults, and historical ground rupture indicate which of the fault systems are seismically active, and are required to estimate more precisely the return period of seismic activity on systems of discrete fault segments. Comprehensive regional compilations are also needed to determine if existing data are sufficient to adequately describe temporal and geographic patterns of seismicity and faulting. At this time, it is not clear that existing data are sufficient to characterize these patterns.

The GPS survey stations have been established in the Death Valley-YM region. The purpose of this survey is to directly investigate contemporary strain in the region and to improve understanding of its influence on geographic distribution and timing of faulting. This task is expected to yield direct measurements of modern tectonic displacements, a result that will lead to considerably improved estimates of earthquake and fault rupture risk. Funding for this task has been provided directly to CalTech from NRC Research; the CNWRA Tectonics Research Project provides for direct participation of the CNWRA staff in the NRC/GPS project.

The literature survey on paleoseismology and geochronology of faulting was completed during this period. The primary objective of this survey is to assess the utility and reliability of methods used to investigate slip history of Quaternary faults. Identification of paleoseismic events in the field (e.g., investigations of fault displacements in trenches and along fault scarps), selection of samples, and careful age estimates of samples selected are essential for quantifying fault slip rates and earthquake recurrence intervals. Uncertainty in age estimates are significant sources of uncertainty in quantitative analyses of existing tectonic models and for developing alternative models. Considering possible complexities resulting from tectonic, erosional, and depositional modification of the stratigraphy and materials available for age determinations, four methods appear potentially applicable at YM for estimating ages of Quaternary faulting events: Carbon-14, Uranium-series (U/Th), Thermoluminescence (TL), and Electron

Spin Resonance (ESR). Carbon-14, U/Th, and TL techniques are applicable to surficial materials (including fault-scarp-derived colluvium and associated soils) and provide maximum or minimum ages of faulting. The ESR method is applicable to quartz in fault gouge and is the only method that directly provides an estimated age of latest fault movement. ESR is also the most experimental of the four techniques discussed. Fault gouge samples to be analyzed must have been at a depth around 250 m when fault movement produced the gouge. ESR may be especially useful for estimating age-of-slip of faults intersected during excavation of the Exploratory Studies Facility (ESF) or other underground facilities at YM.

1.10 FIELD VOLCANISM

The technical objectives of the Field Volcanism Project are to better characterize the impact of volcanism on repository performance and, as a result, better constrain probability models of volcanic disruption of the repository. This characterization is possible through investigation of: (i) mechanics of mafic cinder cone eruptions, (ii) extent and characteristics of shallow hydrothermal and diffuse degassing associated with small volume cinder cone eruptions, and (iii) nature of mafic intrusion geometries and controls on dike propagation in the lithosphere. These studies are critical to provide prelicensing guidance to the U.S. Department of Energy (DOE) and in the license application review, as evinced in specific sections of the License Application Review Plan (LARP) (Section 3.2.1.9, Evidence of igneous activity as a potentially adverse condition; Section 3.2.2.7, Impact of volcanism on groundwater movement; and Section 6.1, Assessment of compliance with the requirement for cumulative releases of radioactive materials). Defensible promulgation of conclusions about probability and consequences of potential volcanic activity in the Yucca Mountain Region (YMR) requires study of Plio-Quaternary cinder cones in the western Great Basin and comparison with modern, recently active cinder cones located elsewhere. Preliminary calculations of the complementary cumulative distribution function (CCDF) for the exceedence probability of normalized release indicates that, although volcanism alone is not likely to disqualify the candidate repository, volcanism does represent a potentially adverse condition. Different models of volcanic activity, from gentle effusive eruptions to normal explosive eruptions, have substantially different impacts on the CCDF, indicating that different eruptive scenarios have an important impact on performance assessment (PA) studies.

To provide confidence, probability models of the potential for volcanic disruption of the repository should incorporate as much geologic information as possible. Dike interactions with pre-existing structures, such as faults, may lead to a focusing of magmatism if these weaknesses can redirect ascending magmas. The analytical model developed as part of the Field Volcanism Research Project suggests an upper bound on the ability of regional crustal structures to focus magmatism. At greater depths, that is, more than 1 km, only high-angle faults can capture and redirect magmas ascending in dikes. At shallow depths, that is, less than 1 km, low-angle faults can redirect magmas. However, at these shallow depths, there is little opportunity for large lateral transport of these magmas, especially because free-surface effects will act on magmas ascending in fault planes at shallow depths. Based on these considerations there is little opportunity for fault planes to capture and transport magmas for map distances of greater than 2 km and never greater than 5 km. This theoretical result would suggest that: (i) knowledge of fault geometry as a function of depth could provide important insight into the likelihood that given faults will focus magma should it ascend through crust in the YMR, and (ii) probability models of volcanic disruption of the candidate repository may be affected by structural controls on magmatism, but only at a local, rather than regional scale. It is emphasized, however, that these models are

preliminary and will be tested using field data, where direct comparisons of dike and fault interaction can be made, and through the study of cinder cone alignment development.

Diffuse degassing at cooling cinder cones produces mass flow and temperature conditions that are not otherwise anticipated for the candidate repository. Conceptual and numerical models, based on steady-state, boundary value solutions, indicate that diffuse degassing measured at the surface can provide a useful measure of heat and mass transfer conditions at depth. Based on the results of a preliminary soil Hg survey, it is clear that degassing is taking place over a broad zone at Cerro Negro volcano. Anomalous soil gas flux has been identified at distances of up to 700 m from the most recently active vent and 17 months after the most recent volcanic activity. These findings indicate that additional measurements of soil degassing at cooling cinder cones will be required in order to fully assess the impact of volcanism on repository performance.

1.11 REGIONAL HYDROLOGY

Yucca Mountain (YM) has been proposed as a potential high-level nuclear waste (HLW) repository in part because of the favorable geochemical and hydrologic environment provided by its 700 m thick unsaturated zone. Siting the repository in the unsaturated zone may limit the potential for waste canister corrosion and dissolution of the waste form. Low water fluxes that are postulated to exist in the unsaturated zone limit the likelihood that dissolved radionuclides will be rapidly transported to the accessible environment. One mechanism that may saturate the repository horizon and compromise favorable conditions at the YM site would be an increase in the elevation of the regional water table. Elevation of the water table may occur due to increased recharge to the regional carbonate system from areas up to 100 km to the north and northeast of YM. Even if elevation of the regional water table does not saturate the repository block, the reduced thickness of the unsaturated zone may significantly diminish travel times in the vadose zone. The research project on Regional Hydrogeologic Processes of the Death Valley Region was initiated to improve understanding of the saturated groundwater flow regime at YM and to assess the influence of the regional flow system on the height of the water table beneath YM. The objectives of this research project are to: (i) analyze existing conceptual models and develop new conceptual models of the regional hydrogeologic flow regime in the Death Valley region that contains YM, and (ii) construct numerical models of regional flow which may be used to assess the potential for the water table beneath YM to rise in response to wetter climatic conditions.

Predictions made with numerical models will be used by the U.S. Department of Energy (DOE) in its license application to demonstrate that the YM site meets the overall performance standards outlined in 10 CFR 60.112 and the geologic subsystem performance standard defined in 10 CFR 60.113(a)(2). In addition, the DOE may choose to use numerical models to demonstrate the absence of potentially adverse conditions including: The effects of future pumping on the regional flow system [10 CFR 60.122(c)(2)]; The potential for deleterious changes to the hydrologic system [10 CFR 60.122(c)(5)]; The potential for changes to the hydrologic conditions resulting from climate change [10 CFR 60.122(c)(6)]; The potential for water table rise [10 CFR 60.122(c)(22)]; and The presence of favorable conditions, including the clear absence of fully saturated pathways connecting the repository to the water table [10 CFR 60.122(b)(8)(ii)]. Understanding of the regional hydrogeologic system developed from this project will be used to guide the review of the DOE license application and to assess the adequacy of the models used by the DOE to demonstrate compliance with the regulatory requirements and environmental standards.

Research in this project is divided into five tasks: (i) Collect and analyze data and existing models; (ii) Construct alternative conceptual models of key hydrogeologic processes in the Death Valley region of the Western Great Basin; (iii) Construct and calibrate mathematical and numerical models of subsurface flow at local, basin, and regional scales; (iv) Use geochemical data to evaluate and refine regional flow models; and (v) Apply models to analyze problems critical to repository performance. Tasks 1 and 2 are scheduled for completion during the first 2 yr of the project with the remaining tasks completed during the third and fourth years. Initial efforts have focused on Task 1. The technical objectives of Task 1 are to: (i) conduct literature reviews on current conceptual models of the regional flow regime; (ii) inventory hydrogeologic data collected from the Death Valley region; and (iii) integrate hydrogeological, hydrochemical, and mineralogical data into a GIS database.

Work has commenced on three activities in Task 1: (i) review of literature characterizing the hydrogeology and hydrogeochemistry of subbasins within the Death Valley region; (ii) collection of hydraulic, geologic, and geochemical data; and (iii) integration of data into a GIS database. For the first activity, estimates of water budgets for subbasins and evaluations of hydrochemical facies data from the Death Valley region have been prepared. For the second activity, hydraulic and water chemistry data have been obtained from the U.S. Geological Survey (USGS) and are being entered into the CNWRA ARC/INFO Geographic Information System (GIS). Only results for the first activity and a brief description of a field trip conducted to enhance understanding of the regional hydrology are reported.

An extensive body of technical literature outlining the hydraulic and hydrochemical information that has been used to construct conceptual models of the hydrogeology of the Death Valley region has been reviewed. These reviews have concentrated on identifying forces external to the flow system that may induce the water table to rise beneath YM and thus have been focused on defining recharge areas, discharge areas, and connecting flow paths. Hydrochemical facies and stable isotope data appear to be the most valuable tools for defining recharge locations, flowpaths, and regions where waters from different aquifers mix. Indeed, with the current paucity of hydraulic data from wells penetrating the carbonate aquifer beneath YM, hydrochemical data may provide the only information as to its source. The importance of geologic structures that control local and regional hydraulic gradients, such as the steep gradients north of YM and between Emigrant Valley and Yucca Flat, will be addressed in subsequent reports. Isotopic data from paleo-spring deposits indicate that the water table has fluctuated above current levels by as much as 115 m in the past. On the basis of previous modeling studies, it is hypothesized that the amplitude of water table fluctuations due to changes in recharge may be controlled by discharge at Franklin Lake Playa. Whether or not this postulated control is sufficient to preclude the water table from saturating the repository block during an extended period of substantially increased recharge will be addressed using predictive models to be developed in Task 3.

1.12 REFERENCES

Bonano, E.J., and R.G. Baca. 1994. *Review of Scenario Selection Approaches for Performance Assessment of High-Level Waste Repositories and Related Issues*. CNWRA 94-002. San Antonio, TX: Center for Nuclear Waste Regulatory Analyses (In preparation).

Connor, C.B., and B.E. Hill. 1993. Estimating the probability of volcanic disruption of the candidate Yucca Mountain repository using spatially and temporally nonhomogeneous Poisson models. *Proceedings, American Nuclear Society Focus '93 Meeting*. La Grange Park, IL: American Nuclear Society.

Crowe, B.M., F.V. Perry, and G.A. Valentine. 1993. *Preliminary Draft: Status of Volcanic Hazard Studies for the Yucca Mountain Site Characterization Project*. Los Alamos National Laboratory Report: Los Alamos, NM: Los Alamos National Laboratory.

Hill, B.E., B.W. Leslie, and C.B. Connor. 1993. *A Review and Analysis of Dating Techniques for Neogene and Quaternary Volcanic Rocks*. CNWRA 93-018. San Antonio, TX: Center for Nuclear Waste Regulatory Analyses.

Hofmann, R.B. 1993. Summary of the May 17-18, 1993, *CNWRA Advisors Meeting and Reports on Fault Displacement and Seismic Hazard Analysis*. CNWRA Report to the U.S. Nuclear Regulatory Commission. San Antonio, TX: Center for Nuclear Waste Regulatory Analyses.

Hsiung, S.M., A.H. Chowdhury, W. Blake, M.P. Ahola, and A. Ghosh. 1992. *Field Site Investigation: Effect of Mine Seismicity on a Jointed Rock Mass*. CNWRA 92-012. San Antonio, TX: Center for Nuclear Waste Regulatory Analyses.

Kemeny, J.M., and N.G.W. Cook. 1990. *Rock Mechanics and Crusted Stresses. Demonstration of a Risk-Based Approach to High-Level Waste Repository Evaluation*. EPRI-NP-7507. Palo Alto, CA: Electric Power Research Institute.

Muir-Wood, R., and G.C.P. King. 1993. Hydrologic signatures of earthquake strain. *Journal of Geophysical Research* 98(B12): 22,035-22,068.

Rojstaczer, S., and S. Wolf. 1992. Permeability changes associated with large earthquakes: An example from Loma Prieta, California. *Geology* 2:211-214.

Sridhar, N., J.C. Walton, G.A. Cragnolino, and P.K. Nair. 1993. *Engineered Barrier System Performance Assessment Codes (EBSPAC) Progress Report—October 1, 1992, through September 25, 1993*. CNWRA 93-021. San Antonio, TX: Center for Nuclear Waste Regulatory Analyses.

Waller, R. 1966. *Effects of the March 1964 Alaska Earthquake on the Hydrology of South-Central Alaska*. U.S. Geological Survey Professional Paper 544-B: 1-28.

Walton, J.C., and S.K. Kalandros. 1992. *TWITCH — A Model for Transient Diffusion, Electromigration, and Chemical Reaction in One Dimension.* CNWRA 92-019. San Antonio, TX: Center for Nuclear Waste Regulatory Analyses.

Wood, S.H., C. Wurts, T. Lane, N. Ballenger, M. Shaleen, and D. Totorica. 1985. The Borah Peak, Idaho Earthquake of October 28, 1983—Hydrologic Effects. *Earthquake Spectra* 2: 127–148.

2 THERMOHYDROLOGY

by Franklin T. Dodge and Ronald T. Green

Investigators: Franklin T. Dodge, and Steve J. Svedeman (SwRI); Ronald T. Green, Randall D. Manteufel, Kristi A. Meyer, and Hannah M. Castellaw (CNWRA)

NRC Project Officer: John D. Randall

2.1 TECHNICAL OBJECTIVES

The technical objective of the Thermohydrology Research Project is to provide laboratory, computational, and theoretical analyses of the thermal and fluid regimes to be expected proximal to heat-generating waste at the proposed high-level radioactive waste (HLW) repository at Yucca Mountain. This information is necessary to predict the performance of the overall system (10 CFR 60.112) and the performance of the barriers that comprise the subsystems of the repository—the Engineered Barrier System (EBS), 10 CFR 60.113(a)(1), and the Geologic Setting (GS), 10 CFR 60.113(a)(2). However, predicting the status of the environment of the repository is difficult because of the time and size scales associated with the proposed Yucca Mountain repository. The laboratory-scale analyses are designed to develop a better understanding of the coupled processes expected to be important at the repository but performed at a scale that will permit meaningful results to be gained in a reasonable time frame. To accomplish this objective, the principles of dimensional analysis are applied to laboratory-scale experiments in order to assess longer-time and larger-scale repository performance.

Information developed within the Thermohydrology Research Project will be used to support specific portions of the License Application Review Plan (LARP) (U.S. Nuclear Regulatory Commission, 1993). Fluid and temperature interactions observed at the laboratory scale and computational exercises conducted to apply these results to a more meaningful scale, such as the canister or repository scale, will provide practical experience and knowledge applicable to the review of description of the individual systems and characteristics of the site (Sections 3.1.1, 3.1.2, 3.1.3, and 3.1.5). Similarly, these studies will provide an information basis for the development of portions of the LARP relating to both favorable and potentially adverse thermohydrological conditions (Sections 3.2.2.1, 3.2.2.2, 3.2.2.3, 3.2.2.4, 3.2.3.1, 3.2.3.2, 3.2.3.4, 3.2.3.5, and 3.2.3.7), because these require information on the coupled flow of heat and water through partially saturated, fractured media. The Thermohydrology Research Project provides an opportunity to assess the interaction of the thermal impact of the HLW upon water present in the repository environment. This knowledge will be critical in the development and support of Section 2.3, Assessment of compliance with the groundwater travel time (GWTT) performance objective, and Section 2.4, Effectiveness of natural barriers against the release of radioactive material to the environment. Additionally, knowledge of the thermal and fluid regimes that will exist in the presence of heat-generating HLW will provide information needed to develop Sections 2.1, Description of engineered systems and components that provide a barrier between the waste and the geologic setting and 2.4, Assessment of compliance with the EBS performance objectives.

Information derived from results of the Thermohydrology Research Project will be germane in addressing Key Technical Uncertainties (KTUs) raised in several Compliance Determination Strategies (CDSs). For example, CDSs 3.3 and 5.4 have both been classified as requiring a Type 5 review, which requires independent research to resolve KTUs that pose a high risk of arriving at a wrong conclusion regarding compliance with the performance objectives and design criteria of 10 CFR Part 60. Specific

KTU topics that will be addressed by work within the Thermohydrology Research Project include the transient regimes of temperature and moisture that are expected to occur proximal to the emplacement of heat-generating HLW. These transient regimes are expected to affect many processes, including the travel time of groundwater, the performance of the EBS, geochemical transport, and thermomechanical mechanisms.

Information resulting from the Thermohydrology Research Project is of critical importance to investigations involving geochemistry, hydrogeology, and material science. This intrinsic reliance is demonstrated in the interaction that exists with other projects sponsored by the U.S. Nuclear Regulatory Commission (NRC) Office of Nuclear Regulatory Research (RES) projects at the Center for Nuclear Waste Regulatory Analyses (CNWRA). In particular, the Integrated Waste Package Experiments (IWPE) Research Project requires knowledge of the expected temperature and liquid saturation of the canister environment in order to determine the performance of the waste package. Of particular interest to the IWPE project is the duration of dry-out proximal to the canisters and the expected time and nature of rewetting. Similarly, the Geochemistry Research Project will base thermodynamic predictions upon the anticipated thermal and fluid regimes. Additionally, the Performance Assessment (PA) Research Project requires this same information for several aspects of the analyses that are conducted as part of the overall PA. Design information provided by the Geochemistry, EBS, and PA projects will assist the Thermohydrology Research Project in establishing the properties of the waste package and the GS environments. This interaction is crucial to the success of all affected projects.

Several projects sponsored by the NRC Office of Nuclear Material Safety and Safeguards (NMSS) are also integrated with the Thermohydrology Research Project. These projects include the resolution of uncertainties in the GWTT rule, which requires an understanding of the nature and extent of the disturbed zone resulting from the heat-generating HLW. Likewise, the design issues related to thermal loading need knowledge of the expected thermal and moisture environment (Nataraja and Brandshaug, 1992). Similar information is also utilized in the Iterative Performance Assessment (IPA) task.

Research within the Thermohydrology Research Project entails laboratory-scale experiments, numerical simulations, computational analyses, and dimensional analysis. The results of the Thermohydrology Research Project through 1991 are summarized in CNWRA 92-006 (Green et al., 1992a). Subsequent reports documenting progress and results of this project include Manteufel and Green (1992), Manteufel et al. (1992), and Green et al. (1992b). This report describes the results of the Thermohydrology Research Project during the second half of 1993.

2.2 CONCEPTUAL PRESSURE-BUOYANCY ANALYTICAL MODEL

Various types of laboratory experiments are used at the CNWRA to validate computer analyses of the thermohydrological response of the proposed HLW repository and to explore physical phenomena in the repository that are not satisfactorily understood at present. The models are much smaller than the actual repository, and the time scale of the experiments is many orders of magnitude shorter than the repository time scale of interest. Thus, the laboratory experiments generally cannot simulate all the important physical phenomena occurring in the repository. To use these experiments as a predictive tool or a model validator, they must be designed to simulate the relative importance of physical phenomena by ensuring that the dimensionless ratios of the phenomena, such as fluid flows and heat transfer rates, have roughly the same numerical value for the experiment as is anticipated for the full-scale situation.

The conceptual model described here focuses on the dimensionless ratios governing the flow of an air-water vapor mixture in a porous medium as a result of localized heating.

In a saturated porous medium, heating the fluid creates density differences, which in the presence of gravity produces a distribution of buoyancy forces in the fluid (i.e., pressure gradients caused by buoyancy). It is well known that the Rayleigh Number is the relevant dimensionless ratio for these conditions. To help explain the new conceptual model, it is reviewed briefly. The dimensionless form of Darcy's law for a buoyancy-driven fluid flow in a saturated porous medium is

$$\tilde{V} = -(\tilde{\nabla}\tilde{P} - \theta k) \tag{2-1}$$

where ~ denotes dimensionless units.

Here, $\tilde{P} = \dfrac{P}{g \rho_g \beta_g \Delta T_0}$ is the dimensionless nonhydrostatic component of the fluid pressure in the porous medium, where g is the acceleration of gravity, ρ_g and β_g are the fluid (here, gas) density and coefficient of thermal expansion, and ΔT_0 is a reference temperature change (e.g., the maximum temperature difference anticipated in the experiment); $\theta = \Delta T / \Delta T_0$ is a dimensionless temperature change equal to the ratio of the actual temperature change at a point to the reference temperature change; and k is the unit vector in the vertical direction (Green et al., 1992a). The gas Darcy velocity V has also been made dimensionless by a characteristic buoyancy-induced velocity, $\dfrac{k_{sat}\, g \rho_g \beta_g \Delta T_0}{\mu_g}$, where μ_g is the gas viscosity and k_{sat} is the saturated liquid permeability of the porous medium. For a typical buoyancy-induced flow, the terms $\tilde{\nabla}\tilde{P}$ and θ have comparable magnitudes (approximately unity), with the result that, for a single-phase fluid, the flow pattern is a circulation consisting of one or more "circulation cells." If the heating rate is large enough to cause a localized phase change of the fluid (liquid to vapor in the hot regions, vapor to liquid in the cold), then the two-phase flow pattern is more complex because of the vapor sink at locations where the vapor condenses.

When the porous medium is not saturated, the flow of the heated fluids may be driven by many mechanisms, depending on the magnitude of heating rates, temperature gradients, saturation levels, permeability, etc. The conceptual model developed in this research allows quantitative estimates of the relative influence of some of these parameters to be determined. The model predicts estimates of the heating conditions and porous medium and fluid characteristics for which the flow of gases in the medium is driven by nonbuoyancy pressure gradients, rather than by buoyancy, in the vicinity of the heat source. The results of the model can be concisely summarized in an Advection Number, Ad. When $Ad >> 1$, pressure gradients are more important than buoyancy and other mechanisms, whereas buoyancy and other mechanisms are important when $Ad << 1$. The conceptual model is based on: (i) a heat conduction analysis to establish the temperature distribution in the medium as a function of local heating rates and media properties, (ii) a thermodynamics model to predict the resulting pressure gradients in the gas, and (iii) Darcy's law to predict the gas flow driven by the pressure gradients. A brief summary of the model is presented in the following section.

2.2.1 Dry-Gas Model

A model is described that applies strictly to a "dry" gas, that is, one in which the pressure and density are interrelated by temperature (e.g., an ideal gas). The model assumes that as dry gas is driven from the heat source by the pressure gradients, it is replenished by a return flow of liquid, which is immediately vaporized (consequently, there is no liquid in the dry gas); without the return flow, the gas outflow from the heated region would eventually cease.

The results of the model can be concisely summarized in a new Ad. When $Ad >> 1$, pressure gradients are more important than buoyancy and other mechanisms, whereas the other mechanisms are important when $Ad << 1$. The conceptual model is based on: (i) a transient heat conduction analysis to establish the temperature distribution in the medium as a function of local heating rates and media properties, (ii) a thermodynamics model to predict the resulting pressure gradients in the gas, and (iii) Darcy's law to predict the gas flow driven by the pressure gradients.

The dimensionless form of Darcy's law to predict gas flow that results from the analysis is

$$\tilde{V} = -\left[\tilde{\nabla}\tilde{P} - \left(\frac{\theta}{\mathrm{Ad}}\right)k\right] \tag{2-2}$$

where Ad is defined as

$$\mathrm{Ad} = \frac{K_s \mu_g}{L k_{sat} \rho_g \rho_s g C_s \beta_g T_{avg}} \tag{2-3}$$

and where K_s, ρ_s, and C_s are reference or characteristic values of the thermal conductivity, density, and specific heat at constant pressure of the solid matrix, and T_{avg} is the average temperature of the affected region near the heat source. L is a characteristic length over which the porous medium temperature increases significantly.

In Eq. (2-2), the dimensionless nonhydrostatic pressure is defined as

$$\tilde{P} = P\left(\frac{k_{sat} \rho_s C_s T_{avg}}{K_s \mu_g \Delta T_0}\right) \tag{2-4}$$

The gas velocity V has been made dimensionless by a characteristic pressure-driven velocity equal to

$$\tilde{V} \sim \frac{k_{rel} K_s \Delta T_0}{\rho_s C_s L T_{avg}} \tag{2-5}$$

where k_{rel} is a characteristic or reference value of the relative permeability of the porous medium for gas flow (which is a function of saturation level). Equations (2-3), (2-4), and (2-5) can be simplified somewhat by recognizing that the combination of porous medium properties $\frac{K_s}{\rho_s C_s}$ is defined as the thermal diffusivity, α_s, of the medium.

The Ad can be interpreted as the ratio of the nonbuoyancy-induced pressure gradient to the buoyancy-induced pressure gradient. For Ad $>>$ 1, then, pressure gradients are the important driving mechanism, and the fluid would generally flow in the direction of decreasing pressure rather than in circulatory patterns. For Ad $\approx$ 1, the pressure gradient and buoyancy terms are comparable in magnitude, and the flow pattern would be somewhat similar to a buoyancy-induced flow. For Ad $<<$ 1, buoyancy forces dominate, and the buoyancy model described by Eq. (2-1) is a more appropriate description of the flow than the new model, Eq. (2-2), proposed here.

2.2.2 Wet-Gas Model

An alternative model for fluid flow assumes that there is sufficient liquid adhering to the porous matrix and remaining in contact with the vapor to maintain the liquid and vapor in thermodynamic equilibrium. In this model, designated as the wet-gas model, the pressure of the vapor is the thermodynamic saturation pressure corresponding to the vapor temperature. Equation (2-2) retains its form, but the characteristic pressure used to make pressure dimensionless in Eq. (2-2) is now the total gas pressure, which is the sum of the partial pressures of the vapor, $P_v = \dfrac{n_v\ \rho_v\ h_{fg}\ \Delta T_0}{T_{avg}}$, and the partial pressure of the air, $P_a = (1 - n_v)\ \rho_a\ R_a\ T_{avg}$. Here, n_v is the mole fraction of vapor in the gas mixture, h_{fg} is the latent heat of vaporization of water, and ρ_v is the saturated density of the water vapor The Clausius-Clapeyron Eq. [(2-3)] has been used to express the vapor pressure in terms of the latent heat. For conditions in which the partial pressure of the vapor is much larger than that of the air, the vapor pressure dominates the gas mixture pressure, and Eqs. (2-3), (2-4), and (2-5) must be modified as indicated below. Conversely, for conditions in which the partial pressure of the air is much larger than that of the vapor, the air pressure dominates the gas mixture pressure, and the dry-gas model given by Eq. (2-3) is sufficient to estimate the flow regime. When both partial pressures are comparable, the flow regime can be estimated by either model. Hence, it is only necessary to formulate an alternative wet-gas model in which the characteristic pressure is assumed to be the partial pressure of the vapor. The modified Ad for the wet-gas model is

$$\mathrm{Ad} = \frac{n_v\ \rho_v\ h_{fg}}{g\,\rho_g\,\beta_g\ LT_{avg}} \tag{2-6}$$

For this model, the dimensionless pressure is expressed as

$$\tilde{P} = P\left(\frac{n_v\ \rho_v\ h_{fg}\ \Delta T_0}{T_{avg}}\right)^{-1} \tag{2-7}$$

and the characteristic vapor velocity is expressed as

$$\tilde{V} \sim \frac{k_{rel}\ k_{sat}\ n_v\ \rho_v\ h_{fg}\ \Delta T_0}{\mu_g\ LT_{avg}} \tag{2-8}$$

Recall that the wet-gas model is applicable to situations in which there is sufficient liquid water in contact with vapor to maintain thermodynamic equilibrium conditions, thus, it is probably not applicable when the liquid saturation level is low (e.g., less than 10 percent).

Note that for both models, Ad is primarily a function of medium and fluid properties; the only direct influence of the heating on Ad is the average temperature T_{avg}. Consequently, estimates of whether the flow regime is pressure- or buoyancy-driven can be made fairly easily.

2.3 ANALYTICAL AND NUMERICAL RESULTS

Scoping calculations and numerical simulations have been conducted to assess the utility of the proposed models (Sections 2.2.1 and 2.2.2) to characterize the transport of air, water, and vapor in nonisothermal, partially saturated porous media. Preliminary scoping calculations have been made from the new models to: (i) help understand results from past the CNWRA experiments, (ii) design a new experiment to investigate pressure-driven flows, (iii) assist in performing VTOUGH numerical simulations, and (iv) evaluate at CNWRA the proposed U.S. Department of Energy (DOE) large heated block experiment at Fran Ridge. For the scoping calculations, a heat conduction model is used to evaluate ΔT_0 and T_{avg} as a function of specified heating rates and estimated media thermal properties. [A conduction model is valid here because the energy balance is dominated by heat conduction in the solid porous medium (Green et al., 1992a)].

2.3.1 Model Calculations

Results of the scoping calculations for a new CNWRA experiment and the DOE large heated block experiment are displayed in Table 2-1. The proposed CNWRA experiment is a cylinder 12 cm long with a diameter of 29 cm, made of a cement-like material, containing an embedded electrical heater. The large block experiment is a block of tuff about 4.5 m high, with a rectangular cross section 3×3 m, containing a series of electrical heaters oriented in a horizontal plane. The dry-gas model was used for all the calculations. Somewhat larger pressures and gas velocities are predicted by the wet-gas model, depending upon the assumed value of the vapor mole fraction.

As can be seen, the Ad is smaller for the media with the larger bulk permeability; these values might be appropriate, for example, in highly fractured zones. For the CNWRA experiment, it appears that the gas flow will always tend to be driven by pressure gradients for any realistic value of k_{sat}. As a point of comparison, the characteristic buoyancy-induced velocities (for conditions under which they would occur) for the experiments would be of the same magnitude as the pressure-induced velocities. Consequently, it can be concluded that the flow distribution or flow pattern is what is primarily affected when conditions change from a buoyancy-driven experiment to a pressure-driven experiment, rather than the magnitude of the velocity.

2.3.2 Numerical Simulations

The flow of heat, air, and water has been simulated for the proposed CNWRA cylindrical experiment using VTOUGH (Pruess, 1987; Nitao, 1989) for a range of assumed conditions. Conditions varied in the simulations include heat load (12 and 24 w) and permeability (10^{-12} and 10^{-16} m^2). The cylindrical experiment was simulated at two heat loads to examine the possible variation in flow regimes resulting from different heat load.

Since the intent of the cylindrical experiment is to create a testable environment with a gas pressure gradient, these initial simulations were performed to evaluate the experiment properties necessary for the gradient to exist. Simulations of the proposed test container indicate that a medium with a

Table 2-1. Estimated parameters for cylindrical and large block experiments

Cylindrical Experiment			Large Block Experiment		
	k_{sat} (m^2)			k_{sat} (m^2)	
Parameter	10^{-12}	10^{-16}	Parameter	10^{-12}	10^{-16}
• Heat rate = 24 w			• Heat rate = 1500 w		
T_{avg} (C)	85	85	T_{avg} (C)	88	88
Ad	10	10^5	Ad	0.6	6,000
Characteristic P (Pa)	3	30,000	Characteristic P (Pa)	15	150,000
Characteristic V (m/s)	2×10^{-6}	2×10^{-6}	Characteristic V (m/s)	5×10^{-7}	5×10^{-7}
• Heat rate = 12 w			• Heat rate = 750 w		
T_{avg} (C)	55	55	T_{avg} (C)	56	56
Ad	10	10^5	Ad	0.6	6,000
Characteristic P (Pa)	1.5	15,000	Characteristic P (Pa)	7.5	75,000
Characteristic V (m/s)	1×10^{-6}	1×10^{-6}	Characteristic V (m/s)	2.5×10^{-7}	2.5×10^{-7}

permeability of 10^{-12} m^2 will not provide an environment with a measurable gradient in the gas pressure. The gas permeability of this medium was apparently sufficiently high that any local increase in the gas pressure was rapidly equilibrated throughout the test container, thus not permitting a gas gradient to form.

The redistribution of heat and water in the cylindrical experiment was simulated at two heat loads (12 and 24 w) for a permeability of 10^{-16} m^2. Temperature approached steady state early in the design period of the experiment (at day five of a 1-yr simulated experiment) in which conduction was the dominant means of heat transport. Temperature profiles for the two heat loads are presented in Figure 2-1. As illustrated, the maximum temperatures are about 85 and 150 °C for heat loads of 12 and 24 w, respectively. Additionally, liquid saturation for the two heat loads at two times (5 d and 1 yr) are illustrated in Figures 2-2 and 2-3. A dry-out zone forms proximal to the heater at both heat loads. The extent of the dry-out zone increases with time, but the most prominent gradient in liquid saturation occurs during the early stages of the test when the lateral distance from the point of less than 10 percent to greater than 80 to 90 percent saturation is small (Figure 2-2).

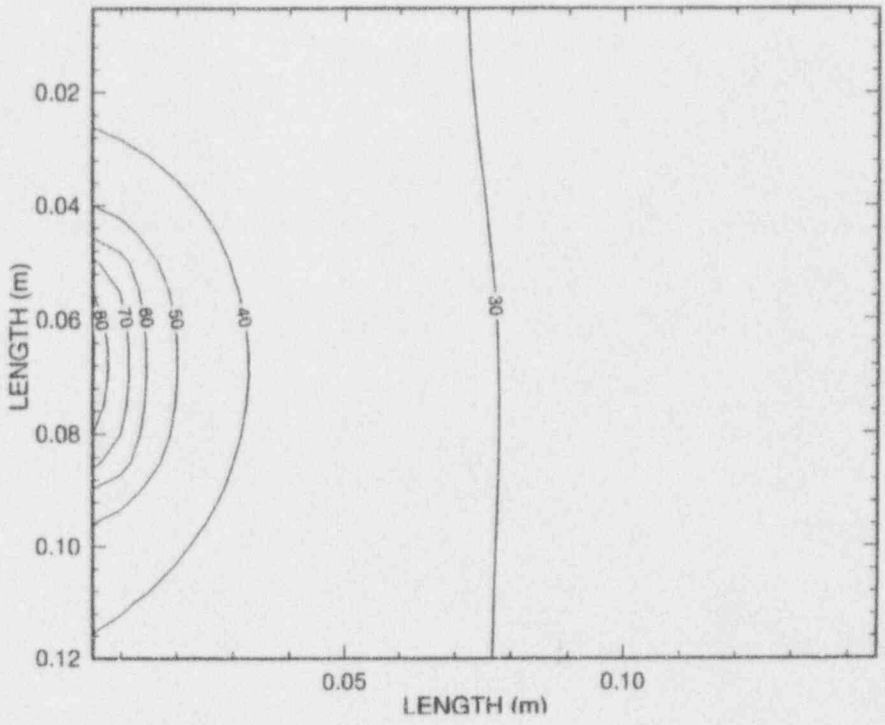

(a)

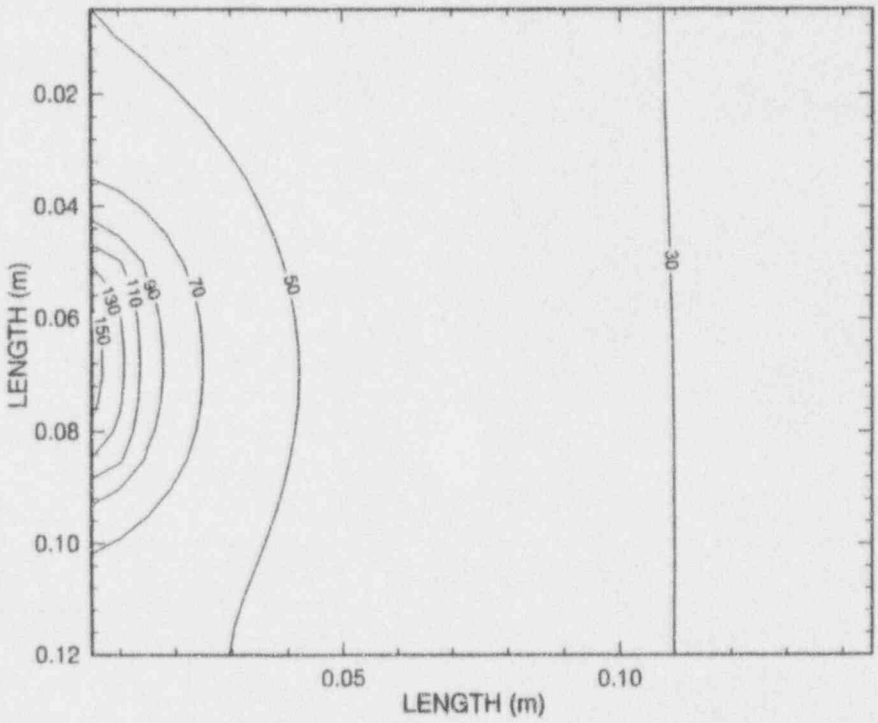

(b)

Figure 2-1. Cylindrical laboratory experiment temperature contours for 12- (a) and 24-w (b) heat loads after 1 yr of simulation. (Temperature is in °C)

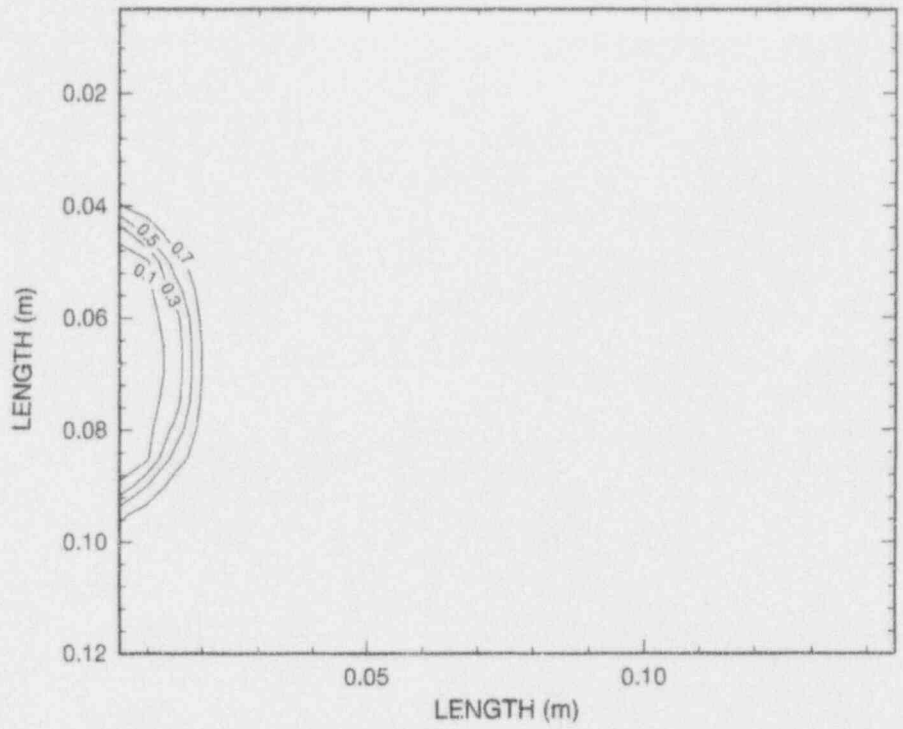

(a)

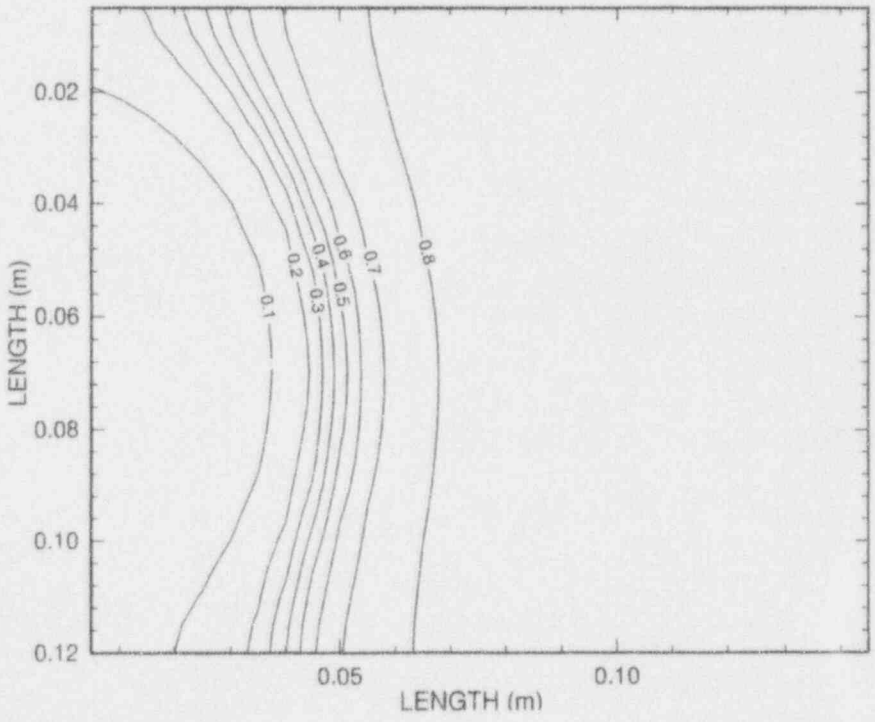

(b)

Figure 2-2. Cylindrical laboratory experiment liquid saturation contours for a 12-w heat load after 5 d (a) and 1 yr (b) of simulation

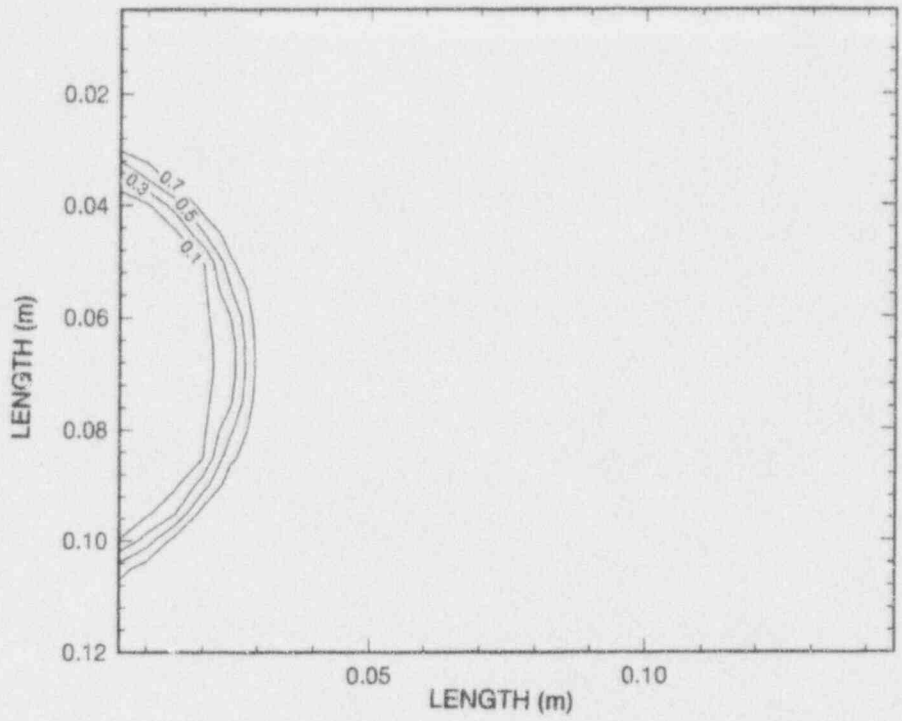

(a)

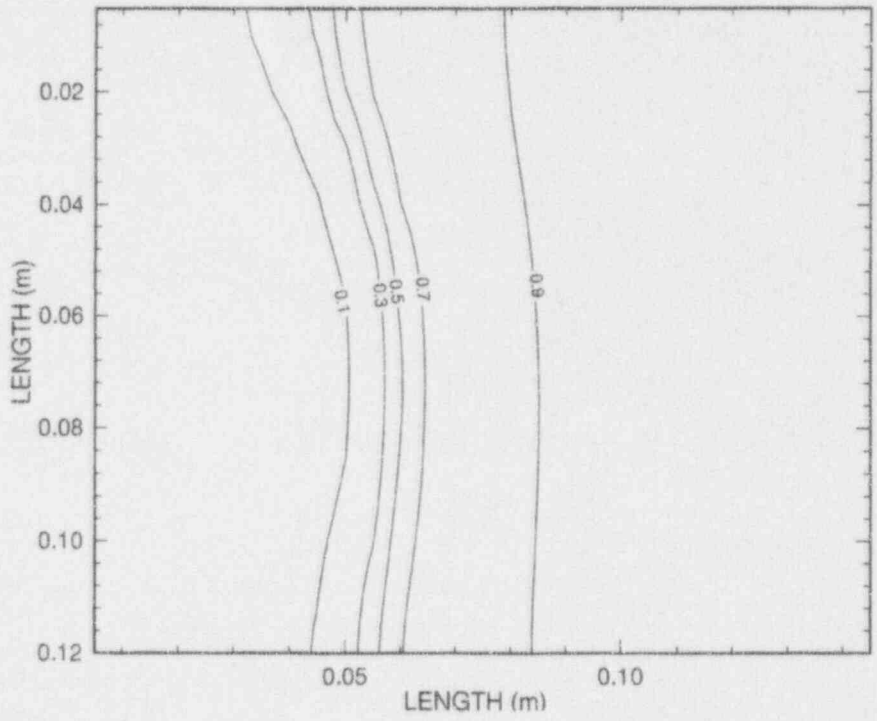

(b)

Figure 2-3. Cylindrical laboratory experiment liquid saturation contours for a 24-w heat load after 5 d (a) and 1 yr (b) of simulation

The flow regimes of gas and liquid phase are illustrated at selected simulation times in Figures 2-4 thru 2-7. Gas flow at early times (i.e., day one in Figures 2-4 and 2-5) indicates no significant differences due to heat load. There is, however, a change in the nature of the flow pattern at 1 yr. Gas flow in the immediate vicinity of the heat source is different for the two cases.

Liquid flow patterns, however, are essentially similar at (50 d) and at late times (1 yr) at both heat loads (Figure 2-6 and 2-7). Of interest is the formation of convection cells at 50 d of simulation. Although the cells are minor in terms of flow quantity, they could be significant at large times, when projected to larger scales of distance.

Gas pressures at two times (1 d and 1 yr) of simulation are illustrated for the two heat loads in Figures 2-8 and 2-9. At late times in the simulation, the gas pressure is dissipated such that the maximum pressure difference in the test container is less than about 2,000 Pa. At early times (e.g., 1 d), however, maximum pressure differences are 25,000 Pa (0.25 bar) and 11,000 Pa (0.11 bar). The maximum gas pressure differences for different times at the two heat loads are presented in Figure 2-10. As illustrated, it appears that significantly large gas pressure gradients may be achievable in the proposed cylindrical experiment with a permeability of 10^{-16} m^2 during the early stages of the experiment.

2.4 ASSESSMENT OF PROGRESS

Information regarding the transience of the thermal and liquid regimes at a HLW repository is critical if the performance of a HLW repository is to be understood and predicted. The repository temperatures and saturations will be functions of numerous physical properties, both of the GS and the EBS. The Thermohydrology Research Project has identified processes that appear to dominate distribution of heat and water at the repository. Determination of the extent and duration of dry-out proximal to the emplaced canisters and the nature of the timing of reflux of water to the canisters, however, have not been accomplished.

Dimensional analysis has provided a methodology with which to assess the significance of processes observed in the laboratory-scale experiments and in other larger scale experiments. This analysis has been important in identifying which processes are important for a particular setting and scale, either experiment or repository.

The DOE has used the numerical codes TOUGH and VTOUGH to model two-phase flow through fractured porous media proximal to heat-generating HLW. VTOUGH has been used in the Thermohydrology Research Project to simulate processes observed in the laboratory-scale experiments. This exercise has provided an opportunity to independently assess the ability of VTOUGH to accurately model the thermal processes observed in the laboratory and to predict the response of future experiments. Although reasonable simulations of some of the processes observed in the laboratory-scale experiments have been accomplished, a definitive assessment of the ability of the code to replicate all feasible processes to be expected at the repository (the subject of a KTU) has not been completed. Preliminary results were presented by Green et al. (1992b); subsequent results will be presented in future progress reports.

2.5 FUTURE PLANS

Analyses of both the cylindrical experiment and the large block heater test will continue. Numerical simulation results of the large block heater test in conjunction with simulation results of the

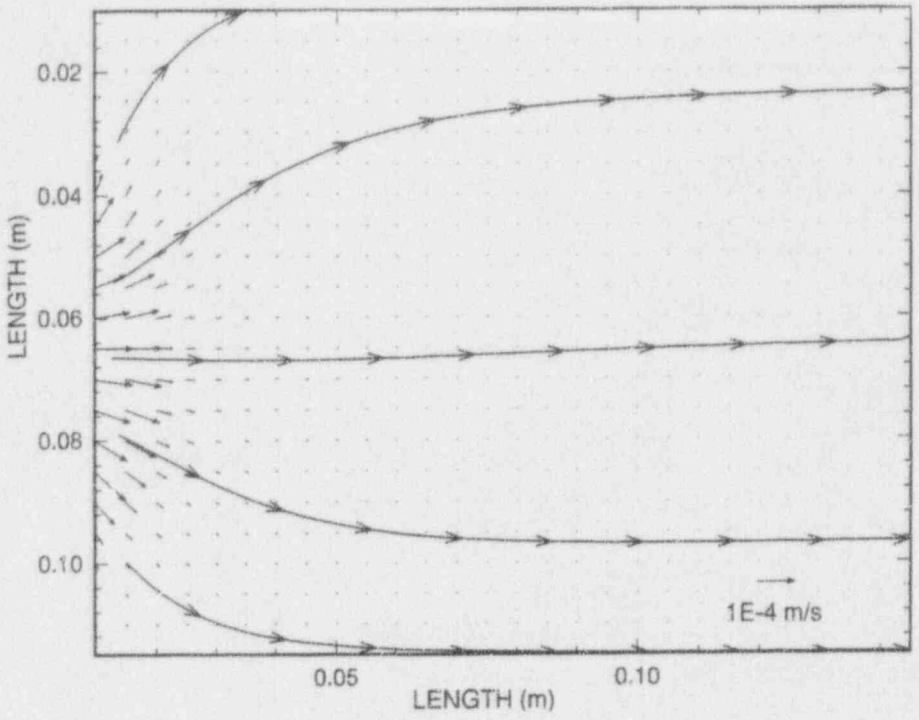

(a)

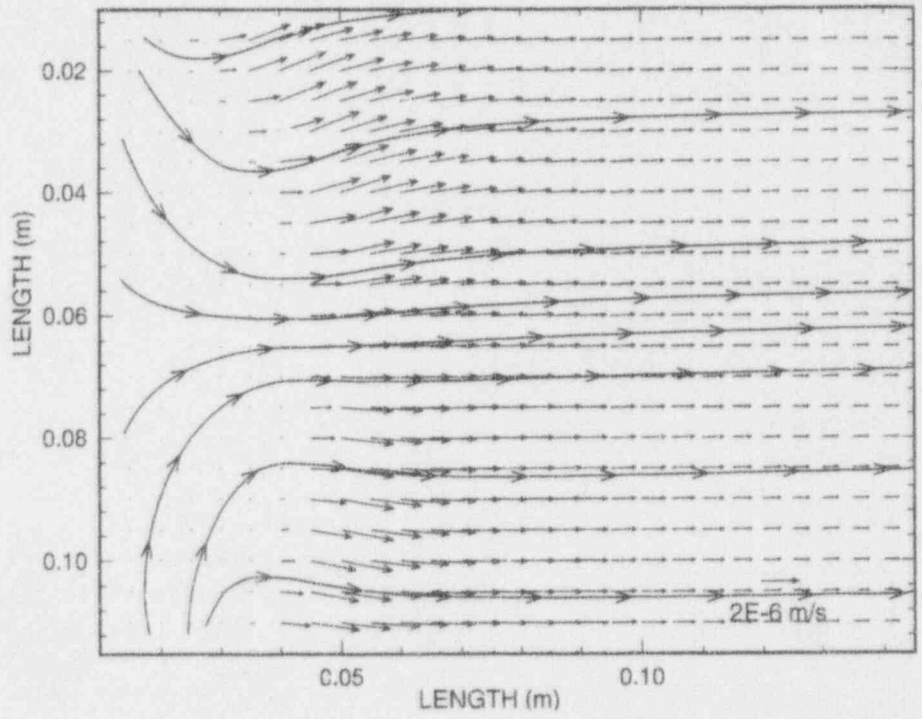

(b)

Figure 2-4. Cylindrical laboratory experiment gas flow (kg/s) for a 12-w heat load after 1 d (a) and 1 yr (b) of simulation. Continuous flow lines indicate instantaneous flow paths at the time of simulation.

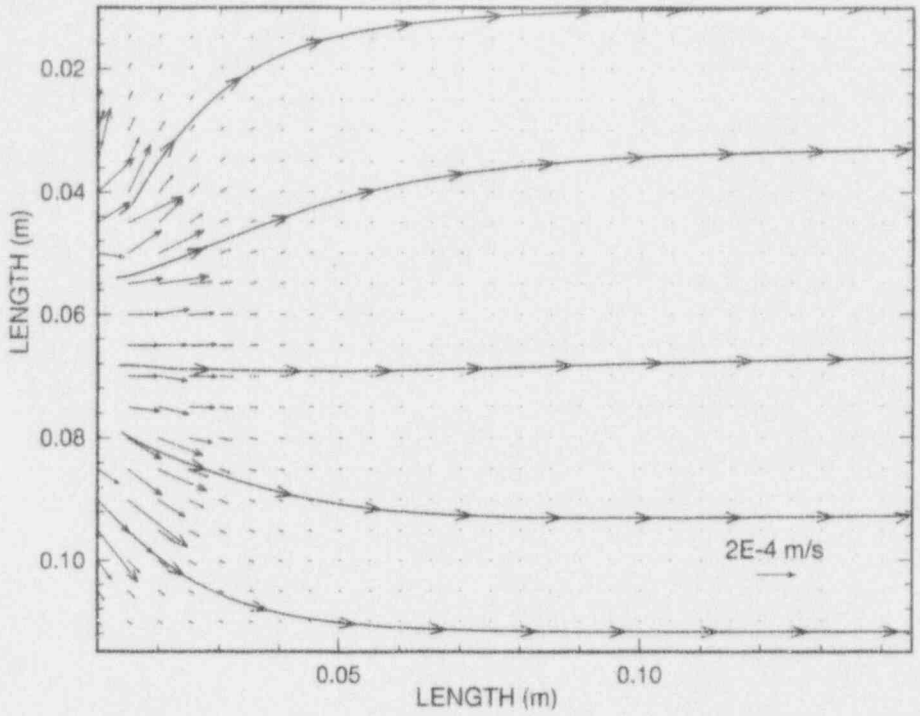

(a)

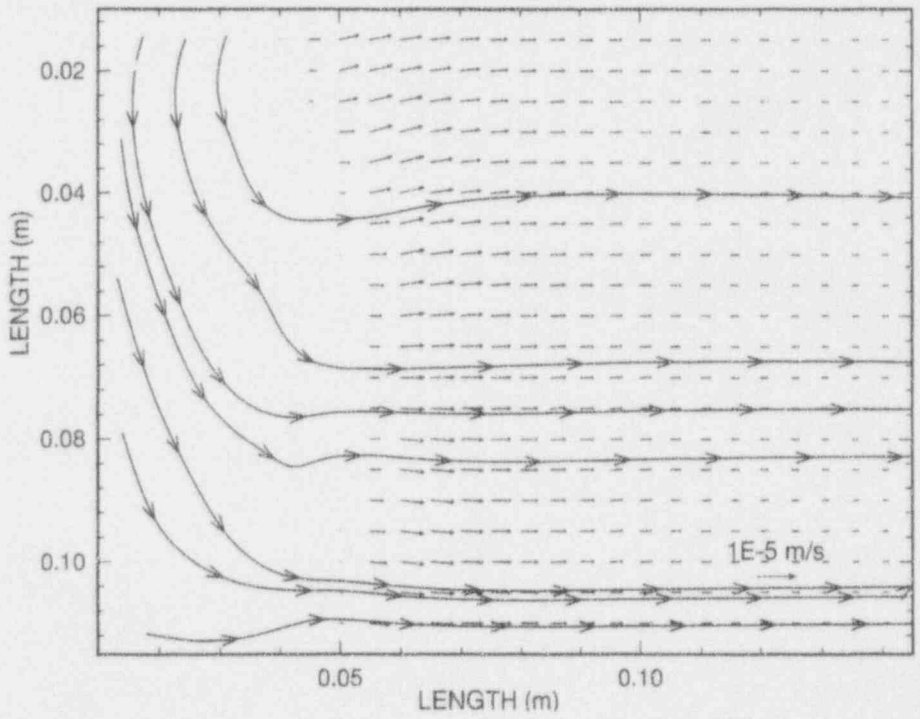

(b)

Figure 2-5. Cylindrical laboratory experiment gas flow (kg/s) for a 24-w heat load after 1 d (a) and 1 yr (b) of simulation. Continuous flow lines indicate instantaneous flow paths at the time of simulation.

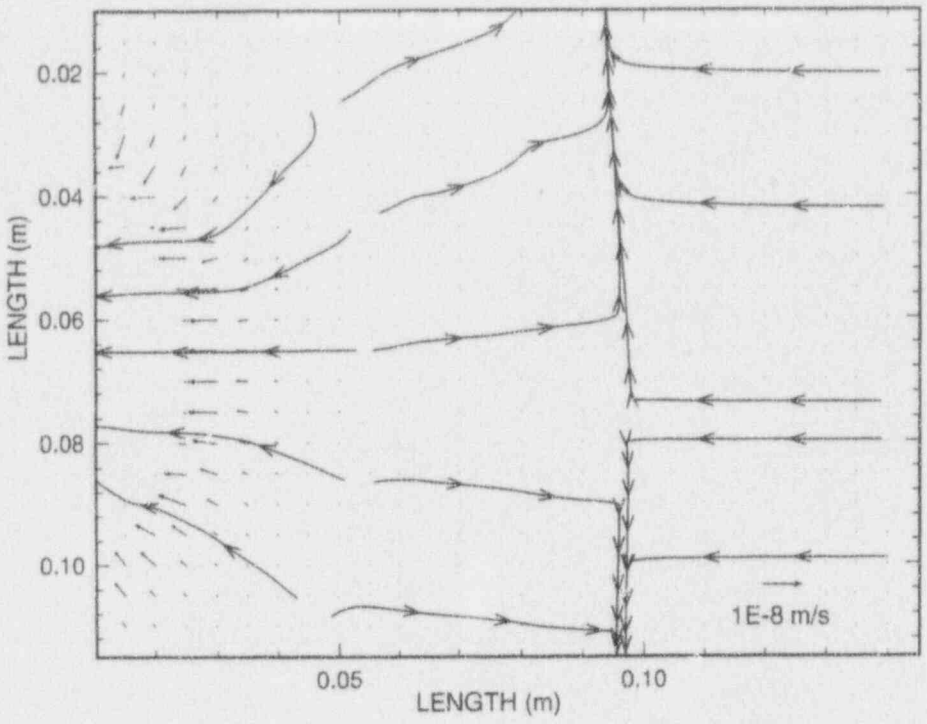

(a)

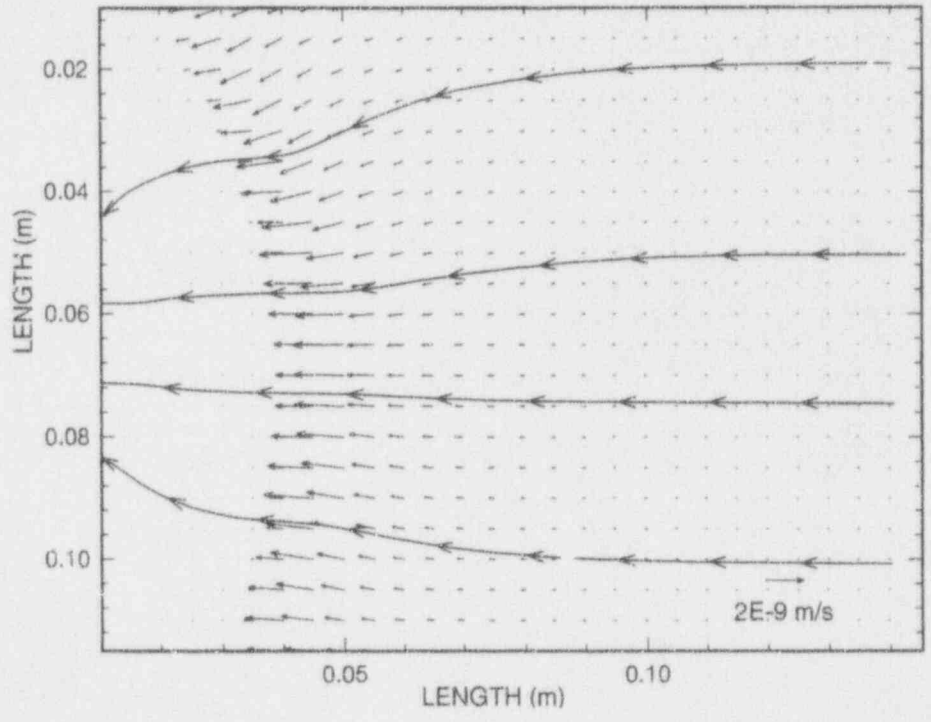

(b)

Figure 2-6. Cylindrical laboratory experiment liquid flow (kg/s) for a 12-w heat load after 50 d (a) and 1 yr (b) of simulation. Continuous flow lines indicate instantaneous flow paths at the time of simulation.

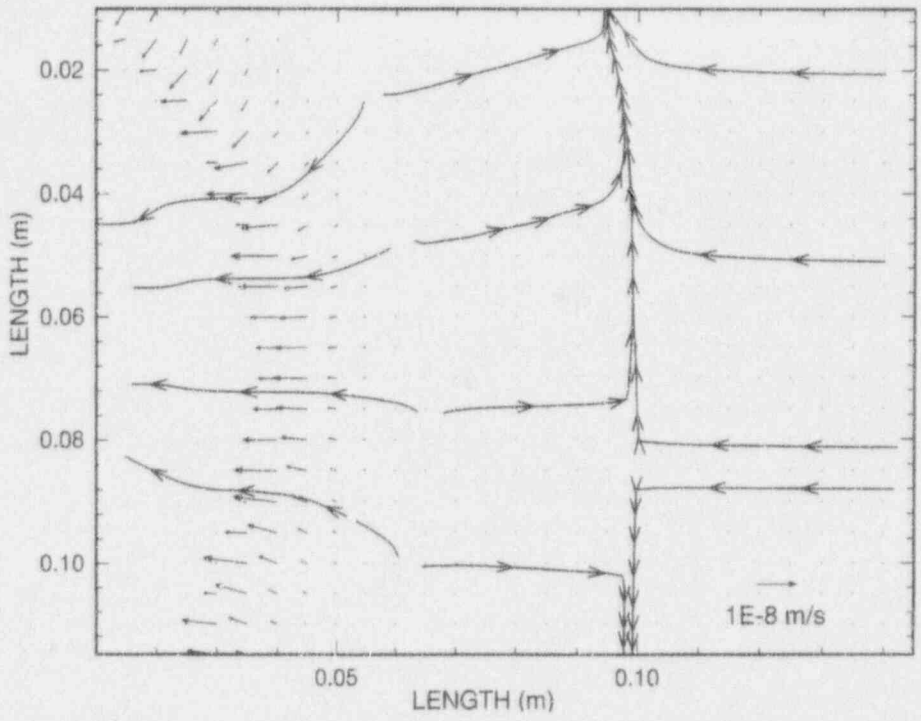

(a)

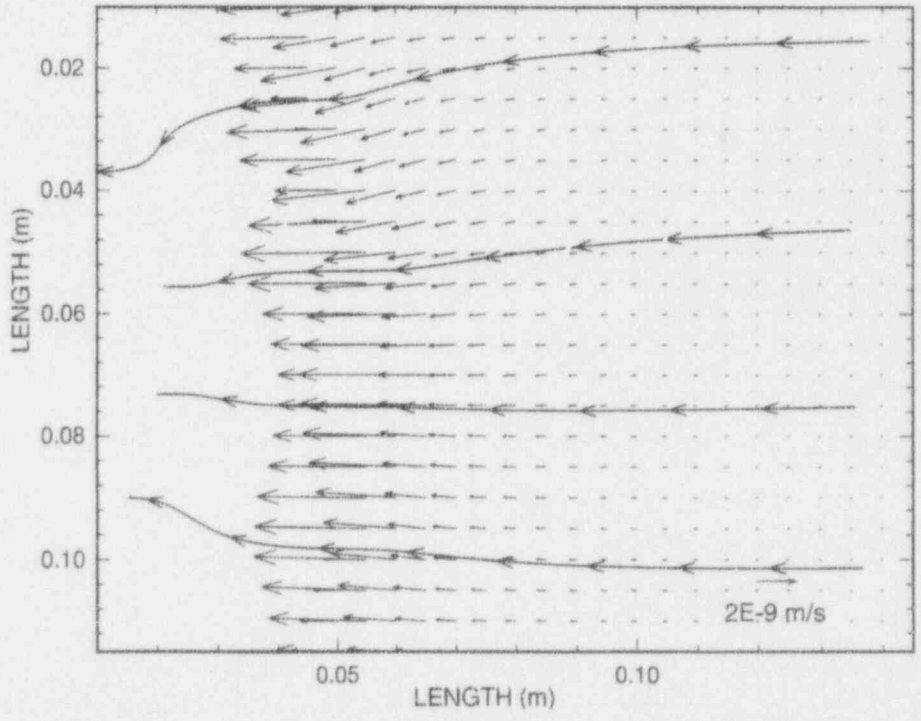

(b)

Figure 2-7. Cylindrical laboratory experiment liquid flow (kg/s) for a 24-w heat load after 50 d (a) and 1 yr (b) of simulation. Continuous flow lines indicate instantaneous flow paths at the time of simulation.

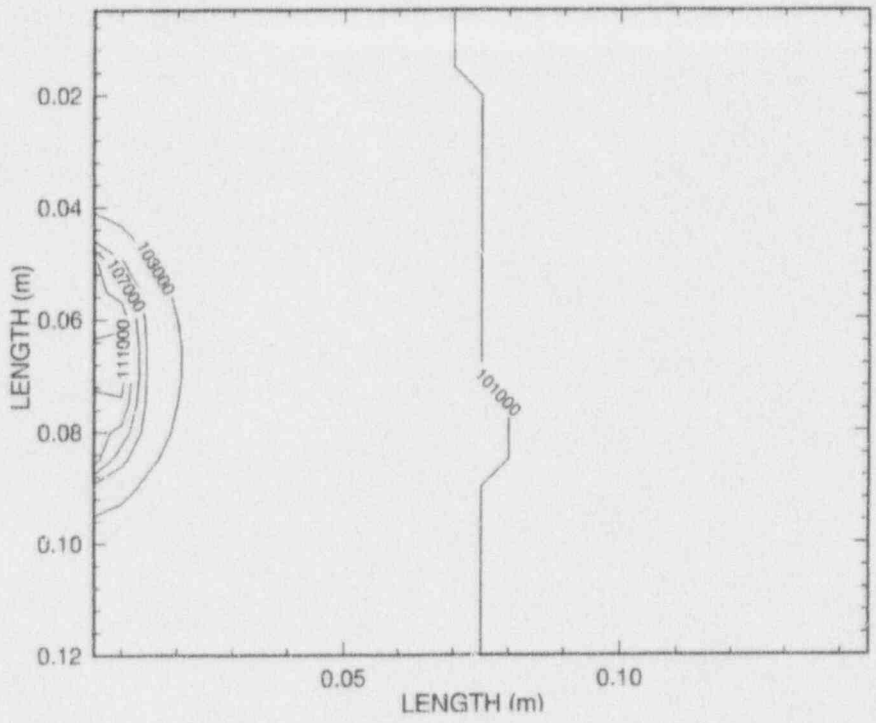

(a)

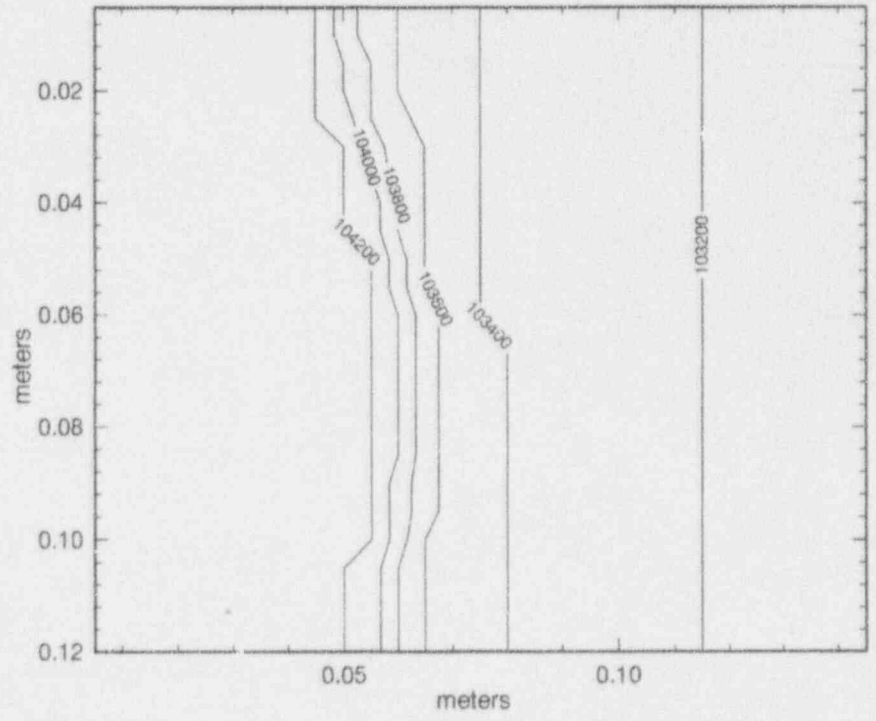

(b)

Figure 2-8. Cylindrical laboratory experiment gas pressure contours (Pa) for a 12-w heat load after 1 d (a) and 1 yr (b) of simulation

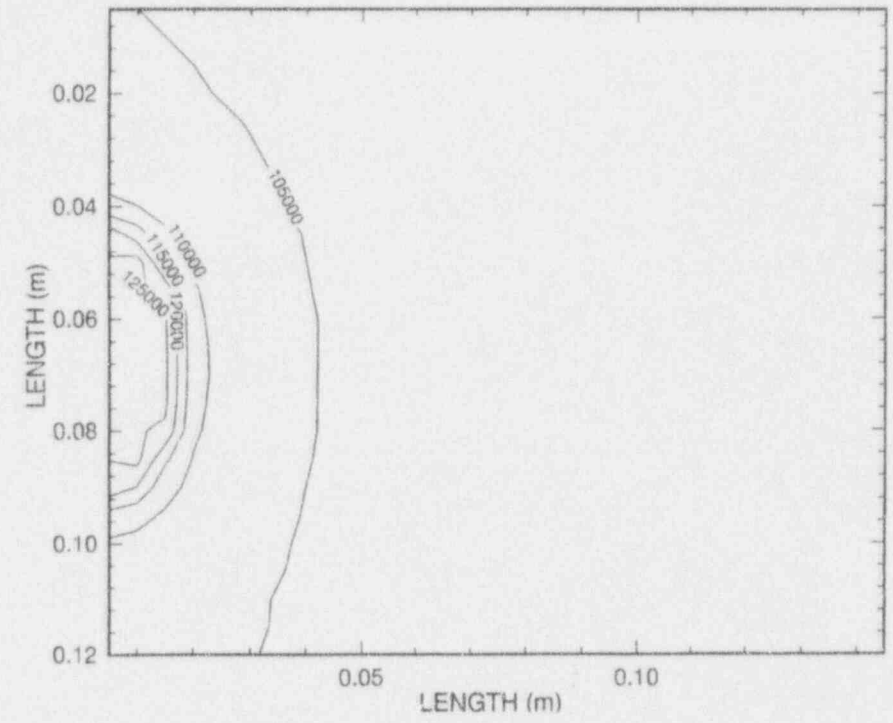

(a)

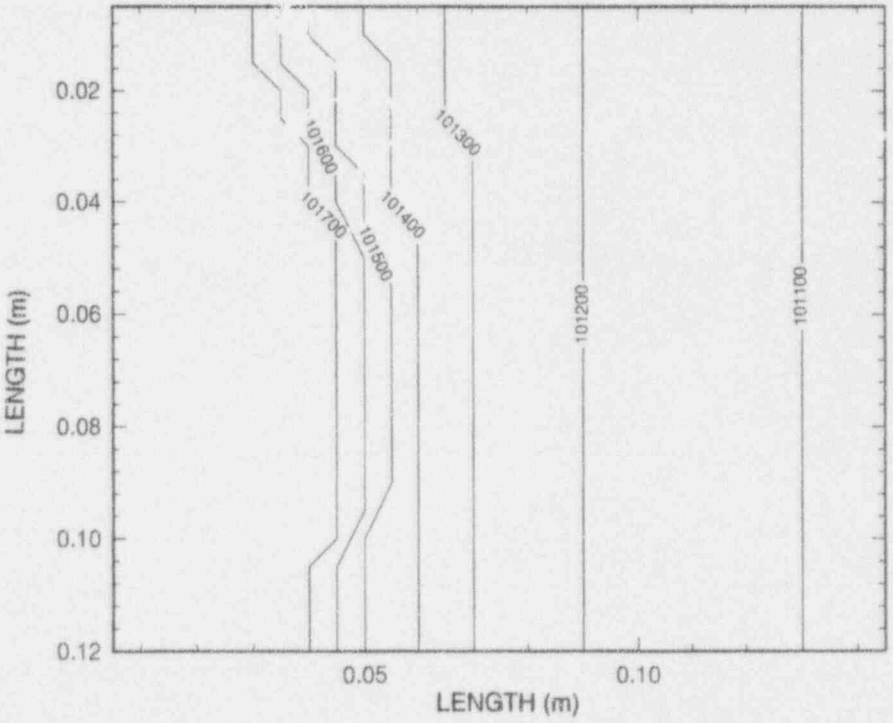

(b)

Figure 2-9. Cylindrical laboratory experiment gas pressure contours (Pa) for a 24-w heat load after 1 d (a) and 1 yr (b) of simulation

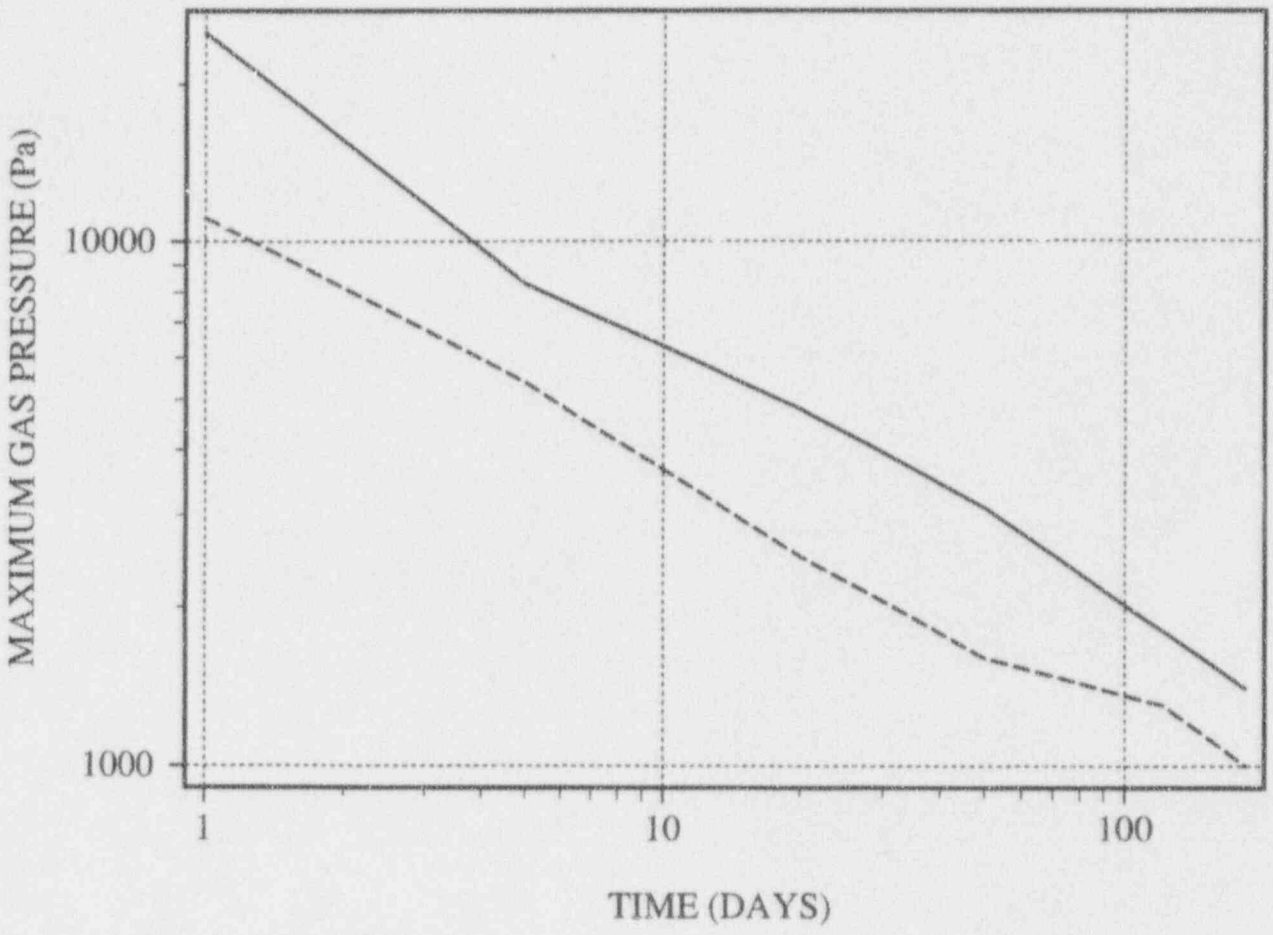

Figure 2-10. Maximum gas pressure differences (Pa) in the cylindrical laboratory experiment at simulation times from 1 d to 3 yr for heat loads of 12 and 24 w

cylindrical experiment (Section 2.3.2) will be evaluated with the dimensional analysis reported in Section 2.3.1 to provide insight on the relative importance of the Ad in the assessment of different repository heat loads.

The adequacy of using concrete to provide a medium that can sustain a gas pressure gradient in the cylindrical experiment will be assessed. If this experiment proves successful, then the concrete-filled cylinder will be used to conduct the gas-gradient experiment. These experiment results will be used to: (i) evaluate the capability of VTOUGH to simulate the cylindrical experiment: and (ii) evaluate the utility of the dimensional analysis, in general, and the Ad, in particular. The current scope of the Thermohydrology Research Project is expected to be completed by September 1994.

Auxiliary experiments and analysis in the phenomenon of preferential flow will continue. These analyses will evaluate the nature of this phenomenon and the impact of geometry and structure on the topology of preferential flow.

2.6 REFERENCES

Green, R.T., R.D. Manteufel, F.T. Dodge, and S.J. Svedeman. 1992a. *Theoretical and Experimental Investigation of Thermohydrologic Processes in a Partially Saturated, Fractured Porous Medium*. NUREG/CR-6026. Washington, DC: U.S. Nuclear Regulatory Commission.

Green, R.T., R.D. Manteufel, and F.T. Dodge. 1992b. *NRC High-Level Radioactive Waste Research at CNWRA, July 1 through December 31, 1992*. B. Sagar, ed. NUREG/CR-5817. CNWRA 92-02S. San Antonio, TX: Center for Nuclear Waste Regulatory Analyses: 3-1 to 3-22.

Manteufel, R.D., and R.T. Green. 1992. *NRC High-Level Radioactive Waste Research at CNWRA, January 1 through June 30, 1992*. W. Patrick, ed. NUREG/CR-5817. CNWRA 92-01S. San Antonio, TX: Center for Nuclear Waste Regulatory Analyses: 3-1 to 3-18.

Manteufel, R.D., and R.T. Green. 1993. *NRC High-Level Radioactive Waste Research at CNWRA, January 1 - June 30, 1993*. B. Sagar, ed. CNWRA 93-015. San Antonio, TX: Center for Nuclear Waste Regulatory Analyses: 3-1 to 3-19.

Manteufel, R.D., R.T. Green, F.T. Dodge, and S.J. Svedeman. 1992. An experimental investigation of two-phase, two-component, nonisothermal flow in a porous medium with a simulated fracture. *Heat and Mass Transfer in Porous Media*. I. Catton, ed. HTD-216. New York: American Society of Mechanical Engineers: 9–18.

Nataraja, M.S., and T. Brandshaug. 1992. *Staff Technical Position on Geologic Repository Operations Area Underground Facility Design - Thermal Loads*. NUREG-1466. Washington, DC: U.S. Nuclear Regulatory Commission

Nitao, J.J. 1989. *V-TOUGH. An Enhanced Version of the TOUGH Code for the Thermal and Hydrologic Simulation of Large-Scale Problems in Nuclear Waste Isolation*. UCID-21954. Livermore, CA: Lawrence Livermore National Laboratory.

Pruess, K. 1987. *TOUGH. User's Guide*. NUREG/CR4645. Washington, DC: U.S. Nuclear Regulatory Commission.

U.S. Nuclear Regulatory Commission. 1993. *Draft License Application Review Plan for the Review of a License Application for a Geologic Repository for Spent Nuclear Fuel on High-Level Radioactive Waste, Yucca Mountain Site, Nevada (LARP)*. NUREG-1323. Washington, DC: U.S. Nuclear Regulatory Commission.

3 SEISMIC ROCK MECHANICS

by Simon M. Hsiung, Mikko P. Ahola, Amitava Ghosh, and Asadul H. Chowdhury

Investigators: Mikko P. Ahola, Asadul H. Chowdhury, Amitava Ghosh, Simon M. Hsiung, Sitakanta Mohanty (CNWRA); Daniel D. Kana (SwRI)

NRC Project Officer: Jacob Philip

3.1 TECHNICAL OBJECTIVES

The technical objective of the Seismic Rock Mechanics Research Project is to conduct laboratory, field, and theoretical analyses to develop techniques that could be used to predict the response of near-field jointed rock mass at the proposed high-level waste (HLW) repository at Yucca Mountain, Nevada, when it is subjected to repetitive seismic (including earthquakes and nuclear explosions at the Nevada Test Site) and thermal conditions. The near-field response includes the response both at the emplacement borehole and the emplacement drift scales. These analyses are designed to develop a better understanding of near-field rock mass behavior under repetitive seismic and thermally induced loads and to obtain fundamental data on the seismic and thermal effects that are important to validate predictive models and verify computer codes for review of repository design [10 CFR 60.131(b)(1), 60.133(e)(1), 60.133(e)(2), 60.133(i), and 60.134], waste retrievability [10 CFR 60.111, 60.133(c), 60.133(e)(1), 60.133(i), and 60.134], and postclosure performance assessment [10 CFR 60.112, 60.113, 60.122(c)(5), 60.122(c)(12), 60.122(c)(14), and 60.122(c)(23)]. Many factors controlling the effect of seismic and thermally induced loads on the near-field jointed rock mass behavior of the proposed repository are poorly understood. The problem is further complicated when the potential coupled effects of thermal loads are considered.

Information developed within the Seismic Rock Mechanics Research Project will be used to support specific portions of the License Application Review Plan (LARP). Detailed laboratory and field studies of stability of underground openings (including vertical emplacement boreholes, if adopted as a concept for waste emplacement) will provide a basis for development and implementation of portions of the LARP relating to Section 4.3, Assessment of Compliance with Design Criteria for Shafts and Ramps; Section 4.4, Assessment of Compliance with Design Criteria for Underground Facility; Section 4.5.2, Assessment of Integrated Geologic Repository Operations Area (GROA) Compliance with the Performance Objectives: Retrievability of Waste; and Section 5.3, Assessment of Compliance with the Design Criteria for the Postclosure Features of the Underground Facility. Knowledge regarding prediction of long-term stability of vertical emplacement boreholes and emplacement drifts (for in-drift emplacement) and potential near-field fluid flow resulting from the coupled effects (including repetitive seismic effects) will support implementation of Section 5.4, Assessment of Compliance with the Engineered Barrier System (EBS) Performance Objectives. Further, knowledge of effects of repetitive seismic and thermal loads (including long-term deterioration of underground openings in the emplacement area) on near-field hydraulic conductivity changes and on the potential to create preferential pathways that may compromise the waste isolation capability of the proposed repository will provide input for Iterative Performance Assessment.

The Compliance Determination Strategies (CDSs) for the LARP sections noted above have been identified as types 4 and 5. It is clear that the Seismic Rock Mechanics Research Project is important in addressing uncertainties raised in CDSs 4.3, 4.4, 4.5.2, 5.3, 5.4, and 6.1, requiring an independent

review capability for assessing Key Technical Uncertainties (KTUs) that pose a high risk of noncompliance with performance objectives of 10 CFR Part 60. Specific KTU topics that will be addressed by the Seismic Rock Mechanics Research Project include the ability to predict the effects of thermal and repetitive seismic loads on stability of emplacement drifts and emplacement boreholes that may affect the performance of the EBS, retrievability of waste, and long-term isolation of waste. For instance, it has already been determined through field experimental studies of the Seismic Rock Mechanics Research Project that repetitive lower-magnitude seismic events can have a much greater influence on the degree of damage to underground openings than a single large-magnitude event (Hsiung et al., 1992).

The Seismic Rock Mechanics Research Project addresses needs identified by the Office of Nuclear Material Safety and Safeguards (NMSS) of the U.S. Nuclear Regulatory Commission (NRC) concerning development of independent capabilities for assessing impacts of repetitive seismic loads on repository design and performance and predicting coupled thermal-mechanical-hydrological (TMH) effects to near-field repository performance. Specific NRC research needs that may be met through this project include: attainment of a better understanding of dynamic response of a jointed rock mass; evaluation of existing rock-joint constitutive models; evaluation of scale effects such that laboratory results can be applied to the field; assessment of potential effects of repetitive seismic loads on change of hydrological properties; identification, through a better understanding, of coupled TMH processes that are relevant to the unsaturated environment; and verification of selected computer code(s) that will be used in the LARP for seismic analyses and prediction of coupled TMH effects on near-field rock mass response.

The Seismic Rock Mechanics Research Project is an integrated effort combining expertise in rock mechanics, mining engineering, engineering geology, and hydrology. The integration will include the exchange of research results between Seismic, Thermohydrology, Integrated Waste Package Experiments (IWPE), and Performance Assessment (PA) Research Projects in the prediction of opening stability and changes in near-field hydraulic conductivity. The Seismic and Thermohydrology projects will complement each other to develop techniques to predict near-field hydraulic conductivity, and flow and transport environment, taking into account matrix flow and stress-dependent fracture flow under thermal conditions. The seismic research will assist in evaluating the mechanical loads that may cause stress/crevice corrosion or structural failure of waste packages, which is a component of EBS evaluations. The combined research and modeling efforts of Seismic and Thermohydrology projects will be useful to evaluate the presence of aqueous environments near the waste package for IWPE research and the near-field flow and transport environment for PA research.

Research within the Seismic Rock Mechanics Research Project includes: characterization of dynamic behavior of single-joint rock in the laboratory using tuff specimens from Apache Leap near Superior, Arizona; a scale model experiment of a rock mass; field studies on the effects of mining-induced seismicity on the rock mass near underground openings and local hydrology; collection of ground shock data; participation in the **DE**velopment of **CO**upled models and their **VAL**idation against **EX**periments (DECOVALEX) program for evaluation of computer codes that are capable of simulating coupled TMH processes; and laboratory studies to understand and identify important thermally induced coupled processes in an unsaturated environment. Earlier reports in this series documenting progress to date include: Hsiung et al. (1993a–e), Ahola et al. (1993), Hsiung and Chowdhury (1993), Ahola et al. (1992), Hsiung et al. (1992), Hsiung and Chowdhury (1991), Kana et al. (1990, 1991), Brady et al. (1990), and Brandshaug et al. (1990). This report describes the results of activities in the Seismic Rock Mechanics Research Project during the second half of 1993.

3.2 SIGNIFICANT TECHNICAL ACCOMPLISHMENTS

3.2.1 Laboratory Investigation of Rock-Joint Behavior

Normally, in analyzing the behavior of underground structures in hard rocks that contain discontinuities such as faults, joints, shear zones, and beddings, the shear behavior of these discontinuities will determine the rock mass deformation and the stability of the underground structures under various loading conditions. Conditions for slip on major pervasive features such as joints and faults or for sliding of individual blocks from the boundaries of excavations are governed by the shear strengths that can be developed by the discontinuities concerned.

However, only limited data under cyclic pseudostatic and dynamic loading conditions are currently available. Consequently, joint behavior under cyclic pseudostatic and dynamic loading is not well understood. To address these issues, a laboratory experimental program for the characterization of rock joints has been undertaken at the Center for Nuclear Waste Regulatory Analyses (CNWRA). In this program, direct shear tests under both cyclic pseudostatic and dynamic loading conditions were conducted on Apache Leap tuff joints in order to obtain a better understanding of the dynamic joint shear behavior. In the following subsections, a summary of the results of these cyclic pseudostatic and dynamic direct shear tests needed for the evaluation of the three rock-joint models is discussed. A detailed discussion of these test results is given by Hsiung et al. (1993d).

The rock-joint specimens used for the cyclic pseudostatic and dynamic direct shear tests were collected from the Apache Leap site near Superior, Arizona. The rock type at the Apache Leap site is a vitrified and densely welded tuff that is moderately and heavily jointed. The rock-joint specimens were prepared from the cores collected from the site to a predetermined size such that the rock block on one side of the joint had a dimension of $305 \times 203 \times 102$ mm, and the rock block on the other side of the joint had a dimension of $203 \times 203 \times 102$ mm. The joint surfaces on both rock blocks were matched when the rock block with smaller size (top block) was seated at the center of the larger size rock block (bottom block).

3.2.1.1 Joint Cyclic Pseudostatic Behavior

A total of 19 fresh joint specimens were tested under cyclic pseudostatic shear loading conditions. The test number designation and the specifications for these tests are given by Hsiung et al. (1993d). During a cyclic pseudostatic direct shear test, the top block was sheared a distance of 50.8 mm in one direction followed by a reversal of shearing back to the original starting position under a predetermined constant normal stress and at a constant velocity of about 4.2×10^{-2} mm. The same process could be repeated on the same joint specimen under a different normal stress level. To aid the discussion, the term forward shearing is used throughout this report to indicate that the top rock block moves away from its original position while the term reverse shearing denotes the top rock block moves toward its original position.

Figure 3-1 shows the shear stress response for test no. 17 (Hsiung et al., 1993d) under various normal stress levels. The test sequence followed an ascending order with respect to the normal stress. There was a time delay in conducting each test. The curve with the 1-MPa normal stress (the first cycle of shearing) illustrates the shear behavior of an originally undamaged (fresh) joint and shows a distinct peak shear strength at the early stage of the shear cycle. The shear strength of the joint gradually reduces

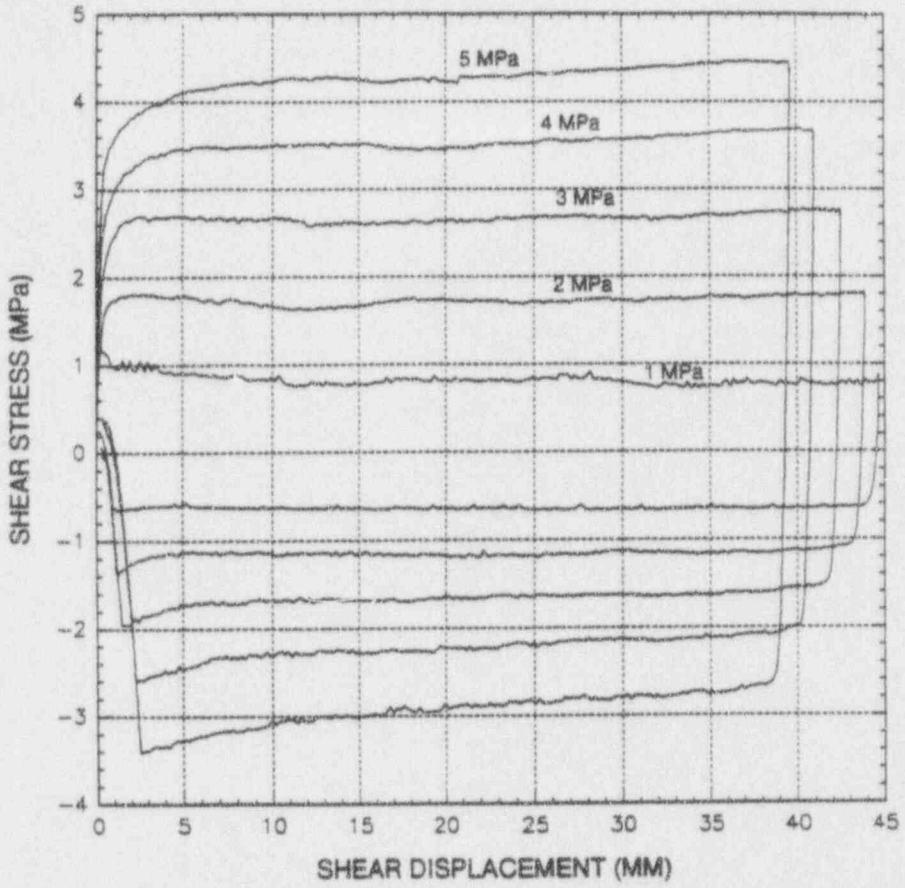

Figure 3-1. Shear stress response of an Apache Leap tuff joint specimen (test no. 17) under pseudostatic cyclic loading conditions as a function of normal stress

to a residual value at greater shear displacements. No distinct peak shear strength was observed for other cycles of shearing. Figure 3-1 also indicates a gradual increase in shear strength during reverse shearing when the top block was approaching its original position. The potential cause of this behavior has been explained by Hsiung et al. (1993d) and will not be repeated in this report. Another feature that can be observed in this figure is that the shear strength during the reverse shearing is smaller than the shear strength during the forward shearing.

The relation between normal displacement (dilation) and shear displacement for test no. 17 is given in Figure 3-2. The test sequence followed an ascending order with respect to the normal stress. This figure indicates that joint dilations at various levels of normal stresses increase during forward shearing. For reverse shearing, there is some degree of hysteresis with the joint dilation decreasing toward zero from below the dilation curve of forward shearing. In general, for repeated shear cycles, the amount of joint dilation decreased with increasing normal stress.

3.2.1.2 Joint Dynamic Response

In addition to the 19 cyclic pseudostatic shear tests, 2 fresh joint specimens were tested under harmonic loading conditions, while 4 others were tested under earthquake loading conditions. The test

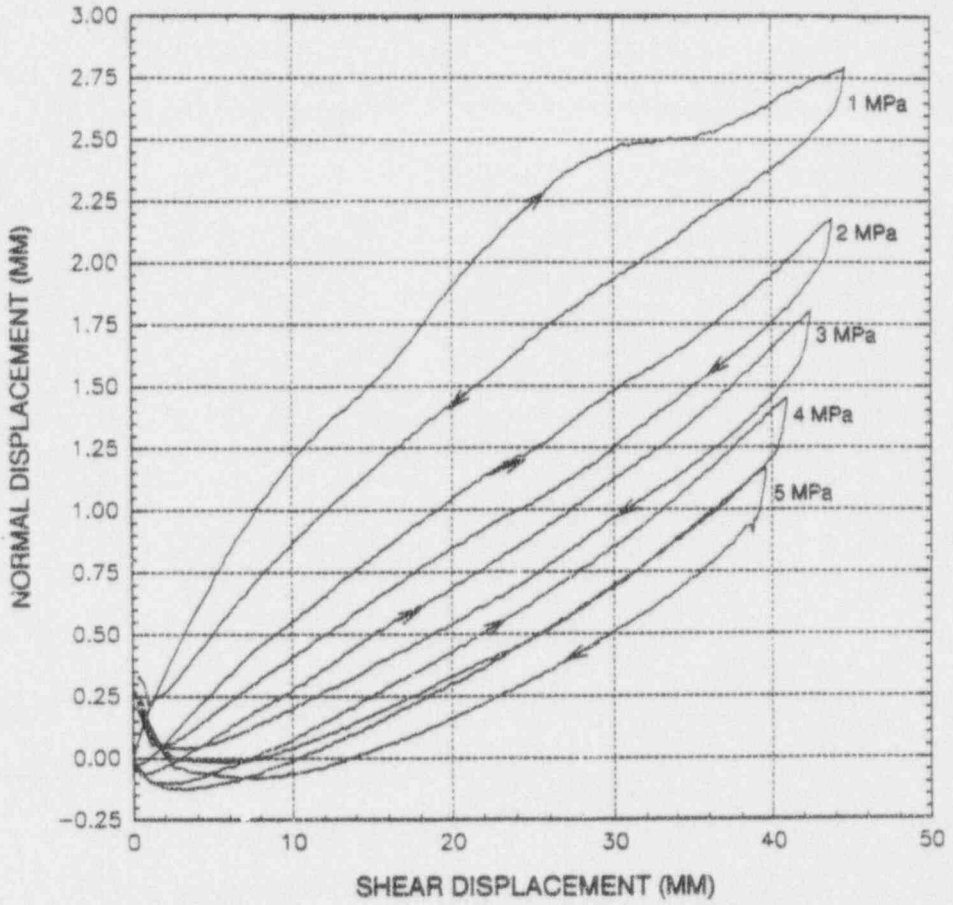

Figure 3-2. Joint dilation curves for test no. 17 specimen under pseudostatic cyclic loading conditions as a function of normal stress

number designation and the specifications for these tests have been given by Hsiung et al. (1993d). Figures 3-3 and 3-4 show the characteristic plot of the joint shear stress versus joint shear displacement under harmonic and earthquake loading conditions, respectively. The harmonic load for Figure 3-3 was generated from a prescribed shear displacement drive input in a sinusoidal waveform. The frequency and amplitude of the harmonic input motion were 1.4 Hz and 12.7 mm, respectively. The earthquake input motion used in Figure 3-4 is shown in Figure 3-5 with a maximum displacement amplitude of 25.4 mm and a dominant frequency of about 0.5 Hz. This displacement input signal was developed based on the acceleration response signal recorded from the Guerrero accelerograph array for the earthquake of September 19, 1985, in Mexico. The development of this displacement input has been discussed by Hsiung et al. (1993d). All figures include the test results of the first three cycles and Figure 3-3 also includes the result of the fortieth cycle.

For Figures 3-3 and 3-4, the experiment started with the shearing of the top rock block from its original position (represented as the zero shear displacement in the figures) toward one end of the bottom rock block until a predetermined maximum value of shear displacement (based on the input displacement time history) was reached. The corresponding shear stress versus shear displacement characteristic curve with this portion of shearing is shown in the top right of the figures (i.e., clockwise progression around the figure). After the maximum shear displacement was reached, the top rock block was moved backward and eventually past its original position. The corresponding shear stress versus

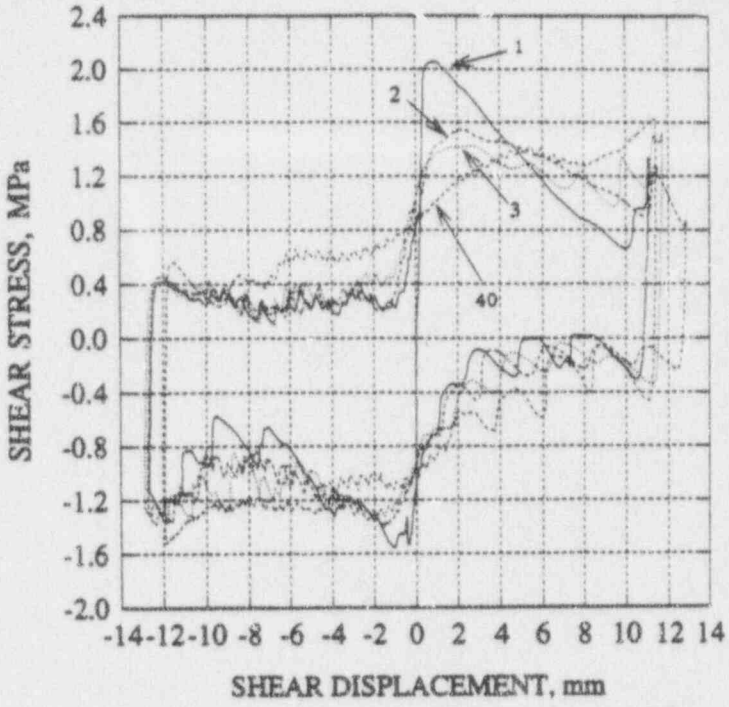

Figure 3-3. Shear stress versus shear displacement curve of a joint under a harmonic load with 1.4-Hz input frequency and 12.7-mm input displacement amplitude (load cycle numbers are indicated in the figure)

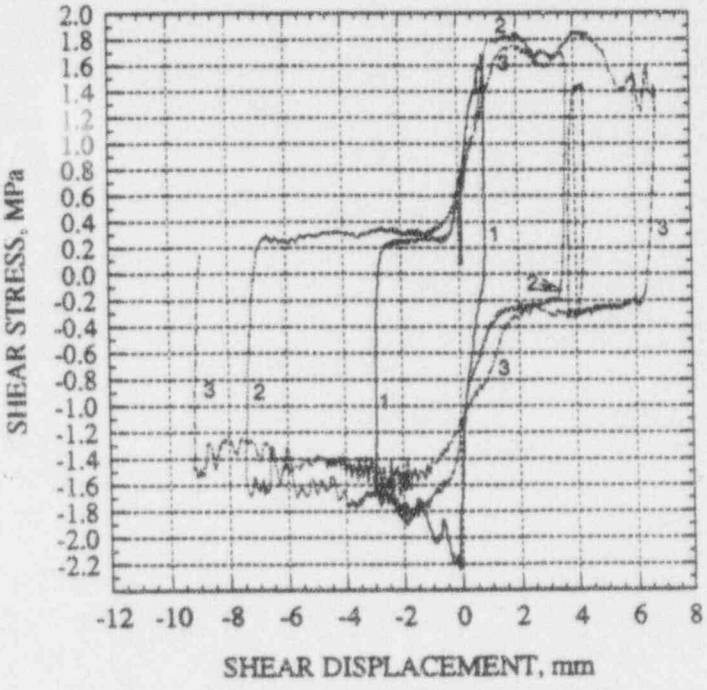

Figure 3-4. Shear stress versus shear displacement curve of a joint under an earthquake load (load cycle numbers are indicated in the figure)

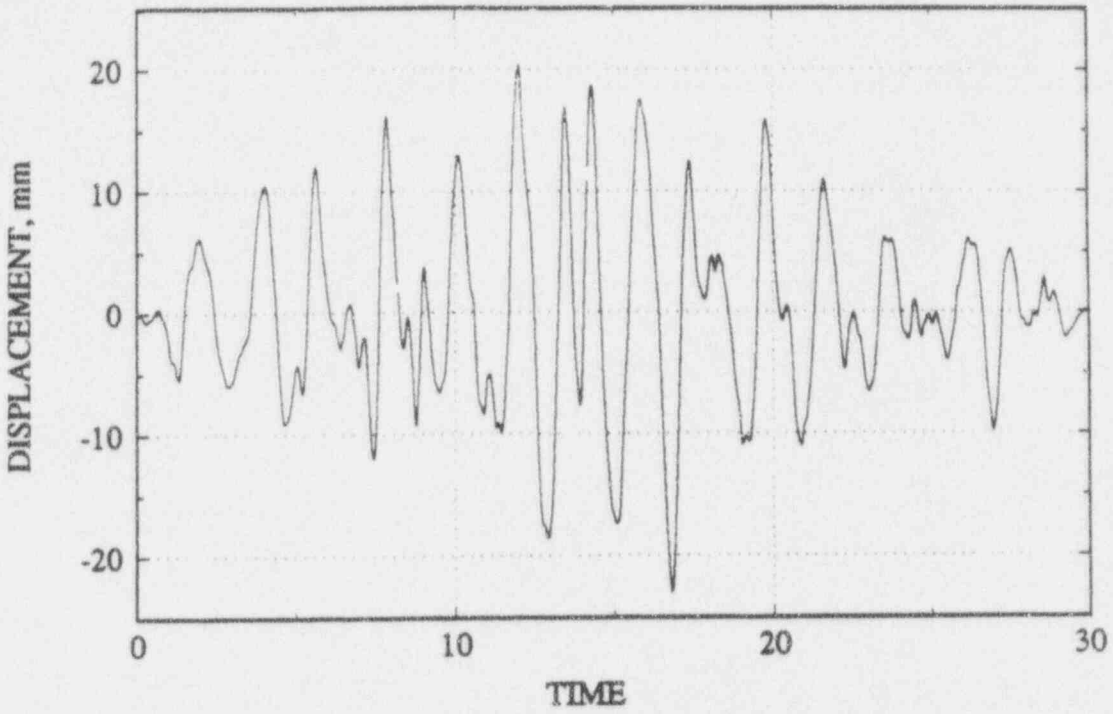

Figure 3-5. Input earthquake displacement time history

shear displacement characteristic curves are presented in the bottom right and bottom left of the figures, respectively. After the maximum shear displacement in the bottom left was reached, the top rock block was moved back to its original position to complete a cycle of shear motion, and the associated shear stress versus shear displacement characteristic curve is presented in the left top of the figures. This process was repeated for a number of cycles. As shown in the figures, the shear stress is assigned to be positive when the shearing is along one direction and becomes negative when the shearing follows the opposite direction. Consequently, the sign for the shear stress denotes the direction of the shear instead of the magnitude of the shear stress.

A peak joint shear strength was observed for the first cycle of both harmonic and earthquake tests if the jointed specimens used for the tests were never shear tested before or did not show signs of past shearing before specimen collection. This observation is consistent with the joint pseudostatic behavior. The phenomenon of wear of the joint is also clearly shown in the figures as the shear stress (joint shear strength) decreases with the number of cycles.

As observed for the cyclic pseudostatic tests (Figure 3-1), one distinct feature of the shear stress versus shear displacement characteristic curve in Figures 3-3 and 3-4 is the smaller shear strength upon reverse shearing as compared to that of forward shearing (the first quadrant versus the fourth quadrant, the third quadrant versus the second quadrant). The equivalent input frequency for the cyclic pseudostatic test as shown in Figure 3-1 is about 2.1×10^{-4} Hz. The same behavior has also been reported by other researchers (Jing et al., 1992; Wibowo et al., 1992; Huang et al., 1993) for rock-joint replicas under cyclic pseudostatic loads.

Figures 3-6 and 3-7 show the corresponding joint normal displacement versus shear displacement characteristic curves for Figures 3-3 and 3-4, respectively. The wear of the joint surfaces

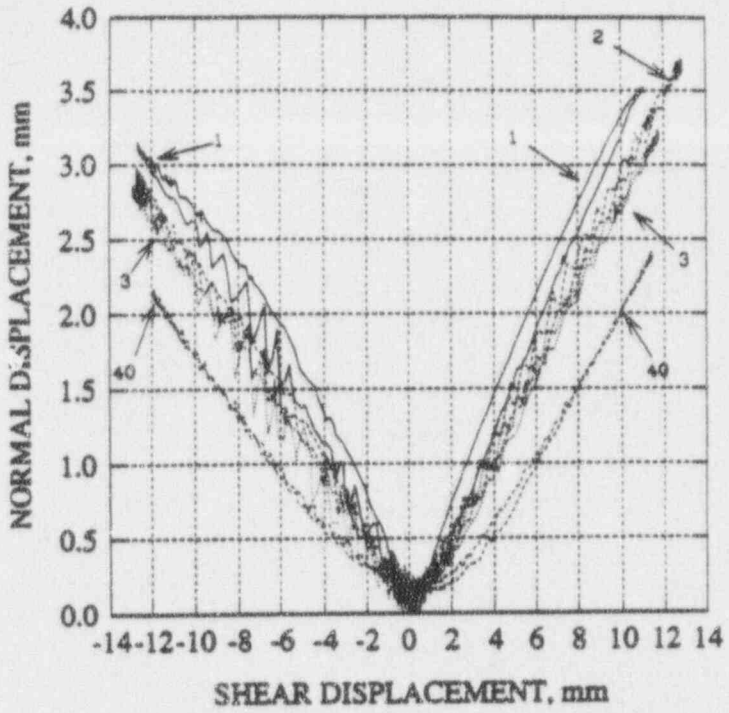

Figure 3-6. Joint normal displacement (dilation) versus shear displacement of a joint under a harmonic load with 1.4-Hz input frequency and 12.7-mm input displacement amplitude

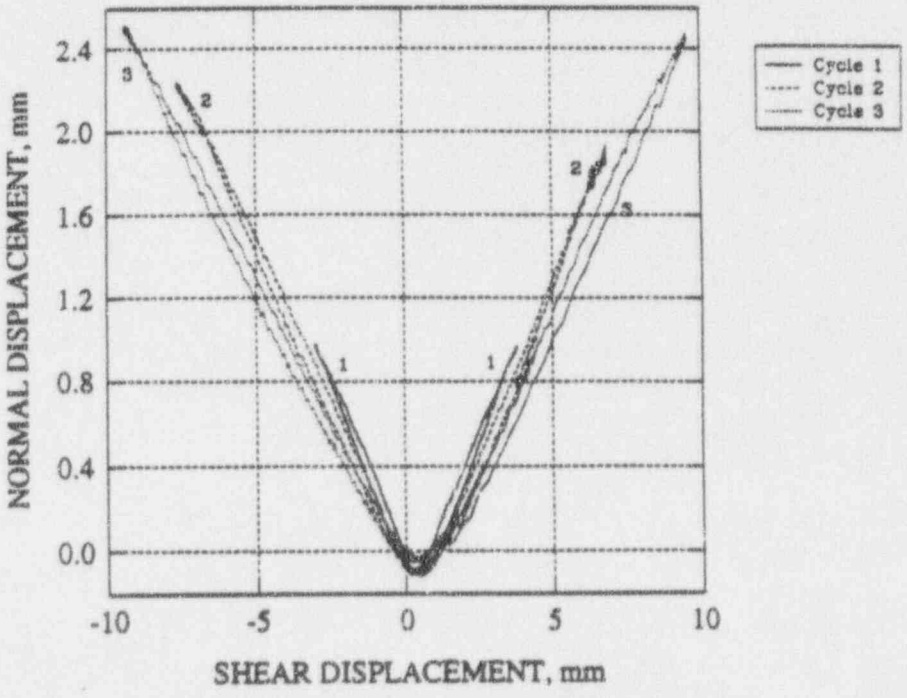

Figure 3-7. Joint normal displacement (dilation) versus shear displacement of a joint under an earthquake load

is a co· nuing process, as is evident in these figures, where the maximum joint normal displacement continues to decrease through the cycles of shearing. It is interesting to note that joint dilation (positive normal displacement) tends to decrease constantly during reverse shearing and may retain a small amount of dilation as the top rock block returns to its original position. The dilation curve is highly nonlinear but generally smooth for at least the first three cycles of the earthquake test results in Figure 3-7 as was the case for the pseudostatic test (Figure 3-2). However, for the harmonic test as shown in Figure 3-6, numerous small-scale stick-slip oscillations continued for many cycles. This observation gives an indication of the potential impact of the input frequencies on joint dilation, which may be related to the existence of small-size rock fragments created in the process of shearing.

In summary, two important distinct features of joint shear response have been identified; one is that the shear strength upon reverse shearing is smaller than that of forward shearing, and the other is that the joint dilation resulting from forward shearing recovers during reverse shearing. These two features occur under various loading conditions. It should be emphasized again that both joint forward and reverse shearing are important phenomena of a rock joint. Reverse shearing can result from an earthquake, thermal load, or both—all of which are expected to be experienced during the life of a HLW repository. Failure to consider these two features of the joint behavior in an underground structural design and performance analysis could result in (i) an overestimation of the stability of emplacement drifts and emplacement boreholes, and (ii) prediction of an incorrect pattern of near-field flow (including preferential pathways for water and gas).

Within the range of variation, the effect of the test input velocity or frequency on joint behavior is found to be minor for the Apache Leap tuff joints. No noticeable effect of the input frequency on the peak joint shear strength and the joint shear strength for the reverse shearing is observed. Consequently, it is possible to ignore the effect of shearing velocity variations, within a range from equivalent static conditions to a velocity comparable to earthquakes, in evaluating joint behavior (Hsiung et al., 1993d). However, the fact that joint behavior in the reverse shearing is distinctly different from that of forward shearing in the sense of joint shear strength, together with the phenomenon that joint dilation recovers during reverse shearing, deserve adequate representation by the rock-joint models. Evaluation of the three rock-joint models and the UDEC computer code is discussed in the following section.

3.2.2 Assessment of Rock-Joint Models/Computer Codes

This research activity is based on two phases of qualification studies. In the first phase, a few currently available computer codes were selected and evaluated against four benchmark problems that have closed-form solutions. Codes with an acceptable performance would be candidates for the second phase of the qualification studies where the dynamic response of well-designed and executed laboratory experiments on single-joint rock specimens will be analyzed. The first phase of the qualification studies on the HONDO II, SPECTROM-331, UDEC, 3DEC, and DECICE codes has been completed, and the results have been reported previously (Hsiung and Chowdhury, 1991, 1993; Hsiung et al., 1993a). This first phase study showed that only UDEC and 3DEC were able to reproduce the analytical solutions of all four benchmark problems. The UDEC code was selected for the second phase study. The objective of the second phase study is to determine whether the existing rock-joint models and associated computer codes can simulate the behavior of a single-joint rock specimen when subjected to dynamic loads.

There are two steps involved in the second phase study. The first is to model the single-joint rock experiments subjected to pseudostatic loads, and the second is to model the joint experiments under

dynamic loads. A detailed discussion on the assessment is given by Hsiung et al. (1993e). A summary of the assessment is provided in this section.

Three commonly used empirical representations for jointed rock behavior were evaluated by explicitly simulating the rock-joint response using the respective constitutive equations. These models were the Mohr-Coulomb, Barton-Bandis, and Continuously-Yielding models.

Careful examination of the constitutive equations for the Mohr-Coulomb, Barton-Bandis, and Continuously-Yielding rock-joint models revealed that all three have adopted essentially the same principle in determining the joint shear strength during reverse shearing. This principle asserts the same joint behaviors under both forward and reverse shearing conditions. With this principle, the same shear strength criterion is applicable to both conditions.

The Mohr-Coulomb joint model is the simplest of the three evaluated in this report that includes a shear failure criterion for a rock joint

$$\tau_o = C + \sigma_n \tan \phi \tag{3-1}$$

where τ_o is shear strength along the joint, σ_n is normal stress across the joint, C is cohesion, and ϕ is friction angle. Once the τ_o is reached, the joint assumes a perfectly plastic deformation. This model does not offer directionality and assumes that no joint wear will occur under either forward or reverse shearing conditions. Consequently, based on this model, the shear strengths are the same for shearing in both directions and under repeated cycles of shearing.

For the other two models, however, joint wear is explicitly considered in the shear strength criteria, and the joint friction behavior is considered to be governed by two friction properties: one is the fundamental friction property or the residual friction property, and the other is the friction property representing joint roughness. The nonlinear joint strength criterion for the Barton-Bandis model can be expressed as (Barton et al., 1985):

$$\tau_o = \sigma_n \tan \left[JRC \log_{10} \left(\frac{JCS}{\sigma_n} \right) + \phi_r \right] \tag{3-2}$$

where JRC is joint roughness coefficient, JCS is joint wall compressive strength, σ_n is joint normal stress, and ϕ_r is residual joint friction angle. The Continuously-Yielding model, using the concept of bounding strength, τ_o, can be expressed as (Cundall and Lemos, 1988)

$$\tau_o = \sigma_n \tan \phi_m \text{ sign } (\Delta u_s) \tag{3-3}$$

where ϕ_m is the current friction angle of the joint and Δu_s is the increment of joint shear displacement. As damage accumulates, ϕ_m is continuously reduced according to

$$\phi_m = (\phi_{mo} - \phi)\, e^{\left(-\frac{u_s^p}{R}\right)} - \phi \qquad (3\text{-}4)$$

where u_s^p is the plastic shear displacement, ϕ_{mo} is the initial friction angle, ϕ is the basic friction angle, and R is a material parameter. As can be seen from the equations, the fundamental or residual friction properties, ϕ_r for the Barton-Bandis model and ϕ for the Continuously-Yielding model, are similar in concept to the friction property in the Mohr-Coulomb joint model. These residual friction properties represent essentially the rock-joint surfaces without roughness, a condition indicating that the joint will not wear. The roughness property is a function of joint shear displacement. The extent of wear increases with joint shear displacement.

To preserve the necessary continuity in joint wear in case of changing direction of shear, both the Barton-Bandis and Continuously-Yielding joint models assert that the remaining friction property at the end of the forward shearing process should control the joint response in the reverse shearing process. In other words, the shear strength at the end of the forward shearing is considered to be the peak shear strength at the beginning of the reverse shearing. As a result, neither of the three rock-joint models can simulate satisfactorily the joint shear experimental behavior during reverse shearing in which the shear strength is different from that at the end of the forward shearing. As observed from the laboratory cyclic pseudostatic and dynamic (harmonic and earthquake) test results, this difference could be large depending upon joint profiles.

The Barton-Bandis and Continuously-Yielding joint models link joint dilation while shearing directly with the roughness properties. The relation between the JRC and dilation angle ψ for the Barton-Bandis model can be expressed in the following form

$$\psi = 0.5\ \mathrm{JRC}\ \log_{10}\left(\frac{\mathrm{JCS}}{\sigma_n}\right) \qquad (3\text{-}5)$$

The dilation angle for the Continuously-Yielding model can be calculated from the following equation

$$\psi = (\phi_{mo} - \phi)\, e^{\left(-\frac{u_s^p}{R}\right)} \qquad (3\text{-}6)$$

Since a joint continues to wear during the process of shearing, the dilation angle used to calculate joint dilation continues to decrease. This implies, therefore, that a joint will eventually stop dilating when it is completely worn. The Mohr-Coulomb joint model calculates dilation based on a constant dilation angle. Dilation starts when shear strength is reached and stops when a critical shear displacement is reached. All three models assume increasing joint dilation, that is, dilation continues to increase regardless of the direction of joint shear. This assumption is not consistent with the joint dilation behavior observed in the laboratory. Laboratory results showed that a joint tends to recover from the forward shearing dilation during reverse shearing with a certain amount of hysteresis between the dilation and dilation recovery curves. The dilation recovery can be complete.

The implementation of these three models in the UDEC code primarily follows the principles described in the two previous paragraphs. Consequently, none of the three rock-joint models implemented

in the UDEC code satisfactorily simulate the joint shear and dilation behaviors observed in laboratory cyclic pseudostatic and dynamic test results that display different mechanisms between forward and reverse shearing. Figure 3-8 gives a typical example of UDEC results showing the joint shear stress versus joint shear displacement relation using the Continuously-Yielding rock-joint model. Furthermore, it has been found that the joint dilation in the Barton-Bandis joint model as indicated in Eq. (3-5) has not been implemented properly in UDEC code. A detailed discussion on the assessment of rock-joint models and computer code UDEC is given by Hsiung et al. (1993e).

In summary, none of the three rock-joint models under evaluation has been found to be capable of predicting joint shear and dilation behaviors under cyclic loading conditions. A new joint model will need to be developed such that the actual joint behavior under cyclic shear loading can be simulated. The work for modifying an existing joint model or developing a new joint model is being performed under Repository Design, Construction, and Operations (RDCO) Subtask 2.3.

3.2.3 Thermal-Mechanical-Hydrological Coupled Modeling (DECOVALEX)

The purpose of this research activity is to increase the understanding of TMH processes for rock mass stability and radionuclide release and transport from a geologic repository. This is being accomplished by NRC/CNWRA participation in an international project called DECOVALEX. DECOVALEX was organized by the Swedish Nuclear Power Inspectorate (SKI) to increase the understanding of coupled TMH processes applied to the underground disposal and isolation of HLW. Eleven funding organizations are currently involved, each supporting one or more research teams. In the DECOVALEX project, modeling is being used to develop and design validation tests of TMH-coupled processes. DECOVALEX is expected to lead to the development and validation of coupled TMH models that are believed to be important to the licensing of a HLW repository.

The final report for Phase I of DECOVALEX (Jing et al., 1993) presents a detailed comparison of results among the various research teams, including the CNWRA, for two benchmark tests (BMTs) and one Test Case (TC) problem. These study problems for Phase I were the Far-Field THM Model (BMT1), the Multiple Fracture Model (BMT2), and the Coupled Stress-Flow Model (TC1).

3.2.3.1 DECOVALEX Phase II Modeling Studies

The modeling work for Phase II of DECOVALEX was recently completed, and the comparison of results among the various research teams, including the CNWRA, for the one BMT and one TC problem is ongoing. These study problems for Phase II were the Near-Field Repository Model (BMT3) and the Coupled Stress-Flow Model (TC1:2). Of these two problems, the BMT3 problem was modeled by the CNWRA team using the discrete-element code UDEC. The detailed discussion of the CNWRA study results is presented by Ahola et al. (1993). A portion of this UDEC analysis of BMT3 was presented in the CNWRA semi-annual report by Hsiung et al. (1993c). The following is a brief discussion of additional results obtained by UDEC for the BMT3 problem during the current reporting period. In addition, a preliminary comparison is made between the CNWRA results and those obtained by two of the other research teams of DECOVALEX.

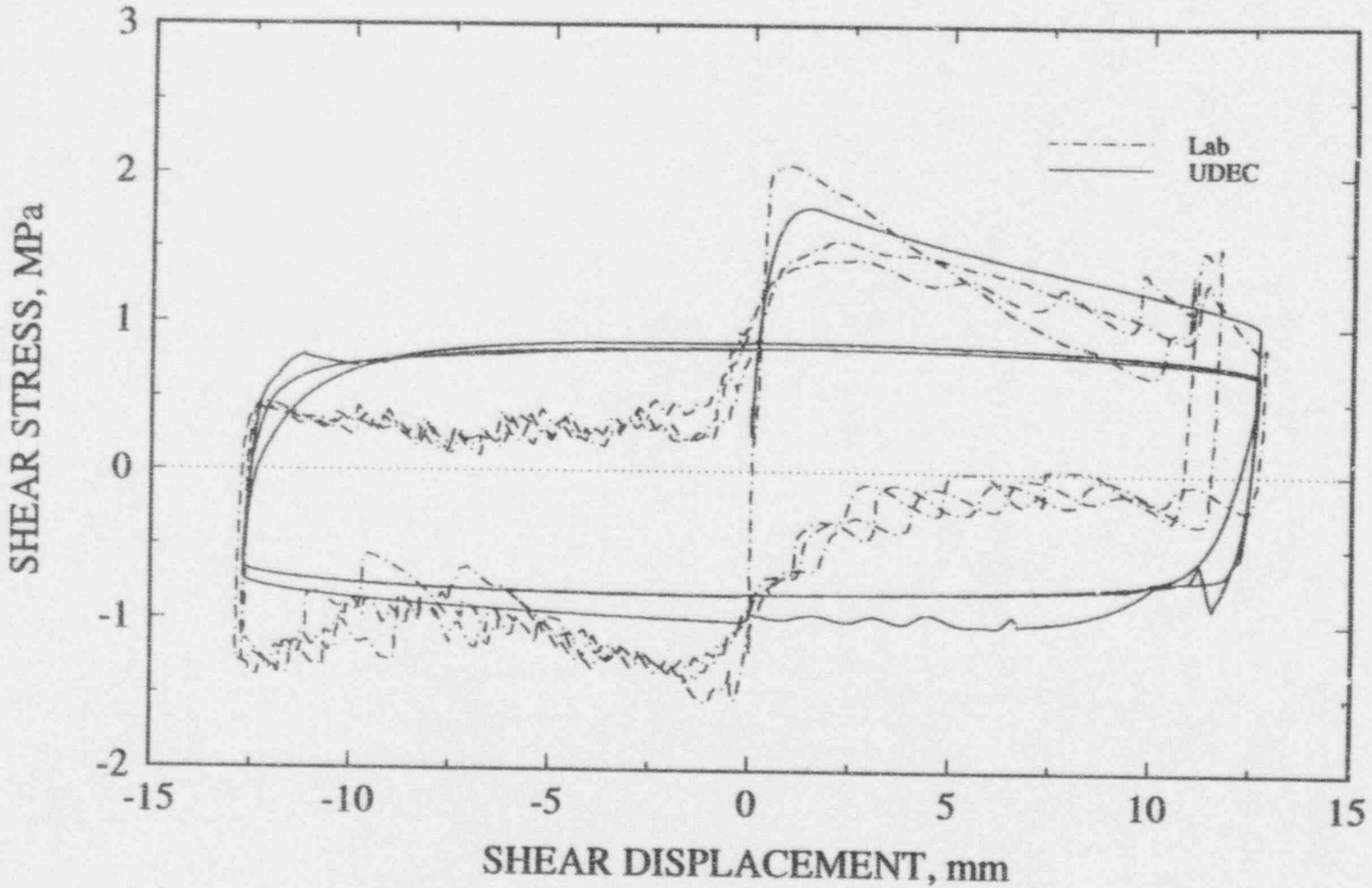

Figure 3-8. Laboratory results and UDEC modeling prediction using Continuously-Yielding joint model of shear stress versus shear displacement of an Apache Leap tuff joint under a harmonic load

3.2.3.2 Near-Field Repository Model (BMT3)

BMT3 was formulated to study the simulation of TMH coupled processes in a near-field, highly fractured, repository environment containing a waste emplacement tunnel and decaying heat source representing the waste canister. The discussion of the problem including specifications, as well as the first UDEC analysis, was previously given by Hsiung et al. (1993c). In that analysis, a number of modeling simplifications were made for the UDEC discrete element analysis due to the high degree of fracturing specified in the problem. For the second analysis, a more detailed discrete element model was developed as a further check to see how sensitive the calculated results for the stresses, displacements, and fluid fluxes were compared to the first UDEC analysis that used a smaller number of fractures than was given in the original problem specifications.

Figure 3-9 shows the two discrete element models used for the UDEC analyses. For both cases, vertical symmetry along the z plane was assumed, which was justified by the problem geometry and boundary conditions as well as the fact that the equivalent permeabilities given in the x and z directions on the 50×50-m scale (i.e., entire model) were approximately equal. This is somewhat expected due to the random nature of the fracture orientations. For the first case (Case A) shown in Figure 3-9a, an equivalent set of uniformly spaced joints was used to represent the rock mass beyond a certain distance from the tunnel boundary to further reduce the number of fractures since they are modeled explicitly with the discrete element method. In this outer region, the hydraulic apertures as well as the mechanical properties of the rectangular discrete element blocks are adjusted to account for the equivalent properties of this region. The discrete element blocks themselves are discretized into triangular finite difference zones to simulate elastic block deformation. The inner region around the emplacement tunnel and heater contained those individual fractures from the problem specifications above an arbitrarily chosen cutoff length of 2 m. The joint and matrix material properties given in the specifications were used in this region. In order to somewhat simplify the geometry of the discrete element blocks within this inner region for discretization into finite difference elements, a set of uniformly spaced horizontal and vertical fractures were input at the same spacing as those in the outer model region. The given fracture data was then superimposed upon this grid in the near-field tunnel region. Artificial joint properties were specified for those portions of the uniformly spaced horizontal and vertical joints within this inner fractured region. The artificial joint properties consisted of high strength and stiffness as well as zero permeability. These conditions mean that the artificial joints are mechanically and hydraulically inactive.

The second UDEC case (Case B) shown in Figure 3-9b is similar to the first case except that fracture data given for the BMT problem were extended to the outer boundaries of the model. This second case still did not include all the fracture data supplied for the problem, only those above an arbitrary cutoff length of 1.5 m. Thus, in addition to increasing the extent of the fractured region modeled, the fracture density around the tunnel for Case B is slightly higher than that for Case A and closer to that of the original BMT specification. Again, for this second case, a uniform set of artificial fractures was first input into the model to aid in simplifying the block geometries. Also, no equivalent material properties were assumed. Figure 3-10a shows a comparison of the normal stress (σ_{xx}) between the two cases along the vertical line (line I) indicated in Figure 3-9a. Likewise, Figure 3-10b shows a comparison of the normal stress (σ_{yy}) between the two cases along the horizontal line (line II) indicated in Figure 3-9a. These results are taken after a period of 4 yr of heating. This time corresponds to the maximum temperature (approximately 172 °C) reached at the heat source. The results show good agreement among the calculated stresses indicating that, at least for the thermomechanical aspect of the analysis, the more simplified UDEC model would be adequate. It should be stated that this conclusion

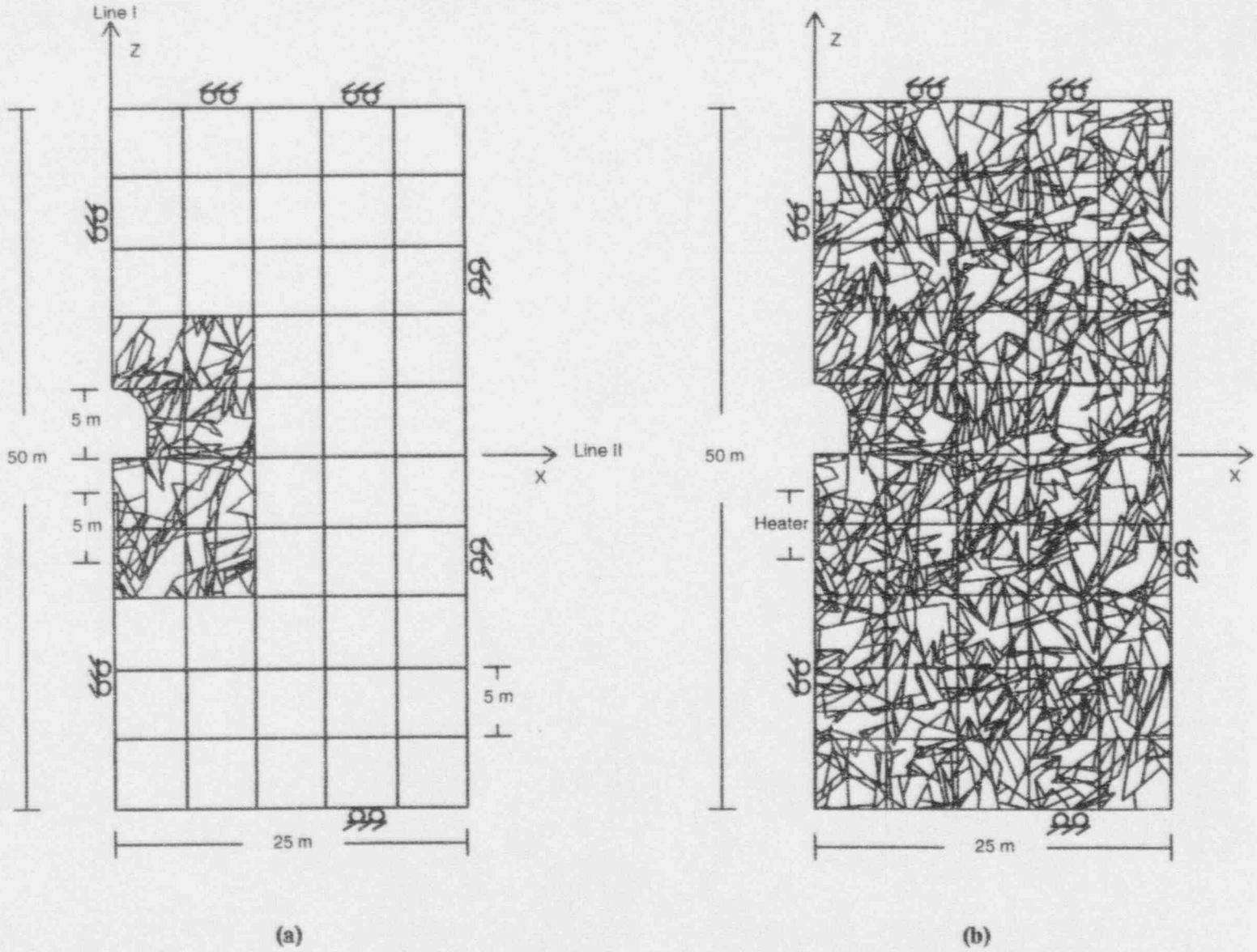

Figure 3-9. UDEC models showing distinct element blocks for the (a) Case A and (b) Case B analyses

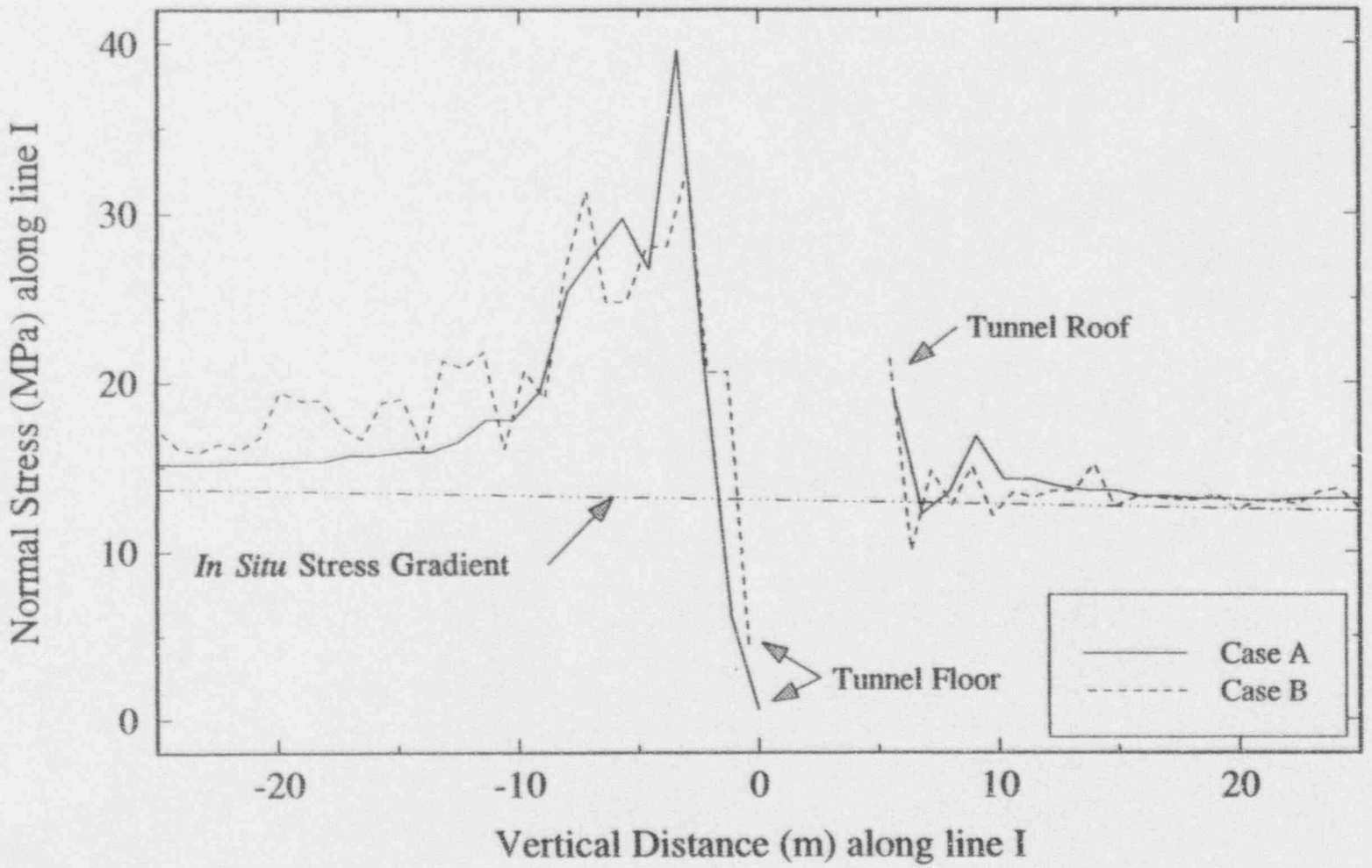

Figure 3-10a. Comparison of normal stresses for the two UDEC cases after 4 yr of heating along vertical line I (i.e., σ_{xx})

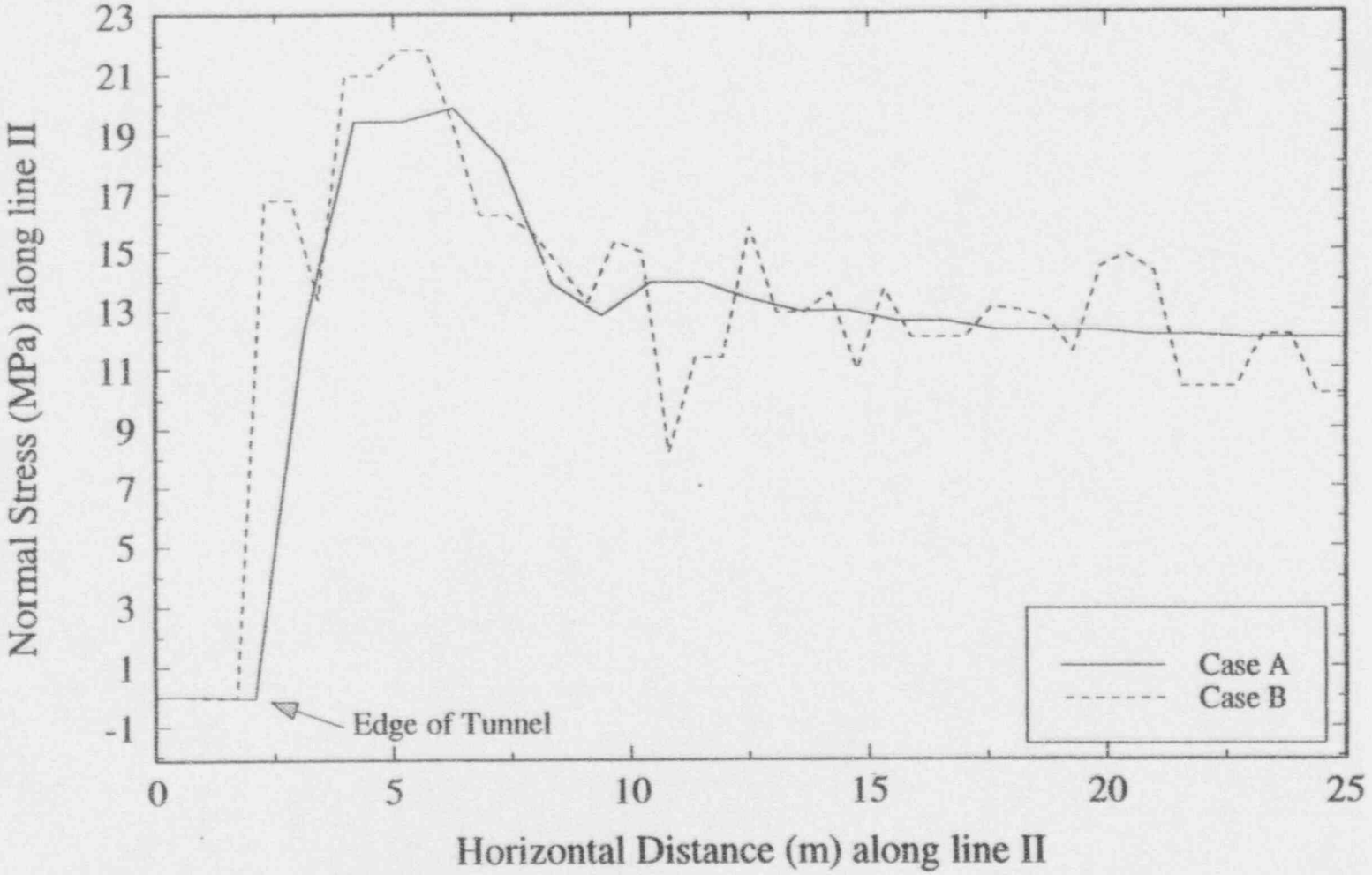

Figure 3-10b. Comparison of normal stresses for the two UDEC cases after 4 yr of heating along horizontal line II (i.e., σ_{yy})

is based solely on comparison of two separate UDEC calculations, with no actual data available. It should be noted that the UDEC analysis for Case A took substantially less computer run time. There was a somewhat larger discrepancy in the calculated flow results between the two cases. For example, at this time of maximum temperature, the calculated fluid flux into the right half of the tunnel boundary for Case A was 8.425×10^{-9} m^3/s versus 2.178×10^{-8} m^3/s for Case B; a difference of approximately 61 percent.

A preliminary comparison of the stresses and displacements obtained from the CNWRA UDEC analysis with those from two other DECOVALEX research teams for BMT3 is shown in Figures 3-11a and b. The location of comparison for these results has the coordinates $x=7.5$ m and $z=-7.5$ m, that is to the right and beneath the tunnel floor. The Swedish research team used the finite difference code FLAC for their analysis, and only presented results up to a period of 4 yr of heating. The French research team used a finite-element code CASTEM-2000 to run two cases, the first being an isotropic material property representation of the specified fracture pattern (Case A), and the second being an anisotropic material property representation (Case B). Figure 3-11a shows a comparison of the vertical displacement among the three codes at the indicated coordinate location as a function of time. Figure 3-11b shows the horizontal stresses calculated among the three codes at the same location. One can see that even though there is good agreement among the displacement results, there is wide discrepancy among the stresses. Both the stresses calculated by the FLAC and CASTEM-2000 codes are believed to be the total stresses, including both the effective stress and pore pressure. The UDEC code, however, does not have matrix flow and thus the stress shown in Figure 3-11b is the mechanical stress calculated within the block nearest the monitoring point. A more appropriate approach would be to compare the effective stress among the codes; however, it is believed that the pore pressure effect would not cause that much improvement in the results. Further discussion is needed among the different research teams to identify and resolve the reasons for the discrepancies among the results. Final comparisons will be made in a report to be issued by the SKI that will document the completion of Phase II of DECOVALEX.

3.3 ASSESSMENT OF PROGRESS TOWARD MEETING PROJECT OBJECTIVES

The primary objective of the Seismic Rock Mechanics Research Project is to identify seismic-related key technical issues that will affect repository design and performance and to develop techniques that could be used to predict the response of near-field jointed rock mass at the proposed HLW repository at Yucca Mountain, Nevada, when it is subjected to repetitive seismic (including earthquakes and nuclear explosions at the Nevada Test Site) and thermal loads. This is being accomplished through laboratory and field experiments as well as computer modeling studies. Closure on several seismic-related issues has been accomplished. For instance, it has been determined through field experimental studies that repetitive, lower-magnitude seismic events can cause greater damage to underground tunnels than a single large-magnitude event. Most designs today consider only the maximum credible seismic event. Such results have been presented to the Nuclear Waste Technical Review Board (NWTRB), and the NWTRB has incorporated these findings in their annual report as guidance for the U.S. Department of Energy (DOE) to consider in its Exploratory Studies Facility (ESF) and repository design (Nuclear Waste Technical Review Board, 1992). The findings on the effect of repetitive seismic events have also directly supported the development of the Compliance Determination Method (CDM) for shafts and ramps design, specifically with regard to establishing review method steps for assessing protection against natural phenomena and environmental conditions [10 CFR 60.131(b)(1)]. These findings will be used further in

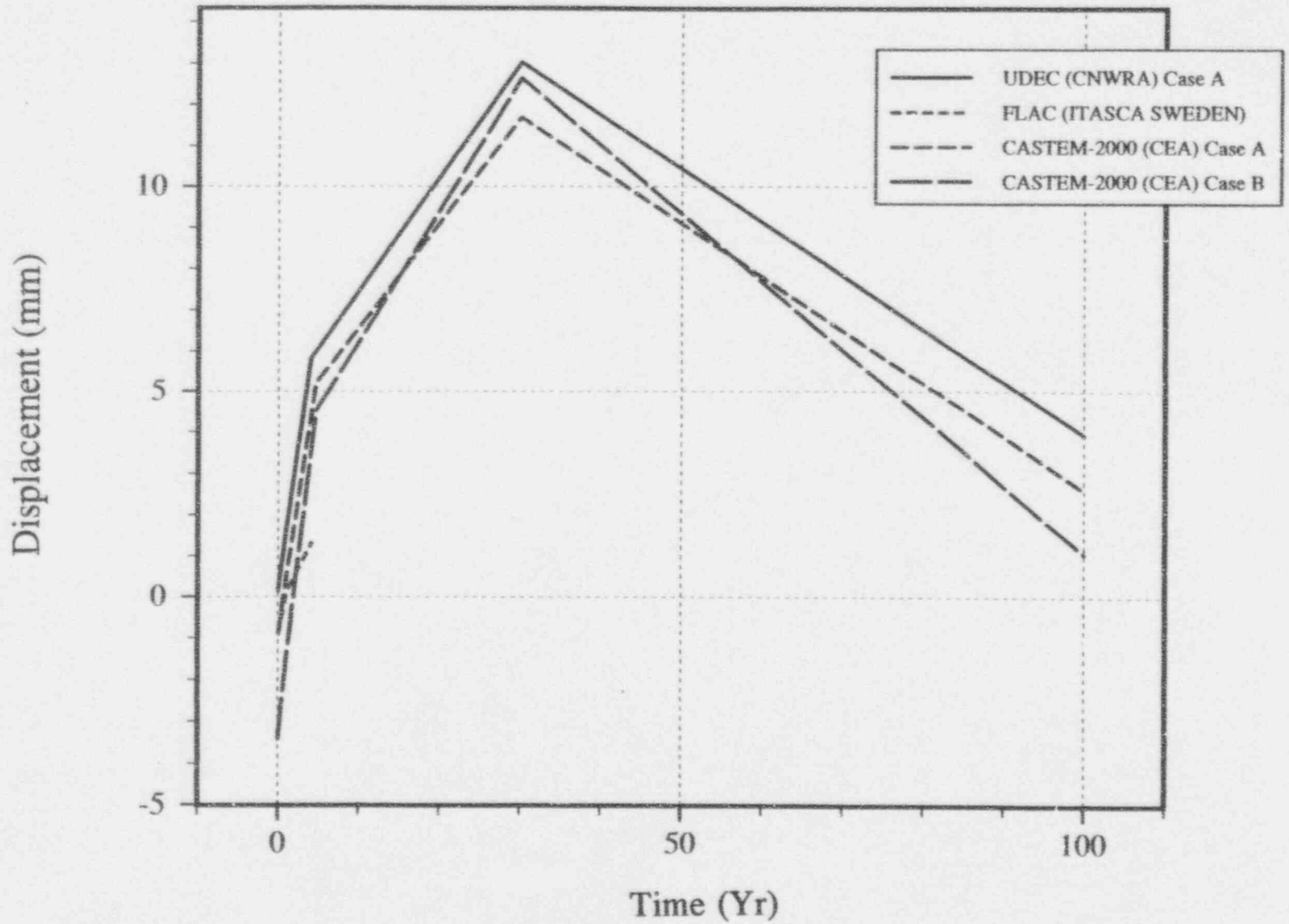

Figure 3-11a. Comparison of results among three computer codes used in DECOVALEX at the location x=7.5 m, z=−7.5 m for vertical displacement

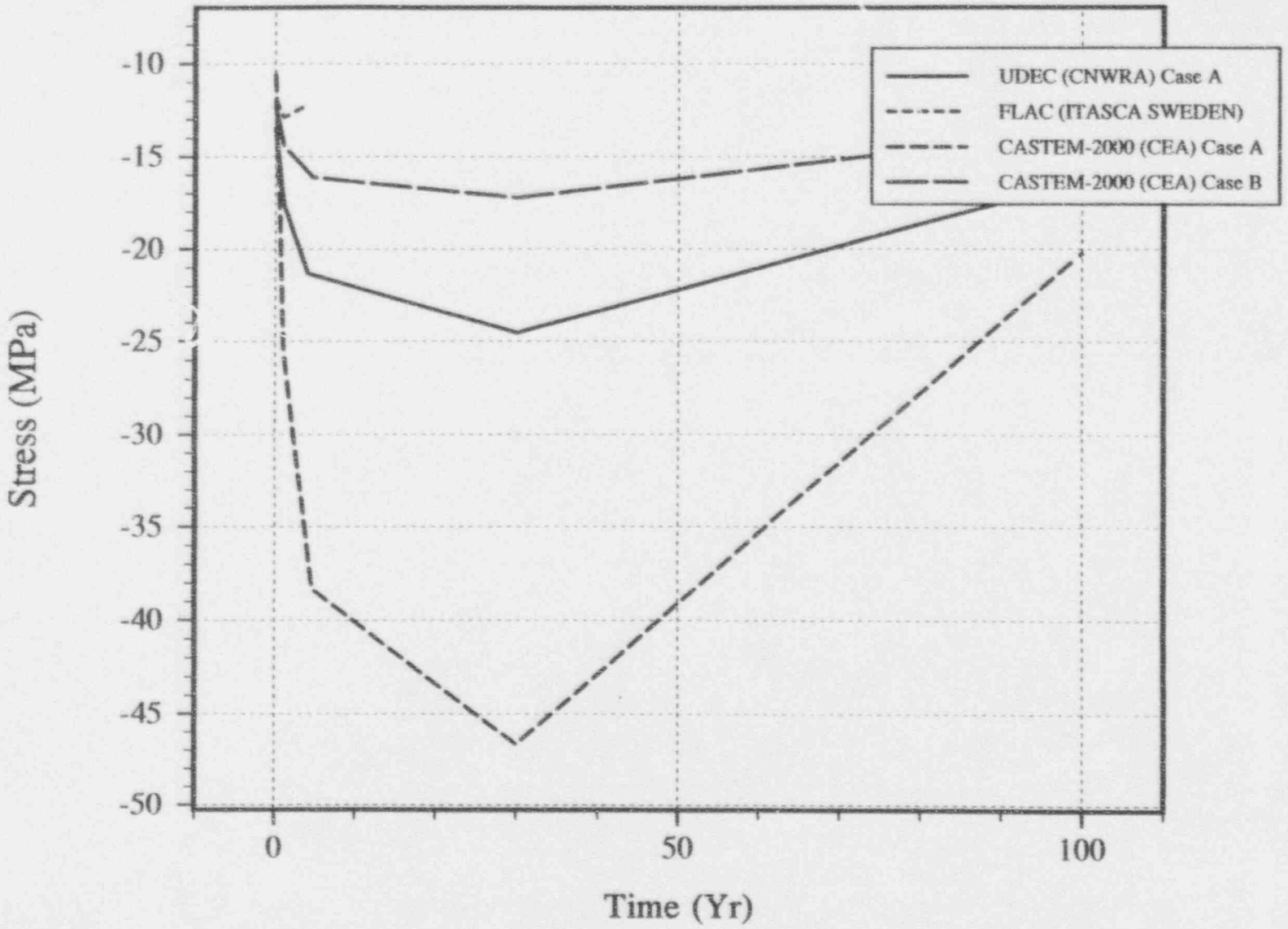

Figure 3-11b. Comparison of results among three computer codes used in DECOVALEX at the location x=7.5 m, z=−7.5 m for horizontal stress

the development of the CDM for RRT 4.4 Assessment of Compliance with Design Criteria for Underground Facility; 5.3 Assessment of Compliance with the Design Criteria for the Postclosure Features of the Underground Facility; 5.4 Assessment of Compliance with the EBS Performance Objectives; and 6.1 Assessment of Compliance with the Requirement for Cumulative Releases of Radioactive Materials. Also, based on the field experiments performed at the Lucky Friday Mine, Mullan, Idaho (Task 5), both the magnitude and duration of water pressure changes due to seismic events were measured to be small (Hsiung et al., 1993f). These results would tend to indicate that significant changes in the water pressure below the proposed repository site, due to seismic events of large magnitude, may not be credible.

Through laboratory experiments and modeling studies, it has been found that the rock-joint models presently incorporated in the computer codes under consideration for use in seismic design in jointed rock masses do not correctly simulate the cyclic pseudostatic and dynamic rock-joint behavior. Through identification of these problems and subsequent enhancement of the rock-joint models, the staff will be better abie to review the DOE repository seismic design and support assessment of repository performance. In addition, several of the design-related CDMs have KTUs related to the impact of repetitive seismic motion on long-term performance of seals. Furthermore, observed deficiencies in the rock-joint model will be used as a basis for developing acceptance criteria in the CDMs relevant to design review of subsurface facilities. Having a verified code for seismic analysis, the staff will have better capabilities to perform independent detailed safety reviews regarding these issues.

The objective of DECOVALEX (Task 9) TMH modeling and coupled experiments is to address KTUs related to the impact of coupled TMH processes on repository design and performance. These activities are to evaluate methodologies including model validation and code verification for coupled TMH modeling of jointed rocks. The work being done in this task is supporting the development of a compliance determination code under technical assistance work for simulating coupled processes. This code will be used by the NRC and the CNWRA for determination of DOE compliance with NRC regulations on thermal and repetitive seismic loads. The results of seismic research have also been used for Site Characterization Plan reviews and are currently being used for ESF Title II Design reviews.

3.4 PLANS FOR NEXT REPORTING PERIOD

A dynamic scale model experiment on a jointed rock mass will be performed during the next reporting period to study cumulative seismic effects. This will provide a better understanding of jointed rock mass behavior subjected to repeated earthquake loads and will generate a complete data set for code verification. Work on DECOVALEX Phase III modeling, modification of the direct shear test apparatus for coupled mechanical-hydrological (MH) experiments, and the MH experiments will be performed.

Review of preliminary KTUs in CDSs indicates a varying degree of uncertainty in issues related to the long-term performance of seals for shafts, ramps, and boreholes of the repository under conditions of elevated repository temperatures and seismic loads (RRT 4.3). The issues include: (i) whether seals are important to repository performance in an unsaturated environment; (ii) if they are judged to be important, whether the seals will remain effective over thousands of years (seal long-term performance), and (iii) whether technology exists to effectively install seals such that the intended performance of the seals can be achieved. There is a significant quantity of data available from industry and through previous NRC contracts with the University of Arizona. These data may be used for assessment of short-term performance of seals, but the conclusions drawn from these data may need to be substantiated through

long-term studies. Toward this end, a new research project in long-term seal performance is under consideration. Technical issues related to the long-term seal performance that are particularly important to licensing include:

- Role in overall repository performance—the DOE preliminary PAs seem to indicate that the contributions of seals to the overall repository performance may be small. Reevaluation of this preliminary assessment on the role of seals is needed to either confirm or rebut the assessment. This reevaluation is considered important since the long-term performance of seals under heated and unsaturated environments is not currently understood. Early determination of the role of seals in the overall repository performance is extremely helpful in streamlining a strategy for addressing this KTU.

- Thermal-mechanical (including repetitive seismic loads) effects on the long-term performance of seals, including the surrounding rock mass.

- Long-term thermal-hydrological effects on the chemical properties of seal materials.

The specific approach toward resolving these technical issues will be formulated in the future through interactions between CNWRA and NRC staff members. It would seem logical that the first issue listed above be resolved first through a preliminary calculation to determine whether there is a need for long-term seal performance research.

3.5 REFERENCES

Ahola, M.P., S.M. Hsiung, L.J. Lorig, and A.H. Chowdhury. 1992. *Thermo-Hydro-Mechanical-Coupled Molding: Multiple Fracture Model BMT2, Coupled Stress-Flow Model TC1. DECOVALEX — Phase I.* CNWRA 92-005. San Antonio, TX: Center for Nuclear Waste Regulatory Analyses.

Ahola, M.P., L.J. Lorig, A.H. Chowdhury, and S.M. Hsiung. 1993. *Thermo-Hydro-Mechanical Coupled Modeling: Near-Field Repository Model, BMT3. DECOVALEX–Phase II.* CNWRA 93-002. San Antonio, TX: Center for Nuclear Waste Regulatory Analyses.

Barton, N.R., S.C. Bandis, and K. Bakhtar. 1985. Strength, deformation and conductivity coupling of rock-joints. *International Journal of Rock Mechanics and Mining Sciences & Geomechanics Abstracts* 22(3): 121–140.

Brady, B.H.G., S.M. Hsiung, and A.H. Chowdhury. 1990. *Qualification Studies on the Distinct Element Code UDEC Against Some Benchmark Analytical Problems.* CNWRA 90-004. San Antonio, TX: Center for Nuclear Waste Regulatory Analyses.

Brandshaug, T., B. Dasgupta, B.H.G. Brady, S.M. Hsiung, and A.H. Chowdhury. 1990. *Qualification Studies on the Finite Element Code HONDO II Against Some Benchmark Analytical Problems.* CNWRA 90-006. San Antonio, TX: Center for Nuclear Waste Regulatory Analyses.

Cundall, P.A., and J.V. Lemos. 1988. Numerical simulation of fault instabilities with the continuously-yielding joint model. *Proceedings of the 2nd International Symposium on Rockbursts and Seismicity in Mines.* Minneapolis, MN: University of Minnesota.

Hsiung, S.M., and A.H. Chowdhury. 1991. *Report on Research Activities for Calendar Year 1990.* B. Sagar, ed. NUREG/CR-5817. CNWRA 90-01A. Washington, DC: U.S. Nuclear Regulatory Commission.

Hsiung, S.M., and A.H. Chowdhury. 1993. *NRC High-Level Radioactive Waste Research at CNWRA For Calendar Year 1991.* W.C. Patrick, ed. NUREG/CR-5817. CNWRA 91-01A. Washington, DC: U.S. Nuclear Regulatory Commission.

Hsiung, S.M., A.H. Chowdhury, W. Blake, M.P. Ahola, and A. Ghosh. 1992. *Field Site Investigation: Effect of Mine Seismicity on a Jointed Rock Mass.* CNWRA 92-012. San Antonio, TX: Center for Nuclear Waste Regulatory Analyses.

Hsiung, S.M., M.P. Ahola, and A.H. Chowdhury. 1993a. *NRC High-Level Radioactive Waste Research at CNWRA January-June 1992.* W.C. Patrick, ed. NUREG/CR-5817. CNWRA 92-01S. Washington, DC: U.S. Nuclear Regulatory Commission.

Hsiung, S.M., M.P. Ahola, A. Ghosh, and A.H. Chowdhury. 1993b. *NRC High-Level Radioactive Waste Research at CNWRA July-December 1992.* B. Sagar, ed. NUREG/CR-5817. CNWRA 92-02S. Washington, DC: U.S. Nuclear Regulatory Commission.

Hsiung, S.M., M.P. Ahola, A. Ghosh, and A.H. Chowdhury. 1993c. *NRC High-Level Radioactive Waste Research at CNWRA January-June 1993.* B. Sagar, ed. CNWRA 93-01S. San Antonio, TX: Center for Nuclear Waste Regulatory Analyses.

Hsiung, S.M., D.D. Kana, M.P. Ahola, A.H. Chowdhury, and A. Ghosh. 1993d. *Laboratory Characterization of Rock-Joints.* CNWRA 93-013. San Antonio, TX: Center for Nuclear Waste Regulatory Analyses.

Hsiung, S.M., A. Ghosh, A.H. Chowdhury, and M.P. Ahola. 1993e. *Evaluation of Rock-Joint Models and Computer Code UDEC Against Experimental Results.* CNWRA 93-024. San Antonio, TX: Center for Nuclear Waste Regulatory Analyses.

Hsiung S.M., A.H. Chowdhury, W. Blake, and J. Philip. 1993f. Field investigation of mining-induced seismicity on local geohydrology. *Proceedings of the Fourth Annual International Conference on High-Level Radioactive Waste Management.* La Grange Park, IL: American Nuclear Society: 913-920.

Huang, X., B.C. Haimson, M.E. Plesha, and X. Qiu. 1993. An investigation of the mechanics of rock joints—part I. Laboratory investigation. *International Journal of Rock Mechanics and Mining Sciences & Geomechanics Abstracts* 30(3): 257-269.

Jing, L., E. Nordlund, and O. Stephansson. 1992. An experimental study on the anisotropy and stress-dependency of the strength and deformability of rock-joints. *International Journal of Rock Mechanics and Mining Sciences & Geomechanics Abstracts*: 29(6) 525-542.

Jing, L., J. Rutqvist, O. Stephansson, C.F. Tsang, and F. Kautsky. 1993. *DECOVALEX-Mathematical Models of Coupled H-T-M Processes for Nuclear Waste Repositories. Report of Phase I.* Stockholm, Sweden: Swedish Nuclear Power Inspectorate.

Kana, D.D., D.C. Scheidt, B.H.G. Brady, A.H. Chowdhury, S.M. Hsiung, and B.W. Vanzant. 1990. *Development of a Rock-Joint Dynamic Shear Test Apparatus*. CNWRA 90-005. San Antonio, TX: Center for Nuclear Waste Regulatory Analyses.

Kana, D.D., B.H.G. Brady, B.W. Vanzant, and P.K. Nair. 1991. *Critical Assessment of Seismic and Geomechanics Literature Related to a High-Level Nuclear Waste Underground Repository*. NUREG/CR-5440. CNWRA 89-001. Washington, DC: U.S. Nuclear Regulatory Commission.

Nuclear Waste Technical Review Board. 1992. *Fifth Report of the U.S. Congress and the U.S. Secretary of Energy*. Washington, DC: Nuclear Waste Technical Review Board.

Rojstaczer, S., and S. Wolf. 1992. Permeability changes associated with large earthquakes: An example from Loma Prieta, California. *Geology* 2: 211–214.

Waller, R. 1966. *Effects of the March 1964 Alaska Earthquake on the Hydrology of South-Central Alaska*. U.S. Geological Survey Professional Paper 544-B: 1–28.

Wibowo, J.T., B. Amadei, S. Sture, and A.B. Robertson. 1992. Shear response of a rock-joint under different boundary conditions: an experimental study. *Conference of Fractured and Jointed Rock Masses*. Preprints. June 3-5, 1992. Lake Tahoe, CA.

4 INTEGRATED WASTE PACKAGE EXPERIMENTS

by Narasi Sridhar, Gustavo A. Cragnolino, and Darrell S. Dunn

Investigators: Narasi Sridhar, Gustavo A. Cragnolino, and Darrell S. Dunn (CNWRA)

NRC Project Officer: Michael B. McNeil

4.1 OVERALL TECHNICAL OBJECTIVES

The overall technical objectives of the Integrated Waste Package Experiments (IWPE) Project are to:

- Conduct waste package experiments to scope and study the key parameters affecting long-term material performance
- Assess waste package materials and designs selected by the U.S. Department of Energy (DOE) and provide independent evaluation for reasonable assurance of long-term performance
- Support the Office of Nuclear Regulatory Research (RES) in addressing the needs of the Division of High-Level Waste Management (DHLWM)

Two Key Technical Uncertainties (KTUs), developed as part of the compliance determination strategy (CDS) related to waste package performance and listed in the License Application Review Plan (LARP), Sections 5.2 and 5.4 (License Application Review Plan, 1992), are addressed in the IWPE program. These are:

- The extrapolation of short-term laboratory and prototype test results to predict long-term performance of waste packages and engineered barrier systems (EBSs)
- The prediction of environmental effects on the performance of waste packages and the EBS

To address the above objectives, the IWPE program is divided into six tasks: Task 1, Corrosion; Task 2, Stress corrosion cracking (SCC); Task 3, Thermal stability of materials; Task 4, Microbially influenced corrosion; Task 5, Other degradation modes and alternate container material performance issues; and Task 6, General reporting.

Results generated within the IWPE program are being used to provide input parameters to waste package performance assessment (PA) models, as well as to verify the model assumptions and predictions. A key area of integration between the IWPE, thermohydrology, and geochemistry projects is in the prediction of environmental evolution very near the waste packages. The fundamental assumption in waste package corrosion studies reported here is the presence of an aqueous environment, at least episodically. This is a conservative assumption because the corrosion rate in a dry steam or dry air environment at anticipated repository temperatures is negligible (Farmer et al., 1991). However, the aqueous environment near the container can have a wide range of compositions. The experimental research and modeling efforts within the thermohydrology and geochemistry projects will assist evaluations of the presence and chemistry of aqueous environments near the waste package. The results of the IWPE Project will identify

the environmental factors of importance to waste package performance and thus guide the investigations of rock-water interactions in the geochemistry projects. Another aspect of the near-field environment is the effect of corrosion of containers/waste forms on the environment chemistry. This is especially important in occluded regions such as crevices between the container and the rock.

4.2 SIGNIFICANT TECHNICAL ACCOMPLISHMENTS

4.2.1 Background

In the United States geologic disposal program, two types of waste package emplacement concepts are being considered: (i) vertical emplacement of a single-wall or double-wall container in a borehole with an air gap between the container and the borehole, and (ii) horizontal emplacement of a double-wall container surrounded by a suitable backfill in the drifts of the underground repository. The vertical emplacement of a thin (e.g., 12-mm thick), single-wall container made of an austenitic alloy is the present reference design, although the horizontal drift emplacement of a double-wall container is receiving increasing attention (Doering, 1993). It has also been proposed that high thermal loading via horizontal drift emplacement of large waste packages, containing up to 21 Pressurized Water Reactor (PWR) fuel assemblies, be used to create a dry-out zone around the EBS for thousands of years that will minimize corrosion and nongaseous radionuclide transport (Ruffner et al., 1993; Buscheck et al., 1993). The drying-out process may create deposition of solids rich in Ca and Si (Beavers et al., 1992; Pabalan and Murphy, 1993). In addition, backflow of the condensate through fractures may result in an aqueous environment around the container, as indicated by the results of some field heater tests (Patrick, 1986; Zimmerman et al., 1986; Ramirez, 1991). The evaporation of water may cause the formation of solutions rich in chloride and sulfate (Abraham et al., 1986; Beavers et al., 1992; Walton, 1993). Hence, a conservative approach to life prediction is to assume the presence of aqueous conditions surrounding the containers. The chemical composition of such an aqueous environment is not known, and a range of concentrations of various species has been explored (Sridhar et al., 1993a).

The approach used in SOurce TErm Code (SOTEC) for the Iterative Performance Assessment (IPA) and in the Engineered Barrier System Performance Assessment Codes (EBSPAC) activities for the prediction of performance of container materials (Sagar et al., 1992; Sridhar et al., 1993b) assumes that corrosion failure modes of importance to life prediction are determined by the corrosion potential. The corrosion potential of the container material, which is a mixed potential dictated by the kinetics of the anodic and cathodic reactions at the surface exposed to the repository environment, changes with time in response to factors such as radiolysis, pH, temperature, and oxygen concentration (Macdonald and Urquidi-Macdonald, 1990). If the corrosion potential exceeds the pit-initiation potential (E_p), pits initiate and propagate into the container wall. If the corrosion potential drops below E_p, pits already initiated continue to grow, but no new pits initiate. Finally, if the corrosion potential drops below the repassivation potential (E_{rp}), all pits repassivate and cease to grow. After repassivation, the corrosion of the container continues in a uniform manner at a low rate determined by the passive current density. This concept of critical potentials has been well established in the literature for pitting and crevice corrosion (Szklarska-Smialowska, 1986). Both E_p and E_{rp} are distributed values and depend on both material and environmental factors. Although two potentials, E_p and E_{rp}, are defined, in long-term prediction, these two potentials may coincide to one critical potential (Tsujikawa et al., 1987; Thompson and Syrett, 1992). Additionally, while the method is illustrated for pitting, analogous parameters have been used to characterize the crevice-corrosion behavior of these alloys (Okayama et al., 1987). The concept of critical potential has been applied to SCC of many alloy-environment combinations (Cragnolino and Sridhar,

1992a), but there are no data for the alloys and environments of interest to the Yucca Mountain (YM) repository. Other environmental degradation phenomena such as hydrogen embrittlement also depend on the corrosion potential, but do not exhibit a critical potential.

The crucial questions in the measurement and use of E_{rp} are its dependence on the extent of prior pit/crevice corrosion, measurement technique, environmental parameters, and microstructural characteristics. The research results reported previously (Cragnolino and Sridhar, 1992b; Sridhar and Cragnolino, 1992a,b; Sridhar et al., 1992; Sridhar et al., 1993a, 1993c) have addressed some of these questions for pitting and crevice corrosion. It was shown that the E_{rp} was independent of the extent of prior pitting and that it decreased logarithmically with an increase in chloride concentration. To a more limited extent, it was also shown that E_{rp} for alloy 825 was not dependent on the pH and concentration of species such as sulfate, bicarbonate, and silica. Another important issue with respect to long-term prediction of container performance is the degree of conservatism entailed in the use of repassivation potentials irrespective of the variations in surface conditions. The effect of surface chromium depletion and surface roughness on localized corrosion of alloy 825 has been addressed in recently published papers (Dunn et al., 1993a,b). It has been shown that the E_{rp} measured on polished specimens is lower (more conservative) than the potentials required to grow pits on a Cr-depleted surface.

However, a more fundamental understanding of E_{rp} through a mechanistic interpretation of the chemistry changes in the crevice/pit and their effect on the electrochemical response of the metal is essential in order to use it with confidence in long-term prediction. The experimental results of chemistry changes inside a controlled-geometry crevice are reported here. Both conditions for initiation and repassivation of crevice corrosion are addressed in these experiments. Crevice corrosion initiation due to changes in the chemistry inside a crevice has been modeled previously (Walton and Kalandros, 1992). However, this model and other similar models cannot, at present, predict the dependence of crevice initiation on potential. A discussion of the modifications required in the crevice corrosion model is also provided.

Studies on the effects of environmental factors and potential on the SCC of two candidate container materials, type 316L stainless steel (SS) and alloy 825, are also included in this report. Slow strain rate tests are being used to define environmental conditions, in terms of solution composition, pH, and temperature, as well as potential ranges that promote SCC in chloride-containing solutions. The goal is to determine whether a critical potential for SCC exists, and then to define the relationship between this potential and the E_{rp} for pitting/crevice corrosion. If such a critical potential for SCC exists, it can be used as a bounding parameter for the prediction of long-term behavior assuming, as a worst case, that the level of residual and imposed stresses on the container would be sufficiently high to induce cracking under the range of environmental conditions anticipated at the repository site. The effect of test technique on SCC is also investigated by using U-bend, constant-deflection tests for longer periods of time.

4.2.2 Localized Corrosion Studies

4.2.2.1 Experimental Procedures

The crevice assembly was constructed by sandwiching the specimen between blocks of polymethyl methacrylate (PMMA) as shown in Figure 4-1. Care was taken in this design to avoid creating reservoirs for solution inside the crevice that tended to reduce the magnitude of chemistry changes. Longitudinal grooves were provided on the bottom crevice assembly so that no crevice corrosion occurred

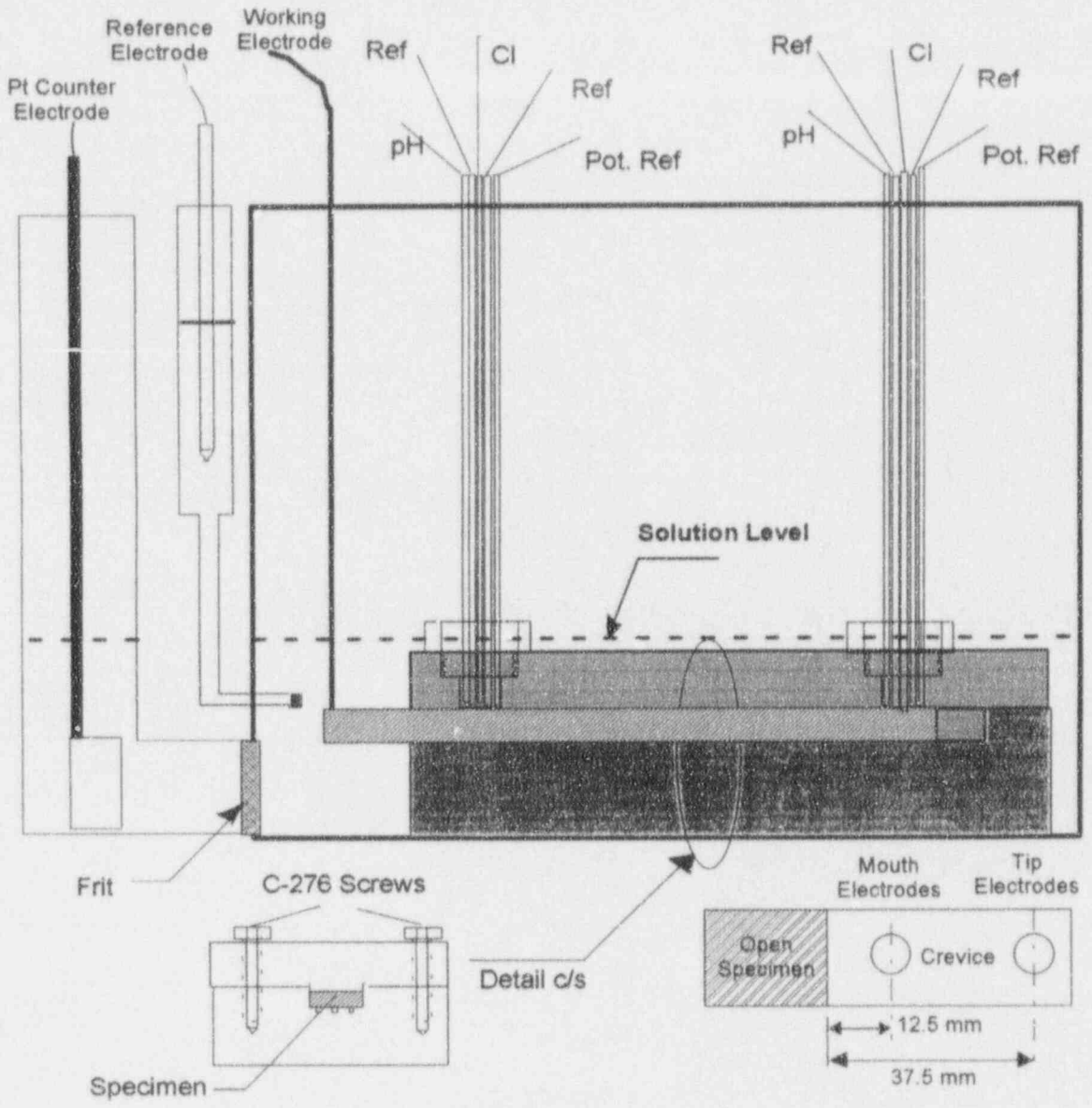

Figure 4-1. A schematic diagram of the cell and specimen used to study changes in crevice chemistry

on the bottom surface. Crevice tightness was controlled by clamping the top and bottom crevice blocks on the specimen using alloy C-276 bolts under a controlled torque of 0.14 N · m (20 in.-oz). Ports in the top crevice assembly for the microelectrodes were located at distances of 1.25 and 3.75 cm from the mouth of the crevice. These locations will be referred to as "mouth" and "tip," respectively. The whole crevice assembly was placed in a glass vessel fitted with a PMMA top that had ports for the various electrodes and gas purging. The solution level was adjusted to be below the electrode ports in the crevice assembly. The glass vessel also had a side compartment connected through a porous glass frit. The side compartment contained the counter electrode (Pt foil). This arrangement minimized the increase in pH in the bulk solution due to cathodic processes on the counter electrode. The cell was placed in a Faraday cage to minimize noise from the high-impedance electrodes.

Alloy 825 and type 304L SS were studied in these experiments. The chemical compositions of these alloys are shown in Table 4-1. The microstructures of these alloys have been described in previous reports (Sridhar et al., 1993a). The specimens were 6.3 cm × 1.3 cm × 3 mm in dimension. All specimens, except the mill-finished specimens, were wet-ground on all surfaces. For the mill-finished specimens, only the top surface was left in the mill-finished condition. Wires of the same alloy as the specimen were spot welded for electrical connection. Spot welding conditions were adjusted such that local heating was minimized and post-test examination indicated that, in most cases, crevice corrosion did not occur in this area.

A Microelectrodes, Inc., Model MI506 flexible glass electrode was used along with a Model MI403 double-junction reference electrode for pH measurements. A Microelectrodes, Inc., Model MI200 chloride (Ag/AgCl) electrode was used along with a double-junction reference electrode for chloride measurements. A separate double-junction reference electrode was used for potential measurements. The outer barrel of the double-junction reference electrodes was filled with the test solution, thus ensuring that the chloride leakage from the reference compartment did not affect the results significantly. For bulk solution measurements, a Microelectrodes, Inc., Model MI402 single-junction reference electrode was used along with glass and chloride electrodes. The pH and chloride electrodes were connected to pH-selective ion meters whose outputs connected to chart recorders. The pH and chloride electrodes were calibrated using standard solutions before and after the experiments to verify their performance. The microelectrodes were about 1 mm in diameter and required about a 1-mm depth of immersion. The ports were filled with Polytetrafluoroethylene (PTFE) tape to reduce the volume of electrolyte collected in these spots. All the potentials are converted to the Standard Hydrogen Electrode (SHE) scale.

The solution compositions consisted of two concentrations of chloride (1,000 ppm and 0.5 M) with a constant concentration of bicarbonate (85 ppm), nitrate (10 ppm), sulfate (20 ppm), and fluoride (2 ppm), all added as sodium salts. The high chloride concentration solution was used for alloy 825 that is more corrosion resistant. The choice of the chloride concentration was guided by prior results of repeated wetting and drying tests using J-13 water (Abraham et al., 1986). The initial pH of the solution at room temperature was approximately 8, while the final pH at room temperature was approximately 9. The rationale for the choice of this solution is provided in a previous report (Sridhar et al., 1993a, 1993b). The solution chemistry has been discussed in a previous report (Pabalan et al., 1990). All tests were performed at room temperature (21 ± 3 °C). All solutions were prepared using high-purity water (17 MΩ/cm resistivity). After the test, the specimens were examined under a stereoscope and scanning electron microscope (SEM). Selected specimens as well as the top half of the crevice block were also scanned using a surface profilometer (Surtronic 3P) using a 10-μm diameter stylus. Accuracy of this instrument was verified using reference blocks.

4.2.2.2 Crevice Gap Estimation

Crevice gap is one of the more difficult parameters to characterize in a given application as well as to control in an experiment. If the crevice is made tight in order to initiate crevice corrosion more easily, then the crevice gap is dependent on the surface finishes of the mating surfaces as well as their hardness as the asperities in their surfaces are compressed together. If the crevice gap is increased, the surface asperities play a relatively small role in defining the crevice gap. However, crevice initiation becomes difficult and corrosion may not initiate within an experimentally convenient time scale. In practice, many engineering components exhibit rather tight crevices. In the present case, the crevice was made tight by clamping two PMMA blocks on the specimen, but a reasonably low torque as noted above

Table 4-1. Chemical compositions of the heats of types 316L and 304L stainless steels (SS) and alloy 825 used in this study

Alloy/Heat	Elemental Composition, wt %										
	Al	C	Cr	Cu	Fe	Mn	Mo	Ni	P	S	Others
304L SS/A	NA	0.022	18.27	0.19	Bal.	1.46	0.15	9.1	0.026	0.005	Si:0.47 N:0.07
316L SS/A	NA	0.014	16.35	0.27	Bal.	1.58	2.07	10.04	0.026	0.018	Si:0.49 N:0.06
316L SS/B	NA	0.019	16.30	NA	Bal.	1.90	2.13	10.18	0.030	0.001	Si:0.50 N:0.03
825/A	0.07	0.010	22.09	1.79	30.41	0.35	3.21	41.06	NA	<0.001	Si:0.19 Ti:0.82
825/B	0.09	0.010	22.07	1.72	29.69	0.40	3.49	41.22	NA	<0.001	Si:0.29 Ti:1.02

A — These heats were from 0.5-in. plate material.
B — These heats were from 0.125-in. sheet material.

was used to minimize plastic flow of the PMMA surfaces. Surface profile measurements before and after clamping did not indicate any significant changes due to plastic deformation.

The surface roughness measurements are listed in Table 4-2 for various surfaces before and after corrosion tests. It can be seen that the surface roughness becomes larger after crevice corrosion tests for the 600-grit surface. Visual observation of the corroded surface also indicated mostly uniform corrosion with some shallow pits. For the 60-grit surface, crevice corrosion did not produce a significant change in surface roughness. The roughness measurements on alloy 825 with various surface finishes indicated that for surfaces finer than 400-grit, the peak-to-valley height did not decrease significantly. There were also considerable differences between surface roughness of the mill-finished specimens. It is possible that the rougher surface of the 12.5-mm plate reflects the effects of grit blasting after annealing and before descaling.

4.2.2.3 Crevice Chemistry in Type 304L Stainless Steel

Based on prior cyclic, potentiodynamic polarization curves for type 304L SS in 0.028 M (1,000 ppm) Cl^- solution, the applied potentials for the crevice chemistry experiments were chosen to be below the breakdown potential (about 0.5 V_{SHE}), but above the repassivation potential (about 0.2 V_{SHE}). In the first series of crevice chemistry experiments, the applied external potential was increased in steps. The results of this trial are shown in Figure 4-2. There was an initial decrease in pH from approximately 9 to about 7 followed by a constant pH regime. The potential drop in the crevice with respect to the external potential attained a relatively constant value of about 50 mV. The crevice current density was about 10^{-7} A/cm^2, which is near the resolution limit of the data acquisition system. When the external potential was raised to 0.4 V_{SHE}, there was an immediate increase in current density which underwent a series of repassivation steps before increasing to a stable high value. A marked change in pH and chloride concentration occurred only after a certain time period following the current increase (Figure 4-2). Simultaneously with the change in pH, there was a decrease in potential at the tip (deepest part of the crevice) and the mouth, the latter being intermediate between the tip and the external potentials. Surprisingly, while the potential and chloride electrodes indicated a difference between the tip and mouth, the pH electrodes did not. Immediately following a decrease in external potential, the crevice repassivated (low current density). The potential difference between the tip and the external reference electrodes decreased again to 50 mV. However, there was no immediate change in pH and chloride concentration. The corrosion inside the crevice was uniform when observed at 70 ×.

In two subsequent series of tests on 600-grit polished specimens, the potential was raised to 0.3 V_{SHE} after 1 hr at open-circuit potential and maintained at that value throughout the test. In this case, after an initial increase, the current decreased to a low value, followed by two more irregular cycles of increase and decrease in current density. There was a small lag in the decrease in pH at the tip of the crevice, but the tip pH eventually decreased to about 4. The tip potential decreased along with the pH, while the chloride increased. This was quite reproducible. In all these tests, the fall and rise in pH lagged slightly the rise and fall of current density. Once a stable crevice growth was established at 0.4 V_{SHE}, the pH did not rise as fast upon reduction in current density. Post-test examination indicated that the corrosion was greater near the tip and was essentially uniform.

The results from a test on a 60-grit finish specimen are compared to those from a 600-grit polished specimen in Figure 4-3. A salient feature of these results is that a much longer time period was needed for initiating crevice corrosion, which agrees with the predictions of all crevice chemistry change models. This can also be seen in the much longer time for the decrease in pH and potential inside the

Table 4-2. Surface roughness measurements on specimens before and after tests

Specimen Description	Uncorroded Area		Crevice Corroded Area	
	R_zDIN, μm	R_{max}DIN, μm	R_zDIN, μm	R_{max}DIN, μm
Type 304L, 60-Grit Finish, Transverse scan	8.3	12.7	10.4	13.2
Type 304L, 600-Grit Finish, Transverse Scan	1.1	1.4	5.4, 8.1, 6.0	14.8, 21, 11.1
Alloy 825, 600-Grit Finish, Transverse Scan	1.6, 1.6	2.0, 2.1	15.8*	35.6*
Alloy 825, 36-Grit Finish, Transverse Scan	41.5	46.7	—	—
Alloy 825, 60-Grit Finish, Transverse Scan	9.3	10.9	—	—
Alloy 825, 120-Grit Finish, Transverse Scan	4.9	6.8	—	—
Alloy 825, 320-Grit Finish, Transverse Scan	1.8	2.3	—	—
Alloy 825, 400-Grit Finish, Transverse Scan	1.8	2.4	—	—
Alloy 825 Mill Finish, 3-mm Sheet	10.7	13.0	15.0	16.3
Alloy 825 Mill Finish, 12.5-mm Plate	34.9	48.9	—	—
Plexiglas, Crevice Block	4.0	4.4	—	—
0.35 micron R_a Reference Block	1.4	1.4	—	—
6.07 micron R_a Reference Block	24.3	24.5	—	—

R_a = Average peak height from center line
R_zDIN = Average peak-valley height
R_{max}DIN = Maximum peak-valley height
* = Includes corroded and uncorroded areas

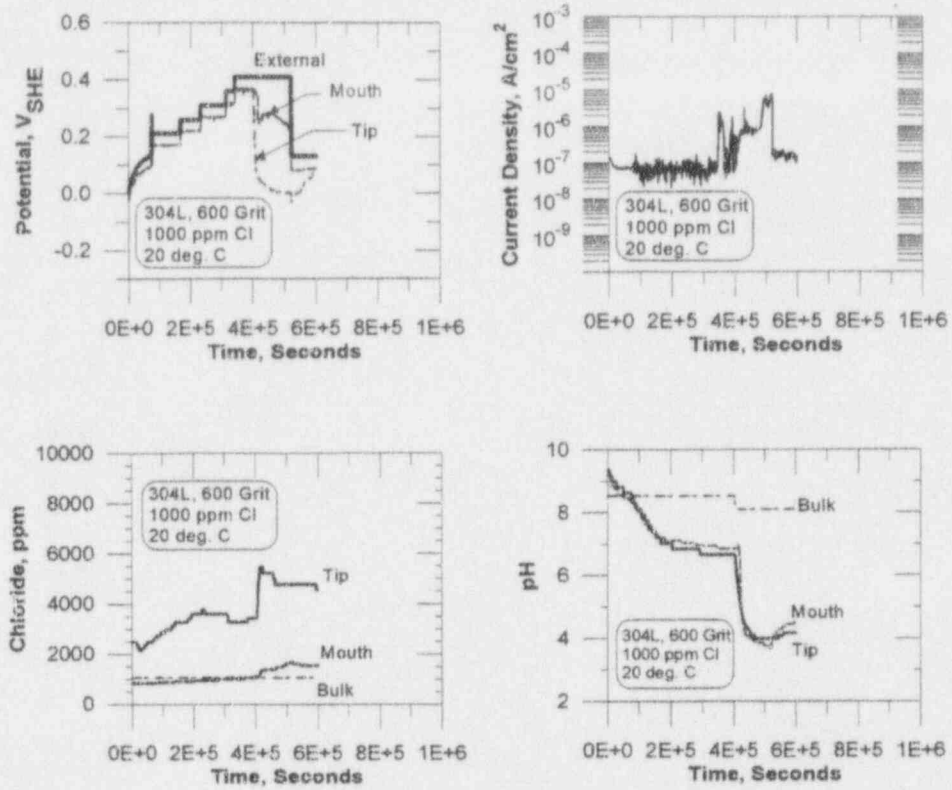

Figure 4-2. Changes in the current density, potential, pH, and chloride concentration inside a type 304L SS (600-grit) PMMA crevice in a 1,000-ppm chloride solution at room temperature (approximately 20 °C)

crevice for the 60-grit specimen. Secondly, the final pH in the crevice was not as low as that for the 600-grit polished specimen. A slightly smaller potential drop was also observed, again in agreement with model prediction. Post-test examination indicated that the corrosion occurred midway between the tip and mouth electrodes and was essentially uniform. One deep pit was noted in the crevice corroded area.

4.2.2.4 Crevice Chemistry in Alloy 825

Based on cyclic, potentiodynamic polarization curves for alloy 825 in 0.028- (1,000 ppm) and 0.5-M chloride solutions (containing other species as reported in the previous section) at room temperature, applied potentials of 0.5 to 0.7 V_{SHE} were chosen so that pitting was not initiated on the open specimens. The chemistry and potential changes in the crevice of a 600-grit polished alloy 825 specimen are shown in Figure 4-4. At an applied potential of 0.5 V_{SHE}, the crevice current density increased quite rapidly to high values. The maximum current density observed in alloy 825 was significantly higher than that in a type 304L specimen under active crevice corrosion. After the current increased, the pH and the potential decreased. The pH value at the tip was found to be higher than that at the mouth, contrary to that observed in type 304L SS. The minimum pH values in the crevice were lower than those observed for type 304L SS. The free-chloride in the crevice decreased below the bulk value. Post-test calibration of the electrodes did not reveal any changes in the electrodes. It is seen that the potential increased to high values after the external potential was switched off.

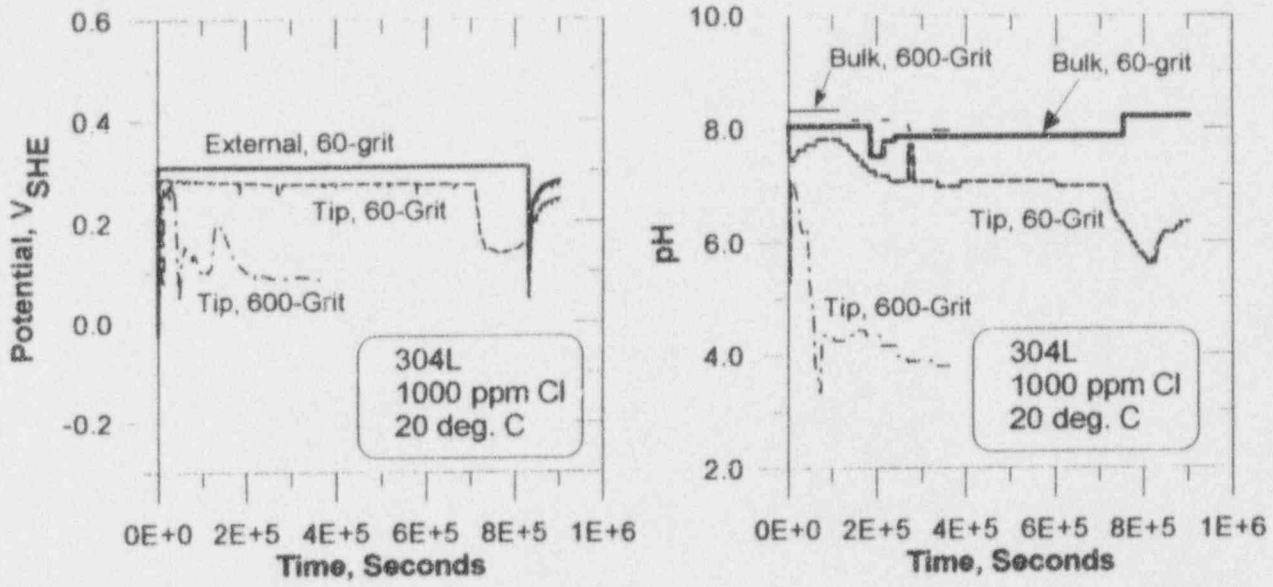

Figure 4-3. Changes in the potential and pH inside a type 304L SS (60-grit) PMMA crevice in a 1,000-ppm chloride solution at room temperature (approximately 20 °C) compared to those in a 600-grit specimen (Constant external potential of 0.3 V_{SHE})

The final pH and potential of the mill-finished specimen were essentially the same as those in the 600-grit finished specimen. However, the decrease in pH and potential occurred more rapidly for the mill-finished specimen. It must be noted that the surface finish of the mill-finished alloy 825 specimen was coarser than a 600-grit finished surface (Table 4-1), and so the accelerated change in potential and pH is more significant than it appeared from measurements. Post-test Energy Dispersive X-ray Analysis (EDS) of the crevice-corroded area indicated a Cr content of 21 percent. As discussed elsewhere (Dunn et al., 1993b), the Cr content of the mill-finished surface was 18 percent. This indicates that the crevice corroded through the chromium-depleted layer. For the mill-finished specimen, no change in chloride concentration with respect to the bulk concentration was observed.

The changes in the crevice conditions for an alloy 825-plexiglass crevice exposed to 1,000-ppm chloride solution are shown in Figure 4-5. Here, a high anodic potential had to be applied to induce crevice corrosion, although the potential was less than the pit initiation potential. The current density was not as high as in the case of 0.5 M chloride solution (Figure 4-4). Interestingly, the chloride concentration at the tip increases just as in the case of type 304L SS. The pH at the tip also decreased as in the previous cases of 600-grit polished alloy 825. The crevice repassivated spontaneously (i.e., without any reduction of externally applied potential). It can be seen from Figure 4-5 that while the crevice tip and mouth potentials reverted back to the external potential values upon repassivation, the pH and Cl^- concentrations did not change.

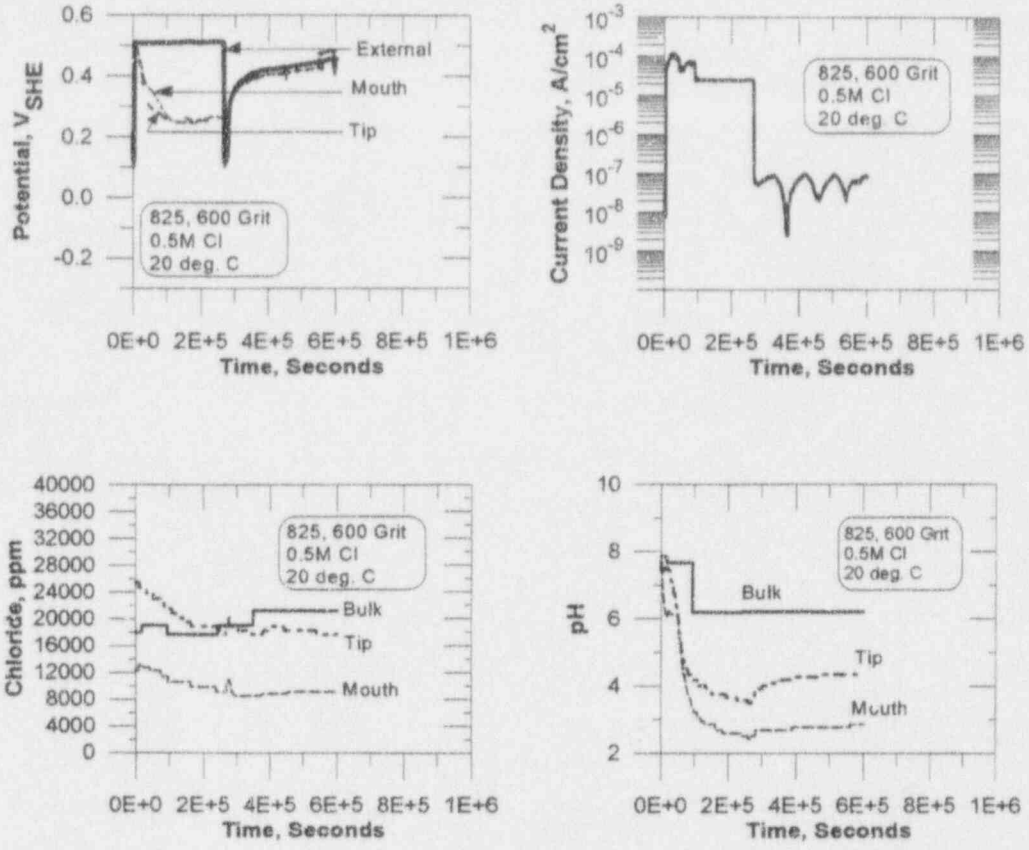

Figure 4-4. Changes in the current density, potential, pH, and chloride concentration inside an alloy 825 specimen (600-grit) PMMA crevice in a 0.5-M chloride solution at room temperature (approximately 20 °C) Constant external potential of 0.5 V_{SHE}

4.2.2.5 Modeling Versus Experimental Results

Crevice corrosion initiation and repassivation have been modeled by investigators for many types of metallic materials. These models can be classified into essentially two types: (i) those that predict that crevice corrosion initiates or repassivates primarily because of chemical changes that occur in a crevice (e.g., Oldfield and Sutton, 1978; Gravano and Galvele, 1984; Sharland, 1992; Walton and Kalandros, 1992; and Alkire and Lott, 1989), and (ii) those that predict that crevice corrosion initiates primarily because of changes in electrode potential inside the crevice (e.g., Xu and Pickering, 1993; Rosenfeld et al., 1978). The majority of the chemistry change models assume the sequence of processes leading to initiation to be: anodic dissolution ⇒ oxygen depletion ⇒ hydrolysis leading to reduction in pH ⇒ chloride ion migration into the crevice ⇒ formation of a "critical crevice solution" leading to depassivation ⇒ active corrosion with an increase in current density and a further decrease in potential. For repassivation according to some of these models, the chemical composition is reversed first followed by a current decrease. However, a variant of this type of mechanism (Alkire and Lott, 1989) suggests that dissolution of MnS inclusions inside the crevice results in generation of thiosulfate ions which, together with chloride, causes depassivation. The Alkire and Lott model does not require a pH drop prior to initiation. The potential-change models hypothesize that the sequence of events leading to initiation is anodic dissolution ⇒ potential gradient due to resistive drop ⇒ change in the internal potential from the passive regime to the active/passive peak when the IR potential drop exceeds a critical value ⇒ increase

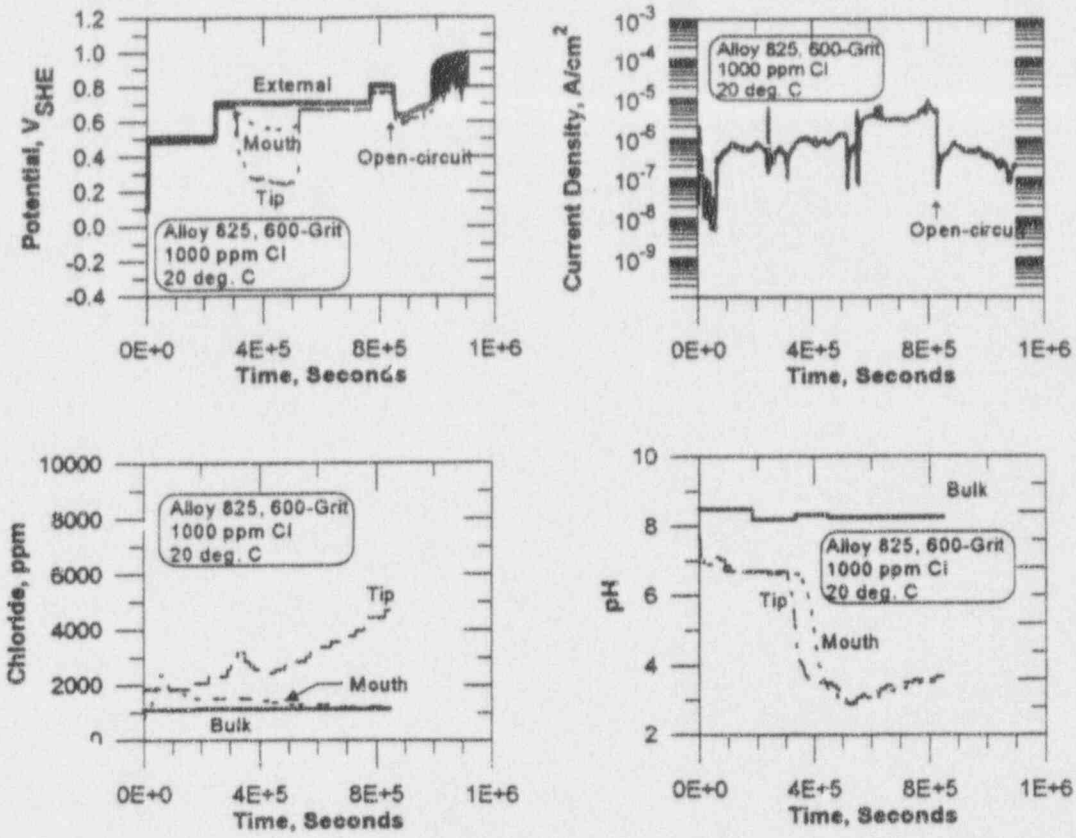

Figure 4-5. Changes in the potential and pH inside an alloy 825 specimen PMMA crevice in a 1,000-ppm chloride solution at room temperature (approximately 20 °C) for mill-annealed and 600-grit polished specimens. External potential stepped to a value of 0.7 V_{SHE}

in crevice corrosion and current. Under conditions where the potential is controlled by a potentiostat instead of a natural redox species, the first type of model would predict that the chemistry inside the crevice will change first followed by an increase in current density. Under the same conditions, the second type of model would predict a drop in potential first, immediately followed by an increase in current density independent of any chemistry changes. However, it must be noted that for SS, as opposed to iron, active-passive peak is observed only in very acidic solutions (Sridhar et al., 1993a) and, hence, the second type of model must also rely on chemistry changes in the crevice before activation of the crevice corrosion for some materials.

On the experimental side, a number of investigators have measured changes in chemistry within artificial pits and crevices of SS and Ni-base alloys (Suzuki et al., 1973; Mankowski and Szklarska-Smialowska, 1975; Turnbull, 1983 and references cited therein; Cavanaugh et al., 1983; Alavi and Cottis, 1987; Sugimoto and Asano, 1990; and Luo et al., 1992). Most of these investigations have shown that:

(i) Once initiated, the pH inside the crevice/pit decreased to quite acidic values. The acidity inside pits/crevices was a function of the Cr and Mo concentration in the solution. Generally, the higher Cr- and Mo-containing alloys produced a lower pH. However, when the Mo content in the alloy was very high, such as alloy C-276, the Mo

concentration in the solution decreased and the resulting pH in the pit was higher than for a lower Mo-containing alloy, such as type 316L SS (Cavanaugh et al., 1983). The total chloride concentration increased to values as high as 12 N. However, there was a maximum in chloride concentration inside pits at intermediate values of pit volumes (Mankowski and Szklarska-Smialowska, 1975). The chloride concentration inside crevices, which can be regarded as large pits, was not found to attain such large values. For example, in pits with a diameter of 1.8 mm, the chloride concentration was found to range from 2 to 6 N (Mankowski and Szklarska-Smialowska, 1975; Sugimoto and Asano, 1990).

(ii) The increase in the acidity and chloride concentration inside pits/crevices was a function of externally applied potential (Turnbull, 1983).

(iii) The pH inside the crevice was lower than could be predicted by hydrolysis of Fe, Ni, and Cr alone (Mankowski and Szklarska-Smialowska, 1975). This was explained to be due to the effect of metallic chlorides in increasing the H^+ ion activity. However, Tsuru et al. (1985), using a simulated crevice device that presumably had a larger volume than the pits examined by other investigators, found that the pH corresponded to that expected by Cr^{3+} hydrolysis alone.

Unfortunately, only a few of the experimental studies undertaken thus far have examined simultaneously both the spatial and temporal variations in the corrosion rate (current density) and chemical changes in the crevice/pit to determine whether chemical changes precede or succeed the initiation of corrosion. For example, Alavi and Cottis (1987) measured the pH and chloride concentration in a crevice coupled to an uncreviced specimen as a function of time and distance. However, they did not report any current density measurements between the creviced and uncreviced specimens (through a zero resistance ammeter). Judging by the decrease in crevice potential, their results suggest that activation of crevice and chemistry changes inside the crevice proceed, at best, simultaneously. There was no indication that the latter precedes the former. Lott and Alkire (1989) reported that they did not observe any change in pH inside the crevice before active corrosion occurred. However, they did not measure changes in these variables continuously with time. Sugimoto and Asano (1990) measured the changes in pH and pCl during a potentiodynamic scan and found that significant pH change occurred only after the breakdown potential was exceeded.

The present experiments indicate that, in contrast to the model predictions, the change in pH, potential and chloride concentration always lagged behind the increase in current. There was considerable scatter in the lag time between the change in current density and the change in chemistry, but it ranged from 12,000 (Cr-depleted alloy 825) to 100,000 s (600-grit finish alloy 825). For type 304L SS, the lag time varied from about 21,000 to 75,000 s. There was no correlation between lag time and the surface finish. Generally, the changes in tip and mouth potentials coincided with changes in pH and chloride concentration. Several alternative explanations can be provided for the lag time between the increase in current and the decrease in pH:

(i) **The MnS dissolution mechanism proposed by Alkire and Lott (1989).** While this is an attractive explanation of the present observations on type 304L SS, similar behavior of alloy 825 cannot be explained by this mechanism. As shown in Table 4-1, the manganese and sulfur contents of the electroslag remelted alloy 825 are much lower than that of type 304L SS. Additionally, the mechanism proposed by Alkire and Lott requires

a critical combination of chloride and thiosulfate. However, chloride concentration showed the same time lag as pH.

(ii) **The IR drop mechanism proposed by Xu and Pickering (1993).** Unlike the case of carbon steel that was considered by Xu and Pickering, an active-passive peak has been observed in SS and alloy 825 only under very acidic conditions prior to total depassivation (Sridhar et al., 1993a). Additionally, this mechanism would predict that crevice corrosion would initiate only at depths where the potential is in the active regime. However, crevice corrosion was not confined to any one depth and was probably related to variations in crevice gap. This mechanism would also predict that the potential inside the crevice would decrease first followed by current increase. The opposite was observed.

(iii) **Pits inside crevice.** Crevice corrosion can also be initiated by the nucleation of pits within the crevice. In this case, a current increase can be observed first if a sufficient number of pit nuclei are formed before sufficient active areas exist to detect pH changes. However, the polarization curves indicate that the external potential in the present series of experiments did not exceed the breakdown potential determined by short-term tests. Nevertheless, because the breakdown potential is time-dependent, the role of pitting in crevice corrosion cannot be ruled out.

(iv) **Micro-crevice under rough surface.** A final explanation considers the chemistry changes under the realistic profile of the crevice surfaces. The mating surfaces consist of a series of ridges that form a crevice consisting of very small to relatively large gaps, depending upon the surface finish. Crevice corrosion is initiated by a decrease in pH at the contact points between peaks that have extremely narrow gaps. Then, depending upon the applied external potential, the active crevice corrosion can spread across larger gaps between surface peaks and valleys. When the area of active corrosion reaches a sufficient extent, the increase in total current becomes noticeable. Because the microelectrode diameter is much larger than the width of the surface ridges, further increase in the volume of solution that is acidified is necessary for the pH drop to be measurable. The effect of external potential is in propagating the crevice nuclei across a wider crevice area. If the external potential is too low, the crevice corrosion nuclei will repassivate because of the increasing crevice gap. This behavior is similar to the nucleation and repassivation of pits within crevices, but differs with respect to the role of local crevice gap. A rougher surface will possess fewer areas of intimate contact between peaks of mating surfaces and a greater proportion of large gaps between peaks and valleys. The role of MnS dissolution is not excluded in this mechanism but can act in conjunction with it.

(v) **Diffusion of ionic species.** Another component of the lag time may be the time that is needed for the diffusion of H^+ and Cl^- from the initial crevice area to the electrodes. Based on the diffusivity of H^+ of 9.3×10^{-5} cm^2/s at 25 °C, the time lag by this argument would range from 100 to 16,000 s, which is much shorter than the observed lag times.

It must be noted that the pH changes at the tip and mouth in many cases are identical (Figure 4-5). If unidirectional transport from the tip outward is assumed, the pH at the mouth would be expected to be higher than the tip. However, the current crevice geometry does not preclude diffusion from the sides of the crevice. Control experiments, where known pH solutions were injected outside the

crevice, indicated that the transport time of H^+ ions is the same for both the tip and mouth and probably from the side of the crevice. Hence, further improvements in the crevice geometry (e.g., a radially symmetrical geometry) are necessary for a better comparison to undimensional model predictions. Such bidirectional diffusion may also explain the complex dependence of pH on depth observed by Alavi and Cottis (1987).

4.2.2.6 Effect of Alloy Composition

A comparison of Figures 4-2 and 4-5 clearly indicates that the pH inside the crevice of alloy 825 is significantly lower than that inside the type 304L SS crevice. This is consistent with the observations of others (Cavanaugh et al., 1983) that Mo-containing alloys exhibit lower crevice pH. The dissolution and hydrolysis of Mo-containing species is quite complex depending upon the potential and acidity of the solution. For example, at high applied potentials dissolution of Mo to form Mo(VI) results in the formation of MoO_4^{2-} and generation of H^+ by the following reaction

$$Mo + 4H_2O \rightleftharpoons MoO_4^{2-} + 8H^+ + 6e^- \qquad (4\text{-}1)$$

On the other hand, consumption of H^+ ions by the molybdate species results in the generation of polynuclear species, such as $Mo_7O_{24}^{6-}$ and $Mo_8O_{26}^{4-}$, by the following reaction.

$$8MoO_4^{2-} + 12H^+ \rightleftharpoons Mo_8O_{26}^{4-} + 6H_2O \qquad (4\text{-}2)$$

A net production of about 6 to 8 hydrogen ions per Mo atom oxidized has been estimated (Cavanaugh et al., 1983). On the other hand, Suzuki et al. (1973) determined that Mo^{3+} was present in pits of type 316L SS polarized to about $-0.2\ V_{SCE}$. Oxidation of Mo^{3+} can occur by the reaction shown in Eq. (4-3).

$$Mo^{3+} + 2H_2O \rightleftharpoons MoO_2 + 4H^+ + 2e^- \qquad (4\text{-}3)$$

Under the applied potentials used for alloy 825, the oxidation of Mo to Mo(VI) is a more plausible reaction (Wanklyn, 1981; Cavanuagh et al., 1983). It is possible that the oxidation of Mo to Mo(VI) can generate a lower pH than that of Fe^{2+}, Ni^{2+}, or Cr^{3+}. Alloy 825 also has a higher concentration of Cr than type 304L SS. The pH measured in the present experiments may be higher than the actual pH in the crevice because of the higher volume required for measurement as well as the effect of higher chloride concentration in increasing the activity of hydrogen ions (Mankowski and Szklarska-Smialowska, 1975).

4.2.2.7 Effect of Repassivation

It can be seen from Figure 4-2 that for type 304L SS, the tip and mouth potentials attained values close to the external potential immediately upon repassivation. However, the pH and chloride concentration did not change significantly for a much longer time. This is in contrast to the behavior observed for pits by Sugimoto and Asano (1990) and suggested by Tsujikawa et al. (1987) in their model for repassivation. However, it seems reasonable that in deep pits or crevices, a reversion of pH and Cl^- to their original values would take a significantly longer time because there must be diffusion out of the crevice. The repassivation occurs essentially because the external potential minus the IR potential drop is below the corrosion potential of the metal in the acidic crevice solution. For shallow pits, the transport processes may become more significant.

Alloy 825 specimens behaved similarly to type 304L specimens in that the pH did not change rapidly upon repassivation (Figure 4-4). However, the potential both inside and outside the crevice increased significantly upon turning off the applied potential. This cannot be explained by a reentry of oxygen because even aerated specimens of alloy 825 did not exhibit such high potentials (Dunn et al., 1993a). One explanation is the reduction of MoO_4^{2-} generated within the crevice during active crevice corrosion. This is consistent with the observation of Wanklyn (1981) that the addition of Mo(VI) to a NaCl solution caused an increase in the corrosion potential of type 316 SS and platinum by more than 0.2 V. It must be noted that the oxidation of Mo to Mo(VI) occurs at potentials greater than about 0.3 V_{SHE}, which is lower than the applied potential for alloy 825 in the present experiments.

4.2.3 Stress Corrosion Cracking Studies

4.2.3.1 Experimental Procedures

The chemical compositions of the heats of type 316L SS and alloy 825 used in this study are given in Table 4-1. The heats of both alloys designated as A were used for the preparation of slow strain rate test specimens. Smooth and notched tensile specimens, machined with the tensile axis perpendicular to the rolling direction, were used in these tests. Experimental details of the slow strain rate tests, including characteristics and dimensions of the specimens, description of the experimental setup, and other relevant information, were previously described (Sridhar et al., 1993c).

To complement the slow strain rate tests in dilute chloride solutions reported previously (Sridhar et al., 1993c), a set of tests was conducted in solutions containing 1,000 ppm chloride with the addition of 0.001 or 0.01 mol/L of $Na_2S_2O_3$. These tests were performed at 95 °C, and the solutions were purged with CO_2. The addition of thiosulfate to the chloride solutions was based on the suggestion of Lott and Alkire (1989) that thiosulfate can be generated by the dissolution of MnS inclusions present in certain austenitic SSs, such as types 304 and 316. In conjunction with chloride, thiosulfate promotes passivity breakdown in these alloys. It is known that transgranular cracking of quench-annealed austenitic SS in chloride solutions is initiated from corrosion trenches or slots, where localized breakdown of the passive films occurred (Silcock and Swann, 1979). Concentrations of thiosulfate equal to 0.001 and 0.01 M were chosen because Newman et al. (1982) reported the most significant decrease in the pitting potential of type 304 SS in chloride-containing solutions by the addition of thiosulfate within that range of concentrations. Potentials were selected to avoid widely distributed pitting corrosion and were then adjusted during the course of the test to avoid significant increases in current associated with pit initiation.

A second set of slow strain rate tests was performed in concentrated chloride solutions prepared with salts of different cations (Mg^{2+}, Li^+, and Na^+). The solutions in this set of tests were fully deaerated with nitrogen. Some of these tests were reported previously (Sridhar et al., 1993c). Additional tests were conducted in concentrated NaCl solutions with the addition of thiosulfate to compare the behavior of alloy 825 with that of type 316L SS. In these tests the solutions were purged with CO_2 and the temperature was controlled at 95 °C.

An extension rate of 1.27×10^{-5} mm/s (5.0×10^{-7} in./s), which represents an initial strain rate of 1.0×10^{-6} s^{-1} for the smooth tensile specimens, was used in the first set of tests. The extension rate was reduced in later tests to 2.8×10^{-6} mm/s (1.1×10^{-7} in./s) to increase the sensitivity of the slow strain rate technique. This represents an initial strain rate of 2.2×10^{-7} s^{-1}. For the notched specimens, this value may represent a strain rate at least two orders of magnitude greater than that above. Therefore, an

extension rate of 7.1×10^{-7} mm/s (2.8×10^{-8} in./s) was used for the testing of notched specimens. All the specimens were placed such that the gauge length was completely immersed in the solution.

The heats of type 316L SS and alloy 825 designated as B in Table 4-1 were used for the preparation of specimens for constant-deflection tests. These heats were obtained in the form of cold-rolled and mill-annealed (MA) sheets, 3.175 mm (0.125 in.) thick. U-bend specimens were machined from these sheets and stressed, without any heat treatment, to a radius of bend curvature of 12.5 mm (0.5 in.) using an appropriate device according to ASTM Practice G 30-90 (American Society for Testing and Materials, 1991). Bolts and nuts made of alloy C-276, electrically isolated from the specimens by zirconia spacers, were used for the single-stage stressing operation. The resulting tensile stress was perpendicular to the rolling direction (transverse specimens), and the total strain on the outer fiber of the bend was estimated to be about 12.7 percent, using the expression given in ASTM G 30-90. After bending, the specimens were cleaned in 10-percent HNO_3 at room temperature for 1 hr to remove any accidental surface contamination with steel particles produced during the bending operation and then rinsed in deionized water.

Constant-deflection tests were conducted simultaneously in four 1-L glass cells using the experimental setup described previously (Sridhar et al., 1993a). Two U-bend specimens were tested simultaneously in each cell. The specimens were partially immersed in the solutions such that the legs of the U-bend were in the vapor space while the apex of the bend was completely submerged in the liquid. One of the specimens was exposed to the solution at a controlled anodic potential, whereas the second one was maintained under open-circuit conditions. The multichannel potentiostat and the remaining electronic instrumentation for controlling the potential and for data acquisition were similar to those described previously (Sridhar et al., 1993c) for the slow strain rate tests.

The constant-deflection tests were performed in solutions similar to those used in slow strain rate tests. Solutions containing 1,000 ppm chloride with and without the addition of $Na_2S_2O_3$ were used in some tests. These solutions were prepared with high purity water with the pH adjusted to 4.0 by the addition of HCl. Concentrated chloride solutions prepared with either LiCl or NaCl were also tested to compare the effects of both cations on the SCC behavior of type 316L SS and alloy 825. These solutions were also prepared with high purity water with the pH adjusted to 4.0. In some tests, $Na_2S_2O_3$ was added to the concentrated NaCl solutions. In most of the cases, the tests were conducted for a period of 21-22 d. In some tests in which no signs of SCC or localized corrosion were observed after an initial test period, the same specimens were tested for an additional time interval.

4.2.3.2 Results

Slow Strain Rate Tests

The results of slow strain rate tests of type 316L SS in solutions containing 1,000- and 10,000-ppm chloride are summarized in Figure 4-6. As indicated previously (Sridhar et al., 1993c), no SCC was observed in these tests, even at relatively high potentials within the range defined by E_{rp} and E_p. The addition of 0.001 or 0.01 mol/L of $Na_2S_2O_3$ to the 1,000-ppm chloride solution did not induce SCC even at applied potentials 278 mV above the open-circuit potential. Also, SCC did not occur in the tests conducted in solutions containing 0.01 mol/L of $Na_2S_2O_3$ even though the strain rate was decreased five times, which implies that the severity of the test was increased with respect to the low thiosulfate concentration tests. Although an O-ring was used to create crevice conditions, the use of a notched specimen did not lead to crack initiation. It was expected that a notch would facilitate crack initiation by

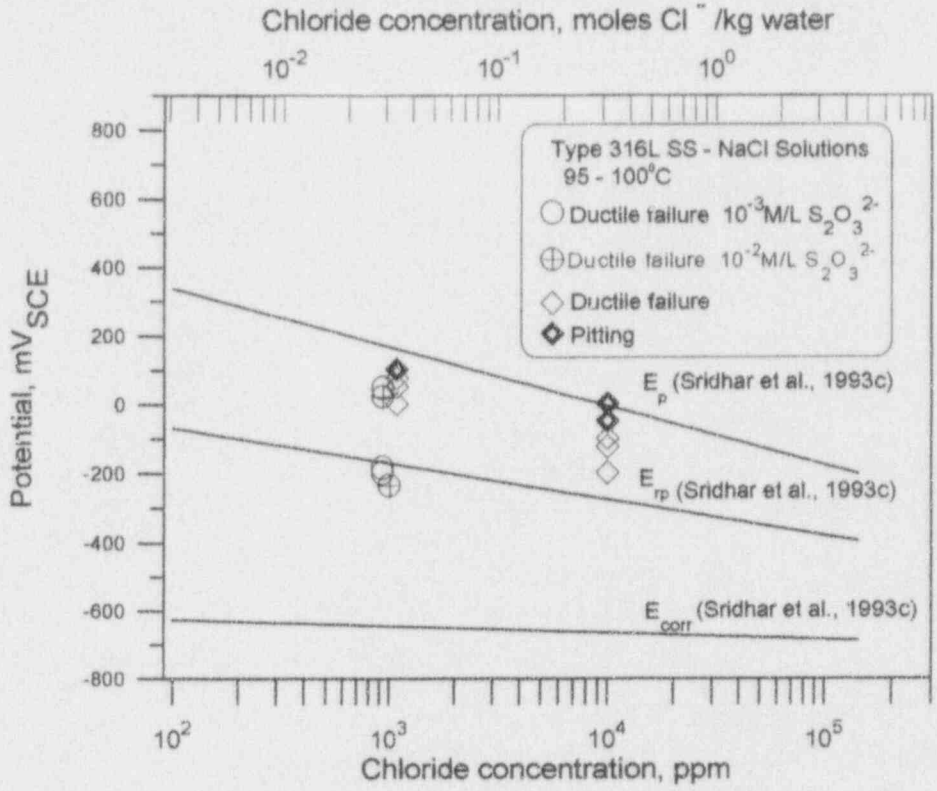

Figure 4-6. Results of slow strain rate tests of type 316L SS in dilute chloride solutions at 95 °C with and without the addition of $Na_2S_2O_3$. [Data points are shown in relation to pitting (E_p), repassivation (E_{rp}), and corrosion (E_{corr}) potentials as a function of chloride concentration in deaerated solutions.]

localized intensification of the stress, avoiding the simultaneous initiation of several cracks. Although a very low extension rate was applied to the notched specimen, no SCC occurred after 950 hr of straining.

The results of tests conducted on type 316L SS in various concentrated chloride solutions of different cations (Mg^{2+}, Li^+, and Na^+) using smooth tensile specimens are summarized in Figure 4-7. The details of these tests have been reported previously (Sridhar et al., 1993c). In the range of chloride concentrations extended from 9.1 to 14 mol/kg water, SCC was observed regardless of the cation, both at an anodic potential as well as at the corrosion potential. The initial tests of this set were conducted at 120 °C in 40-percent $MgCl_2$ solution (14.0 mol Cl^-/kg water) at the corrosion potential (approximately -0.3 V_{SCE}) and at a slightly anodic potential (-0.28 V_{SCE}). SCC was observed under both conditions in which elongation values of 7.4 and 4.6 percent were obtained, respectively. Similar results were obtained at a lower temperature (110 °C) in a less concentrated solution (30-percent $MgCl_2$) in which the chloride concentration is 9.1 mol/kg water. In this case, a decrease in the elongation to failure from 49.4 to 15.2 percent was observed by increasing the potential to slightly anodic values with respect to the open-circuit potential. Other details regarding crack appearance and morphology were previously reported (Sridhar et al., 1993c).

SCC was also observed in four tests conducted at 120 and 110 °C in concentrated LiCl solutions acidified to pH 2.0 by the addition of HCl. The pattern was similar to that found in $MgCl_2$ solutions at

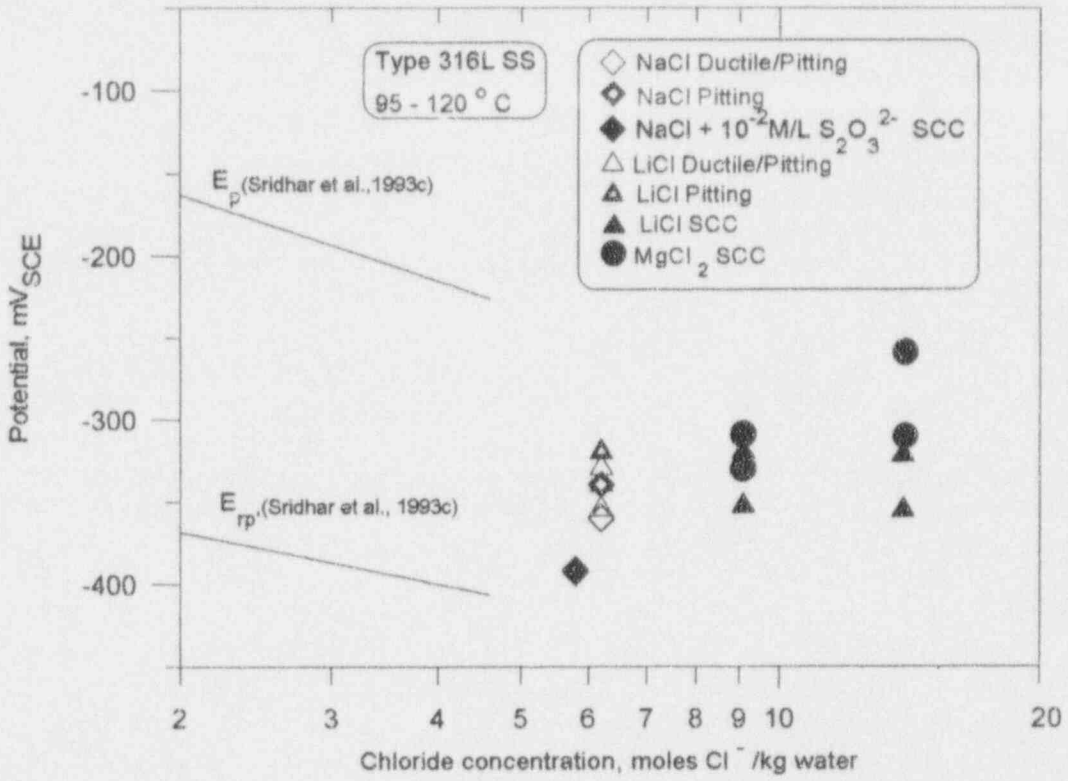

Figure 4-7. Results of slow strain rate tests of type 316L SS in concentrated chloride solutions of different cations ($MgCl_2$, LiCl, and NaCl) at temperatures ranging from 95 to 120 °C, with and without the addition of $Na_2S_2O_3$. [Data points are shown in relation to pitting (E_p) and repassivation (E_{rp}) potentials as a function of chloride concentration in deaerated solutions.]

equivalent chloride concentrations. SCC occurred under open-circuit conditions, but cracking susceptibility increased significantly with anodic polarization. These observations were confirmed by fractographic examination. Extensive areas of intergranular and transgranular SCC were observed in these fractographs. It appears, however, that the proportion of intergranularly cracked areas was smaller than that observed under equivalent conditions in $MgCl_2$ solutions. The susceptibility to SCC, as evaluated from the elongation to failure values and the appearance of the fracture surfaces, decreased with decreasing chloride concentration and temperature.

Tests were conducted at 95–100 °C in a less concentrated chloride solution (6.2 mol/kg water) in which the pH was adjusted by the addition of HCl. This concentration was chosen because it is close to the solubility of NaCl at 95 °C, which is equal to 6.7 mol/kg water (Linke, 1965), with the purpose of comparing the behavior in NaCl with that in LiCl solutions. No SCC was observed in these tests regardless of the cation. The corrosion potential measured in these solutions was -0.35 ± 0.01 V_{SCE}. In the test conducted under open-circuit conditions, ductile failure occurred. However, in most of the other tests, the application of a slight anodic potential (few millivolts in some cases) led to the occurrence of pitting corrosion accompanying the ductile failure. To avoid the occurrence of pitting corrosion, the potential was diminished by about 25 mV during the course of some tests maintaining the current well below 1 mA. No quasi-cleavage features, typical of transgranular SCC, or the grain faces characteristic of intergranular SCC were noted in SEM examinations of the fracture surfaces even though in some tests

a significant reduction in the elongation to failure was observed. Some irregular pits, around 100 μm, were observed on the side surfaces. The complete absence of secondary cracks, however, was the dominant feature.

In contrast, SCC was observed on smooth tensile specimens of type 316L SS in 5.8 mol/kg of water NaCl solutions containing 0.01 M $Na_2S_2O_3$, as shown in Table 4-3. SCC of type 316L SS was observed at the open-circuit potential, which was found to be -0.39 V_{SCE}, a value approximately 40 mV lower than that in the absence of thiosulfate and also at lower applied potentials (-0.42 to -0.39 V_{SCE}). To avoid the occurrence of pitting corrosion, the potential in the test conducted potentiostatically was maintained during most of the test time below the open-circuit potential, which may explain the increased elongation to failure obtained in this test with respect to that under open-circuit conditions. Under the same conditions, ductile failure prevailed in the case of alloy 825, both at the open circuit and at anodic applied potential, but was accompanied by pitting corrosion at the vapor/solution interface. As shown in Table 4-3, no SCC was observed in a notched specimen of alloy 825 tested at a very low extension rate, initially under open-circuit conditions and later in the course of the test, that lasted for 1,104 hr, under an anodic applied potential.

Constant Deflection Tests

Table 4-4 summarizes the results of constant deflection tests using U-bend specimens of type 316L SS in dilute (1,000-ppm) chloride solutions at 95 °C. After 528 hr (22 d) of testing, a crack was observed at an applied potential about 40 to 80 mV anodic to the open-circuit potential (-0.18 V_{SCE}), but not under open-circuit conditions in a companion specimen. The crack was observed on the leg of the U-bend specimen above the vapor/solution interface. No cracking was detected in subsequent tests conducted for two consecutive periods of 504 and 672 hr. All the specimens exhibited localized corrosion in the form of small pits mainly located in the legs of the U-bends above the vapor/solution interface.

Unlike the case of slow strain rate tests, SCC was observed in most of the specimens tested in dilute chloride solutions with the addition of 0.01 M of thiosulfate. Cracking was found to be more severe in the presence of thiosulfate, even though the addition of this species decreased the corrosion potential by approximately 100 mV in solutions purged with an oxygen/nitrogen mixture simulating air. Cracks were always found above the vapor/solution interface despite the fact that the legs are the less stressed part of the U-bend specimens. SCC was observed in one test, even at the open-circuit potential. In this test, however, the potential was higher (-0.13 V_{SCE}) because no gas was bubbled into the solution. No SCC was detected in the specific case of the specimen tested under open-circuit conditions in the remaining tests included in Table 4-4, in which the N_2/O_2 gas mixture was bubbled into the solution. In the final set of tests summarized in Table 4-4, SCC was detected after a total exposure time of 1,176 hr, although no cracking was observed during the initial test period that extended for 504 hr.

Table 4-5 summarizes the results of the tests conducted in concentrated chloride solutions. SCC was observed in almost all the U-bend specimens of type 316L SS with the exception of one specimen tested in 6.2 molal NaCl at the open-circuit potential, in which pitting corrosion was observed in the bend area. LiCl solutions appear to be marginally more aggressive in terms of promoting SCC, because SCC was observed in all the tests conducted in a solution containing a chloride concentration equal to or greater than 5.8 mol/kg of water, regardless of the application of an anodic overpotential. In the case of NaCl solutions, no SCC was detected under open-circuit conditions at 6.2 molal, but this test lasted only 288 hr. On the other hand, the addition of thiosulfate or the application of an anodic overpotential

Table 4-3. Slow strain rate tests of type 316L SS and alloy 825 in concentrated chloride solutions with the addition of thiosulfate at 95 °C ($\dot{\epsilon} = 2.2\times10^{-7}\ s^{-1}$)

Alloy	Solution	E_{corr} (V_{SCE})	E_{app} (V_{SCE})	Current (Amps)	Initial pH	Final pH	Elong. (in.)	Failure Time (hr)	Test Results
Type 316L SS	5.8 mol NaCl/kg water + 0.01 M $Na_2S_2O_3$	−0.391	−0.420 to −0.391	10^{-6} to 5×10^{-5}	—	—	0.090	241	SCC
Type 316L SS	5.8 mol NaCl/kg water + 0.01 M $Na_2S_2O_3$	−0.393	O.C.	O.C.	—	—	0.061	155	SCC
Alloy 825	5.8 mol NaCl/kg water + 0.01 M $Na_2S_2O_3$	−0.336	O.C.	O.C.	3.4	3.8	0.235	593	Pitting/ductile failure. Pits at vapor/solution interface.
Alloy 825	5.8 mol NaCl/kg water + 0.01 M $Na_2S_2O_3$	−0.261 to −0.325	O.C. and −0.322	10^{-6}	3.4	—	0.103[a]	1104[a]	No SCC
Alloy 825	5.8 mol NaCl/Kg water + 0.01 M $Na_2S_2O_3$	−0.339	−0.325	10^{-6} to 10^{-5}	3.4	3.8	0.180	454	Pitting/ductile failure. Pits at vapor/solution interface.

[a]Notched specimen; no failure at extension rate of 7.1×10^{-7} mm/s
O.C. — open circuit

Table 4-4. Summary of U-bend test results for type 316L SS in dilute chloride solutions at 95 °C

Solution	Purging Gas	E_{corr} (V_{SCE})	$E_{applied}$ (V_{SCE})	Current (Amps)	Initial pH	Final pH	Test Time (hr)	Results
1,000 ppm Cl^- as NaCl	79% N_2 21% O_2	−0.13	O.C. −0.13 to −0.23	—	—	—	528	No SCC, shallow pits above vapor/solution interface
1,000 ppm Cl^- as NaCl	79% N_2 21% O_2	−0.11 −0.18[a]	O.C.	—	4.3 4.1[a]	— 5.8[a]	504 672[a]	No SCC No SCC, shallow pits on leg above vapor/solution interface[a]
1,000 ppm Cl^- as NaCl	79% N_2 21% O_2	−0.18	−0.14 to −0.10	10^{-5} to 10^{-3}	—	—	528	SCC, on leg above vapor/solution interface
1,000 ppm Cl^- as NaCl	79% N_2 21% O_2	−0.07 −0.19[a]	−0.55 to −0.00 −0.10[a]	10^{-6} to 10^{-4}	4.3 4.1[a]	— 5.8[a]	504 672[a]	No SCC, shallow pits on leg No SCC, pits on leg in vapor phase[a]
1,000 ppm Cl^- as NaCl + 0.01 M $Na_2S_2O_3$	—	−0.13	O.C.	—	—	—	288	SCC above vapor/solution interface, pits at vapor/solution interface
1,000 ppm Cl^- as NaCl + 0.01 M $Na_2S_2O_3$	—	−0.13	−0.11 to −0.02	10^{-5} to 10^{-4}	—	—	288	SCC on leg above vapor/solution interface

Table 4-4. Summary of U-bend test results for type 316L SS in dilute chloride solutions at 95 °C (cont'd)

Solution	Purging Gas	E_{corr} (V_{SCE})	$E_{applied}$ (V_{SCE})	Current (Amps)	Initial pH	Final pH	Test Time (hr)	Results
1,000 ppm Cl^- as NaCl + 0.01 M $Na_2S_2O_3$	79% N_2 21% O_2	−0.27	O.C. −0.27 to −0.20	—	—	—	528	No SCC, pits above vapor/solution interface
1,000 ppm Cl^- as NaCl + 0.01 M $Na_2S_2O_3$	79% N_2 21% O_2	−0.27	−0.22	10^{-5}	—	—	528	SCC at top of leg above vapor/solution interface
1,000 ppm Cl^- as NaCl + 0.01 M $Na_2S_2O_3$	79% N_2 21% O_2	−0.24 −0.24	O.C.	—	4.9 4.6[a]	— 8.3[a]	504 672[a]	No SCC, shallow pits on leg SCC under bolt washer above vapor/solution interface[a]
1,000 ppm Cl^- as NaCl + 0.01 M $Na_2S_2O_3$	79% N_2 21% O_2	−0.20	−0.15 to 0.00	10^{-6} to 10^{-5}	4.9	—	504	No SCC, pits and corrosion products on leg
		−0.14[a]	−0.100[a]	10^{-5} to 10^{-4}[a]	4.6[a]	8.3[a]	672[a]	SCC on leg above vapor/solution interface and pits on leg[a]

[a] — second test period after initial period of 504 hr
O.C. — open circuit

Table 4-5. Summary of U-bend test results for type 316L SS and alloy 825 in concentrated chloride solutions at 95 °C

Material	Solution	Purging Gas	E_{corr} (V_{SCE})	$E_{applied}$ (V_{SCE})	Current (Amps)	Initial pH	Final pH	Test Time (hr)	Results
316L SS	5.8 molal Cl^- as LiCl	79% N_2 21% O_2	−0.34	O.C.	—	—	—	528	SCC on bend and leg
316L SS	5.8 molal Cl^- as LiCl	79% N_2 21% O_2	−0.34	−0.29	10^{-4}	—	—	528	SCC on bend and leg, pits on bend
316L SS	9.03 molal Cl^- as LiCl	—	−0.35	O.C.	—	—	—	288	SCC on bend and leg
316L SS	9.03 molal Cl^- as LiCl	—	−0.35	−0.32	10^{-5} to 10^{-3}	—	—	288	SCC on bend and leg
316L SS	5.94 molal Cl^- as NaCl	79% N_2 21% O_2	−0.34	O.C.	—	—	—	528	SCC around pit on bend
316L SS	5.94 molal Cl^- as NaCl	79% N_2 21% O_2	−0.35	−0.35 to −0.30	10^{-4}	—	—	528	SCC on bend and leg, pits on bend
316L SS	6.2 molal Cl^- as NaCl	—	−0.39	O.C.	—	—	—	288	Pit on bend
316L SS	6.2 molal Cl^- as NaCl	—	−0.39	−0.48 to −0.34	10^{-5} to 10^{-3}	—	—	288	SCC on leg

Table 4-5. Summary of U-bend test results for type 316L SS and alloy 825 in concentrated chloride solutions at 95 °C (cont'd)

Material	Solution	Purging Gas	E_{corr} (V_{SCE})	$E_{applied}$ (V_{SCE})	Current (Amps)	Initial pH	Final pH	Test Time (hr)	Results
316L SS	6.2 molal Cl^- as NaCl + 0.012 molar $Na_2S_2O_3$	—	−0.35	O.C.	—	—	—	288	SCC on bend and leg
316L SS	6.2 molal Cl^- as NaCl + 0.012 molar $Na_2S_2O_3$	—	−0.35	−0.34	10^{-5} to 10^{-4}	—	—	288	SCC on bend and leg, some shallow pits
Alloy 825	5.8 molal Cl^- as LiCl	79% N^2 21% O^2	−0.26 In vapor phase[a]	O.C.	—	3.4 3.8[a]	— 3.0[a]	504 672[a]	No SCC No SCC[a]
Alloy 825	5.8 molal Cl^- as LiCl	79% N^2 21% O^2	−0.22	−0.24 to −0.22	10^{-5} to 10^{-3}	3.4	—	504	No SCC, pits on bend
Alloy 825	5.8 molal Cl^- as LiCl	79% N^2 21% O^2	−0.26	−0.25	10^{-5} to 10^{-4}	3.8	3.0	672	No SCC, pits on bend and on leg above vapor/solution interface

Table 4-5. Summary of U-bend test results for type 316L SS and alloy 825 in concentrated chloride solutions at 95 °C (cont'd)

Material	Solution	Purging Gas	E_{corr} (V_{SCE})	$E_{applied}$ (V_{SCE})	Current (Amps)	Initial pH	Final pH	Test Time (hr)	Results
316L SS	6.2 Molal Cl^- as NaCl + 0.012 molar $Na_2S_2O_3$	—	−0.35	O.C.	—	—	—	288	SCC on bend and leg
316L SS	6.2 Molal Cl^- as NaCl + 0.012 molar $Na_2S_2O_3$	—	−0.35	−0.34	10^{-5} to 10^{-4}	—	—	288	SCC on bend and leg, some shallow pits
Alloy 825	5.9 molal Cl^- as NaCl	79% N^2 21% O^2	−0.17 In vapor phase[a]	O.C.	—	3.8 3.9[a]	— 2.9[a]	504 672	No SCC No SCC[a]
Alloy 825	5.9 molal Cl^- as NaCl	79% N^2 21% O^2	−0.16	−0.16	10^{-4} to 10^{-3}	3.8	—	504	No SCC, pit on leg
Alloy 825	5.9 molal Cl^- as NaCl	79% N^2 21% O^2	−0.27	−0.26	10^{-4} to 10^{-3}	3.9	2.9	672	No SCC, corrosion on leg

[a] — second test period after initial test period of 504 hr
O.C. — open circuit

promoted cracking in the same time interval. In this concentrated chloride solution, the addition of thiosulfate did not have a significant effect on the corrosion potential.

No SCC of alloy 825 was observed in concentrated NaCl or LiCl solutions under the conditions that promoted SCC of type 316L SS. In two tests conducted simultaneously in NaCl and LiCl solutions, specimens were initially immersed for 504 hr in the liquid phase under open-circuit conditions and then exposed for an additional period of 672 hr to the vapor phase. No SCC was observed under either condition, nor under anodic applied potentials. More extended tests are being conducted to evaluate whether cracking of alloy 825 can be initiated in these solutions at 95 °C after prolonged exposure times.

4.2.3.3 Discussion

The results shown in Figure 4-7 are consistent with the hypothesis (Cragnolino and Sridhar, 1992a; Tamaki et al., 1990; Tsujikawa et al., 1994) that SCC occurs only above a critical potential related to the repassivation potential for localized corrosion. The results plotted in Figure 4-7 clearly indicate that MA type 316L SS failed by SCC in slow strain rate tests when exposed to $MgCl_2$ and LiCl solutions at chloride concentrations greater than or equal to 9.1 mol/kg water and temperatures above 100 °C. On the other hand, SCC did not occur in LiCl and NaCl solutions in which the chloride concentration was 6.2 mol/kg water. These results indicate that under the experimental conditions used in these tests, particularly in terms of temperature and strain rate, SCC cannot be promoted regardless of the cation at chloride concentrations less than or equal to 6.2 mol/kg water, even at acidic pHs. Instead of SCC, the dominant failure mode was ductile failure accompanied by pitting corrosion. Since Beavers and Koch (1992) have asserted that the inability to reproduce the SCC of austenitic SS in dilute chloride solutions using slow strain rate tests may be due to the use of relatively high extension rates, the strain rate was decreased by almost a factor of five from 1×10^{-6} to 2.2×10^{-7} s^{-1} in specific tests. Nevertheless, cracks were not initiated. In this concentration range, it was difficult to avoid the occurrence of pitting as a predominant phenomenon. Although the potentials selected seem to be well below the extrapolation of the line representing the dependence of E_p with chloride concentration, which defines the electrochemical conditions for pit nucleation, pitting corrosion was observed in all these specimens. It should be noted, however, that in most of these tests the pH changed from values close to 2.5 before the test to values higher than 6.0 at the end of the test, probably due to the evaporation of HCl. It is possible that this increase in pH may render the environment less aggressive in terms of susceptibility to SCC.

The addition of thiosulfate to the chloride solutions promoted SCC at a slightly lower chloride concentration (5.8 mol/kg water) as shown in Figure 4-7 and Table 4-3. At an even lower chloride concentration (1,000-ppm), however, ductile fracture was the failure mode. No SCC was observed in these tests regardless of the increase in thiosulfate concentration, the decrease in strain rate, the application of an anodic potential, or the use of a notched specimen.

Contrary to the results of slow strain rate tests in dilute chloride solutions, SCC was often observed in constant deflection tests, even in the absence of thiosulfate, as summarized in Table 4-4. The presence of thiosulfate, however, significantly enhanced SCC susceptibility. Cracks were mostly detected above the vapor/solution interface, indicating that the local environment created as a liquid film on the specimen surface could be more detrimental than the bulk liquid environment. The existence of stagnant conditions, promoted by the elimination of a purging gas, appears to create a more severe environment than that arising from the continuous bubbling of synthetic air. This is apparently reflected in the higher potential obtained without gas purging (-0.13 V_{SCE}) with respect to that (≈ -0.20 V_{SCE}) measured in the presence of purged air. It is possible that H_2S, generated by reduction of thiosulfate at the metal

surface, could be more easily oxidized by oxygen in a process assisted by the solution agitation promoted by gas bubbling and, therefore be eliminated from the solution as a cracking promoter.

In more concentrated chloride solutions, SCC of type 316L SS was observed in constant deflection tests conducted in both LiCl and NaCl solutions at concentrations (5.8 mol/kg water) at which no cracking was detected in slow strain rate tests. The addition of thiosulfate increased even further the susceptibility to SCC in agreement with the result obtained in the slow strain rate tests included in Table 4-3.

Alloy 825 was found to be more resistant to SCC in concentrated chloride solutions containing thiosulfate than type 316L SS, as revealed by a comparison of the results of slow strain rate tests for both alloys shown in Table 4-3. This can be expected from the composition of the alloy, as discussed previously (Cragnolino and Sridhar, 1992a). The higher nickel content of alloy 825, combined with a higher level of chromium and molybdenum, makes this alloy far more resistant to SCC in chloride containing environments than any of the austenitic SS. This is confirmed by the data shown in Table 4-5 in which the behavior of type 316L SS and alloy 825 is compared in LiCl and NaCl solutions of the same chloride concentration (5.8 mol/kg water) using U-bend specimens.

The SCC resistance of alloy 825 needs to be explored under a wide range of environmental conditions because the alloy exhibits a significant susceptibility to localized corrosion, particularly in the vapor phase under conditions leading to the formation of a liquid film on the surface. SCC can occur as a competitive phenomenon when the tendency to localized corrosion becomes marginal. Then, the initiation of cracks could be promoted by the alteration of surface or near-surface conditions by the introduction of very localized plastic deformation via cold work or microchemical modifications through surface depletion of some alloying element or thickening of the passive film by oxidation in air. Additional experiments are needed to clarify these uncertainties. In particular, more prolonged constant deflection tests using U-bend specimens under a variety of controlled potential and surface conditions, including the formation of crevices, are required to attain a better understanding of the events leading to crack initiation.

4.2.4 Conclusions and Recommendations

4.2.4.1 Localized Corrosion

The changes in chemistry and potential inside a well-defined crevice as a function of applied potential were monitored using micro-pH, chloride, and reference electrodes. The pH and chloride concentration do not change in the crevice before active crevice corrosion is detected by the increase in current. This is in contrast to many crevice corrosion models. This discrepancy between experiments and existing models can be explained by either considering the dissolution behavior of MnS inclusions in alloys that have significant amounts of these inclusions, or by assuming that crevice nuclei do initiate by a decrease in pH as proposed by the models, but require some growth time before they can be detected by the microelectrodes. In this concept, crevice corrosion does not occur uniformly throughout a certain depth in the crevice where a critical solution composition is attained, but initiates in small regions where the gap is the smallest, such as between peaks of surface asperities. Once initiated, crevice nuclei can grow laterally provided the external potential is sufficiently positive or there is an oxidizing species that raises the corrosion potential sufficiently high. This can explain the common observation of the effect of external potential or oxidizing species not predicted by many crevice corrosion models. Many finite-

difference-based crevice corrosion models can be adapted to variable gaps, although none have attempted to do so over scales corresponding to surface roughness profiles.

The measured rate of change of pH and chloride in the crevice is slower for rougher surfaces as expected from model predictions. Alloy 825 showed a greater lowering of pH inside the crevice than type 304L SS which can be attributed to the oxidation of Mo to Mo(VI). The formation of molybdate in the crevice may also explain the increase in the corrosion potential upon repassivation of alloy 825.

Repassivation of a stably growing crevice did not result in any significant increase in pH or decrease in chloride concentration inside the crevice over the experimental time period. However, the difference between the external and internal potentials became narrower, indicating that repassivation of a deep crevice is not controlled by transport-driven changes in internal chemistry but by the external potential (modified by IR drop) decreasing to the corrosion potential of the active alloy in the acidic crevice solution.

4.2.4.2 Stress Corrosion Cracking

The applicability of critical potentials for localized corrosion for predicting SCC cracking is being studied using slow strain rate and constant deflection tests on type 316L SS and alloy 825. The results generated thus far are consistent with the assumption that the repassivation potential for localized corrosion constitutes a lower bound for the critical potential for SCC. However, the occurrence of SCC was found to be dependent on test technique. In slow strain rate tests, SCC of type 316L SS was promoted by concentrated chloride solutions (>9.1 mol/kg water) above 100 °C, and at lower chloride concentrations and temperatures by the presence of thiosulfate. However, no SCC was observed with that technique at chloride concentrations lower than 6 mol/kg water, even in the presence of thiosulfate. On the other hand, SCC of type 316L SS was observed using U-bend specimens in constant deflection tests conducted in concentrated chloride solutions or in more dilute solutions containing thiosulfate. In dilute solutions, cracking was found to be confined to the region above the liquid water-vapor interface. No SCC of alloy 825 was observed in either slow strain rate or constant deflection tests under environmental conditions similar to those used for testing type 316L SS, indicating that alloy 825 is far more resistant to SCC than the SS.

The need to study the effect of crevice conditions and concentration process at the vapor/solution interface on the initiation of cracks is emphasized to explore the full range of environmental and electrochemical potential that can cause cracking of these alloys in chloride containing solutions at temperatures close to the boiling point.

4.3 PROGRESS TOWARD MEETING PROJECT OBJECTIVES

The approach that is currently being used in the IPA Phase 2 (Wescott et al., 1994) and the Substantially Complete Containment Example Analysis (Cragnolino et al., 1994) codes for assessing the container performance involves consideration of critical potentials and the corrosion potential. These codes will eventually support the development of Compliance Determination Methodologies (CDMs). The results of the IWPE project described in the previous sections support the methodologies of performance assessment adopted thus far. Modifications to detailed auxiliary analyses codes such as TWITCH (Walton and Kalandros, 1992), suggested by the experimental findings, would enable a better prediction of environmental evolution inside crevices and place parameters such as repassivation potential used in

PA codes on a sounder technical basis. Longer-term constant deflection tests will confirm the existence of a critical potential for SCC.

4.4 PLANS FOR THE NEXT REPORTING PERIOD

Long-term tests under controlled potentials, anticipated to continue for time periods ranging from a few months to 5 yr, are necessary to verify several of the concepts discussed before. These tests, which are continuing, will verify whether the E_{rp} for deep pits is a conservative parameter for predicting pit initiation and repassivation for all surface conditions. Tests with intentional crevices under potentiostatic control will also verify whether the E_{rp} for deep pits can be used to predict initiation and repassivation of crevice corrosion. In conjunction with these controlled potential tests, tests under naturally aerated conditions and with specimens surrounded by crushed tuff will also be conducted where the corrosion potential will be monitored. Ongoing results of these tests will be reported in future semi-annual reports.

A radially symmetrical crevice design would enable a better comparison of model and experiments. Additionally, the effect of solute transport on repassivation may become important for shallow crevices. Hence, this will be investigated by varying the crevice depth. Finally, the changes in crevice chemistry under natural redox conditions need to be investigated.

Slow strain rate tests will be continued with the aim of completing them during the next reporting period. Creviced specimens will be tested to evaluate the effect of crevice chemistry on the initiation of cracks. Double U-bend specimens will be used to develop crevice conditions in the region of highest tensile stress in constant deflection tests to explore conditions that may lead to cracking in relatively dilute chloride solutions. Long-term SCC tests will be continued for periods extended from a few months to several years.

In order to understand the long-term behavior of container materials, their microstructural changes as a result of thermal exposure need to be understood. These studies are being performed in Task 3. As part of this task, methods to quantify the grain boundary sensitization of alloy 825 are being developed. While such test techniques exist for SS such as type 304L, no method for rapidly and sensitively estimating grain boundary sensitization of alloy 825 exists. The results from these studies will be presented in the next semi-annual report as a basis for further studies in this area.

4.5 REFERENCES

American Society for Testing and Materials. 1991. Standard Practice for Making and Using U-Bend Stress-Corrosion Test Specimens. *Annual Book of Standards*. Philadelphia, PA: American Society for Testing and Materials: 03(02): 96–101.

Abraham, T., H. Jain, and P. Soo. 1986. *Stress Corrosion Cracking Tests on High-Level Waste Container Materials in Simulated Tuff Repository*. NUREG/CR-4619. Washington, DC: U.S. Nuclear Regulatory Commission.

Alavi, A., and R.A. Cottis. 1987. The determination of pH, potential and chloride concentration in corroding crevices on 304 stainless steel and 7475 aluminum alloy. *Corrosion Science* 27(5): 443–451.

Alkire, R.C., and S.E. Lott. 1989. The role of inclusions on initiation of crevice corrosion of stainless steel. II. Theoretical studies. *Journal of the Electrochemical Society* 136(11): 3,256–3,262.

Beavers, J.A., and G.H. Koch. 1992. Limitations of the slow strain rate test for stress corrosion cracking testing. *Corrosion* 48: 256–264.

Beavers, J.A., N.G. Thompson, and C.L. Durr. 1992. *Pitting, Galvanic, and Long-Term Corrosion Studies on Candidate Container Alloys for the Tuff Repository*. NUREG/CR-5709. Washington, DC: U.S. Nuclear Regulatory Commission.

Buscheck, T.A., D.G. Wilder, and J.J. Nitao. 1993. Large-scale *in situ* heater tests for hydrothermal characterization at Yucca Mountain. *Proceedings of the Fourth Annual International High-Level Radioactive Waste Management Conference*. La Grange Park, IL: American Nuclear Society: 1854–1872.

Cavanaugh, M.A., J.A. Kargol, J. Nickerson, and N.F. Fiore. 1983. The anodic dissolution of a Ni-base superalloy. *Corrosion* 39(4): 144–150.

Cragnolino, G.A., and N. Sridhar. 1992a. *A Review of Stress Corrosion Cracking of High-Level Nuclear Waste Container Materials — I*. CNWRA 92-021. San Antonio, TX: Center for Nuclear Waste Regulatory Analyses.

Cragnolino, G.A., and N. Sridhar. 1992b. *Integrated Waste Package Experiments. NRC High-Level Radioactive Waste Research at CNWRA, January 1 Through June 30, 1992*. W.C. Patrick, ed. CNWRA 92-01S. San Antonio, TX: Center for Nuclear Waste Regulatory Analyses.

Cragnolino, G.A., N. Sridhar, J. Walton, R. Janetzke, J. Wu, and P. Nair. 1994. *Substantially Complete Containment — Example Analysis of a Reference Container*. CNWRA 94-003. San Antonio,TX: Center for Nuclear Waste Regulatory Analyses.

Doering, T.W. 1993. Robust waste package concept (multibarrier). *Proceedings of the Fourth Annual International High-Level Radioactive Waste Management Conference*. La Grange Park, IL: American Nuclear Society: 551–557.

Dunn, D.S., N. Sridhar, and G.A. Cragnolino. 1993a. The effect of surface conditions on the localized corrosion of a candidate high-level waste container material. *Corrosion Control for Low-Cost Reliability. Proceedings of the Twelfth International Corrosion Congress*. Houston, TX: NACE International: 5B: 4,021–4,030.

Dunn, D.S., N. Sridhar, and G.A. Cragnolino. 1993b. Effects of surface conditions on the localized corrosion of alloy 825 high-level waste container material. Paper No. 94-138. *Corrosion '94*. Houston, TX: NACE International.

Farmer, J.C., G.E. Gdowski, R.D. McCright, and H.S. Ahluwalia. 1991. Corrosion models for performance assessment of high-level radioactive waste containers. *Nuclear Engineering and Design* 129: 57–88.

Gravano, S.M., and J.R. Galvele, 1984. Transport processes in passivity breakdown – III. Full hydrolysis plus ion migration buffers. *Corrosion Science* 24(6): 517–534.

License Application Review Plan. 1992. *Draft License Application Review Plan for the Review of a License Application for a Geologic Repository for Spent Nuclear Fuel and High-Level Radioactive Waste, Yucca Mountain, Nevada.* NUREG-1323. Washington, DC: U.S. Nuclear Regulatory Commission: Office of Nuclear Material Safety and Safeguards.

Linke, W.F. 1965. Solubilities: Inorganic and metal organic compounds. Washington, DC. *American Chemical Society*: 959.

Lott, S.E., and R.C. Alkire. 1989. The role of inclusions on initiation of crevice corrosion of stainless steel. I. Experimental studies. *Journal of The Electrochemical Society* 136(4): 973–979.

Luo, J.L., Y.C. Lu, and M.B. Ives. 1992. Use of microelectrodes to determine local conditions within active pits. *Materials Performance* 31(10): 44–47.

Macdonald, D.D., and M. Urquidi-Macdonald. 1990. Thin-layer mixed-potential model for corrosion of high-level nuclear waste canisters. *Corrosion* 46(5): 380–390.

Mankowski, J., and Z. Szklarska-Smialowska. 1975. Studies on accumulation of chloride ions in pits growing during anodic polarization. *Corrosion Science* 15: 493–501.

Newman, R.C., H.S. Isaacs, and B. Alman. 1982. Effects of sulfur compounds on the pitting behavior of type 304 stainless steel in near-neutral chloride solutions. *Corrosion* 38: 261–265.

Okayama, S., Y. Uesugi, and S. Tsujikawa. 1987. The effect of alloying elements on the repassivation potential for crevice corrosion of stainless steels in 3% NaCl solution. *Corrosion Engineering* 36: 157–168.

Oldfield, J.W., and W.H. Sutton, 1978. Crevice corrosion of stainless steels. *British Corrosion Journal* 13(1): 13–22

Pabalan, R.T., and W.M. Murphy. 1993. Unsaturated mass transport (Geocnemistry). *Report on Research Activities for July 1 Through December 31, 1992.* CNWRA 92-02S. San Antonio, TX: Center for Nuclear Waste Regulatory Analyses.

Pabalan, R.T., W.M. Murphy, and P. Bertetti. 1990. Unsaturated mass transport (Geochemistry). *Report on Research Activities for the Quarter July 1 Through September 30, 1990.* CNWRA 90-03Q. San Antonio, TX: Center for Nuclear Waste Regulatory Analyses.

Patrick, W.C. 1986. *Spent Fuel Test—Climax: An Evaluation of the Technical Feasibility of Geologic Storage of Spent Nuclear Fuel in Granite—Final Report.* UCRL-53702. Livermore, CA: Lawrence Livermore National Laboratory.

Ramirez, A.L., ed. 1991. *Prototype Engineered Barrier System Field Test (PEBSFT) Final Report* UCRL-ID-106159. Livermore, CA: Lawrence Livermore National Laboratory.

Rosenfeld, I.L., I.S. Danilov, and R.N. Oranskaya. 1978. Breakdown of the passive state and repassivation of stainless steels. *Journal of the Electrochemical Society* 125(11): 1,729–1,735.

Ruffner, D.J., G.L. Johnson, E.A. Platt, J.A. Blink, and T.W. Doering. 1993. Drift emplaced waste package thermal response. *Proceedings of the Fourth Annual International High-Level Radioactive Waste Management Conference*. La Grange Park, IL: American Nuclear Society: 538–543.

Sagar, B., R.B. Codell, J.C. Walton, and R.W. Janetzke. 1992. *SOTEC: A Source Term Code for High-Level Nuclear Waste Geologic Repositories. User's Manual Version 1.0.* CNWRA 92-009. San Antonio, TX: Center for Nuclear Waste Regulatory Analyses.

Sharland, S.M. 1992. A mathematical model of the initiation of crevice corrosion in metals. *Corrosion Science* 33(2): 183–201.

Silcock, J.M., and P.R. Swann. 1979. Nucleation and growth of transgranular stress corrosion cracks in austenitic stainless steels. *Environment-Sensitive Fracture of Engineering Materials*. Z.A. Foroulis, ed. Warrendale, PA: The Metallurgical Society of AIME: 133–152.

Sridhar, N., and G.A. Cragnolino. 1992a. Long-term life prediction of localized corrosion of Fe-Ni-Cr-Mo high-level nuclear waste container materials. *Corrosion '93, Paper No. 93197.* Houston, TX: National Association of Corrosion Engineers.

Sridhar, N., and G.A. Cragnolino. 1992b. Integrated waste package experiments. *NRC High-Level Radioactive Waste Research at CNWRA, July 1 Through December 31, 1992*. W.C. Patrick, ed. CNWRA 92-02S. San Antonio, TX: Center for Nuclear Waste Regulatory Analyses.

Sridhar, N., G.A. Cragnolino, J.C. Walton, and D. Dunn. 1992. Prediction of crevice corrosion using modeling and experimental techniques. *Application of Accelerated Corrosion Tests to Service Life Prediction of Materials*. G.A. Cragnolino and N. Sridhar, eds. ASTM STP 1194. Philadelphia, PA: American Society for Testing and Materials.

Sridhar, N., G.A. Cragnolino, and D. Dunn. 1993a. *Experimental Investigations of Localized Corrosion of High-Level Waste Container Materials*. CNWRA 93-004. San Antonio, TX: Center for Nuclear Waste Regulatory Analyses.

Sridhar, N., J.C. Walton, G.A. Cragnolino, and P.K. Nair. 1993b. *Engineered Barrier System Performance Assessment Codes (EBSPAC) Progress Report—October 1, 1992, through September 25, 1993*. CNWRA 93-021. San Antonio, TX: Center for Nuclear Waste Regulatory Analyses.

Sridhar, N., G.A. Cragnolino, and D. Dunn. 1993c. Integrated Waste Package Experiments. *NRC High-Level Radioactive Waste Research at CNWRA January-June 1993*. B. Sagar, ed. CNWRA 93-01S. San Antonio, TX: Center for Nuclear Waste Regulatory Analyses.

Sugimoto, K., and K. Asano. 1990. Analysis of localized corrosion on stainless steel by micro-complex pH-pCl electrode. *Advances in Localized Corrosion*. H. Isaacs et al., ed. Houston, TX: National Association of Corrosion Engineers: 375–379.

Suzuki, T., M. Yamabe, and Y. Kitamura. 1973. Composition of anolyte within local anode of stainless steel. *Corrosion* 29(1): 18–22.

Szklarska-Smialowska, Z. 1986. *Pitting Corrosion of Metals*. Houston, TX: National Association of Corrosion Engineers: 201–236.

Tamaki, K., S. Tsujikawa, and Y. Hisamatsu. 1990. Development of a new test method for chloride stress corrosion cracking of stainless steel in dilute NaCl solutions. *Advances in Localized Corrosion*. H.S. Isaacs, U. Bertocci. J. Kruger, and S. Smialowska, eds. Houston, TX: National Association of Corrosion Engineers: 207–214.

Thompson, N.G., and B.C. Syrett. 1992. Relationship between conventional pitting and protection potentials and a new, unique pitting potential. *Corrosion* 48(8): 649–659.

Tsujikawa, S., Y. Soné, and Y. Hisamatsu. 1987. Analysis of mass transfer in a crevice region for a concept of the repassivation potential as a crevice corrosion characteristic. *Corrosion Chemistry within Pits, Crevices, and Cracks*. A. Turnbull, ed. London, U.K.: Her Majesty's Stationary Office: 171–186.

Tsujikawa, S., T. Shinohara, and W. Lichang. 1994. Spot-welded specimen potentiostatically kept just above the crevice repassivation potential to evaluate stress corrosion cracking susceptibility of improved type 304 stainless steels in NaCl solutions. *Application of Accelerated Corrosion Tests to Service Life Prediction of Materials*. G.A. Cragnolino and N. Sridhar, eds. ASTM STP 1194. Philadelphia, PA: American Society for Testing and Materials: In press.

Tsuru, T., K. Hashimoto, and S. Haruyama. 1985. Mass transport and solution chemistry in localized corrosion cell. *Critical Issues in Reducing the Corrosion of Steels*. H. Leidheiser and S. Haruyama, eds., Houston, TX: National Association of Corrosion Engineers: 110–120.

Turnbull, A. 1983. The solution composition and electrode potential in pits, crevices, and cracks. *Corrosion Science* 23(8): 833–870.

Walton, J.C. 1993. Effects of evaporation and solute concentration on presence and composition of water in and around the waste package at Yucca Mountain. *Waste Management* 13: In press.

Walton, J.C., and S.K. Kalandros. 1992. *TWITCH — A Model for Transient Diffusion, Electromigration, and Chemical Reaction in One Dimension*. CNWRA 92-019. San Antonio, TX: Center for Nuclear Waste Regulatory Analyses.

Wanklyn, J.N. 1981. The role of molybdenum in the crevice corrosion of stainless steels. *Corrosion Science* 21(3): 211–225.

Wescott, R.G., M.P. Lee, N.A. Eisenberg, and T.J. McCartin, eds. 1994. *Phase 2 Demonstration of the NRC's Capabilities to Conduct a Performance Assessment for a High-Level Waste Repository*. NUREG-1464. Washington, DC: U.S. Nuclear Regulatory Commission.

Xu, Y., and H.W. Pickering. 1993. The initial potential and current distributions of the crevice corrosion process. *Journal of the Electrochemical Society* 140(3): 658–668.

Zimmerman, R.M., R.L. Schuch, D.S. Mason, M.L. Wilson, M.E. Hall, M.P. Board, R.P. Bellman, and M.P. Blanford. 1986. *Final Report: G-Tunnel Heated Block Experiment*. SAND84-2620. Albuquerque, NM: Sandia National Laboratories.

5 GEOCHEMICAL NATURAL ANALOG RESEARCH

by English C. Pearcy, Ronald T. Green, William M. Murphy

Investigators: English C. Pearcy, Bret W. Leslie, William M. Murphy, James D. Prikryl, and Ronald T. Green

NRC Project Officer: Linda A. Kovach

5.1 TECHNICAL OBJECTIVES

The technical objective of the Geochemical Natural Analog Research Project is to provide field, laboratory, and theoretical analyses of natural systems that are analogous to some aspects of the proposed high-level waste (HLW) repository at Yucca Mountain (YM), Nevada. These analyses are designed to develop a better understanding of the utility and limitations of natural analog studies when employed to support a license application for a HLW repository and to provide fundamental data on the long-term behavior of HLW within a repository environment. Natural systems that have operated for periods comparable to that required for HLW disposal (i.e., 10^3–10^4 yr and greater) (U.S. Environmental Protection Agency, 1989) provide the only opportunity to obtain observational knowledge of the long-term behavior of HLW components. Such information is important for support of long-term predictive models of repository performance assessment (PA) (U.S. Nuclear Regulatory Commission, 1987). Many factors affecting the long-term behavior and interaction of the waste form and engineered barrier system (EBS) with the geochemical environment of the proposed repository are poorly known. The absence of this basic information severely limits the confidence with which PA models may be evaluated.

The Geochemical Natural Analog Research Project will be important in addressing uncertainties raised in a number of Compliance Determination Strategies (CDSs). Specific Key Technical Uncertainties (KTUs) that will be supported include those in CDSs 3.3, 3.2.2.1, 3.2.2.9, 3.2.2.12, 3.2.3.3, 3.2.3.5, 6.1, and 6.2. Data and interpretations developed within the Analog Research Project will assist resolution of KTU topics including: (i) equal or increased capacity of alteration mineral assemblages to inhibit radionuclide migration; (ii) uncertainty in identifying geochemical processes that reduce radionuclide retardation; (iii) uncertainty in determining the magnitude of the effect of the geochemical processes that reduce radionuclide retardation; (iv) conceptual model representations of the natural and engineered systems; (v) variability (temporal, spatial, etc.) in model parametric values, developing conceptual and mathematical groundwater flow models; and (vi) uncertainty in modeling groundwater flow caused by the lack of codes tested against field and laboratory data.

The Geochemical Natural Analog Research Project is required by its nature to be an integrated effort combining expertise in geochemistry, hydrology, and structural geology among others. This need for interdisciplinary input is reflected in a number of technical interfaces with other U.S. Nuclear Regulatory Commission (NRC) Office of Nuclear Regulatory Research (RES) projects. An active and ongoing connection has been established with the PA Research Project (Chapter 7 of this document). Within the Geochemical Natural Analog Research Project, the hydraulic properties of welded silicic tuff from the Nopal I analog site are being measured; these data are being analyzed within the PA Research Project to allow more complete interpretation of long-term transport of uranium through tuff at the site. Observations and measurements from the Geochemical Natural Analog Research Project are also being used within the Sorption Research Project (Chapter 6 of this document) as a comparison to laboratory

studies. Additionally, results from the Geochemical Natural Analog Research Project are being used to guide and develop the anticipated Near-Field Environment Research Project. Specifically, at the Nopal I site, it has been observed that alteration phases formed after uraninite (a spent fuel analog material) are dominated by the minerals uranophane, soddyite, and weeksite. The Nopal I analog suggests that these phases are likely to be important to radionuclide transport in a YM repository; the Near-Field Environment Research Project may include experiments to determine thermodynamic properties of those minerals so that their behavior may be modeled. Similarly, results and expertise from the uraninite characterization at Nopal I are being used to guide the design of potential spent fuel waste form experiments within the EBS Waste Form Characterization work for the NRC Office of Nuclear Material Safety and Safeguards (NMSS).

The Geochemical Natural Analog Research Project addresses needs identified by the NMSS concerning assessment of the degree to which data from analogous sites may be extrapolated to support modeling for a repository site and evaluation of means to derive reasonable assurance that PA models can be validated using data from natural analogs. Specific NRC research needs that may be met through this project include: (i) comparison of laboratory sorption, mineral stability, leaching, and kinetic data with observations from natural systems; (ii) evaluation of radionuclide transport in unsaturated tuff; (iii) assessment of the effects of oxidation state on leaching and radionuclide release; and (iv) investigation of coupled interactions affecting radionuclide release and transport.

Research within the Geochemical Natural Analog Research Project includes work at two sites: the Nopal I uranium deposit in the Peña Blanca district, Chihuahua, Mexico (field work initiated February 1991), and the Akrotiri archaeologic site on Thera (Santorini), Greece (field work initiated June 1992). Earlier reports in this series documenting progress to date include Leslie et al. (1993); Pearcy and Leslie (1993); Pearcy et al. (1993a,b); Pearcy and Murphy (1990, 1991a–c). This report describes recent results from the Akrotiri Site.

5.2 SIGNIFICANT TECHNICAL ACCOMPLISHMENTS

The Center for Nuclear Waste Regulatory Analyses (CNWRA) research at the Akrotiri site has focused on contaminant transport over a particularly well-constrained time period of 3,600 yr by considering metallic artifacts as localized sources for transport of exotic (i.e., introduced) chemical components. Initial field and laboratory research have established a close comparison between the Akrotiri site and aspects of the proposed repository at YM, including silicic tuffaceous host rocks, a semiarid climate, an unsaturated hydrologic regime, and a chemically oxidizing environment (Murphy et al., 1991; Pearcy et al., 1993a; Pearcy and Murphy, 1991d). The discovery location of bronze artifacts in room Delta 3 of the Akrotiri excavation has been identified as a promising site at which to collect samples and to make observations relevant to elemental transport. Preliminary analyses have developed an effective leachate technique for resolving low concentrations of transported metals (Pearcy et al., 1993a). A high-resolution magnetometer survey of unexcavated areas was conducted to identify buried metallic artifacts, and the hydraulic saturation state of the Minoan tuff in which the artifacts were buried has been estimated at 0.14 to 0.38 (Pearcy et al., 1993a).

Recent work on the Akrotiri analog comprises field research including sampling of the Delta 3 (and other) artifacts, detailed mapping of Delta 3, sampling of the Cape Riva tuff (above which the Delta 3 artifacts were buried), field measurement of hydraulic properties of the Cape Riva tuff, and the Minoan tuff (within which the artifacts were buried), acquisition of historical meteorologic data for the

area, and observation of the site and area hydrology. Laboratory analyses completed subsequent to the most recent field research include optical microscopy, x-ray diffractometry (XRD), and energy-dispersive spectrometry (EDS) of corrosion products from the Delta 3 bronzes and porosity and bulk density measurements of host tuff samples.

5.2.1 Mineralogic and Chemical Analyses of Delta 3 Bronze Corrosion Products

A group of bronze artifacts was discovered in room Delta 3 of the Akrotiri site (Figure 5-1) during archaeologic excavations in September 1970 (Marinatos, 1971). The precise locations and positions of the artifacts at the time of their discovery were deduced using photographs taken during excavation of the artifacts by the archaeologists and by the National Geographic Society (Figure 5-2). The artifacts were buried in this position beneath volcanic tuff, building debris, and volcanic midflow debris for a period of 3,600 yr (Hammer et al., 1987).

During their 3,600-yr burial, the bronzes underwent considerable corrosion in the ambient oxidizing environment. Samples of bronze corrosion products were received from Dr. A. Michailidou at the Akrotiri excavation from a collection of such material archived at the site. Sample SAN-056 is a portion of the bronze corrosion products developed on Ewer X4 in room Delta 3 of the Akrotiri site. SAN-056 was chosen for detailed characterization because it is the largest of the samples of bronze corrosion products obtained (about 100 mg); other corrosion product samples have undergone more limited study. Ewer X4 was excavated from Delta 3 on September 9, 1970, and is one of five large bronze artifacts unearthed by archaeologists in that location. Observations of Ewer X4 and the other Delta 3 artifacts have been reported previously (Pearcy et al., 1993a).

The bronze corrosion products provide an indication of the composition of the original artifact and are the source from which elements from the ewer have migrated into the enclosing tuffs. Optical microscopy studies of SAN-056 show it to consist of extremely fine-grained crusts of Cu oxides and oxyhydroxides, which tend to be segregated into largely monomineralic zones. These characteristics are common to all corrosion product samples observed from Delta 3. Mineralogic characterization by XRD [Automated (RADIX) Siemens D500 XRD; Cu tube, Ni filter, 40 kV, 30 mA; scan 2-70° at 0.01° step; count 1.0 s; JADE/MDI software] shows SAN-056 to consist dominantly of cuprite (Cu_2O) and paratacamite [$Cu_2(OH)_3Cl$] (Figure 5-3). Both cuprite and paratacamite are common oxidation products of metallic copper in natural deposits. The occurrence of paratacamite in the Delta 3 samples may have been made more likely by the proximity of the Akrotiri site to the ocean (about 250 m horizontal and 23 m vertical) and the resultant infiltration of Cl from sea spray.

Semi-quantitative EDS analyses (AMRAY 1645 SEM with Tracor Northern 8502S EDS, 20 kV beam, 100 s counting time) of SAN-056 show it to be composed of Cu, Cl, and Fe with lesser amounts of Ti. Strong peaks were also obtained for Si, Al, Ca, and K; however, these elements probably occur in particles of volcanic ash adhering to or physically incorporated within the corrosion products. Samples SAN-010, SAN-018, and SAN-055 were also analyzed by EDS. SAN-010 was the only sample with detectable Sn, Mn, and Co. SAN-055 contained trace Ag, and both SAN-055 and SAN-010 had traces of S. The compositional variability indicated by these analyses is likely a function of the mineralogic heterogeneity of the oxidized crusts and of the small sample sizes (e.g., mg). It is likely that the elements associated with the Cu and Cl (e.g., Fe, Ti, Ag) are included within the copper minerals by solid solution, but it is possible that they form discrete phases that occur in amounts too small to be resolved optically or by XRD. No chemical analyses of the Delta 3 bronzes have been reported in the literature. Bronzes from other areas within the Akrotiri excavation, however, consist dominantly of Cu, Sn, and Pb, with minor Fe and As, as well as many other trace constituents (Slater, 1980).

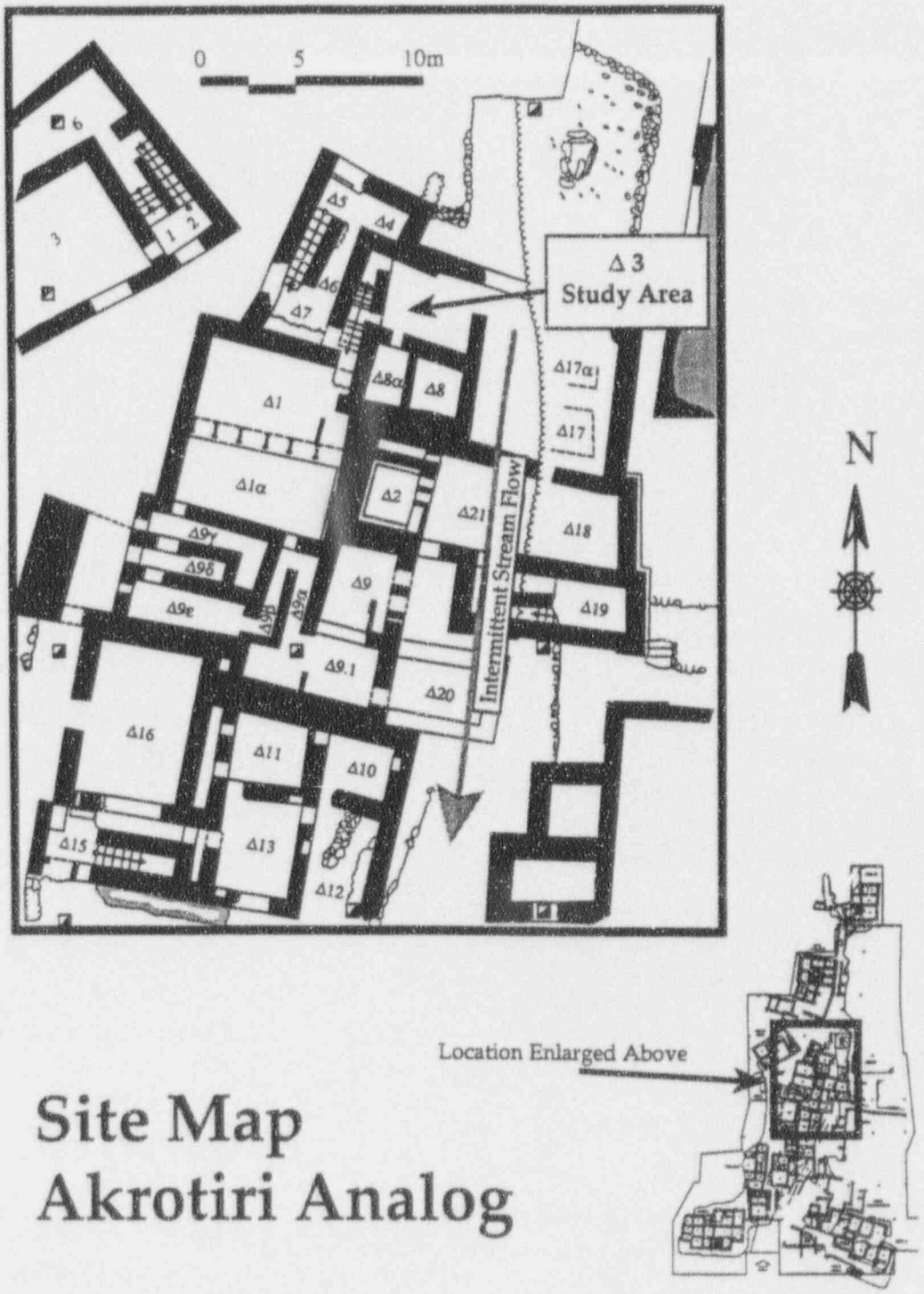

Figure 5-1. This map shows the extent of the Akrotiri archaeologic excavation at the end of the 1993 field season (September 1993). Information upon which this map is based was provided by Christos Doumas, director of the excavation. The lower right corner of this figure shows the full extent of the current excavation; all of the area indicated is covered by protective roofing.

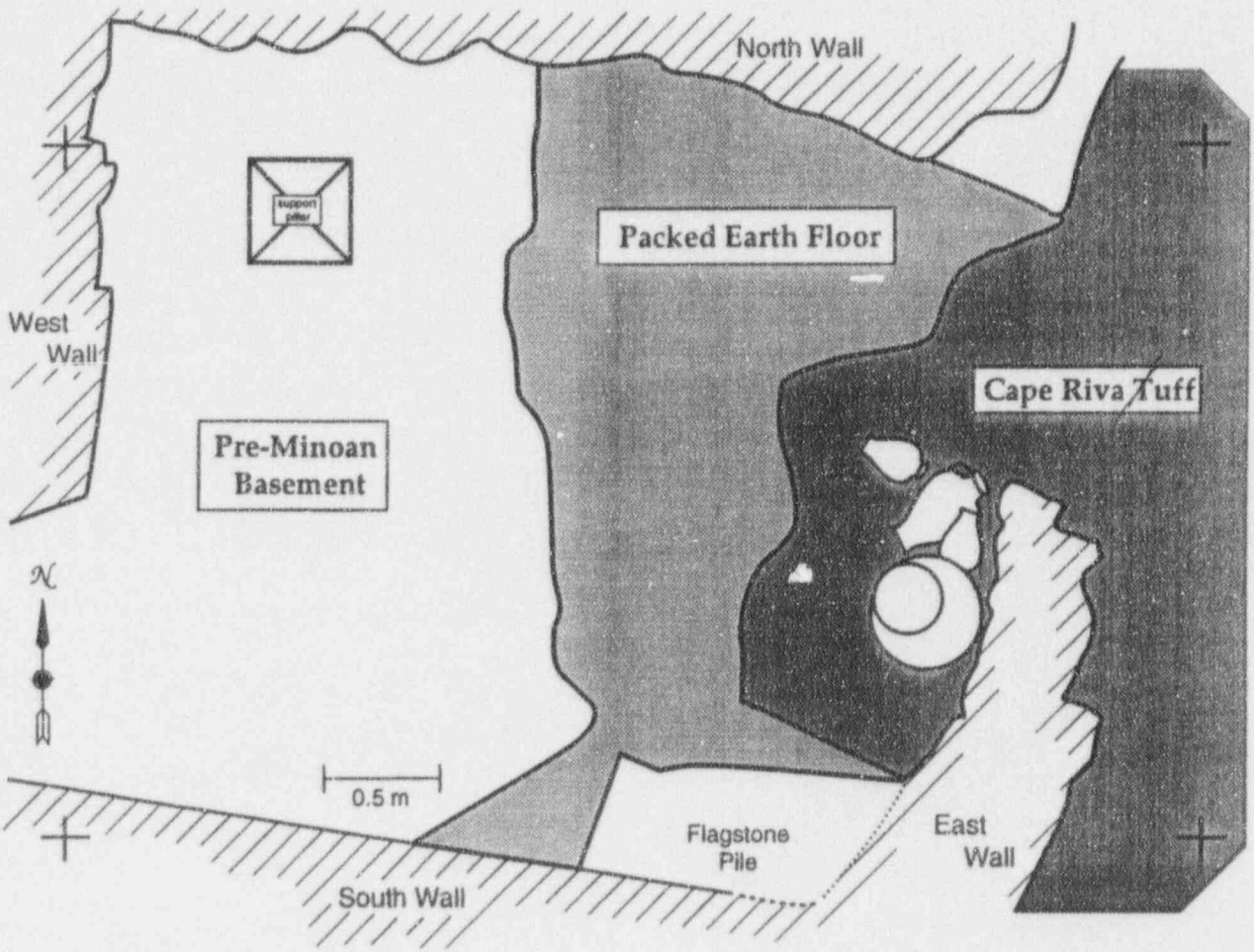

Figure 5-2. This map shows detailed locations within room Delta 3. The pre-Minoan Basement is about 2 m lower than the rest of the Delta 3 floor. The packed earth floor was constructed of clay and building debris directly upon the bedrock and tapers in thickness from 5 to 0 cm. The Cape Riva tuff is the bedrock above which the bronze artifacts were discovered. Positions of the artifacts were definitively interpreted from a set of photographs taken at the time of excavation.

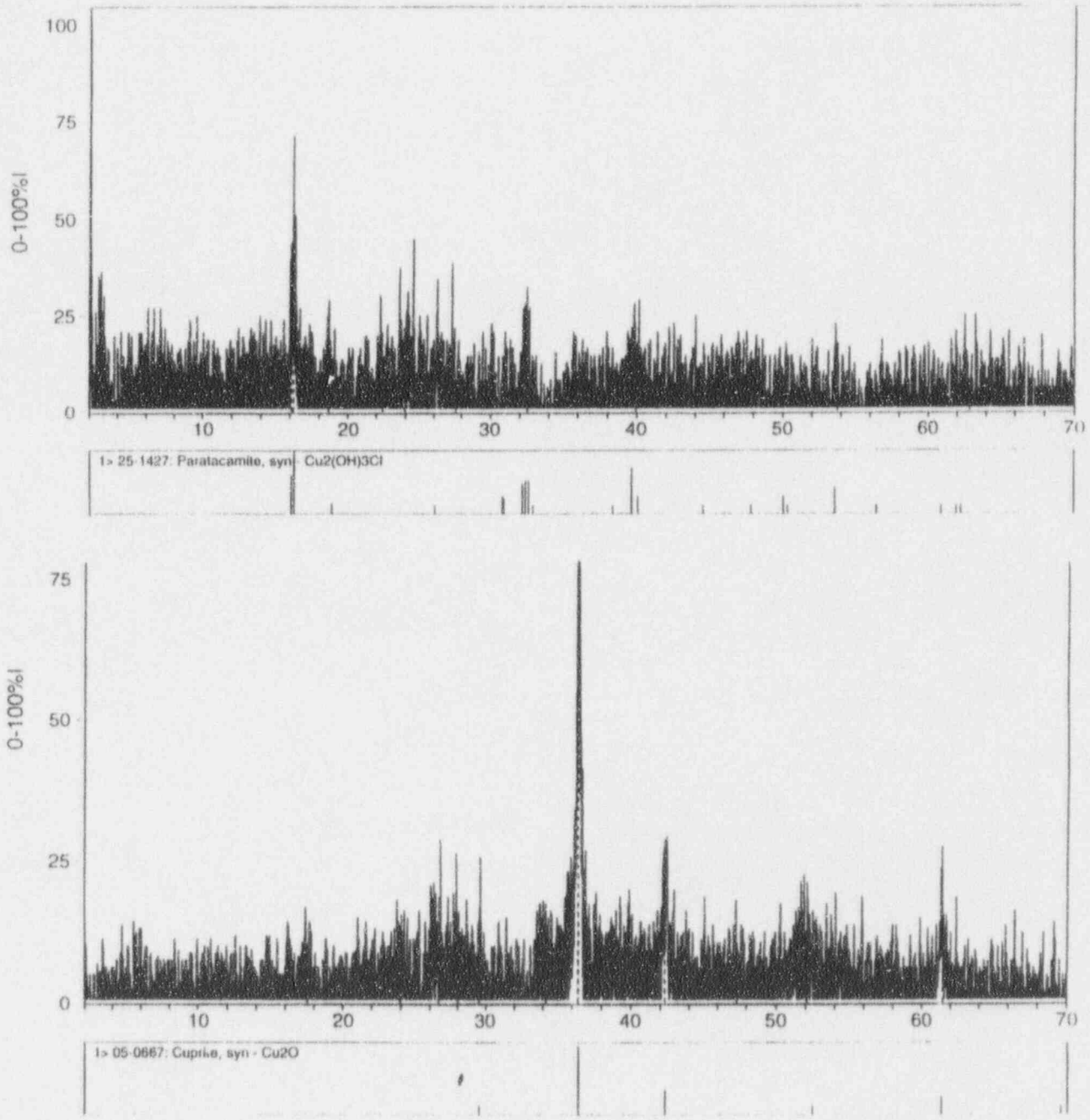

Figure 5-3. These plots show the mineralogic composition of a sample of bronze corrosion products from one of the Delta 3 ewers as determined by powder XRD. The corrosion products occur in largely monomineralic zones composed of cuprite (Cu_2O) and paratacamite [$Cu_2(OH)_3Cl$]. Characteristic diffraction maxima are shown for each mineral.

5.2.2 Hydraulic Property Measurements

Field measurements were conducted to determine the hydraulic properties of both the Minoan tuff, through which infiltrating waters flowed to the anthropogenic horizon at Akrotiri, and the underlying Cape Riva tuff, into which trace metals from the artifacts are postulated to have been transported. *In situ* studies were conducted for saturated hydraulic conductivity, sorptivity, and unsaturated hydraulic conductivity. Moisture content and matric potential were measured *in situ* on the Minoan tuff; the greater welding of the Cape Riva tuff precluded these tests on that formation. Porosity, bulk density, and moisture content measurements were conducted in the CNWRA hydraulic property measurements laboratory.

In situ moisture content in the Minoan tuff and in other materials at several locations at the Akrotiri site was measured using time-domain reflectometry (TDR, Trase System 1 Model 6050XI, Soilmoisture Equipment). TDR measures the speed of an electromagnetic pulse emitted down parallel transmission lines inserted into the subsurface (Topp et al., 1980; Zegelin et al., 1989). The speed of the pulse is dependent on the dielectric constant of the medium that is in contact with and surrounding the transmission line. The dielectric constant is sensitive to water contained in the medium but not to the composition of the medium (e.g., water has a dielectric constant of about 80 while most earthen materials have values in the range of 2 to 3). Moisture content was measured in the Minoan tuff at 4 locations in the side wall of the stream bed upgradient from the excavation and at 14 locations under the excavation roof. Moisture content was also measured at two locations in excavated materials at the site. TDR measurements at additional locations were limited by the inability to insert the parallel transmission guides fully into the subsurface. Moisture content measurements were more variable for surface measurements in the Minoan tuff than for those at depth. Surface volumetric moisture content measurements in the Minoan tuff varied from 0 to about 7 percent. Moisture content was measured at depths of about 0.4 to 0.9 m to be about 4 to 7 percent. The moisture content of excavated Minoan ash (measured at two locations, within 1 hr of excavation) varied from 7 to 9 percent. The moisture content of samples of the Minoan tuff collected at the surface within the roofed area of the excavation was measured in the laboratory to be approximately 3 to 4 percent. The moisture content of Minoan samples collected from a depth of 0.5 m was measured in the laboratory to be 12 to 32 percent. The moisture content of the Cape Riva formation was not measured.

Matric potential was measured *in situ* using electrical resistance measurements of buried gypsum blocks. Matric potential measurement is predicated on the premise that moisture in the gypsum block (approximately 3 cm in diameter and 3 cm long) becomes equilibrated with moisture in the medium in which the gypsum block is buried. The matric potential is related to the measured electrical resistance through a calibration curve. Two gypsum blocks (Model 5201, Soilmoisture Equipment) were buried into the west wall of the stream bed approximately 20 m upgradient of the Akrotiri excavation. A third gypsum block was buried underneath the roofed area of the excavation about 3 m from the location where the permeameter tests on the Minoan tuff were conducted. At each location, a borehole was drilled to about 0.5 m depth with a hand auger, a gypsum block placed at the bottom of the hole, and the hole packed with cuttings from the drilling. One of the gypsum blocks installed in the side wall of the stream bed was subsequently removed and buried in the Minoan tuff under the roofed area near the location of the third gypsum block. A sufficient period of time was provided for the gypsum blocks to hydraulically equilibrate with the subsurface as indicated by the eventual stabilizing of the measured electrical resistance. The matric potential of the Minoan tuff in the stream bed wall was calculated to be

approximately 1.0 bar. The matric potential of the Minoan tuff underneath the excavation roof was calculated at the two locations to be 0.8 to 1.0 bar.

Saturated hydraulic conductivity was measured on both the Minoan and Cape Riva tuff formations using a Guelph permeameter (Model 2800K1, Soilmoisture Equipment). The Guelph permeameter is a field instrument that employs a Marriotte tube to establish a constant hydraulic head at the point of infiltration. Hydraulic heads of 5 and 10 cm of water were used in these measurements. *In situ* hydraulic conductivity was measured at two locations in the Cape Riva formation -- one location approximately 3 m northeast of the discovery location of the Delta 3 bronzes and the other in the floor of the basement within Delta 3. Hydraulic conductivity calculated from infiltration measured at the location 3 m from the site of the bronzes was 4.02×10^{-4} cm/s This value is consistent with measured hydraulic conductivities for fractured igneous rocks (Freeze and Cherry, 1979).

In situ saturated hydraulic conductivity measurements were made at two locations in the Minoan tuff. These measurements were made within the roofed area approximately 40 m southeast of the location of the Delta 3 bronzes. Saturated hydraulic conductivities calculated for these two sets of infiltration measurements were similar, 2.09×10^{-3} and 4.12×10^{-3} cm/sec. These values are consistent with the hydraulic conductivity of clean to silty sands (Freeze and Cherry, 1979).

Sorptivity and unsaturated hydraulic conductivity measurements of both tuff formations were made with a Guelph permeameter adapted to a tension infiltrometer (Adapter 2800K3, Soilmoisture Equipment). In general, the sorptivity measurements were made using measurements from the early periods of infiltration (from the start of infiltration up to about 4 to 5 min) using

$$S = \frac{I}{t^{1/2}} \tag{5-1}$$

where S is sorptivity (cm/s$^{0.5}$), I is cumulative water intake per unit area (cm^3/cm^2), and t is time (s). Saturated hydraulic measurements (Philip, 1969) were made using values for sorptivity and late time results when infiltration approached steady-state conditions (Warrick and Broadridge, 1992; White and Sully, 1987)

$$Q = K_{wet} + \frac{2.2S^2}{\pi\, r_o(\theta_{wet} - \theta_{dry})} \tag{5-2}$$

where Q is steady-state flux (cm^3/cm^2-s), K_{wet} is the hydraulic conductivity corresponding to the water supply potential, r_o is the radius of the disc infiltrometer, and θ_{wet} and θ_{dry} are the volumetric water contents at the supply potential and at initial conditions, respectively.

Measurements made at two locations in the Cape Riva formation were located approximately 1 m east of the discovery location of the Delta 3 bronzes. A thin (less than 1.5 cm) layer of Minoan ash (sieved to less than 4 mm) was placed between the porous membrane of the tension infiltrometer and the Cape Riva formation to ensure an adequate hydraulic connection. Although infiltration measurements were made at tensions that varied from 14 to 233 cm at each of the two locations, only one set of sorptivity measurements was made at each location. Sorptivity measurements were made at ten different locations in the Minoan tuff formation. All measurements were made on an excavated level area of otherwise undisturbed Minoan tuff in the southeast portion of the covered portion of the Akrotiri site.

These measurements were conducted on a surface made level to provide adequate contact between the porous membrane and the Minoan tuff.

Unsaturated hydraulic conductivity measurements were made at the locations where sorptivity measurements were made. Measurements for unsaturated hydraulic conductivity were made at tensions that varied from 14 to 233 mm. Although the maximum tension at which unsaturated hydraulic conductivity was measured was not relatively large, most groundwater flow occurs at relatively low tensions because hydraulic conductivity declines rapidly with an increase in tension. Additionally, the practical limit for measurement of unsaturated hydraulic conductivity using a tension infiltrometer is a tension not greater than 250 mm.

Sorptivity values calculated using Eq. (5-1) were used to calculate unsaturated hydraulic conductivity in Eq. (5-2). These values are illustrated for the appropriate suction pressure in Figure 5-4. Unsaturated hydraulic conductivity decreases as suction pressure increases, as illustrated by the straight lines regressed through each data set (Figure 5-4). Measured values for saturated hydraulic conductivity should exceed unsaturated hydraulic conductivity values; however, measured saturated hydraulic conductivity values for the Minoan tuff (2.09×10^{-3} and 4.12×10^{-3} cm/s) and for the Cape Riva formation (4.02×10^{-3} cm/s) are less than the measured unsaturated hydraulic conductivity values. The source for this discrepancy is not yet known and is currently under investigation.

5.2.3 Local Hydrologic Setting of Delta 3

The hydrology of the Delta 3 site and its local area (i.e., the drainage basin controlling flow toward Delta 3) is an important factor affecting transport of chemical components from the Delta 3 bronzes into the surrounding tuff. The Delta 3 room at Akrotiri is located on the west side of a central corridor, which in Minoan time was the path of a shallow covered water drainage system (Figure 5-1). Following the Minoan eruption, a small intermittent stream developed parallel to this same general course and partially eroded into the buildings of the site. Field observations and interpretations of photographs taken during the early stages of excavation indicate that the bronze artifacts extracted from Delta 3 were buried to the west of the stream and below it by a meter or more of volcanic deposits and building debris (composed primarily of volcanic materials). Water infiltration during intermittent flow of the stream may have played a role in corrosion of the bronzes and transport of dissolved corrosion products into the surrounding rock. The stream was dammed during early stages of excavation in the 1960's, and flow was permanently diverted around the archaeological site during the 1970 season (Marinatos, 1971). Upstream from the site the natural stream system has been obscured by agricultural use; below the site, the stream system has been obscured by road development. Similar conditions of cultural alteration may have existed for centuries. The drainage basin for the small stream extends to the north to near the crest of the caldera rim and to the east and west to low, gentle divides with adjacent stream valleys. The portion of the drainage basin above the Akrotiri archaeological site is approximately 0.5 km^2. The maximum elevation at the crest of the caldera is approximately 80 m above sea level, and Delta 3 is at 23 m. The distance from the crest to Delta 3 is 1 km. The average slope along this line is approximately 6 percent.

Stream flow occurs only during periods of heavy rainfall. Rainfall records obtained from the Hellenic National Meteorological Service for Santorini for the period 1974 to 1991 indicate 12 mo in which monthly rainfall exceeded 10 cm. The maximum monthly rainfall during this period occurred in January 1981, when 21.66 cm of rainfall was recorded. The maximum daily rainfall for this 18-yr period occurred in March 1982, when 11.45 cm of rainfall were recorded in 24 hr. Anecdotal evidence

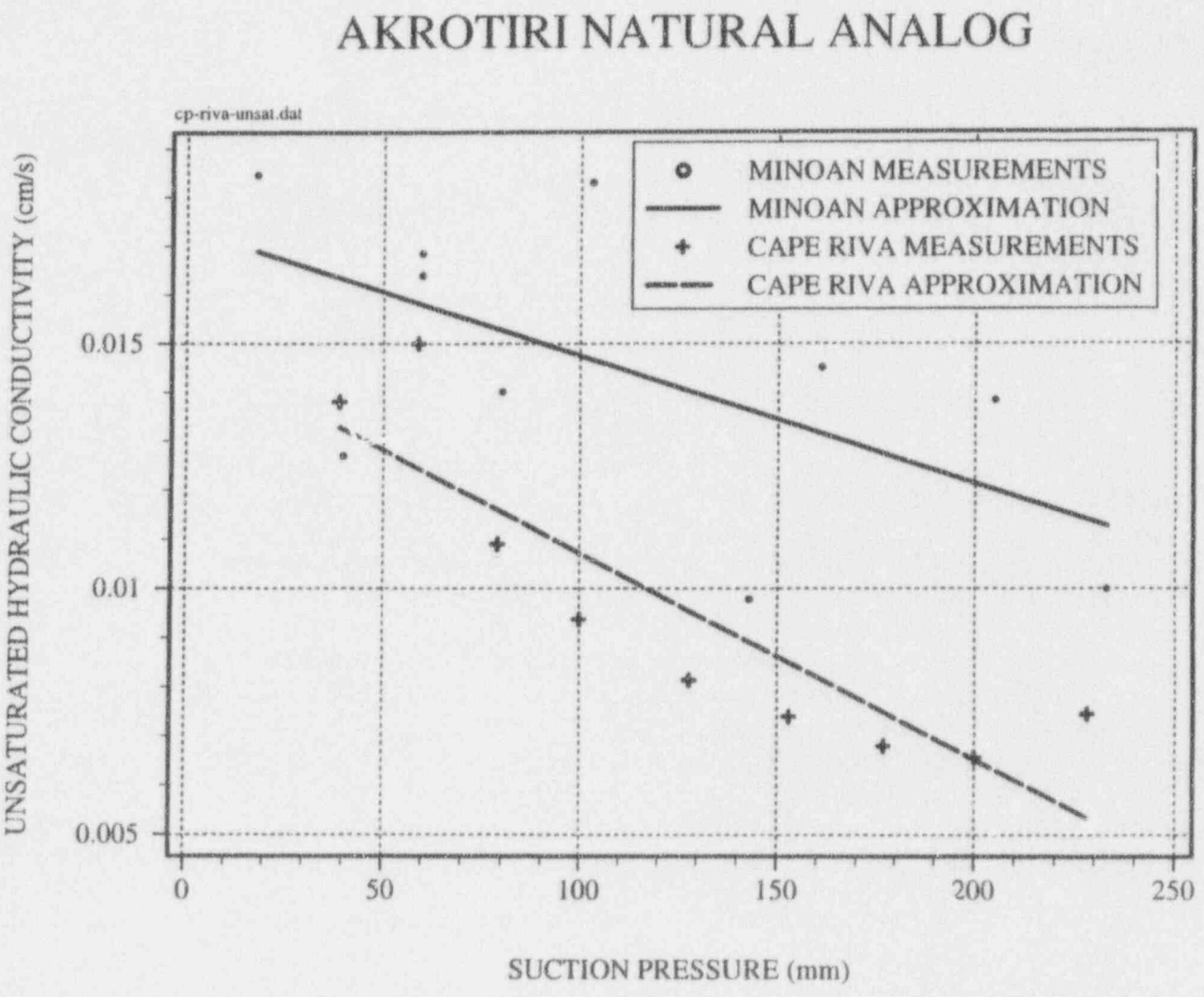

Figure 5-4. Unsaturated hydraulic conductivity measured in the Minoan tuff and the Cape Riva formation using a disc infiltrometer. Trend lines were determined by regression.

(discussions with local farmers) suggests that 12 occurrences of stream flow in 18 yr may be a reasonable approximation for this small drainage. Therefore, 10 cm of rainfall may represent a threshold for stream flow in the small drainage above the Akrotiri site. A rainfall of 10 cm over the 0.5 km^2 drainage basin above the site corresponds to a large volume, approximately 50,000 m^3, of water.

An estimate of rainfall runoff can be provided using established engineering techniques (U.S. Bureau of Reclamation, 1977). Runoff can be assumed ultimately to accumulate by overland flow in the stream channel of the Akrotiri drainage basin. The method involves estimating a value of either the initial abstraction (I) or the maximum potential infiltration (S). Initial abstraction is the amount of rain that falls and soaks into the soil prior to initiation of runoff. The maximum potential infiltration is the maximum potential difference between precipitation (P) and direct runoff (Q). These parameters are related empirically by

$$I = 0.2S \tag{5-3}$$

For any one storm, runoff is then given as a function of precipitation and maximum potential infiltration by an empirical approximation based on measurements in many watersheds

$$Q = \frac{(P - 0.2S)}{(P + 0.8S)} \tag{5-4}$$

where all variables have units of length, for example, centimeters of rainfall. This equation is calibrated for soil conditions antecedent to the storm for which values of I and S correspond to average conditions prior to maximum annual floods in the studied watersheds. From the preceding discussion of historical rainfall, 10 cm appears to be a reasonable estimate for I. This estimate leads to S=50 cm from Eq. (5-3), implying that the maximum infiltration capacity is almost never exceeded in the Akrotiri watershed because it is unlikely to rain 50 cm in any storm. Values of 10 and 50 cm for I and S, respectively, correspond to soils that have relatively low potential for runoff as described by the U.S. Bureau of Reclamation (1977). These values appear to be reasonable for the Akrotiri site because of the coarse-grained, unconsolidated, and porous materials of the Minoan deposits. Adopting these estimates, the maximum daily storm recorded in the 1974 to 1991 period, 11.45 cm, would lead to direct runoff, Q, of 0.04 cm from Eq. (5-4). Integrated over the 0.5 km^2 catchment area, total runoff is only 200 m^3, which would correspond to maximum potential stream discharge. For comparison, monthly rainfall in excess of 7.5 cm fell nearly 30 times in the 1974 to 1991 period. Assuming the critical value of precipitation prior to the onset of runoff is only 7.5 cm, from Eqs. (5-3) and (5-4), less than 0.4 cm of runoff would occur in response to a storm of 11.45 cm, or approximately 3 percent of the total rainfall.

This analysis indicates that almost all precipitation infiltrates directly; even in the heaviest rainstorms only a small fraction of precipitation results in runoff. Therefore, transport of elemental species from buried artifacts by infiltration and percolation of locally precipitated water may be a dominant mechanism, and transport due to infiltration resulting from stream flow may be considered negligible. In contrast, during rare periods of continuous stream flow, the area immediately beneath the stream may receive continuous infiltration. Therefore, in the area directly under the stream bed the maximum potential infiltration may be approached. The maximum potential infiltration can be estimated from Eq. (5-4) to be between 37.5 and 50 cm for values of I between 7.5 and 10 cm. Much infiltration during storms is subsequently released by evapotranspiration, so water fluxes at depth (e.g., past buried artifacts) would be generally less than infiltration values.

5.2.4 Alluvium at the Akrotiri Site

Field reports of the excavation of bronze artifacts from Delta 3 in 1970 describe artifacts being removed from among sediments, sand, and ash. The nature of these materials is significant for the study of elemental transport because of its impact on the hydrologic and transport properties of the medium and because of its relation to flow in the small stream adjacent to Delta 3. Although the nature of these materials will remain uncertain because they were removed during excavations in 1970, field observations suggest that the material included ash from the Phase II Minoan ash fall and "gravel lenses and epiclastic sediments ... related to floods between pyroclastic flows" of Phase IV of the Minoan eruption (Heiken and McCoy, 1984).

Sediments are well exposed in the walls of the Akrotiri excavation with a thickness that varies widely and over short distances up to at least 5 m. In room Delta 17, which is east and south of Delta 3, and Delta 8, which is directly south of Delta 3 (Figure 5-1), alluvial sediments up to tens of centimeters in thickness are interbedded with ash, mud, and building debris containing pot shards. It is likely that bronze artifacts in Delta 3 were buried in similar material. Deposition of this material was probably synchronous with Minoan volcanism rather than associated with subsequent fluvial activity in the small stream valley. This conclusion is supported by the occurrence of interbedded ash, the preservation of casts of wooden Minoan building materials in similar deposits in Building B, and the apparent continuity of sediments near Delta 3 with the thick epiclastic deposits in room Xeste and in the walls of the excavation.

5.2.5 Conclusions

Field mapping of the Delta 3 area and interpretation of photographs taken during the 1970 excavation have definitively established the spatial relationships of the bronze artifacts to local bedrock exposures and to the projected path of an historically present intermittent stream. These results allow informed sampling of host tuff profiles and interpretation of past hydrologic conditions. Samples have been collected of corrosion products from the Delta 3 artifacts. Mineralogic analyses of these corrosion products show them to be composed largely of cuprite (Cu_2O) and paratacamite [$Cu_2(OH)_3Cl$]. Chemical analyses show compositions dominated by Cu and Cl with minor Fe, Ti, and Ag. These analyses provide an indication of the composition of the original artifacts and the source from which elements have migrated from the artifacts into the tuff.

Field measurements of current hydraulic properties and interpretations of past hydrologic conditions have placed constraints on these factors. Field measurements were conducted of both the Minoan tuff through which infiltrating waters flowed to the anthropogenic horizon at Akrotiri and the underlying Cape Riva tuff, into which trace metals from the artifacts have been transported. Hydraulic conductivity of the unwelded Minoan ash was determined to be 2.09×10^{-3} to 4.12×10^{-3} cm/s, whereas the measured hydraulic conductivity of the welded Cape Riva tuff was 4.02×10^{-4} cm/s.

An intermittent stream is interpreted to have been significant to the infiltration of water into room Delta 3. Based on observations of local topography, the size of the drainage basin feeding the stream has been estimated at 0.5 km^2. Using historical meteorologic data, constraints have been placed on conditions likely to produce intermittent flow through the stream. Field observations of locally present alluvial deposits suggest that deposition of this material was probably synchronous with Minoan volcanism rather than associated with subsequent fluvial activity in the stream valley.

5.3 ASSESSMENT OF PROGRESS TOWARD MEETING PROJECT OBJECTIVES

Work at both the Akrotiri site and at the Nopal I analog is proceeding well towardsmeeting project plan expectations. Research results presented in this report and elsewhere (e.g., Pearcy et al., 1993c) have begun to provide a realistic understanding of the utility and limitations of natural analog studies when employed to support a license application for a HLW repository. Specifically, fundamental data have been gathered and interpreted on U mineral characteristics, stabilities, and alteration sequences in a geologic environment comparable to that anticipated for the proposed YM repository. This information is required for development and evaluation of reasonable PA models for radionuclide transport. For example, data being gathered within the Geochemical Natural Analog Research Project on the matrix hydraulic properties of silicic tuff are being used within the PA Research Project to support modeling efforts. Additionally, progress has been made in evaluation of the roles of fracture and matrix transport of U in a YM-like environment. This information has been used in the development of CDSs 3.2.3.3 (mineral assemblages), 3.2.3.5 (geochemical processes), and 5.4 (EBS).

Progress to date at Akrotiri includes definition of specific areas for analog study, completion of initial observations confirming similarities to YM, completion of preliminary analyses of source term compositions, and constraints on conceptual models of hydraulic infiltration (e.g., Murphy et al., 1991; Pearcy et al., 1993a; and data reported here). Specifically, samples collected in room Delta 3 may allow a closely constrained (in time and space) study of elemental transport under conditions comparable to those anticipated at YM.

The U.S. Department of Energy (DOE) has initiated analog research related to a YM repository. The DOE is studying water/rock interactions in hot springs in New Zealand in an attempt to validate the EQ3/6 computer code. In addition to these efforts, other DOE analog research is under consideration (e.g., Chapman et al., 1992). CNWRA work at Peña Blanca and at Akrotiri provides a strong base of experience from which to evaluate DOE analog studies. Results from CNWRA analog research allow informed comment on selection of sites, site characterization techniques, applications of the analog data, and use of the analog data for assessment of aspects of a YM repository.

5.4 PLANS FOR THE NEXT REPORT PERIOD

Field research anticipated during the next report period (January 1 to June 30, 1994) includes work at the Peña Blanca site. Field research at the Akrotiri site is anticipated for July or August 1994. Clearing, geologic mapping, gamma mapping, and sampling of additional areas of Level +00 of the Nopal I site at Peña Blanca are planned to be completed. This work will extend the Level +00 studies into an altered vitrophyre that has been juxtaposed by faulting with the high-grade uranium deposit. The vitrophyre is the only portion of the Nopal I deposit in which zeolite minerals have been reported to occur; zeolite minerals are likely to be important to radionuclide retardation at YM.

Laboratory research during the next reporting period is planned to include continued U content and rare earth content measurements on samples from Nopal I. Optical microscopy, scanning electron microscopy, energy dispersive x-ray analyses, and powder diffraction x-ray analyses are planned for both Nopal I samples and Akrotiri samples. Transmission electron microscopy studies of the composition and structure of Nopal I uraninite are planned to continue. Compositions of the Delta 3 bronze corrosion

products are planned to be quantified by inductively coupled plasma mass spectrometry. Laboratory measurement of the matrix hydraulic properties of the Nopal I tuff will continue.

Modeling and data interpretation activities planned during the next report period include calculations of fracture patterns (relative positions, interconnectedness, and orientations) and interpretations of those patterns relative to uranium transport at Nopal I. Interpretations will continue of the hydrologic data from the Akrotiri site to allow assessment of the effects of intermittent water infiltration over the 3,600 yr burial period. Specifically, boundary conditions and physical properties (based on field and laboratory measurements and observations reported here) will be developed, and it is anticipated that the PORFLO code will be used to develop initial flow models for Akrotiri.

5.5 REFERENCES

Chapman, N., P.L. Cloke, J.-C. Petit, J.A.T. Smellie and A.E.J. van Luik. 1992. *Applications of Natural Analogue Studies to Yucca Mountain as a Potential High Level Radioactive Waste Repository*. Las Vegas, NV: Office of Civilian Radioactive Waste Management: U.S. Department of Energy.

Freeze, R.A., and J.A. Cherry. 1979. *Groundwater*. Englewood Cliffs, NJ: Prentice-Hall, Inc.

Hammer, C.U., H.B. Clausen, W.L. Friedrich, and H. Tauber. 1987. The Minoan eruption of Santorini in Greece dated to 1645 BC? *Nature* 328: 517-519.

Heiken, G., and F. McCoy, Jr. 1984. Caldera development during the Minoan eruption, Thira, Cyclades, Greece. *Journal of Geophysical Research* 89: 8,441-8,462.

Leslie, B.W., E.C. Pearcy, and J.D. Prikryl. 1993. Geochemical natural analogs. *NRC High-Level Radioactive Waste Research at CNWRA January - June 1992*. NUREG/CR-5817. CNWRA 92-01S. Washington, DC: U.S. Nuclear Regulatory Commission.

Marinatos, S. 1971. *Excavations at Thera IV*. Athens, Greece: University of Athens.

Murphy, W.M., E.C. Pearcy, and P.C. Goodell. 1991. Possible analog research sites for the proposed high-level nuclear waste repository in hydrologically unsaturated tuff at Yucca Mountain, Nevada. *Fourth Natural Analogue Working Group Meeting and Poços de Caldas Project Final Workshop, Pitlochry, Scotland, 18-22 June 1990*. Final Report °EUR 13014 EN. B. Come and N.A. Chapman, eds. Brussels, Belgium: Commission of the European Communities: 267-276.

Pearcy, E.C., and B.W. Leslie. 1993. Geochemical natural analogs. *NRC High-Level Radioactive Waste Research at CNWRA January 1 through June 30, 1993*. W.C. Patrick, ed. CNWRA 93-01S. San Antonio, TX: Center for Nuclear Waste Regulatory Analyses: 7-1 to 7-20.

Pearcy, E.C., and W.M. Murphy. 1990. Geochemical natural analogs. *Report on Research Activities for Calendar Year 1990*. NUREG/CR-5817. CNWRA 90-01A. Washington, DC: U.S. Nuclear Regulatory Commission.

Pearcy, E.C., and W.M. Murphy. 1991a. Geochemical natural analogs. *Report on Research Activities for the Quarter April 1 through June 30, 1991*. W.C. Patrick, ed. CNWRA 91-02Q. San Antonio, TX: Center for Nuclear Waste Regulatory Analyses: 7-1 to 7-7.

Pearcy, E.C., and W.M. Murphy. 1991b. Geochemical natural analogs. *Report on Research Activities for the Quarter January 1 through March 31, 1991*. W.C. Patrick, ed. CNWRA 91-01Q. San Antonio, TX: Center for Nuclear Waste Regulatory Analyses: 7-1 to 7-7.

Pearcy, E.C., and W.M. Murphy. 1991c. Geochemical natural analogs. *Report on Research Activities for the Quarter July 1 through September 30, 1991*. W.C. Patrick, ed. CNWRA 91-03Q. San Antonio, TX: Center for Nuclear Waste Regulatory Analyses: 7-1 to 7-9.

Pearcy, E.C., and W.M. Murphy. 1991d. *Geochemical Natural Analogs Literature Review*. CNWRA 90-008. San Antonio, TX: Center for Nuclear Waste Regulatory Analyses.

Pearcy, E.C., B.W. Leslie, W.M. Murphy, and R.T. Green. 1993a. Geochemical natural analogs. *NRC High-Level Radioactive Waste Research at CNWRA July 1 through December 31, 1992*. W.C. Patrick, ed. CNWRA 92-02S. San Antonio, TX: Center for Nuclear Waste Regulatory Analyses: 7-1 to 7-27.

Pearcy, E.C., W.M. Murphy, R.T. Green, B.W. Leslie, and J.D. Prikryl. 1993b. Geochemical natural analogs. *NRC High-Level Radioactive Waste Research at CNWRA Calendar Year 1991*. NUREG/CR-5817. CNWRA 91-01A. Washington, DC: U.S. Nuclear Regulatory Commission.

Pearcy, E.C., J.D. Prikryl, W.M. Murphy, and B.W. Leslie. 1993c. *Uranium mineralogy of the Nopal I Natural Analog Site, Chihuahua, Mexico*. CNWRA 93-012. San Antonio, TX: Center for Nuclear Waste Regulatory Analyses.

Philip, J.R. 1969. Theory of infiltration. *Advances in Hydroscience* 5: 215–305.

Slater, E.A. 1980. Late bronze age Aegean metallurgy in the light of the Thera analyses. *Thera and the Aegean World*. C. Doumas, ed. London, England: Thera and the Aegean World, Inc.: 197–215.

Topp, G.C., J.L. Davis, and A.P. Annan. 1980. Electromagnetic determination of soil water content: Measurements in coaxial transmission lines. *Water Resources Research* 16: 574–582.

U.S. Bureau of Reclamation. 1977. *Design of Small Dams*. Washington, DC: U.S. Government Printing Office.

U.S. Environmental Protection Agency. 1989. *Environmental Radiation Protection Standards for Management and Disposal of Spent Nuclear Fuel, High-Level and Transuranic Radioactive Wastes*. Title 40, Protection of the Environment, Part 191, 40 CFR 191.13. Washington, DC: U.S. Government Printing Office.

U.S. Nuclear Regulatory Commission. 1987. *Disposal of High-Level Radioactive Wastes in Geologic Repositories*. Title 10, Energy, Part 60, 10 CFR 60.21(c)(1)(ii)(F). Washington, DC: U.S. Government Printing Office.

Warrick, A.W., and P. Broadridge. 1992. Sorptivity and macroscopic capillary length relationships. *Water Resources Research* 23(2): 427–431.

White, I., and M.J. Sully. 1987. Macroscopic and microscopic capillary length and time scales from field infiltration. *Water Resources Research* 23(8): 1,514–1,522.

Zegelin, S.J., I. White, and D.R. Jenkins. 1989. Improved field probes for soil water content and electrical conductivity measurement using time domain reflectometry. *Water Resources Research* 25: 2,367–2,376.

6 SORPTION MODELING FOR HLW PERFORMANCE ASSESSMENT

by Roberto T. Pabalan and David R. Turner

Investigators: Roberto T. Pabalan, David R. Turner, James D. Prikryl, F. Paul Bertetti Todd B. Dietrich, and Stephen Sassman (CNWRA)

NRC Project Officer: George F. Birchard

6.1 TECHNICAL OBJECTIVES

A fundamental concern in evaluating the suitability of Yucca Mountain, Nevada, as a repository for high-level nuclear waste (HLW) is the possibility of radionuclide migration from the repository to the accessible environment as dissolved constituents in groundwaters. An important mechanism for attenuating radionuclide migration is sorption of radionuclides on minerals encountered along the flow paths. Sorption is specifically referred to in 10 CFR 60.122(b) as a favorable geochemical condition that would tend to inhibit radionuclide migration and "favorably affect the ability of the geologic repository to isolate the waste." Conversely, geochemical processes that "would reduce sorption of radionuclides" are listed [10 CFR 60.122(c)(8)] as potentially adverse conditions that could reduce the effectiveness of the natural barrier system.

To support the U.S. Nuclear Regulatory Commission (NRC) HLW program, the Center for Nuclear Waste Regulatory Analyses (CNWRA) is conducting research activities under the Sorption Modeling for HLW Performance Assessment (PA) Research Project. The broad objective is to develop a sufficient understanding of radionuclide transport issues so that timely prelicensing guidance can be provided to the U.S. Department of Energy (DOE) and a sound basis be available for evaluating the DOE license application. The results will be used to support the NRC License Application Review Plan (LARP), particularly Sections 3.2.3.2, 3.2.3.3, and 3.2.3.5 pertaining to favorable and potentially adverse geochemical conditions and processes at a potential repository site, and Section 3.4, which addresses the effectiveness of natural barriers against the release of radioactive material to the environment. Laboratory and modeling studies of radionuclide sorption, retardation, and transport, which are central to the Sorption Research Project, will provide independent bases for addressing Key Technical Uncertainties (KTUs) identified during development of Compliance Determination Strategies (CDSs), which are an integral part of LARP. Specifically, the following KTUs will be addressed by this research project:

- Identity and magnitude of the effects of geochemical processes that reduce radionuclide retardation
- Parametric representation of retardation processes
- Capacity of alteration mineral assemblages to inhibit radionuclide migration
- Effect of degree of saturation on radionuclide sorption and transport

In addition, development of Compliance Determination Methods (CDMs) for evaluating compliance with the regulatory requirements will use data and models generated from this research project.

Results arising from this project will be integrated with those from other CNWRA activities. For example, data on uranium sorption will be used in interpreting data on uranium distribution and migration at the Peña Blanca field site of the Geochemical Natural Analog Research Project (Chapter 5), as well as in developing conceptual models for radionuclide transport/retardation in near- and far-field environments related to the PA Research Project (Chapter 7) and the Iterative Performance Assessment (IPA) Phase 3. Results of activities undertaken during the second half of 1993 are discussed in the sections that follow.

6.2 HYDROGEOCHEMICAL MODELING

6.2.1 Introduction

Traditional approaches have modeled radionuclide retardation using parametric models that rely on purely empirical parameters. One KTU in evaluating the suitability of Yucca Mountain as a site for a geologic HLW repository is the ability of such models to accurately represent geochemical processes that could contribute to radionuclide sorption and retardation. Surface complexation models (SCM) have been largely developed and refined as a mechanistic approach to investigating the pH-dependent sorption behavior of toxic species such as Zn^{2+}, Cd^{2+}, Pb^{2+}, and CrO_4^{2-} on simple (hydr)oxides such as goethite (α-FeOOH), rutile (TiO_2)and ferrihydrite [$Fe(OH)_3$], (Davis and Leckie, 1978; Rai et al., 1988; Dzombak and Morel, 1990). Similar studies have begun to be performed to study the sorption of key radionuclides (especially actinides) on a variety of minerals, including both simple (hydr)oxides and more complex minerals such as micas and clays (Riese, 1982; Tripathi, 1984; Kent et al., 1988; Kohler et al., 1992). To take full advantage of this research for PA, there is a need to apply SCMs to radionuclide sorption. Recent work (Pabalan and Turner, 1993) has focused on using a uniform approach to develop a set of consistent parameters for commonly used SCMs for different simple (hydr)oxides. With these parameters in place, it is possible to use SCMs to interpret existing data and to compare model performance in predicting radionuclide sorption on these different simple minerals as a function of changes in system chemistry. It may also be possible to use the SCM approach to examine radionuclide sorption on more complex rock-forming minerals such as zeolites, feldspar, and mica.

Three commonly used SCMs include the Diffuse Layer (DLM), Constant Capacitance (CCM), and Triple Layer (TLM) Models. The conceptual bases and assumptions for these models are discussed in detail elsewhere (Westall and Hohl, 1980; Davis and Kent, 1990; Pabalan and Turner, 1993). In brief, all SCMs employ equilibrium reactions involving protonation/deprotonation of amphoteric surface functional groups (XOH^0) to describe the acid-base behavior of a mineral surface.

$$XOH^0 + H^+ = XOH_2^+ \qquad (\text{Protonation}, K_+) \tag{6-1}$$

$$XOH^0 = XO^- + H^+ \qquad (\text{Deprotonation}, K_-) \tag{6-2}$$

where K_+ and K_- are referred to as intrinsic surface acidity constants. Sorption is represented by postulating the formation complexes at the mineral/water interface between these sites and the cations and

anions in solution. Surface reactions are assumed to be analogous to aqueous speciation reactions. This requires an additional assumption regarding the stoichiometry of the surface reactions(s). A typical surface reaction (for the sorbing cation C^{z+} in this case) takes the general form

$$XOH^0 + C^{z+} = XO\text{-}C^{(z-1)} + H^+ \quad (\text{Complexation}, K_C) \tag{6-3}$$

where $XO-C^{(z-1)}$ represents the surface complex with a total charge of z-1.

The electrostatic attraction and repulsion of these sites for charged species in solution form the basis for surface complexation models. For surface species, activity expressions are corrected for electrostatic effects by assuming an exponential Boltzmann relationship. The total number of available surface sites in mineral-H_2O systems (sites/L) is calculated based on the product of specific surface area (A_{SP} in m^2/g), site density (N_S in sites/nm^2), and solid concentration (c_S in g/L) in the liquid. In a given system, mass action, mass balance, and model-specific charge/potential constraints can be used in a manner analogous to that employed by geochemical aqueous speciation programs (Westall and Hohl, 1980; Allison et al., 1991) to determine distribution of the element of interest between the dissolved and sorbed phases.

The DLM and CCM both assume that protonation/deprotonation and adsorption occur in one plane at the surface/solution interface, and that only those ions specifically adsorbed in this "o-plane" contribute to the total surface charge. In the DLM, the Stern-Grahame extension of the Gouy-Chapman relationship for symmetrical electrolytes is used to describe the interdependence between electrolyte concentration (ionic strength), charge, and electrostatic potential. In contrast to the DLM, the CCM assumes that the charged surface is separated from the bulk solution by a layer of constant capacitance; surface charge is related to surface potential through a simple linear equation. In its formulation, the CCM does not explicitly consider ionic strength effects. Therefore, in a strict sense, CCM acidity constants are only valid at one ionic strength; new values are necessary if conditions change. More elaborate than the DLM and CCM, the TLM divides the mineral/water interface into three layers. In its original construction (see Davis and Kent, 1990), protonation/deprotonation of surface sites (K_+ and K_-) is restricted to the innermost o-plane, and specifically adsorbed ions are assigned to the β-plane (i.e., outer-sphere complexes). Subsequent modifications provide for inner-sphere complexes to describe strongly bound metals. The outermost layer, the d-plane, is made up of a diffuse region of counterions extending into the bulk solution. Like the DLM, the TLM uses the Gouy-Chapman relationship and is applicable at different ionic strengths. The TLM also handles ionic strength effects through provisions for background electrolyte adsorption.

Although the SCM approach is not an explicit mechanistic model of processes at the mineral surface at the atomistic level, it incorporates aspects of thermodynamic principles to describe the mineral/water interface. As such, the difference SCM use a set of parameters that describe an idealized, but physically reasonable model of the electrostatic and acid-base behavior of a given mineral. While there is still uncertainty in the complexes formed at the surface, current research is under way using spectroscopic techniques to determine surface species (e.g., Manceau and Charlet, 1991) and provide some independent support of modeling efforts. In spite of these limitations, theoretically based SCMs represent a critical step toward more mechanistic models and are able to predict for the effects of changes in the solution and surface chemistry in a quantitative way that most purely empirical methods such as a linear K_d model cannot.

The major drawback of the models is the complexity inherent in their construction, which limits practical applications in PA. This complexity is reflected in the number of parameters used in each model. The DLM is the simplest model, requiring only four types of adjustable parameters: protonation (K_+); deprotonation (K_-); binding constants (such as $K_{UO_2^{2+}}$); and site density (N_S). The CCM shares these four parameters plus a capacitance term (C_1) for charge/potential relationships. As the most elaborate model, the TLM requires eight types of adjustable parameters: the four used by the DLM, and binding constants for sorbing background electrolytes (K_{Cation} and K_{Anion} such as $K_{Na}+$, $K_{NO3}-$); and capacitances for the inner and outer layers (C_1 and C_2, respectively).

Parameter values are imperfectly known and, in practice, have been used as multiple fitting parameters specific to a particular data set. Because of fundamental differences in how the models treat the mineral/water interface and the tendency to use model-specific parameters, it is difficult to directly compare the results of different studies (Westall and Hohl, 1980). One recently advocated approach is the characterization of the mineral surface using "standard" values for parameters such as acidity constants, site density, and capacitances that are uniformly applied in all contaminant systems (Davis and Kent, 1990; Dzombak and Morel, 1990; Hayes et al., 1990). While this approach may not represent the exact processes operating at the mineral/water interface, once the mineral surface is characterized, the number of adjustable parameters is limited to the binding constant(s) for the assumed surface complexes. This serves to establish a baseline for future comparison of modeling results and also provides for future development of a consistent sorption database for PA.

Using this uniform approach to interpret available potentiometric titration data and the nonlinear least squares parameter optimization program FITEQL, Version 2.0 (Westall, 1982), Pabalan and Turner (1993) established a set of consistent parameters for the DLMs, CCMs, and TLMs for nine different (hydr)oxides. The following discussion uses these parameters to examine actinide sorption on different types of surfaces. All sorption modeling results were calculated using MINTEQA2, Version 3.11 (Allison et al., 1991) and the radionuclide database developed at the CNWRA (Turner et al., 1993; Turner, 1993). The reader is referred to these studies and the references therein for more details on the methods employed and thermodynamic data sources.

6.2.2 Modeling Radionuclide Sorption on Simple (Hydr)oxides—Effects of Surface-Area/Solution Volume Ratio

To examine sorption as a function of mineral surface area, recent studies at the CNWRA have focused on uranium(6+) [also UO_2^{2+} or uranium(6+)] sorption on α-alumina (α-Al_2O_3). Efforts were undertaken to investigate the ability of surface complexation models to predict the observed changes in sorption using the model parameters developed previously (Pabalan and Turner, 1993). Because it is the simplest SCM, attention was focused on the DLM.

In addition to data on the mineral properties and the acidity constants to describe acid-base behavior of the surface, FITEQL requires the input of a chemical equilibrium model for the system under investigation. For readily hydrolyzable elements such as UO_2^{2+}, the chemical system quickly becomes complicated with the inclusion of equilibrium constants for the formation of aqueous uranyl-hydroxy-carbonato species. For this reason, the resultant binding constants are dependent on the quality and extent of the thermodynamic data available for the system of interest. Implicit in this statement is that binding constants derived using FITEQL are valid only for the thermodynamic data used in constructing the chemical equilibrium model. For uranium, the equilibrium constants used in the chemical equilibrium

models submitted to FITEQL were selected from the internally consistent NEA Thermodynamic Database (Grenthe et al., 1992). All data were corrected for ionic strength effects using the Davies equation. If the same data sources are used, the binding constants can be applied in sorption/speciation codes such as MINTEQA2 (Allison et al., 1991) to model uranium sorption once corrected to a reference state of I=0 M. To maintain simple models as much as possible, a single monodentate uranium surface species was assumed.

The input parameters used in setting up the FITEQL run to interpret the alumina sorption data are given in Table [illegible] The data sets for each of the three surface-area/solution-volume ratios considered were interpreted [illegible] FITEQL, and the resulting binding constants were combined, based on the standard deviation [illegible] ed by FITEQL (see Dzombak and Morel, 1990 for details), to yield a weighted best estimate. Based on the statistical measure of goodness-of-fit provided by FITEQL (see Westall, 1982 for details), assuming the formation of the surface species $XO\text{-}(UO_2)_2CO_3(OH)_3^0$ was able to reproduce the observed sorption behavior quite well (Figure 6-1). Not surprisingly, the binding constants determined for each individual data set (solid lines) provide the best fit to the observed data. However, the binding constants for the different data set [illegible] differ appreciably (Table 6-1), and the weighted value (dashed lines) also provides a reasonable f [illegible] data. The fact that the binding constants are similar for all three data sets suggests that fitting only one data set would predict the sorption behavior of the other two data sets well. For example, the binding constant determined for the 2.09 m^2/g data set (Log K=12.64) is quite close to the weighted value (Log K=12.73) and results in a fit similar to that shown by the dashed line in Figure 6-1. For the highest surface-area/solution-volume ratio, the model predicts a steep sorption edge that diverges from the observed values at pH less than about 5. This suggests that noncarbonate uranyl species such as UO_2^{2+} or UO_2OH^+ may be necessary to fine-tune the model at lower pH and produce the best fit to the data. For PA, the benefits of achieving improved accuracy in this fashion should be weighed against the [illegible] nal computational time required by the added level of complexity.

6.2.3 Modeling Radionuclide Sorption on Complex Rock-Forming Minerals

Radionuclide sorption data are available for a number of common rock-forming minerals such as clays, micas, and zeolites, which, because of their abundance, may contribute significantly to sorption processes at Yucca Mountain. Typically, these minerals have a fixed-charge component due to Al^{3+} substitution for tetrahedral Si^{4+}, but many also exhibit a pH-dependent variable surface charge similar to simple (hydr)oxides (Kent et al., 1988; Siegel et al., 1992). In contrast to simple (hydr)oxides, only rarely are potentiometric titration data available for these minerals (e.g., Riese, 1982). However, because these minerals are more complex, the development of a pH-dependent surface charge may be due to more than one type of site.

Recent studies have proposed modeling radionuclide sorption on complex rock-forming minerals assuming a heterogeneous surface composed of different site types with acid-base behavior controlled independently of one another (Brady and Walther, 1992). For example, using a TLM, Rai et al. (1988) modeled chromate (CrO_4^{2-}) adsorption on kaolinite assuming a heterogeneous surface composed of stoichiometric proportions of silanol ($SiOH^0$) and aluminol ($AlOH^0$) sites. Similar approaches have been proposed to model radionuclide sorption on kaolinite, including uranium (Kohler et al., 1992), thorium, and radium (Riese, 1982).

The uranium(6+)-kaolinite sorption data of Payne et al. (1992) and neptunium(5+)-biotite sorption data of Nakayama and Sakamoto (1991) were investigated using this approach. Surface areas for

Table 6-1. DLM binding constants (Log K) for forming the indicated surface complex, determined using FITEQL, Version 2.0 (Westall, 1982) and sorption data for the uranium(6+)-α-alumina system. Acidity constants are from Pabalan and Turner (1993). N_S=2.31 sites/nm^2; Reported A_{SP} (m^2/g) are: RM 8005=2.09; RM 8006=0.229; RM 8007=0.0686. Uranium(6+)$_T$=95 ppb (4.4×10^{-7} M). Values corrected to I=0 M using Davies equation.

Uranium(6+)-α-alumina$_{(a)}$	
Surface Complex	**DLM: Log $K_{(b)}$**
$AlOH_2^+$	8.33±0.15
AlO^-	−9.73±0.12
$AlO\text{-}(UO_2)_2CO_3(OH)_3^0$ - [RM 8005]	12.64±0.01
$AlO\text{-}(UO_2)_2CO_3(OH)_3^0$ - [RM 8006]	12.70±0.01
$AlO\text{-}(UO_2)_2CO_3(OH)_3^0$ - [RM 8007]	12.91±0.01
$AlO\text{-}(UO_2)_2CO_3(OH)_3^0$ - Weighted	12.73±0.19

(a)Data for the chemical equilibrium model are from NEA Thermodynamic Database for Uranium (Grenthe et al., 1992).

(b)Reported uncertainties represent 95-percent confidence limit for acidity constants and weighted binding constant. For best-fit surface complexes, listed uncertainty represents standard deviation (±1σ) reported by FITEQL.

these minerals were taken from Allard et al. (1983). End-member stoichiometries were assumed for kaolinite ($Al_2Si_2O_5$) and biotite [$K(Mg,Fe)_3AlSi_3O_{10}(OH)_2$]. The total number of sites was calculated based on the assigned surface area, solid concentration in suspension, and a site density of 2.31 sites/nm^2 as recommended by Davis and Kent (1990). These sites were divided between $AlOH^0$ and $SiOH^0$ based on the stoichiometric proportions for kaolinite and biotite ($AlOH^0$:$SiOH^0$ = 1:1 and 1:3, respectively). The acid-base behavior of each site type was assumed to be independent of the other site type, and sites were modeled using the acidity constants determined for SiO_2 and α-alumina in earlier studies (Pabalan and Turner, 1993). The thermodynamic data for uranium are from the NEA database (Grenthe et al., 1992), and neptunium data are from the latest release of the EQ3/6 database (Release Data0.com.r16; Lemire, 1984). With these data as input into the chemical equilibrium model, and the sorption data from the two studies, FITEQL, Version 2.0 (Westall, 1982) was used to determine binding constants for the different surface complexation models. For the diffuse-layer model, the estimated binding constants are listed in Table 6-2, and the results are shown in Figure 6-2.

Contaminant speciation (especially for actinides) can vary rapidly as a function of pH (Turner, 1993). For this reason, sorption edges that extend over wider pH ranges, such as those exhibited by the uranium(6+)-kaolinite and neptunium(5+)-biotite data, tend to require more than one surface complex (Davis and Leckie, 1978; Dzombak and Morel, 1990). The approach taken here is greatly simplified

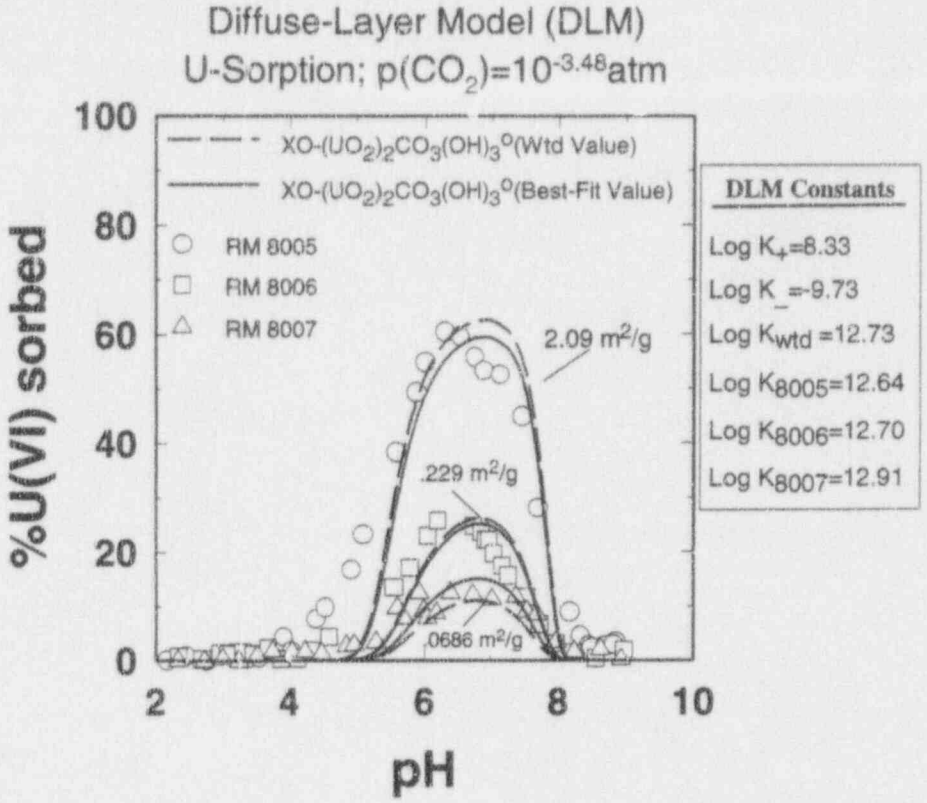

Figure 6-1. DLM modeling results for uranium(6+)-α-alumina sorption (under atmospheric CO_2) assuming the formation of a single surface complex, XOH_2-$(UO_2)_2CO_3(OH)_3$. Model parameters and binding constants are given in Table 6-1.

compared to the heterogeneous binding sites likely to be found at the surface. For both sheet silicates, sorption behavior is likely to be due to a combination of ion exchange at intracrystalline sites and surface complexation along edge sites. For biotite, other site types (e.g., Fe, Mg) probably also contribute to pH-dependent surface charge. Nevertheless, the relatively simple DLM is able to reproduce the observed behavior quite well (Figure 6-2). However, as discussed earlier, the added complexity of multiple surface species tends to make the practical application of SCMs more difficult in PA.

In addition to α-alumina, experiments at the CNWRA have focused on sorption behavior in the uranium(6+)-H_2O-CO_2-clinoptilolite system. The data exhibit the same type of sorption behavior as that shown by α-alumina, with a steep sorption edge over a fairly narrow pH range from 4 to 6 with a maximum at about 6.5 and a sharp desorption edge at more basic pH values. A similar approach to that taken for the uranium(6+)-kaolinite and neptunium(5+)-biotite sorption data discussed previously was taken for clinoptilolite. The nominal formula for Na-clinoptilolite is ($Na_2Al_2Si_{10}O_{24} \cdot 8H_2O$), yielding a Si:Al ratio of 5:1. The clinoptilolite used in the CNWRA experiments is slightly enriched in silica relative to the idealized form ($Na_{1.807}K_{0.123}Ca_{0.0031}Mg_{0.0349}$)($Al_{1.948}Fe^{3+}_{0.044}$)($Si_{10.044}Ti_{0.0044}$)$O_{24} \cdot 7.43H_2O$, and yields a Si:Al ratio of 5.15:1 (Pabalan et al., 1993). This ratio was used in SCM modeling studies of the sorption data. Because surface area measurements are not yet available for this clinoptilolite a BET surface area of 16 m^2/g was assumed (Los Alamos National Laboratory, 1993). Site density was fixed at 2.31 sites/nm^2 (Dzombak and Morel, 1990; Davis and Kent, 1990), and as, with kaolinite, the acidity constants for SiO_2 and α-alumina were used with thermodynamic data from the NEA uranium

Table 6-2. DLM binding constants (Log K) for forming the indicated surface complexes, determined using FITEQL, Version 2.0 (Westall, 1982) and sorption data for the uraninum(6+)-kaolinite (Payne et al., 1992) and neptunium(5+)-biotite (Nakayama and Sakamoto, 1991) systems. Stoichiometric proportions of $SiOH^0$ and $AlOH^0$ of 1:1 and 3:1 are assumed for kaolinite and biotite, respectively. Acidity constants are from Pabalan and Turner (1993). N_S=2.31 sites/nm^2; A_{SP}=11 m^2/g and 8 m^2/g for kaolinite and biotite, respectively (Allard et al., 1983). Uranium(6+)$_T$=10^{-6} M; Neptunium(5+)$_T$=6×10^{-6} M. Values corrected to I=0 M using Davies equation.

Uranium(6+)-kaolinite (Payne et al., 1992)[a]		Neptunium(5+)-biotite (Nakayama and Sakamoto, 1991)[a]	
Surface Complex	**DLM: Log $K_{(b)}$**	**Surface Complex**	**DLM: Log $K_{(b)}$**
$SiOH_2^+$	n.a.	$SiOH_2^+$	n.a.
$AlOH_2^+$	8.33±0.15	$AlOH_2^+$	8.33±0.15
SiO^-	−7.20±0.05	SiO^-	−7.20±0.05
AlO^-	−9.73±0.12	AlO^-	−9.73±0.12
$SiO\text{-}UO_2^+$	0.96±0.04	$SiOH\text{-}NpO_2^+$	2.86±0.06
$AlO\text{-}UO_2^+$	2.18±0.10	$AlOH\text{-}NpO_2^+$	4.15±0.03
$SiOH\text{-}UO_2^{2+}$	5.73±0.16	$SiO\text{-}NpO_2OH^-$	−11.58±0.02
$AlOH\text{-}UO_2^{2+}$	9.20±0.03	$AlO\text{-}NpO_2OH^-$	−12.39±0.17
$SiO\text{-}UO_2OH^0$	−5.84±0.44	---	---
$AlO\text{-}UO_2OH^0$	−4.74±0.59	---	---

n.a. — $pH_{ZPC} \approx 2.8$ for SiO_2; $SiOH_2^+$ not considered in this pH range.

[a]Data for the chemical equilibrium model are from NEA Thermodynamic Database for Uranium (Grenthe et al., 1992); neptunium data are from the EQ3/6 database (Release Data0.com.r16; Lemire, 1984).

[b]Reported uncertainties represent 95-percent confidence limit for acidity constants. For surface complexes, listed uncertainty represents standard deviation ($\pm1\sigma$) reported by FITEQL.

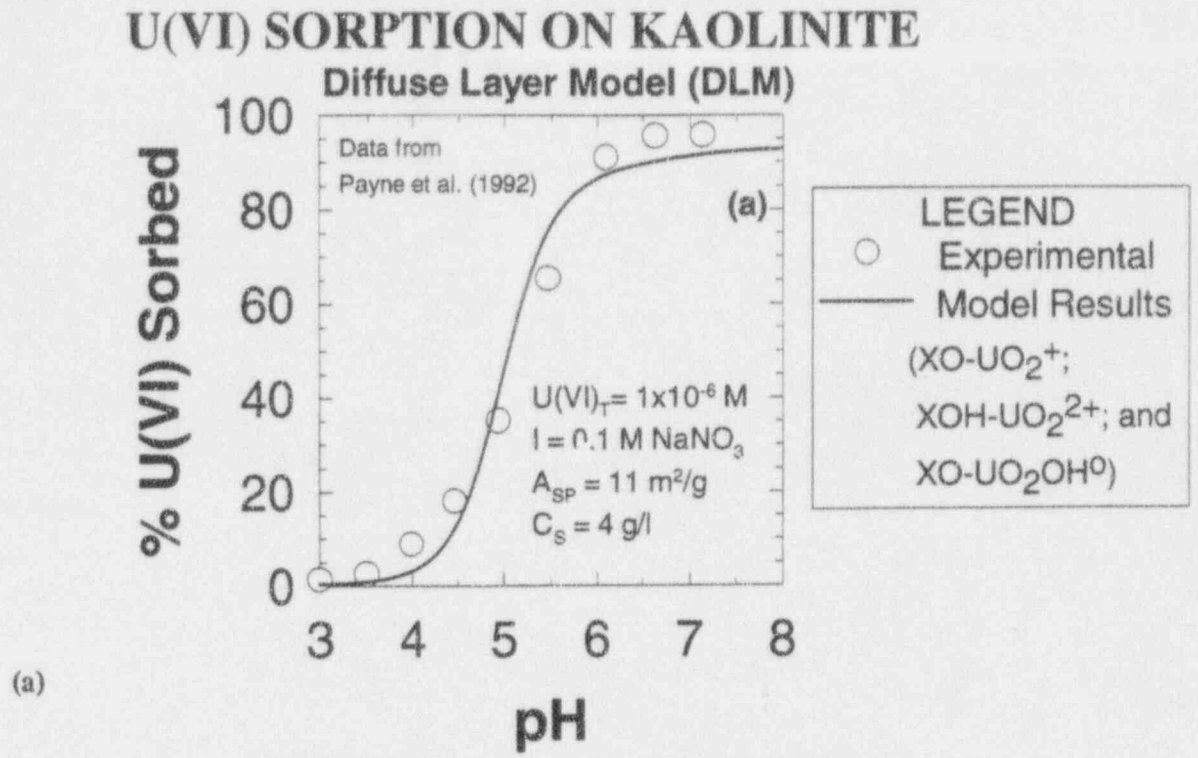

(a)

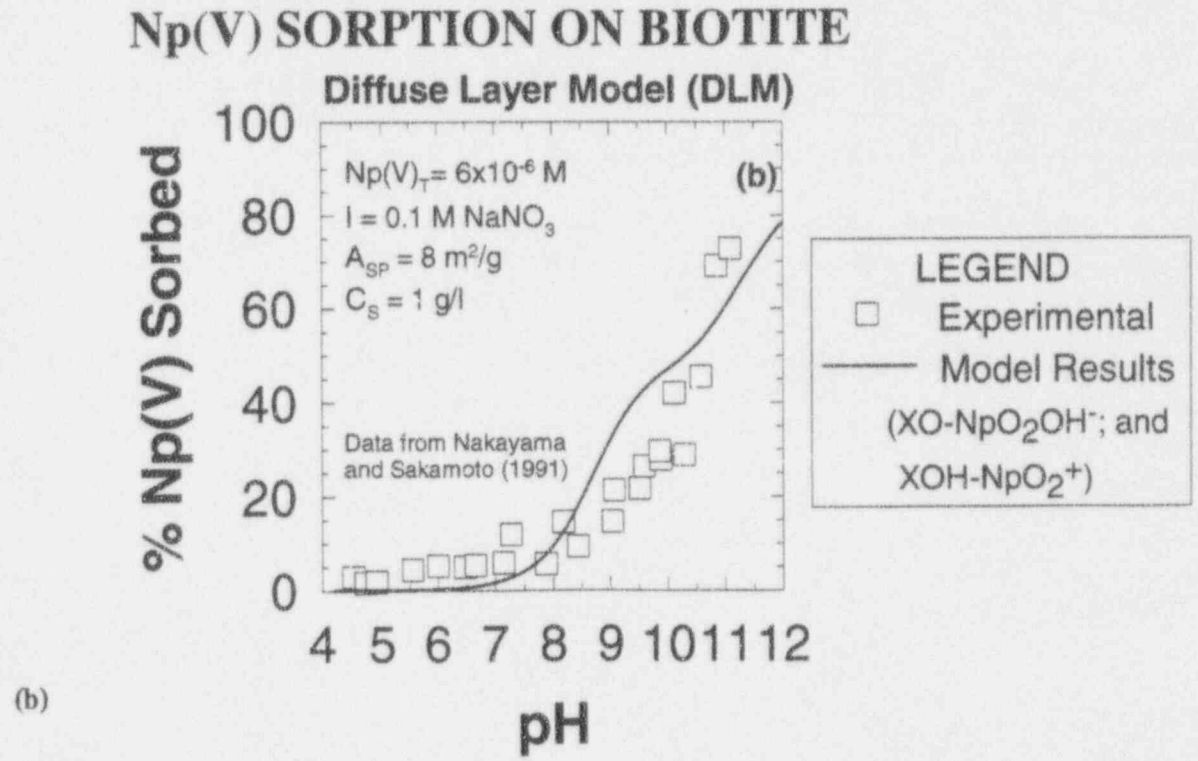

(b)

Figure 6-2. DLM modeling results for: (a) uranium(6+)-kaolinite sorption (Payne et al., 1992); (b) neptunium(5+)-biotite sorption (Nakayama and Sakamoto, 1991). Model parameters and binding constants are given in Table 6-2.

database (Grenthe et al., 1992) to construct the chemical equilibrium model for FITEQL. Based on the interpretation of the 50-ppb sorption data, values for the estimated binding constants are given in Table 6-3; these values are typically within 0.1 log units of values determined by fitting the 500-ppb data. Modeling results calculated using the values in Table 6-3 are shown in Figure 6-3.

Given the constraints on the conceptual approach used, the DLM is able to reproduce the sorption and desorption edges for the 5-, 50- and 500-ppb data. For the 5-, and 50-ppb data, the model results for $SiOH\text{-}UO_2CO_3^0$ and $AlOH\text{-}UO_2^{2+}$ fall slightly short of the sorption maximum. For the 500-ppb data, the surface complexes $SiO\text{-}UO_2^+$ and $AlO\text{-}UO_2^+$ predict the maximum fairly well, though the predicted maximum is shifted to a slightly lower pH. These modeling results suggest the formation of different surface species at the silanol and aluminol sites. This assumption is reasonable given the large differences in pH_{ZPC} between SiO_2 and α-alumina (2.8 and 8.9, respectively). Modeling also suggests that different surface species form at the different uranium concentrations. This suggestion is also reasonable given the significant changes in speciation predicted with changes in total uranium(6+) concentration (Turner, 1993).

As in most cases, it is possible to improve the fit to sorption data by postulating additional surface species. It is also possible that sorption involving fixed-charge ion exchangers like clays and zeolite is more complicated than the surface processes assumed in surface complexation models. It is important to remember, however, that the added benefits of improving accuracy in this fashion must be weighed against the additional computational burden imposed by the added complexity.

6.2.4 Summary and Conclusions

Experimental sorption data indicate that radionuclide (especially actinide) sorption is a complex function of the physical and chemical conditions of the system under consideration. Current PA approaches, however, tend to rely on purely empirical methods to model radionuclide sorption. Because these models do not explicitly account for changes in system chemistry, extrapolation of laboratory data beyond experimental conditions is uncertain. The purpose of this study is to move toward a uniform mechanistic model for radionuclide sorption that allows for the prediction of complex sorption behavior and quantitatively accounts for changes in the physical and chemical conditions.

SCMs are one type of mechanistic approach to modeling sorption processes. These models use similar approaches to correct for electrostatic effects at the charged mineral/water interface, but differ in how the interface is conceptualized. The complexity of these models also varies with the types of adjustable parameters, ranging from four for the DLM to eight for the TLM. Traditional applications rely on adjusting different parameters to match a given data set. Because of the number of parameters, this method is likely to result in a nonunique fit and makes comparisons between models and between studies difficult.

A first attempt has been made to develop and apply a standard set of SCM parameters to radionuclide sorption (Pabalan and Turner, 1993). Using available potentiometric titration data, model-specific values for K_+, K_-, K_{Cation}, and K_{Anion} were developed for the CCMs, DLMs, and TLMs using a uniform approach (Dzombak and Morel, 1990; Hayes et al., 1990). In this way, only a single type of adjustable parameter, the binding constant, remains to model radionuclide sorption data. Since the user can still specify the types of complexes forming at the mineral surface, there is still flexibility in this modeling approach.

Table 6-3. DLM binding constants (Log K) for forming the indicated surface complexes, determined using FITEQL, Version 2.0 (Westall, 1982) and 50-ppb sorption data for the uranium(6+)-clinoptilolite system. Stoichiometric proportions of $SiOH^0$ and $AlOH^0$ (5.15:1) are assumed for clinoptilolite. Acidity constants are from Pabalan and Turner (1993). N_S=2.31 sites/nm^2; A_{SP}=16 m^2/g (Los Alamos National Laboratory, 1993). Values corrected to I=0 M using Davies equation.

Uranium(6+)-clinoptilolite[a]	
Surface Complex	**DLM: Log $K_{(b)}$**
$SiOH_2^+$	n.a.
$AlOH_2^+$	8.33±0.15
SiO^-	−7.20±0.05
AlO^-	−9.73±0.12
$SiOH\text{-}UO_2^{2+}$	5.89±0.01
$AlOH\text{-}UO_2^{2+}$	9.24±0.01
$SiO\text{-}UO_2^+$	0.19±0.01
$AlO\text{-}UO_2^+$	2.69±0.01
$SiO\text{-}UO_2OH^0$	−6.30±0.01
$AlO\text{-}UO_2OH^0$	−4.26±0.01
$SiOH\text{-}UO_2CO_3^0$	15.58±0.01
$AlOH\text{-}UO_2CO_3^0$	19.25±0.01

n.a. — $pH_{ZPC} \approx 2.8$ for SiO_2; $SiOH_2^+$ not considered in this pH range.

(a)Data for the chemical equilibrium model are from NEA Thermodynamic Database for Uranium (Grenthe et al., 1992).

(b)Reported uncertainties represent 95-percent confidence limit for acidity constants. For surface complexes, listed uncertainty represents standard deviation ($\pm 1\sigma$) reported by FITEQL.

These parameters were used in conjunction with the FITEQL code to model other available sorption data. In the case of α-alumina, the DLM and a relatively simple conceptual model invoking a single-surface complex was able to model the effects of variable surface-area/solution-volume ratio reasonably well. In addition to simple (hydr)oxides, it is also possible to apply these models to more complex rock-forming minerals. Assumption of stoichiometric proportions of different site types enabled the DLM to be used to model relatively complex sorption behavior for several different types of complex multioxides including clay, mica, and zeolite, all minerals that are present at Yucca Mountain.

From this study, it is apparent that the application of SCMs to radionuclide sorption behavior proceeds through a logical progression of steps from mineral properties to acidity constants to

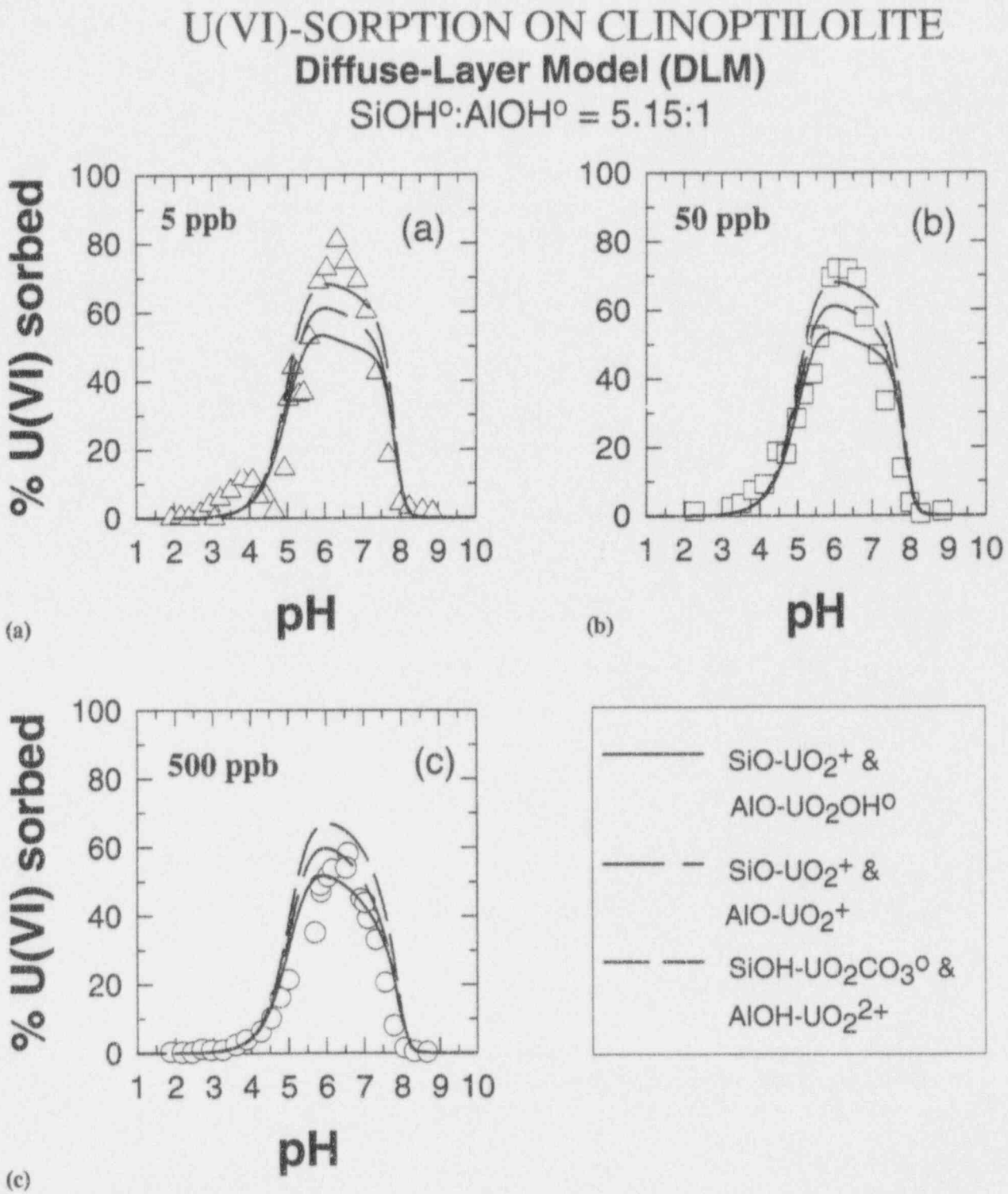

Figure 6-3. DLM modeling results for uranium(6+)-clinoptilolite sorption (under atmospheric CO_2) for: total uranium = (a) 5 ppb; (b) 50 ppb; (c) 500 ppb. Model parameters and binding constants are given in Table 6-3.

radionuclide binding constants. For this reason, any radionuclide binding constants are dependent on the acidity constants used in the FITEQL optimization run; if these acidity constants are modified by the incorporation of new potentiometric titration data or changes in parameter values assumed while interpreting the present data, all radionuclide binding constants must be re-evaluated. In addition, the tabulated binding constants are dependent on the thermodynamic data available. Any significant changes in the data likewise require a recalculation of the necessary parameters.

From the point of view of describing the mineral/water interface, it must be emphasized that the results given here are dependent on the assumptions used in constructing the conceptual model, particularly in selecting the complexes formed at the surface. In some cases, especially for single-layer models such as the CCM and DLM, the model is unable to distinguish between like-charged surface complexes; independent lines of evidence such as proton release data or spectroscopic information are necessary to identify likely choices. Although some spectroscopic data such as EXAFS are available for actinides, due to analytical limitations they typically exist for fairly concentrated solutions (millimolar) at single pH values. Additional EXAFS work will be required to ascertain the extent to which SCMs best represent the mineral/water interface.

For the purposes of PA, a principle of parsimony was adopted where possible in defining possible surface complexes. Within this framework, the DLM was able to reproduce the general aspects of actinide sorption behavior while using a far simpler representation of the mineral/water interface than the TLM. This method may be preferred where simpler models are desirable to strike a balance between accuracy of the conceptual model and the computational resources required by geochemistry in PA calculations. Despite these limitations, the SCM approach is able to quantitatively incorporate the effects of changes in solution and surface chemistry to an extent that is well beyond the capabilities of a purely empirical method such as the linear kd model. As additional data become available for characterizing mineral surfaces, the SCMs represent a crucial step toward a mechanistic model of sorption at the mineral/water interface.

6.3 SORPTION EXPERIMENTS

To develop an understanding of radionuclide sorption processes and the important physical and chemical parameters that affect sorption behavior in the Yucca Mountain environment, experiments are being conducted to investigate the sorption behavior of uranium on geologic media. During the second half of 1993, experiments were completed to determine the possible effects of pH, uranium concentration, and ionic strength on the sorption of uranium(6+) on clinoptilolite, which is the predominant zeolite mineral occurring underneath Yucca Mountain. In addition, because surface adsorption is the predominant mechanism for uranium sorption, even for zeolites like clinoptilolite (Pabalan et al., 1993), and because the ratio of fluid-volume to mineral-surface-area can vary significantly along a fluid flow-path, experiments were also conducted to determine the effect of solid-surface-area to solution-volume ratio on uranium(6+) sorption. The latter experiments, which used α-alumina as the sorbent phase, also provided information on possible differences in uranium sorption behavior on different types of minerals. Experimental methods and results are discussed in the following section.

6.3.1 Experimental Procedures

6.3.1.1 Uranium Sorption on Na-clinoptilolite

The sorption experiments were conducted by reacting 0.1 g of Na-clinoptilolite (75-150 μm) with 50 ml of uranium solutions in fluorinated ethylene propylene (FEP) Teflon® bottles. The aqueous

solutions had initial uranium concentrations of 5, 50, or 500 ppb and were prepared using a ^{233}U solution standard issued by the DOE New Brunswick Laboratory as Certified Reference Material (CRM) 111-A. This standard solution had a total uranium concentration of 50.5 ppm (99.5% ^{233}U). All uranium solutions were prepared in FEP Teflon® containers. Most of the experiments were conducted at an ionic strength close to 0.1 m using a $NaNO_3$ matrix. To study the possible effect of ionic strength on uranium sorption, additional experiments were conducted in a 1.0-m $NaNO_3$ matrix.

Prior to addition of the solid phase, the initial pH of each solution was adjusted to a value in the range 2.0 to 9.0 at approximately 0.25-pH intervals by the addition of HNO_3 or $NaHCO_3$. The amount of reagent needed to achieve the desired initial pH of the uranium solutions was estimated using the EQ3NR geochemical code (Version 3245.R124) with database Data0.com.R12. The solutions, which were kept open to atmospheric $CO_2(g)$ throughout the experiment, were agitated using gyratory shakers. For uranium solutions with added $NaHCO_3$, it took at least 10 d to equilibrate with atmospheric $CO_2(g)$ and reach a constant pH.

After all solutions had attained a constant pH, 500 μl samples were taken from each solution using Eppendorf micropipets to determine initial uranium concentrations. Na-clinoptilolite powder was then added to each solution, and the mixtures were allowed to equilibrate. Control experiments, which consisted of uranium solutions without added clinoptilolite, were used to determine potential losses of uranium to the container walls and to correct for any increase in uranium concentration due to evaporation of experimental solutions. After about 10 d, samples were taken from each solution to determine the final uranium concentration. The equilibrium pH of each solution was also measured. Subsequently, reverse experiments were initiated by adjusting the pH of some of the experimental solutions to lower or higher pH by the addition of HNO_3 or $NaHCO_3$. After an additional period of about 10 d, the pH of the solutions was measured, and aqueous samples were taken to determine the uranium concentrations at the end of the reverse experiment. Uranium concentrations of the experimental and control solutions were all analyzed with a Packard Model 1900 TR Liquid Scintillation Analyzer.

6.3.1.2 Uranium Sorption on α-alumina

In these experiments, α-alumina (α-Al_2O_3), which is issued by the National Institute of Standards and Technology (NIST) as CRM for measurements of specific surface area of powders, was selected as the sorbent phase. Specifically, Reference Materials (RM) 8005, 8006, and 8007, with reported surface areas of 2.09, 0.229, and 0.0686 m^2/g, respectively, were used. The α-alumina powders were considered suitable because their surface areas are relatively well-constrained and their dense structure prevents intracrystalline ion exchange reactions to occur with the uranium in solution. To minimize altering the surfaces of the α-alumina, the powders were not washed or treated in any way before their use in the experiments.

The sorption experiments on α-alumina were conducted at a constant solid-mass/solution-volume, but variable sorbent-surface-area/solution-volume ratio, by reacting 0.1 g of RM 8005, 8006, or 8007 with 40 ml of ^{233}U solutions in 50-mL Teflon® FEP centrifuge tubes. The solutions all had initial concentrations of ~95 ppb U in a 0.1-m $NaNO_3$ matrix. In a manner similar to the clinoptilolite experiments already described, the initial pH of the uranium solutions was adjusted by the addition of HNO_3 or $NaHCO_3$, and the solutions were kept open to atmospheric $CO_2(g)$ through the duration of the experiment. Control solutions were also included to allow corrections for container sorption and evaporation of solution. The α-alumina powder was added after all solutions had attained a constant pH and after aqueous samples had been taken to determine the initial uranium concentration.

After about 2 wk, the mixtures were centrifuged at 13,000 rpm for about 20 min to separate the liquid and solid phases, and aqueous samples were taken for liquid scintillation analysis. The equilibrium pH of each solution was also measured.

6.3.2 Results and Discussion

6.3.2.1 Uranium Sorption on Na-clinoptilolite

Results of the experiments using Na-clinoptilolite are shown in Figures 6-4 to 6-7. Figure 6-4 compares the relative amounts of uranium lost from 5-, 50-, and 500-ppb U solution due to sorption on container walls. This figure shows that significant amounts of uranium are lost from solution to the container, particularly at low initial ΣU. Container sorption is strongly dependent on solution pH and reaches a maximum at pH values between 5 and 6. The pH at which maximum sorption occurs shifts to more acidic conditions with decreasing initial ΣU. Figure 6-5 shows a comparison of the overall %U lost from solution with the %U sorbed on the container from solutions with initial ΣU equal to 5, 50, and 500 ppb. As shown in this figure, the component of the total uranium lost from solution due to container sorption becomes greater with decreasing initial uranium concentration.

Figure 6-6 shows the %U sorbed on clinoptilolite as a function of pH for solutions with initial ΣU equal to 5, 50, and 500 ppb. It is evident from this figure that uranium sorption on clinoptilolite is strongly dependent on pH. The amount of uranium sorbed increases sharply at pH values above about 4 (adsorption edge) and decreases sharply at pH values above about 6.5 (desorption edge). It reaches a maximum value at pH ~ 6.3. In addition, at constant pH the %U sorbed increases with decreasing initial ΣU, although the relative increase in %U sorbed is smaller at lower ΣU. Also shown in Figure 6-6 are the data points for the reverse experiments, which generally plot along the same sorption and desorption trends as the forward data points. This correspondence between forward and reverse data indicates that the uranium sorption reactions are reversible.

In Figure 6-7(a), the overall %U lost from solution is compared with and the %U sorbed on container from an initially 50-ppb U solution in a 0.1- or 1.0-m $NaNO_3$ matrix. The data show that an increase in ionic strength decreased both the overall sorption and container sorption. Although the total uranium lost from solution is smaller at higher ionic strength, the relative amounts of uranium sorbed on clinoptilolite, which are plotted in Figure 6-7(b) and which have been corrected for container sorption, do not significantly change with variations in ionic strength.

6.3.2.2 Uranium Sorption on α-alumina

The results of the experiments using α-alumina are shown in Figure 6-8. The data show a strong dependence of uranium sorption on α-alumina with pH, which has also been observed for uranium sorption on clinoptilolite. At constant pH, the total uranium sorbed increases as the sorbent-surface-area/solution-volume ratio increases, but the increase is not directly proportional to the reported surface areas of the α-alumina powders. For example, a maximum sorption of 60 percent occurred on the highest surface area powder (RM 8005; 2.09 m^2/g), whereas RM 8006 (0.229 m^2/g) and RM 8007 (0.0686 m^2/g) had maximum uranium sorption of 27 and 14 percent, respectively. Sorption maxima occur between a pH of 6.2 and 6.3, regardless of the surface area of the α-alumina. The adsorption and desorption edges at higher surface-area/solution-volume ratios enclose those at lower ratios. In other words, at a fixed volume of solution, the adsorption edge shifts to more acidic pH with increasing surface area of the solid,

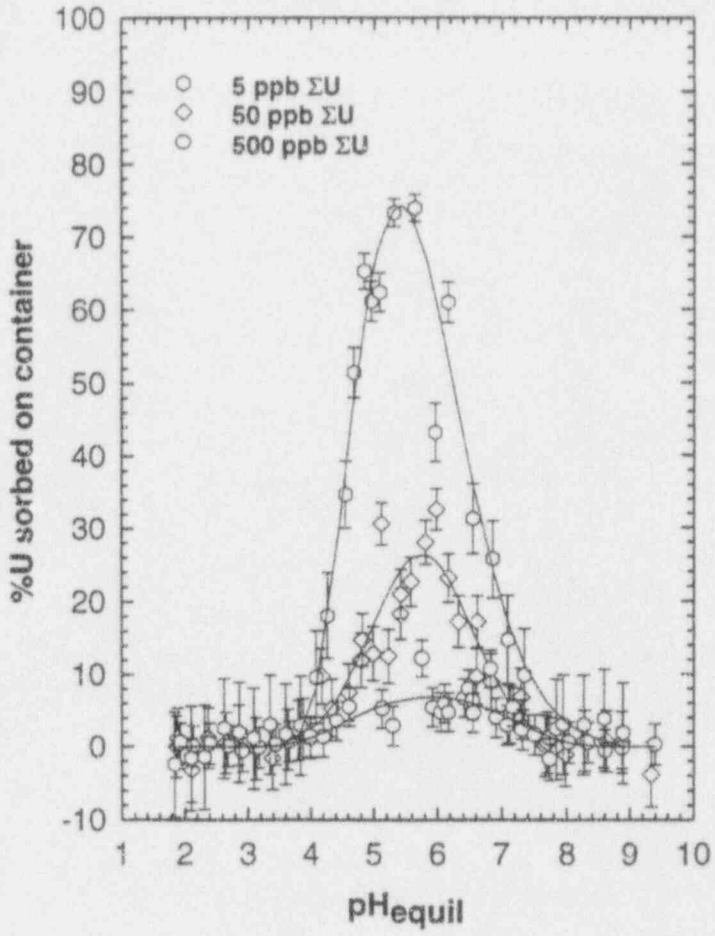

Figure 6-4. %U lost from solution due to sorption on container wall. Best fits to container sorption data, which were used to correct the overall sorption data shown in Figure 6-5, are indicated by the curves.

whereas the desorption edge shifts to more alkaline pH. A similar shift in pH with increasing surface area was reported by Tripathi (1984) for uranium(6+) sorption on the iron oxide mineral goethite.

The experimental data discussed previously were evaluated using surface-complexation models as part of the activities in Task 2 of this research project. Some of the results of the modeling effort are given in Section 6.2.

6.4 ASSESSMENT OF PROGRESS TOWARD MEETING PROJECT OBJECTIVES

The broad objective of this project is to develop sufficient understanding of issues relevant to radionuclide transport. An important mechanism for attenuating radionuclide transport is sorption of radionuclides on minerals encountered along the flow paths.

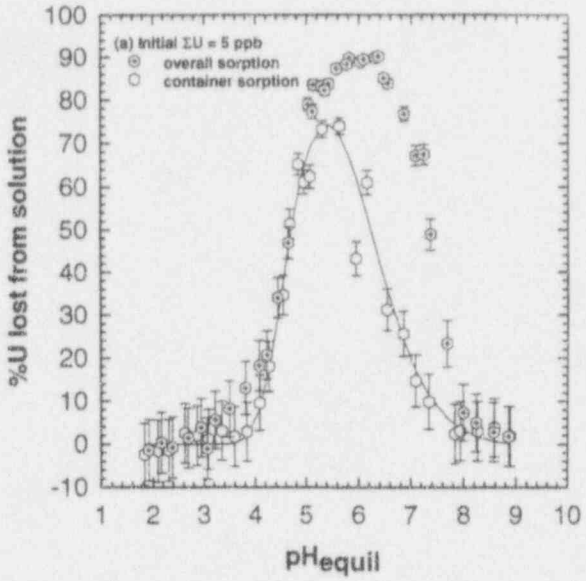

(a)

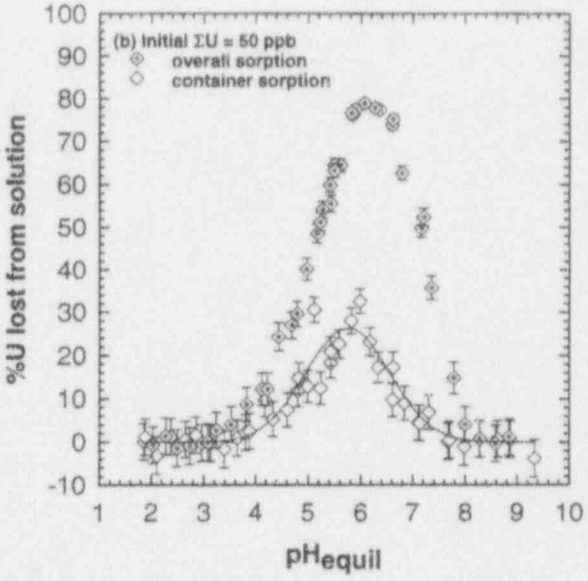

(b)

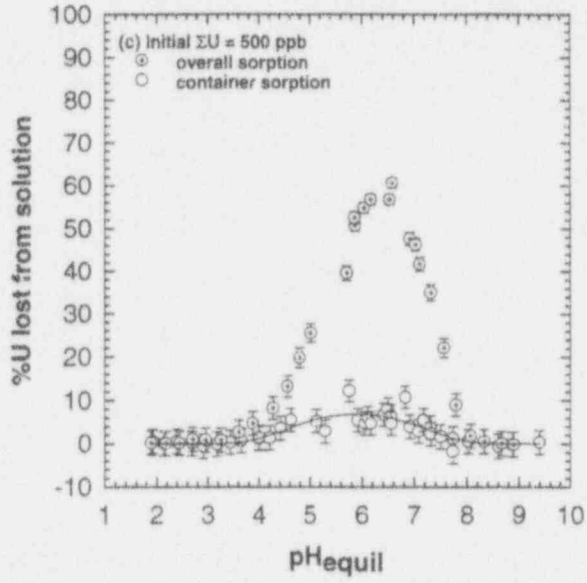

(c)

Figure 6-5. Overall %U lost from solution compared with %U sorbed on container for initial ΣU = 5, 50, and 500 ppb

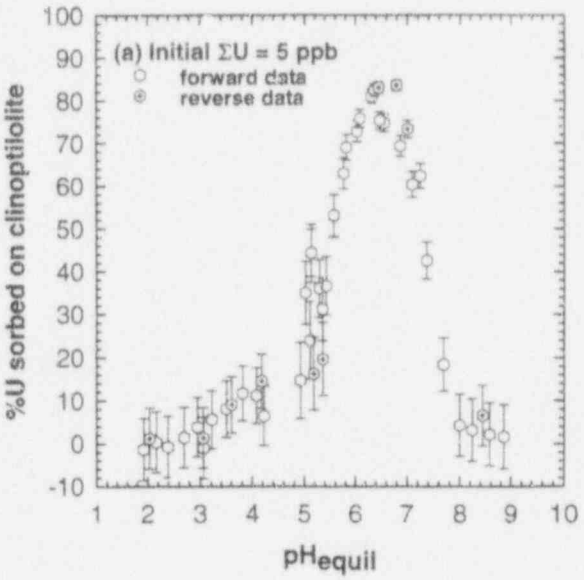

(a)

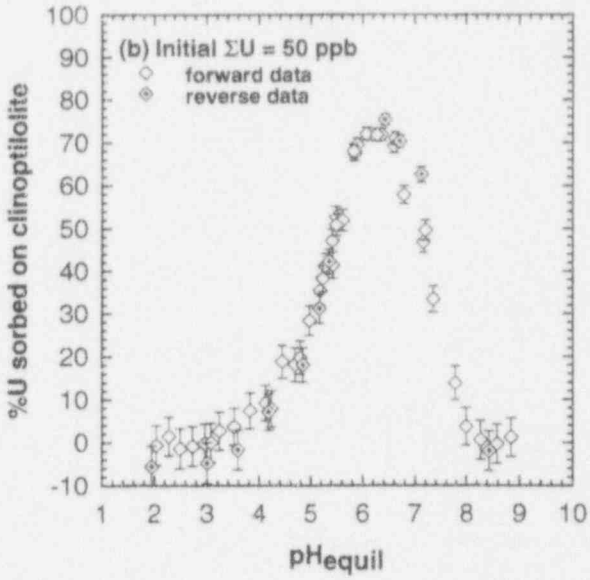

(b)

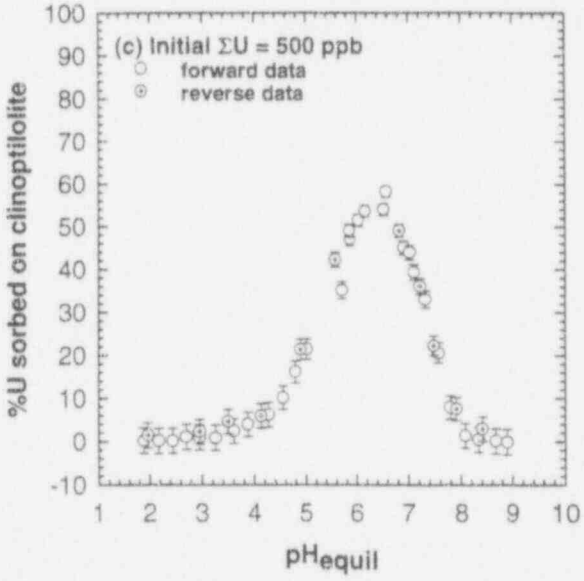

(c)

Figure 6-6. %U sorbed on clinoptilolite calculated from data shown in Figures 6-4 and 6-5. Data from reverse experiments are also shown.

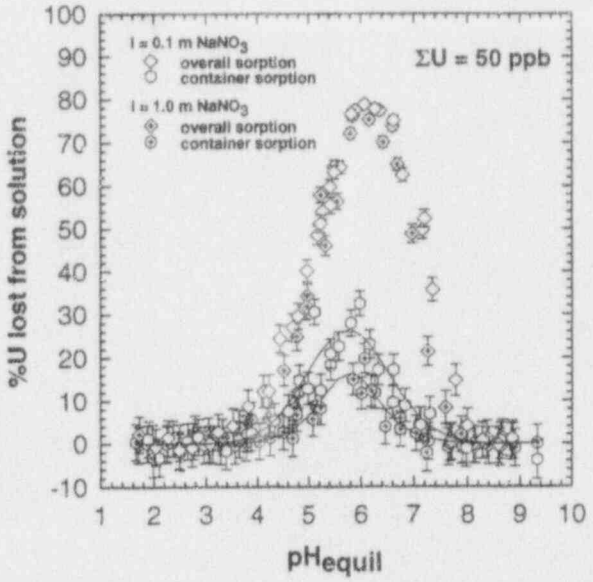

(a)

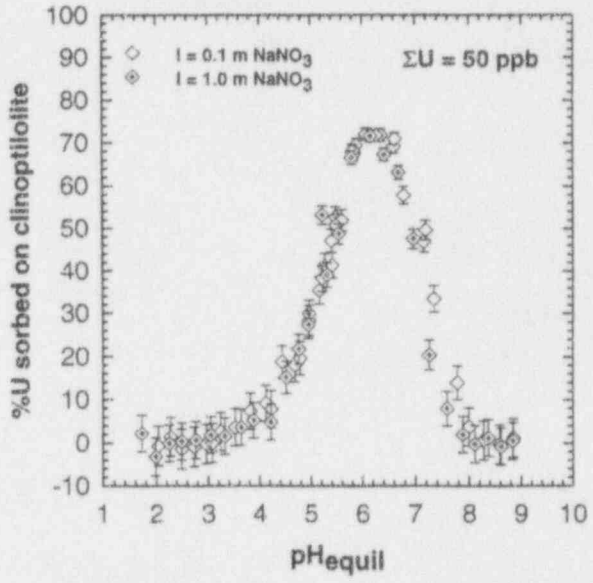

(b)

Figure 6-7. Effect of ionic strength: (a) Comparison of overall %U lost from solution and %U sorbed on container from an initially 50 ppb U solution in a 0.1- or 1.0-m $NaNO_3$ matrix. (b) Comparison of %U sorbed on clinoptilolite (corrected for container sorption) from an initially 50 ppb U solution in a 0.1- or 1.0-m $NaNO_3$ matrix.

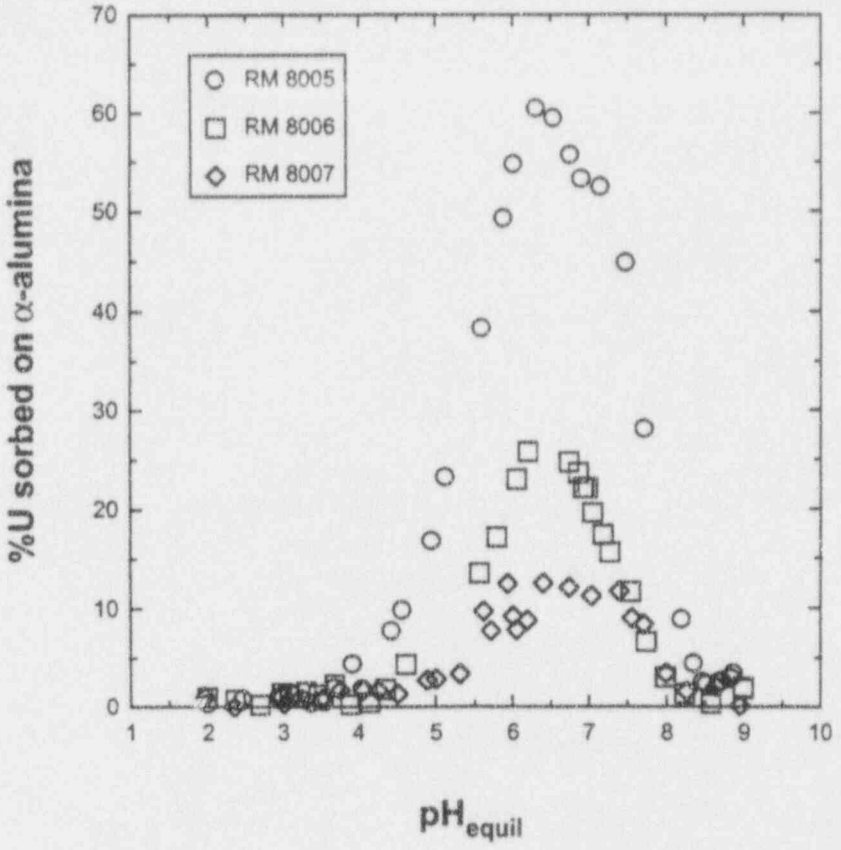

Figure 6-8. Results of sorption experiments on α-alumina. Initial ΣU=95 ppb. The circles, squares, and diamonds represent data for solutions that utilized RM 8005 (2.09 m^2/g), RM 8006 (0.229 m^2/g), and RM 8007 (0.0686 m^2/g), respectively.

Modeling efforts using SCM methods for actinide sorption, combined with results of laboratory experiments on uranium sorption, are providing an understanding of the important parameters that control the sorption behavior of uranium. For example, the experimental results reported here demonstrate that uranium sorption on clinoptilolite and α-alumina, which are sorbents of very different mineralogic and surface properties, are strongly sorbed at near-neutral pH (~6.3). However, in both systems, the amount of uranium sorbed is strongly dependent on pH and decreases steeply away from near-neutral pH. The ratio of sorbent-surface-area to solution-volume ratio also influences sorption; that is, as the ratio increases, the relative amount of uranium sorbed on the solid also increases. Some dependence on total uranium concentration in solution was also observed. However, it appears that ionic strength has a negligible effect on the sorption behavior of uranium. Because of their theoretical basis, relatively simple surface complexation models are able to account for these behaviors in a quantitative way that exceeds the capability of purely empirical models. Because of the strong dependence on pH and sorbent-surface-area/solution-volume ratio, modeling of sorption processes will likely require that changes in groundwater chemistry and in rock/fluid ratio be appropriately accounted for in PA calculations if retardation by sorption processes is included.

The similarity in the pH-dependence of uranium sorption on clinoptilolite and α-alumina is important. It may help identify simplified approaches to modeling sorption and thus help in the development of CDMs relevant to the KTUs identified in Section 6.1 and in developing conceptual

models related to the PA Research Project and the IPA Phase 3. The information derived from the laboratory experiments may also help interpret data on uranium distribution and migration at the Peña Blanca field site of the Geochemical Natural Analog Research Project.

6.5 PLANS FOR NEXT REPORT PERIOD

Now that a uniform set of SCM parameters has been established, modeling efforts will continue to explore the application of SCM methods to available radioelement sorption data. Particular effort will be focused on using these techniques to model actinide sorption on complex multioxide minerals. After binding constants are determined, it may be possible to predict sorption behavior as a function of changing chemistry such as pCO_2. Where possible, checks will be made using uranium sorption data generated from Task 3 experiments. It may also be feasible to extend SCM methods to mixtures of more than one mineral and natural materials, such as crushed tuff and soils.

Experiments studying uranium sorption on clinoptilolite will continue, but these efforts will focus on the possible effect of pCO_2 on the sorption equilibrium. Additional experiments on α-alumina will also be conducted, but will use mixtures of α-alumina with different surface areas. To develop a better understanding of the effects of mineral properties to sorption processes, new uranium sorption experiments will be initiated using montmorillonite and quartz as the sorbent phases. In order to get data on the surface properties, such as pH_{zc} and pzc, of these various minerals, a Mettler potentiometric titrator is being set up for acid-base titration of mineral samples, as well as a Micromeritics Zeta Potential Analyzer for electrophoretic measurements. Flow experiments using column techniques will also be initiated using uranium as the sorbing radionuclide and quartz sand as the sorbent phase. The data generated from these experiments will continue to be utilized in the modeling activities being conducted under Task 2 of this project. The calculational results presented here for Task 2 were obtained using FITEQL, Version 2.0 (Westall, 1982) and MINTEQA2, Version 3.11 (Allison et al., 1991). These codes are not currently in the CNWRA configuration management system.

6.6 REFERENCES

Allard, B., M. Karlsson, E.L. Tullborg, and S.A. Larson. 1983. *Ion Exchange Capacities and Surface Areas of Some Major Components and Common Fracture Filling Materials of Igneous Rocks*. KBS 83-64. Göteborg, Sweden: Chalmers University of Technology.

Allison, J.D., D.S. Brown, and K.J. Novo-Gradac. 1991. *MINTEQA2/PRODEFA2, A Geochemical Assessment Model for Environmental Systems: Version 3.0 User's Manual*. EPA/600/3-91/021. Athens, GA: U.S. Environmental Protection Agency.

Brady, P.V., and J.V. Walther. 1992. Surface chemistry and silicate dissolution at elevated temperatures. *American Journal of Science* 292: 639–658.

Davis, J.A., and D.B. Kent. 1990. Surface complexation modeling in aqueous geochemistry. *Mineral-Water Interface Geochemistry*. M.F. Hochella, Jr. and A.F. White, eds. Reviews in Mineralogy Volume 23. Washington, DC: Mineralogical Society of America: 177–260.

Davis, J.A., and J.O. Leckie. 1978. Surface ionization and complexation at the oxide/water interface 2. Surface properties of amorphous iron oxyhydroxide and adsorption of metal ions. *Journal of Colloid and Interface Science* 67: 90–107.

Dzombak, D.A., and F.M.M. Morel. 1990. *Surface Complexation Modeling: Hydrous Ferric Oxide*. New York, NY: Wiley and Sons.

Grenthe, I., J. Fuger, R.J. Lemire, A.B. Muller, C. Nguyen-Trung, and H. Wanner. 1992. *Chemical Thermodynamics Series, Volume 1: Chemical Thermodynamics of Uranium*. New York, NY. Elsevier.

Hayes, K.F., G. Redden, W. Ela, and J.O. Leckie. 1990. *Application of Surface Complexation Models for Radionuclide Adsorption: Sensitivity Analysis of Model Input Parameters*. NUREG/CR-5547. Washington, DC: U.S. Nuclear Regulatory Commission.

Kent, D.B., V.S. Tripathi, N.B. Ball, J.O. Leckie, and M.D. Siegel. 1988. *Surface-Complexation Modeling of Radionuclide Adsorption in Subsurface Environments*. NUREG/CR-4807. Washington, DC: U.S. Nuclear Regulatory Commission.

Kohler, M., E. Wieland, and J.O. Leckie. 1992. Metal-ligand-surface interactions during sorption of uranyl and neptunyl on oxides and silicates. *Proceedings of the 7th International Symposium on Water-Rock Interaction (WRI-7). Volume 1: Low Temperature Environments*. Y.K. Kharaka and A.S. Maest, eds. Rotterdam, Netherlands: A.A. Balkema: 51–54.

Lemire, R.J. 1984. *An Assessment of the Thermodynamic Behavior of Neptunium in Water and Model Groundwater From 25 to 150 °C*. AECL-7817. Pinawa, Manitoba: Atomic Energy of Canada Limited.

Los Alamos National Laboratory. 1993. Monthly Activity Report for April 1993.

Manceau, A., and L. Charlet. 1991. Sorption and speciation of heavy metals at the oxide/water interface: From Microscopic to Macroscopic. *Environmental Pollution 1*: 401–408.

Nakayama, S., and Y. Sakamoto. 1991. Sorption of neptunium on naturally-occurring iron-containing minerals. *Radiochemica Acta* 52/53: 153–157.

Pabalan, R.T., and D.R. Turner. 1993. Sorption modeling for HLW performance assessment. *NRC High-Level Radioactive Waste Research at CNWRA January Through June 1993*. B. Sagar, ed. CNWRA 92-02S. San Antonio, TX: Center for Nuclear Waste Regulatory Analyses: 8-1 to 8-18.

Pabalan, R.T., J.D. Prikryl, P.M. Muller, and T.B. Dietrich. 1993. Experimental study of uranium(6+) sorption on the zeolite mineral clinoptilolite. *Scientific Basis for Nuclear Waste Management XVI MRS Symposium. Proceedings*. C.G. Interrante and R.T. Pabalan, eds. Pittsburgh, PA: Materials Research Society: 294: 777–782.

Payne, T.E., K. Sekine, J.A. Davis, and T.D. Waite. 1992. Modeling of radionuclide sorption processes in the weathered zone of the Koongarra ore body. *Alligator Rivers Analogue Project Annual Report, 1990-1991*. P. Duerden, ed. Australian Nuclear Science and Technology Organization: 57-85.

Rai, D., J.M. Zachara, L.E. Eary, C.C. Ainsworth, J.E. Amonette, C.E. Cowan, R.W. Szelmeczka, C.R. Resch, R.L. Schmidt, D.C. Girvin, and S.C. Smith. 1988. *Chromium Reactions in Geologic Materials*. EPRI-EA-5741. Palo Alto, CA: Electric Power Research Institute.

Riese, A.C. 1982. *Adsorption of Radium and Thorium onto Quartz and Kaolinite: A Comparison of Solution/Surface Equilibria Models*. Ph.D. Dissertation. Golden, CO: Colorado School of Mines.

Siegel, M.D., V.S. Tripathi, M.G. Rao, and D.B. Ward. 1992. Development of a multi-site model for adsorption of metals by mixtures of minerals: 1. Overview and preliminary results. *Water-Rock Interaction: Proceedings of the 7th International Symposium on Water-Rock Interaction*. Y.K. Kharaka and A.S. Maest, eds. Rotterdam, Netherlands: A.A. Balkema.

Tripathi, V.S. 1984. *Uranium(6+) Transport Modeling: Geochemical Data and Submodels*. Unpub. Ph.D. Dissertation. Stanford, CA: Stanford University.

Turner, D.R. 1993. *Mechanistic Approaches to Radionuclide Sorption Modeling*. CNWRA 93-019. San Antonio, TX: Center for Nuclear Waste Regulatory Analyses.

Turner, D.R., T. Griffin, and T.B. Dietrich. 1993. Radionuclide sorption modeling using the MINTEQA2 speciation code. *Materials Research Society Symposium Proceedings: Scientific Basis for Nuclear Waste Management---XVI MRS Symposium*. C.G. Interrante and R.T. Pabalan, eds. Pittsburgh, PA: Materials Research Society: 294: 783-789.

Westall, J.C. 1982. *FITEQL: A Computer Program for Determination of Chemical Equilibrium Constants From Experimental Data, Version 2.0*. Rpt. 82-02. Corvallis, OR: Department of Chemistry, Oregon State University.

Westall, J.C., and H. Hohl. 1980. A comparison of electrostatic models for the oxide/solution interface. *Advances in Colloid and Interface Science* 12: 265-294.

7 PERFORMANCE ASSESSMENT RESEARCH

By Robert G. Baca, Randall D. Manteufel, Sitakanta Mohanty, Stuart A. Stothoff, and Gordon W. Wittmeyer

Investigators: Robert G. Baca, Ronald T. Green, Randall D. Manteufel, Sitakanta Mohanty, Stuart A. Stothoff, and Gordon W. Wittmeyer (CNWRA); Christopher J. Freitas (SwRI); Evaristo J. Bonano and Mohan S. Seth (Consultants)

NRC Project Officer: Timothy J. McCartin

7.1 TECHNICAL OBJECTIVES

Postclosure Performance Assessment (PA), as a scientific evaluation process, will provide the quantitative basis for judging the acceptability of the proposed repository system at Yucca Mountain (YM). In conducting a PA, the U.S. Nuclear Regulatory Commission (NRC) will utilize a hierarchy of models and codes. The top level or total-system PA (TSPA) code, which is being developed under the NRC Nuclear Material Safety and Safeguards (NMSS) Iterative Performance Assessment (IPA) activity, models a wide variety of processes, phenomenological interactions, and future system states, but in a necessarily simplified manner. In contrast, the lower-level codes in this hierarchy are very sophisticated, but model only a few processes in a very detailed manner. Quite interestingly, both types of codes typically exceed the computational limits of conventional computers and push the capability of the most advanced, high-performance supercomputers. The technical objectives of the PA Research Project are to develop advanced PA modeling technology in three specific areas: (i) alternate conceptual models of key phenomena and future system states (i.e., disruptive scenarios), (ii) efficient and robust computational and computer techniques for solving the model equations, and (iii) formalized approaches for testing and evaluating (i.e., validating) computer models.

One of the primary programmatic objectives of the PA Research Project is to provide modeling technology that will benefit the NRC IPA exercises. Another, and equally important, programmatic objective is to provide the knowledge base necessary for supporting: (i) revision of the postclosure PA Compliance Determination Strategies (CDSs) (i.e., CDS 6.1, 6.2, and 6.3), and (ii) development of postclosure performance Compliance Determination Methods (CDMs) that will be incorporated into appropriate sections of the License Application Review Plan (LARP). Specifically, this research project is contributing to the knowledge base for addressing key technical uncertainties (KTUs) associated with:

(i) Conceptual models

(ii) Mathematical models

(iii) Model parameters

(iv) Future system states

(v) Model validation

At present, the KTU related to the first three items resulted in the associated CDS being typed as Review Level 4, while the CDS associated with the fourth item is typed Review Level 5; these KTUs are broadly

addressed in Tasks 1 and 2 of this research project. The last KTU requires a type Review Level 5 of CDS 6.1, Assessment of Compliance with the Requirement for Cumulative Releases of Radioactive Materials, and is being addressed in a focused effort under Task 3 of this research project. In addition, the practical experience and expertise gained from this research project will place the NRC and the Center for Nuclear Waste Regulatory Analyses (CNWRA) in a position to thoroughly and independently evaluate the U.S. Department of Energy (DOE) PA models and codes.

Because of its multidisciplinary nature, the PA Research Project is an integrated programmatic effort drawing on expertise from such technical areas as hydrology, geochemistry, structural geology, volcanology, seismology, climatology, computational fluid dynamics, and computer science. At present, the PA Research Project is programmatically integrated with the NMSS IPA activity and three other Office of Nuclear Regulatory Research (RES) projects: (i) the Geochemical Analog of Contaminant Transport in Unsaturated Rock Research Project, (ii) the Sorption Modeling for High-Level Waste Performance Assessment Research Project, and (iii) the Stochastic Unsaturated Flow and Transport Project. In relation to the Geochemical Analog of Contaminant Transport in Unsaturated Rock Research Project, data from rock cores obtained from the Peña Blanca field site are being analyzed to improve conceptual and mathematical models of: (i) variably saturated flow in the fractured-porous tuff, and (ii) radionuclide transport in discrete fractures and diffusion into and out of the rock matrix. In addition, data on diffusion and sorption coefficients, compiled under the Sorption Modeling for High-Level Waste Performance Assessment Research Project, will contribute to conceptual/mathematical model development of radionuclide transport phenomena. Simulation studies conducted under the Stochastic Unsaturated Flow and Transport Research Project have identified a number of computational aspects that currently limit the practical application of detailed hydrologic codes (e.g., BIGFLOW) to the YM site. Work conducted under Task 2 of the PA Research Project is being focused to reduce or remove these computational limitations.

The PA Research Project is designed to address a number of user needs identified by the NMSS for postclosure PA. Specific research needs include: (i) selection of means to identify and screen scenarios, (ii) efficient integration of mathematical models into high-level waste (HLW) PA methodology, (iii) validation of mathematical models, (iv) evaluation of mathematical models, (v) evaluation of mathematical flow and transport models applicable to unsaturated fractured rock and application to a range of scales and heterogeneities, and (vi) appraisal of the applicability of existing mathematical models of hydrologically and chemically coupled flow and transport.

Research conducted under the PA Research Project is divided among three major tasks. The first task, Conceptual Model Development, focuses on developing conceptual/mathematical models in two areas: (i) flow and transport phenomena, and (ii) disruptive event scenarios. In the second task, Computational Model Development, research is directed toward the development of advanced numerical methods necessary to implement PA conceptual and mathematical models. Under the third task, Model Evaluation, a general model validation strategy is being developed based on the experience gained from the INTRAVAL project test cases. Work completed on these tasks has been reported in previous semi-annual research reports. This section describes the results of the PA Research Project for the second half of 1993.

7.2 SIGNIFICANT TECHNICAL ACCOMPLISHMENTS

Significant progress was made in this reporting period toward the technical objectives of the three major tasks of the PA Research Project. In Task 1, for example, two related activities on disruptive event scenarios were completed. The products of these two activities will directly benefit the IPA Phase 3 planning process. Also part of Task 1, work continued on the development of hydrologic conceptual models as a joint effort with the Geochemical Analog of Contaminant Transport in Unsaturated Rock Research Project. For Task 2, research was performed on a new computational technique referred to as the method of contours. As part of Task 3, the hydrologic model validation exercise using the YM data set was completed. Research results and findings for each task are summarized in the following subsections.

7.2.1 Task 1—Conceptual Model Development: Disruptive Events/Scenarios

Two related studies were conducted consisting of: (i) an independent review and critique of the IPA Phase 2 disruptive event scenario models and modules, and (ii) a state-of-the-art review of scenario selection methodologies. In this section, the selected aspects of the first study are highlighted; additional information on this study can be found in the letter report entitled Review and Critique of the NRC/CNWRA Scenario Methodology Used in IPA Phase 2. The IPA Phase 2 scenarios consisted of four distinct types of events and processes (EPs) that were modeled in the TSPA for the YM site. In particular, the four types of disruptive EPs considered were: (i) climate change (pluvial), (ii) volcanism, (iii) human intrusion (drilling), and (iv) seismo/tectonics (seismic).

7.2.1.1 Basis for Disruptive Events and Processes Selection

The different implementations of disruptive events in recent TSPAs for YM are summarized in Table 7-1. This table contains information for the two IPA phases by the NRC (1992; 1994), two phases by Electric Power Research Institute (EPRI) (1990; 1992), the first phase by Sandia National Laboratories (SNL) (1992), and Pacific Northwest Laboratory (PNL) (1993). Each of the four types of disruptive EPs was selected based on its potential for affecting repository performance through either enhanced release of radioactive waste from the Engineered Barrier System (EBS), or enhanced transport of waste through the Geologic Setting (GS). The rationale for each of the EPs is summarized here.

Climate change is most frequently represented by a change in the infiltration rate and in the elevation of the water table. Increased infiltration and water table rise affect the release of radionuclides from the repository by accelerating the corrosion of waste packages and accelerating the liquid transport through the geologic medium. From the NRC IPA, it has been consistently found that infiltration rate has a significant impact on repository performance (U.S. Nuclear Regulatory Commission, 1992; 1994).

Volcanic events have the potential of occurring at YM and leading to magma interactions with waste packages (Connor and Hill, 1993). The primary effect of volcanic activity is waste entrainment in ascending magma that, for extrusive events may lead to ejection of waste at the ground surface. For intrusive events, the magma may interact with waste packages to accelerate their failure and release of radionuclides into the GS. From the recent IPA calculations, it was determined that climate change and volcanism are dominant EPs at high- and low-probabilities, respectively.

Table 7-1. Comparison of implementations of disruptive scenarios for Yucca Mountain

	Climate Change	Volcanism	Human Intrusion	Seismo/ Tectonics
NRC Phase 1 (1992)	• Increased Infiltration • Water Table Rise	—	• Drilling - Exhume WP - Exhume CR	—
NRC Phase 2 (1994)	• Increased Infiltration • Water Table Rise	• Waste Entrainment in Magma	• Drilling - Exhume WP - Exhume CR	• Vibratory WP Failure - WP Impingement onto Borehole Wall - WP Stress Exceeds Material Yield Stress
SNL TSPA 91 (1992)	• Increased Infiltration	• Waste Entrainment in Magma	• Drilling - Exhume WP - Waste into Saturated Zone	—
PNL (1993)	• Increased Infiltration	• Waste Entrainment in Magma	• Drilling - Exhume WP - Exhume CR - Waste into Tuff Aquifer - Waste into Carbonate Aquifer	• Literature Review on Water Table Rise
EPRI Phase 1 (1990)	• Increased Infiltration	• Waste Entrainment in Magma • Water Table Rise	—	• WP Failure due to Primary and Secondary Faulting • Water Table Rise
EPRI Phase 2 (1992)	• Increased Infiltration - Current - Greenhouse - Micropluvials • Water Table Rise	• Waste Entrainment in Magma • Water Table Rise	• Drilling - Exhume WP • Excavation - Exhume WP	• WP Failure due to Primary and Secondary Faulting • Water Table Rise

CR = Contaminated Rock, WP = Waste Package

Human intrusion is most frequently represented by exploratory drilling through the repository. Drilling may cause a direct release of radionuclides to the ground surface or rapid transport of waste to the saturated zone (e.g., Sandia National Laboratories, 1992; Pacific Northwest Laboratory, 1993). Direct release is caused by drilling through a waste package, thereby mobilizing and mixing the waste with the drilling fluid, exhuming the waste, and distributing the contents onto the ground surface. Even if a drill bit misses a waste package, it may exhume radionuclides by removing contaminated rock.

Seismo/tectonic events are presently perceived as the least important EP for YM, and different implementations have focused on a variety of effects. For example, the EPRI implementation focuses on a different set of failure mechanisms than the NRC implementation. In contrast, there is much more agreement on the importance and/or consequences of the other disruptive scenarios. The recent IPA effort models premature failure of waste packages due to vibratory ground motion resulting in early release of radionuclides from the waste packages. Two modes of waste package failure are considered in the NRC IPA effort: (i) waste package impingement onto the borehole wall, and (ii) mechanical stresses exceeding the material yield stress as the waste package vibrates in the borehole. In comparison, the EPRI effort concentrated on primary and secondary faulting, that may give rise to sufficiently large rock displacements that waste packages located along seismic slip planes would rupture under the mechanical load. In addition, the EPRI effort modeled the rise in the water table due to seismic events.

From the summary of the available TSPAs highlighted in Table 7-1, it has been consistently found that climate change (especially increased infiltration) has a strong effect on the predicted performance of the proposed repository. Because of its greater importance relative to the other scenarios, additional discussion of the climate change scenario for YM is presented here.

7.2.1.2 Climate Change

The YM site is located in an area with a climate that is classified as mid-latitude desert, with annual precipitation less than 150 mm and extremes of temperature. Rainfall is sporadic, sometimes torrential, and can lead to local flooding. It has been estimated that only 0.33 percent of the annual precipitation (~0.5 mm) reaches the deeper units of the unsaturated zone (U.S. Department of Energy, 1988).

The most probable climate change of significance is thought to be either a trend towards cooler/wetter conditions or relatively short periods of wetter conditions (tens to hundreds of years). The significance of wetter conditions is that infiltration would increase, thereby increasing both the release (due to increased corrosion of waste packages) and transport (due to higher liquid flow rates in the ground) of radionuclides.

Description and Critique of Current Module

In IPA Phase 2, the climate change is modeled as increased infiltration and elevated water table due to the occurrence of a pluvial climate. Increased infiltration and water table rise are considered the primary effects of increased precipitation. The current implementation is relatively straightforward and is depicted in a logic diagram in Figure 7-1. The pluvial climate is assumed to occur immediately after closure of the repository and continue for 10,000 yr. The infiltration rate is determined by a random sampling from a LogUniform probability distribution function (PDF) between 5 and 10 mm/yr (as compared with the 0.1 to 5 mm/yr in the base case). The water table is modeled to rise 100 m above the present elevation during a pluvial climate. The consequence for a pluvial climate is implemented through

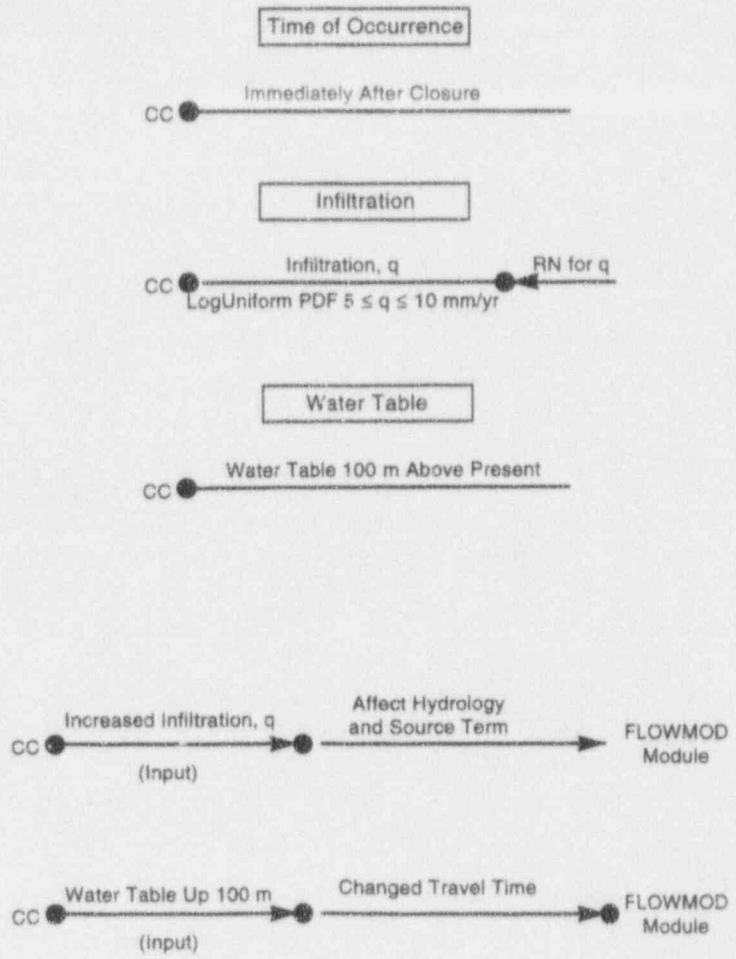

Figure 7-1. Logic diagrams for both description and consequence of climate change as implemented in IPA Phase 2

the FLOWMOD consequence module that accounts for hydrologic effects on the source term (SOTEC consequence module) and decreased travel path in the unsaturated zone. One conclusion of the IPA Phase 2 effort was that infiltration for the pluvial climate scenario has a large impact on repository performance (U.S. Nuclear Regulatory Commission, 1993).

At present, there is no provision in the Total Performance Assessment (TPA) code for time-varying infiltration, as steady-state conditions are assumed to exist at all times. This is a restriction on the predictive capability of the code to model physical events.

The PDFs for infiltration for each of the four most recent TSPAs are compared in Figure 7-2. For the NRC/CNWRA IPA Phase 2 effort, the base case and pluvial case are combined into a single PDF. In comparison, the EPRI Phase 2 and PNL TSPAs use discrete models for infiltration where:

- EPRI Phase 2 (Electric Power Research Institute, 1992)

  for $0 < \text{time} < 1{,}000$ yr
  $q = 0.9$ mm/yr with probability $= 1.0$

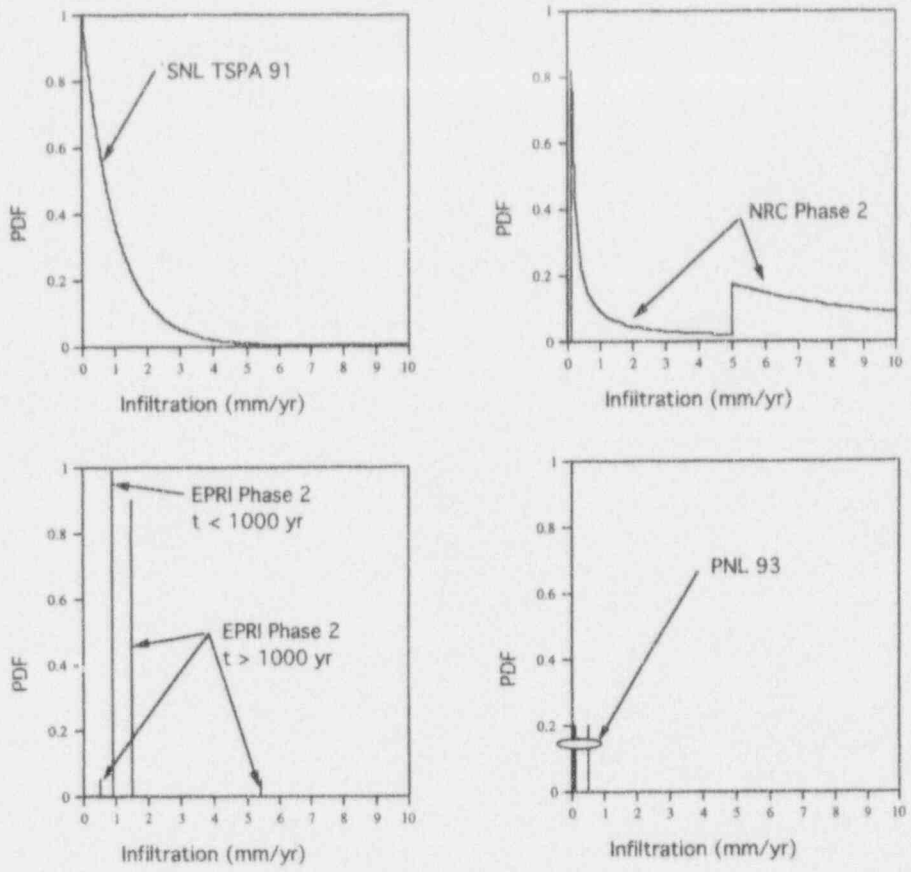

Figure 7-2. Comparison of infiltrations used in four recent PAs for Yucca Mountain

for 1,000 yr < time < 10,000 yr
q = 0.5 mm/yr with probability = 0.05
q = 1.5 mm/yr with probability = 0.90
q = 5.4 mm/yr with probability = 0.05 (pluvial case)

- PNL TSPA (Pacific Northwest Laboratory, 1993)

for q = 0.0 mm/yr with probability = 0.2
q = 0.01 mm/yr with probability = 0.2
q = 0.05 mm/yr with probability = 0.2
q = 0.1 mm/yr with probability = 0.2
q = 0.5 mm/yr with probability = 0.2

The NRC/CNWRA IPA Phase 2 and SNL TSPA 1992 use continuous PDFs (U.S. Nuclear Regulatory Commission, 1993):

- NRC/CNWRA IPA Phase 2

  LogUniform PDF, $0.1 < q < 5$ mm/yr with probability = 0.36 (base case)

  LogUniform PDF, $5 < q < 10$ mm/yr with probability = 0.64 (pluvial)

- SNL TSPA 1991 (Sandia National Laboratories, 1992):

  Beta (~ Exponential) PDF, E[q] = 1.0 mm/yr

The most striking conclusion is the wide variability between TSPAs for this input data. Also, infiltration has been found to be a very important parameter that influences the predicted performance of the system. Interestingly, infiltration processes at the site scale were not identified as a KTU in existing CDSs and are not currently being addressed by any of the CNWRA research projects.

Recommendations for Improvement

The current module is quite simplistic. The simple treatment of infiltration rates is assumed to be conservative, but the degree of conservatism is not characterized. Accordingly, the following are recommended:

- Investigate the linkages between climate and infiltration, possibly through a stochastic modeling study of infiltration processes

- Assess the importance of temporally and spatially varying infiltration, especially the influence of short-term, torrential thunderstorms on infiltration

- Assess the effect of incorporating data from a recent expert elicitation (DeWispelare et al., 1993) into the climate module

7.2.2 Task 2—Computational Model Development: Method of Contours

Conventional numerical techniques using finite-difference and finite-element methods are used to solve conservation equations. Such methods are known to have difficulty accurately handling sharp gradients that may occur when conservation equations (such as the advection-dispersion equation and Richards' equation) are dominated by advection. Remedies to this difficulty typically entail a good deal of additional computational burden. Since PA relies heavily on the repeated accurate solution of conservation equations, accurate, robust, and computationally inexpensive solutions to such problems are greatly desirable.

An improved computational method based on the method of contours is presented here. The theoretical framework of this method is similar to the classical method of characteristics (Lucier, 1986; Holden et al., 1988; Dafermos, 1972). Although the method of characteristics is traditionally applied to purely advection problems, it is extended to advection-diffusion problems following the approach of

Stothoff (1991). In the previous work, the method was shown to be extremely effective in solving simple problems featuring sharp gradients. In the current work, the applicability of the approach to the types of problems encountered in PA is examined.

By placing a computational mesh on selected values of the dependent variable, the solution profile is discretized in the dependent variable, rather than in the spatial variable. Time-stepping is performed by explicitly moving the mesh nodes with the characteristic velocity of the dependent variable. The proposed technique is based on the classical Buckley-Leverett (1942) solution method; however, the dispersion and source terms are included in a straightforward way. Stothoff (1991; 1992), Stothoff and Pinder (1992), have recently applied the method of contours to advection-dispersion and two-phase flow equations in both one and two dimensions.

7.2.2.1 Computational Procedure

To illustrate the computational procedure, consider a typical conservation equation in one spatial dimension

$$\frac{\partial \theta}{\partial t} + \frac{\partial q}{\partial x} = R \tag{7-1}$$

where θ is the dependent variable of interest, q is the flux of the variable of interest, and R is a source term. By expanding the total derivative of θ and evaluating for a particular value of θ

$$\frac{d\theta}{dt} = \frac{\partial \theta}{\partial t} + v_\theta \frac{\partial \theta}{\partial x} = 0 \tag{7-2}$$

where v_θ is the characteristic velocity. Substituting Eq. (7-2) into Eq. (7-1) and rearranging, the characteristic velocity is obtained

$$v_\theta = \left(\frac{\partial q}{\partial x} - R \right) \frac{1}{\partial \theta / \partial x} = \left(\frac{\partial q}{\partial \theta} - \frac{R}{\partial \theta / \partial x} \right) \tag{7-3}$$

The above expression is exact.

At time t, the instantaneous characteristic velocity v_θ is obtained at each node. A Courant-like criterion is used for stepping through time. Given the set of nodal velocities, a time step Δt is found by requiring that the change in length of each element over Δt is less than some fraction of the length at time t; each node is moved by the distance $v_\theta \Delta t$. All results presented here use a value of 10 percent; a smaller criterion has not been found to significantly change the accuracy of the procedure (Stothoff, 1991). Note that each node can be handled independently.

Dispersive effects can be straightforwardly incorporated in the spatial operator. In the mixed finite elements, θ and the spatial derivative of θ are approximated as piecewise constant between mesh nodes. Each mesh node is assigned a value for the dependent variable; each element is assigned the average value of θ for the two mesh nodes. By linearly interpolating between the nodal values, the gradient of θ is obtained. Finally, $q(\theta, \partial\theta/\partial x)$ is approximated as a piecewise constant function between

each node. Any functional relationships imbedded in q must be evaluated at the piecewise constant value of θ. With these approximations

$$\frac{\partial q}{\partial \theta} \approx \frac{q^+ - q^-}{\theta^+ - \theta^-} \tag{7-4}$$

where the superscripts refer to the values on either side of the node.

This procedure fails when the gradient of θ is small or zero, such as occurs when there is an extremum. In such cases, a standard explicit method can be used to calculate the rate of change of θ over time. The time-rate-of-change is evaluated by

$$\frac{\partial \theta}{\partial t} + \frac{q^+ - q^-}{x^+ - x^-} = R \tag{7-5}$$

where x^+ and x^- are evaluated at the midpoint of the adjacent element. The velocity of a node when $\partial\theta/\partial x$ is nearly zero is not well defined. In this work, all nodes in such a low-gradient region are advected by linearly interpolating the velocity of the well-defined moving nodes at the ends of the region to interior nodes. A problem-dependent criterion is required defining what is considered low-gradient.

When source terms are important, lumping the source term into the characteristic velocity can introduce spurious oscillations, as shown in the next section. An alternative procedure uses an operator-splitting technique to treat flux terms independently of source terms. With this approach, the characteristic velocity does not incorporate the source term; the source term is applied as a direct adjustment to the discretized values of θ. Accordingly, the values of θ must be redistributed periodically to maintain resolution.

When fluxes do not depend on the gradient of θ it is immaterial whether fluxes are calculated before the sources are applied or after; otherwise, alternating the order in which the two are calculated is desirable. This requires a certain amount of care in time-stepping. For the examples presented, solutions obtained by evaluating the fluxes before applying decay are identical (to at least seven significant digits) to solutions obtained by applying the source correction alternating between the beginning and the end of each time step.

7.2.2.2 Advection-Dispersion Equation

The advection-dispersion equation is a well-studied model equation with applications in diverse fields. The conservation equation in one dimension is

$$\frac{\partial c}{\partial t} + \frac{\partial q}{\partial x} = -\lambda c \tag{7-6}$$

where c is concentration. Standard advective-dispersive contaminant flux is assumed

$$q = vc - D\frac{\partial c}{\partial x} \tag{7-7}$$

To evaluate the predictions of the proposed technique, an analytic solution defined on a semi-infinite domain is used, with v, D, and λ constant, and imposed conditions of $c(t \le 0,\ x \ge 0) = 0$, $c(t>0,\ x=0) = c_0$, and $c(t>0,\ x=\infty) = 0$. The solution for this boundary value problem is widely published (e.g., Bear, 1972).

For the purposes of demonstration, a set of parameters are chosen ranging from highly advection-dominated to more reaction- and diffusion-dominated. Choosing a length scale L, ramp initial conditions are imposed over L and simulations are carried to $T = 7500L/v$. Defining dimensionless numbers $Pe = vL/D$ and $Da = \lambda L/v$, a set of simulations with $Pe = 10^3$ and $Da = 0$, with $Pe = 10^3$ and $Da = 10^{-4}$, and with $Pe = 10^{-2}$ and $Da = 10^{-4}$ are presented. Each problem is repeated with the concentration profile evenly discretized in concentration with 10, 20, 40, 80, and 160 elements.

The solutions are shown in Figures 7-3, 7-4a, and 7-4b; the total length labeled in the figures is 10,000 L. In the diffusion-dominated case (Figure 7-3), as few as 20 elements are sufficient to resolve the distribution. In the advection-dominated case (Figure 7-4a), the position of the front is determined with ten elements; however, the effect of the initial condition mismatch persists for the 7,500 length scales of the simulation. The computational solution converges to a position ahead of the analytic solution by the amount of mass in the system at the onset of the simulation, as shown in Figure 7-4b.

In the reaction-dominated case (see Figures 7-5a and 7-5b), the method converges toward the analytic solution upon refinement. When using the characteristic velocity with decay included, a nonphysical sinusoidal perturbation upstream of the front develops. The perturbation increases in frequency and decreases in magnitude as the resolution increases. On the other hand, when the operator-splitting procedure is followed, the perturbation is damped at the cost of extra decay in the vicinity of the cusp. In both schemes, inaccuracy is attributable to insufficient resolution of the cusp.

Not surprisingly, computational effort is least when advection dominates (the system is most hyperbolic). With $O(N)$ characteristics discretizing the profile, Lucier (1986) shows that optimal-order accuracy $[O(N^{-1})]$ in L^1 is obtained using the piecewise constant approximation for purely hyperbolic cases. The diffusion-dominated case above exhibits at least $[O(N^{-1})]$ convergence as well.

7.2.2.3 Richards' Equation

Richards' equation is another well-studied conservation equation describing the conservation of moisture in partially saturated soil. The moisture conservation equation is written (assuming water as incompressible)

$$\frac{\partial \theta}{\partial t} + \frac{\partial q}{\partial x} = 0 \tag{7-8}$$

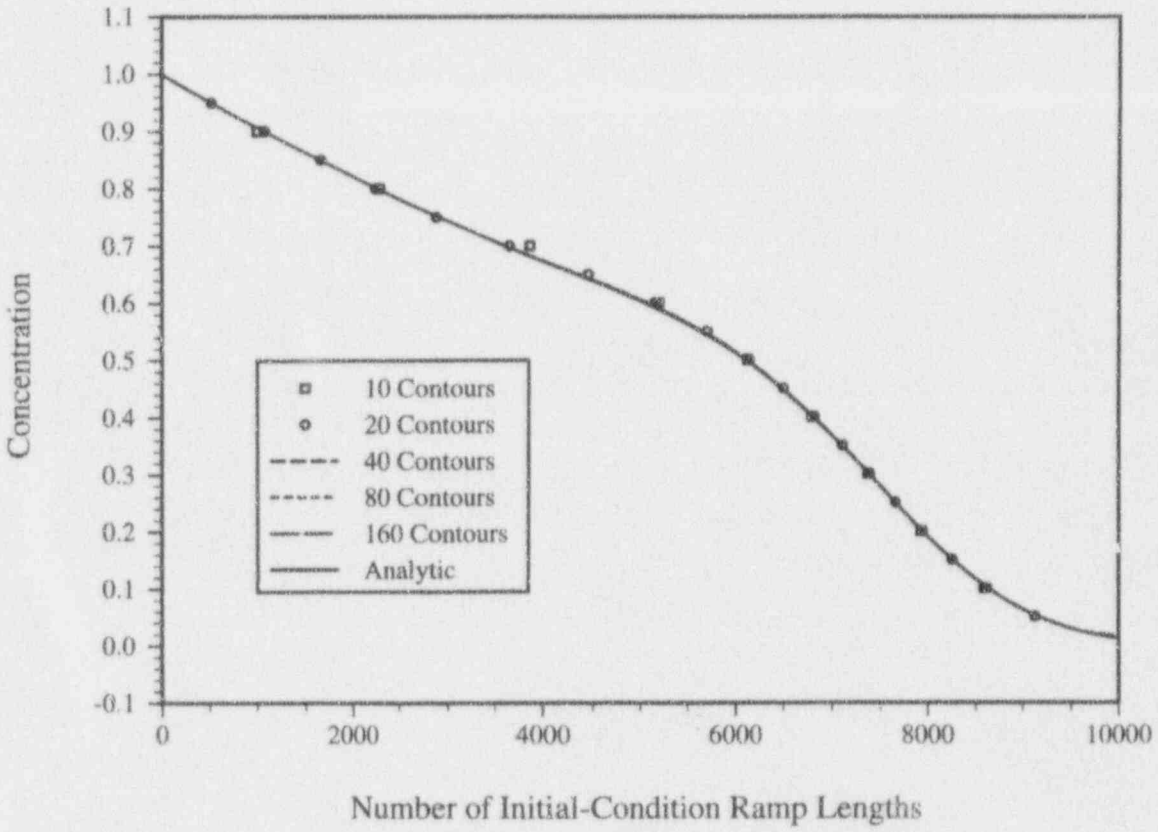

Figure 7-3. Diffusion-dominated solutions Pe=10^{-2} and Da=10^{-4}

where

$$q = -k\lambda\left(\frac{\partial P}{\partial x} + \rho g \frac{\partial z}{\partial x}\right) \tag{7-9}$$

θ is volumetric moisture content, k is intrinsic permeability, $\lambda(\theta)$ is relative permeability (k_r) divided by viscosity, P is water pressure, ρ is density, g is acceleration due to gravity, and z is elevation. This is often consolidated into a more compact representation

$$q = -K(\psi)\left(\frac{\partial \psi}{\partial x} + \frac{\partial z}{\partial x}\right) \tag{7-10}$$

where $\psi = P/\rho g$ and $K = \rho g k \lambda = K_{sat} k_r$.

Various approaches for solving the conservation equation have been proposed in the literature, each of which takes advantage of constitutive relationships between θ and P to eliminate one of these dependent variables from the governing equation. The approach followed herein is to use a moisture-based formulation, so that flux is expressed as

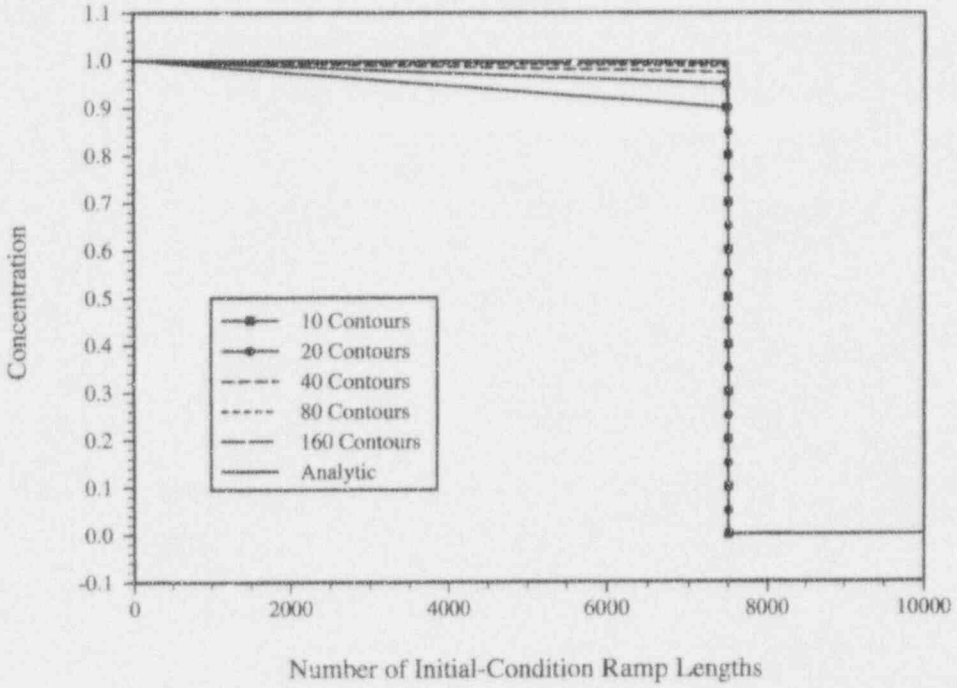

(a)

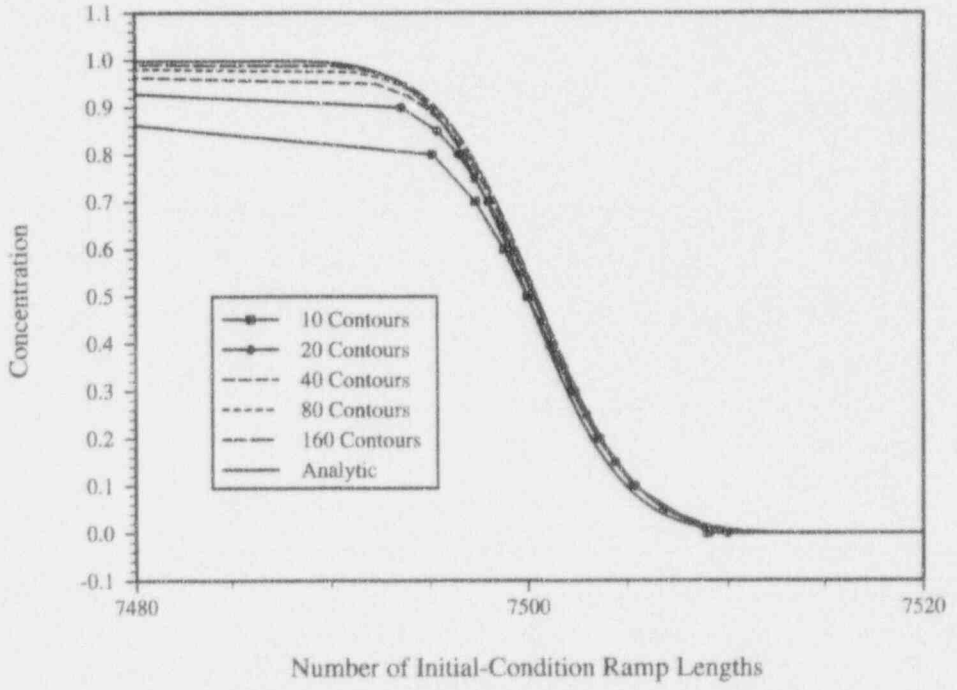

(b)

Figure 7-4. Advection-dominated solutions Pe = 10^3 and Da = 0: (a) 0 to 10,000*L, and (b) 7,480 to 7,520*L

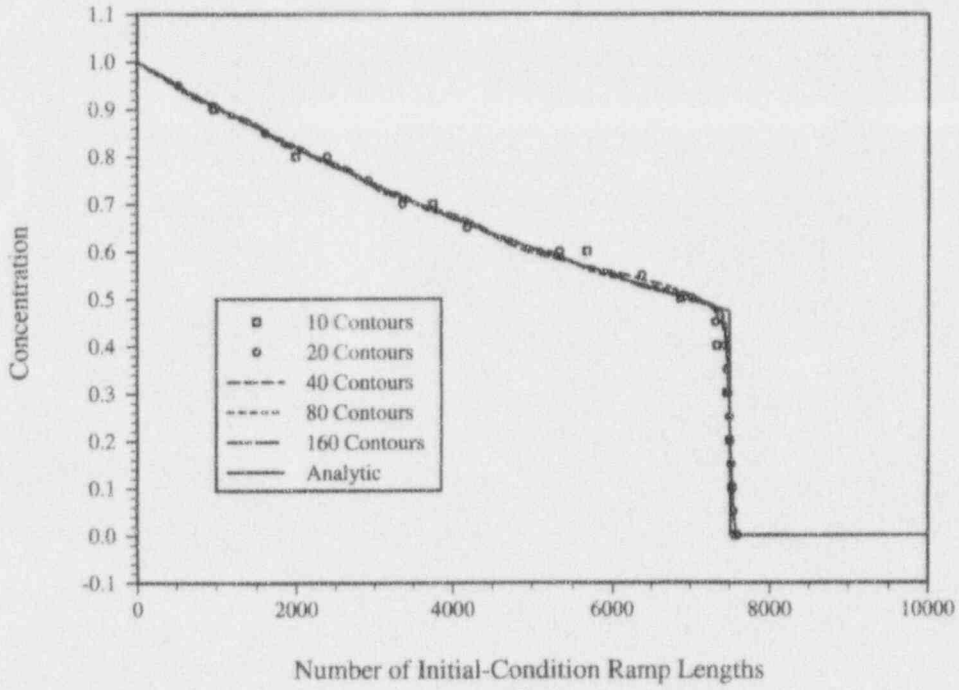

(a)

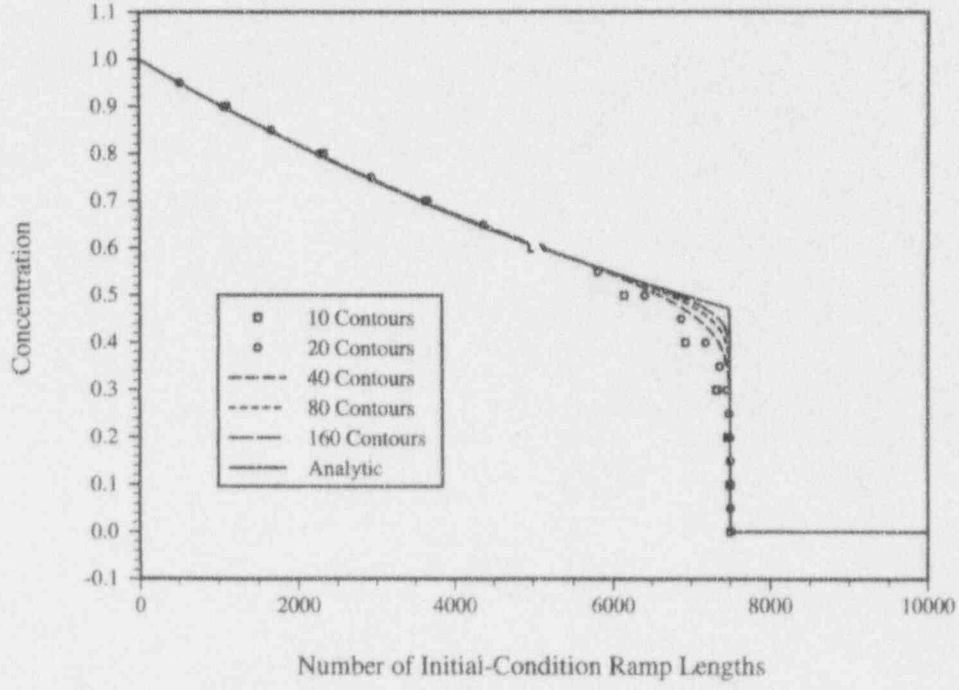

(b)

Figure 7-5. Reaction-dominated solutions $Pe = 10^3$ and $Da = 10^{-4}$: (a) characteristic velocity incorporates decay, and (b) decay incorporated using operator splitting

$$q = - k\lambda \left(\frac{dP}{d\theta} \frac{\partial \theta}{\partial x} + \rho g \frac{\partial z}{\partial x} \right) \tag{7-11}$$

As the response time for pressure is nearly instantaneous compared to the response time for moisture content, water pressure is assumed continuous throughout a region where moisture content is above the residual moisture content. Thus, in general, moisture content is discontinuous at material discontinuities. At such a discontinuity, by adopting a pressure-based representation for the conservation equation

$$\frac{d\theta}{dP} \frac{\partial P}{\partial t} + \frac{\partial q}{\partial x} = 0 \tag{7-12}$$

Noting that $\partial P/\partial t$ is identical on each side of the discontinuity, and using Eq. (7-5), the flux across the discontinuity is

$$q^* = \frac{(L\theta')^+ q^- + (L\theta')^- q^+}{(L\theta')^+ + (L\theta')^-} \tag{7-13}$$

where q^* is the flux across the discontinuity, one side of the discontinuity is denoted by $+$ and the other by $-$, L is the distance between the element midpoint and the discontinuity, and $\theta' = d\theta/dP$. Numerical experimentation bears out that the θ' terms should be evaluated at the moisture content adjacent to the discontinuity (rather than the usual procedure of evaluating all quantities at element midpoints). Further, in order to compensate for roundoff errors, at the end of each time step the saturations on either side of the discontinuity are adjusted toward the average pressure at the discontinuity.

Two comparison cases are presented. In both comparisons, soil properties are described with the van Genuchten-Mualem model

$$\theta(\psi) = \theta_r + \frac{\theta_s - \theta_r}{[1 + (\alpha |\psi|)^n]^m} \tag{7-14}$$

and

$$K(\psi) = K_{sat} \frac{\left\{1 - (\alpha |\psi|)^{n-1} \left[1 + (\alpha |\psi|)^n\right]^{-m}\right\}^2}{\left[1 + (\alpha |\psi|)^n\right]^{m/2}} \tag{7-15}$$

The first comparison follows Chapter 9.2.2.1 in CNWRA (1993), with benchmarking against the UNSAT1D code written by Celia (1991). In this comparison, the invasion of water from the top of a one-dimensional (1D) vertical column is simulated, where the column was assumed to have the uniform properties of $\alpha = 0.0335\ \text{cm}^{-1}$, $\theta_s = 0.368$, $\theta_r = 0.102$, $n = 2$, $m = 0.5$, and $K_{sat} = 9.22 \times 10^{-3}$ cm/s, and is 100 cm in length. For purposes of comparison, the initial pressure head throughout the column was -1000 cm, with an imposed pressure head of -75 cm at the column top. Noting that there is an initial ramp condition imposed by linear basis functions, each simulation was run with a linear saturation profile

corresponding to the ramp condition on the coarsest mesh (boundary condition saturation to initial condition saturation in 2.5 cm). The simulations were terminated after 1 day.

Several solutions are shown in Figure 7-6a. Finite element solutions result from discretizing the column into 40, 200, 800, and 4,000 elements, respectively, whereas the method of contours results are for discretizations of the saturation profile into 10, 20, 40, 80, and 160 moving contours, respectively. From Figure 7-6a, it appears that all of the solutions are essentially identical, aside from the coarsest finite-element solution. By plotting the vicinity of the front (Figure 7-6b), the differences between the solutions are magnified. As expected, under refinement the two schemes converge toward the same solution.

The procedures both perform well from the standpoint of mass balance. The finite-element procedure is inherently mass-conservative (Celia, 1991), while the worst mass balance error for the method of contours is 2.9×10^{-8} for the 10-contour solution, where mass balance is calculated as the ratio of the difference between net inflow and mass accumulated to the net inflow.

The 20-moving contour solution, with 995 time steps, is about as close to the true solution as the 200-element solution, with 1500 time steps. Comparison of computational effort is not straightforward, as the method of contours procedure is coded in Matlab scripts whereas UNSAT1D is coded in FORTRAN; further, each time step in the finite element procedure requires several iterations to accommodate nonlinearities. Still, for this case it appears that there is some computational advantage in using the method of contours.

The second example is a more challenging modeling exercise. The comparison in the first example is extended by including two low-permeability layers near the top of the column. The top, middle, and bottom layers are the same material as in the first example. The low-permeability layers are assumed to have the uniform properties of $\alpha = 0.044\ \text{cm}^{-1}$, $\theta_s = 0.0265$, $\theta_r = 0.312$, $n = 2.2$, $m = 0.545$, and $K_{sat} = 4.3\times10^{-3}$ cm/s, and each are 10 cm in length. The low-permeability layers are separated by a 10-cm layer of high-permeability material. There is an 8.75-cm layer of high-permeability material at the top of the column, and the bottom of the column is also filled with high-permeability material. Identical initial and boundary conditions are imposed as in the first example; however, the simulations are stopped after 4 days of simulated time.

Several solutions are shown in Figure 7-7. The finite-element solutions result from discretizing the column into 40, 200, 800, and 4,000 elements respectively; the method of contours solutions result from discretizing the saturation profile into 10, 20, 40, and 80 moving nodes. In order for the method of contours to capture redistribution of moisture at layer boundaries, additional nodes are needed within the layers. For the 10-node simulation, these additional nodes are distributed approximately every 2.5 cm, and are refined as the number of moving contours increase. Agreement is shown between the UNSAT1D code results and the method of contour calculations, although the method of contour results exhibit mass balance errors of about 4 percent.

Preparing this particular example pointed out some areas where the moving contour approach has difficulty. The standard explicit scheme, used where the solution has low-gradient nodes, is not mass-conserving due to the explicit time stepping, thus mass balance can be significantly impaired. Mass balance problems can be exacerbated when a front hits a material discontinuity, for there is no clear-cut method for switching from moving-contour nodes to low-gradient nodes at such a discontinuity. Further,

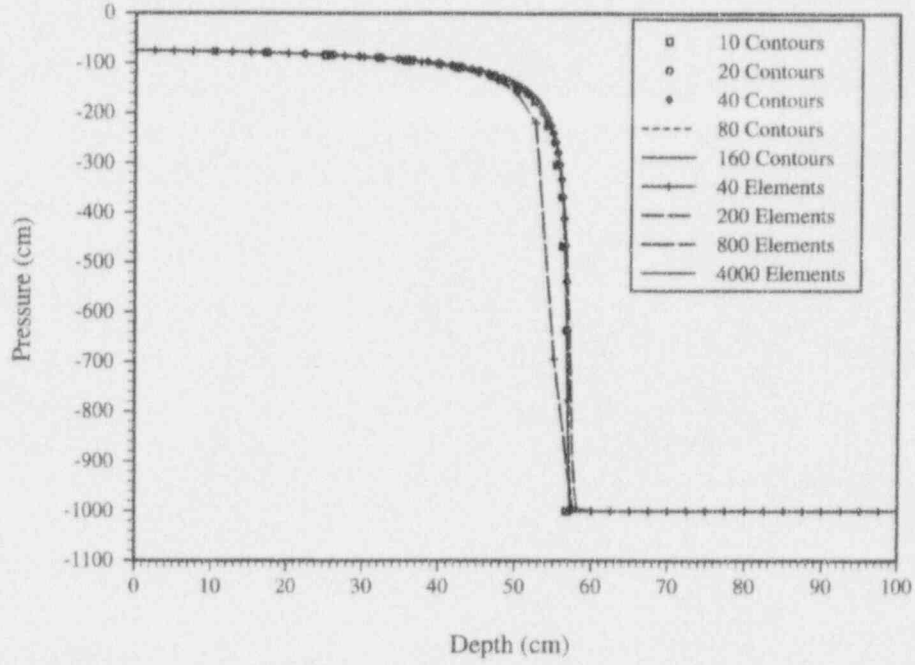

(a)

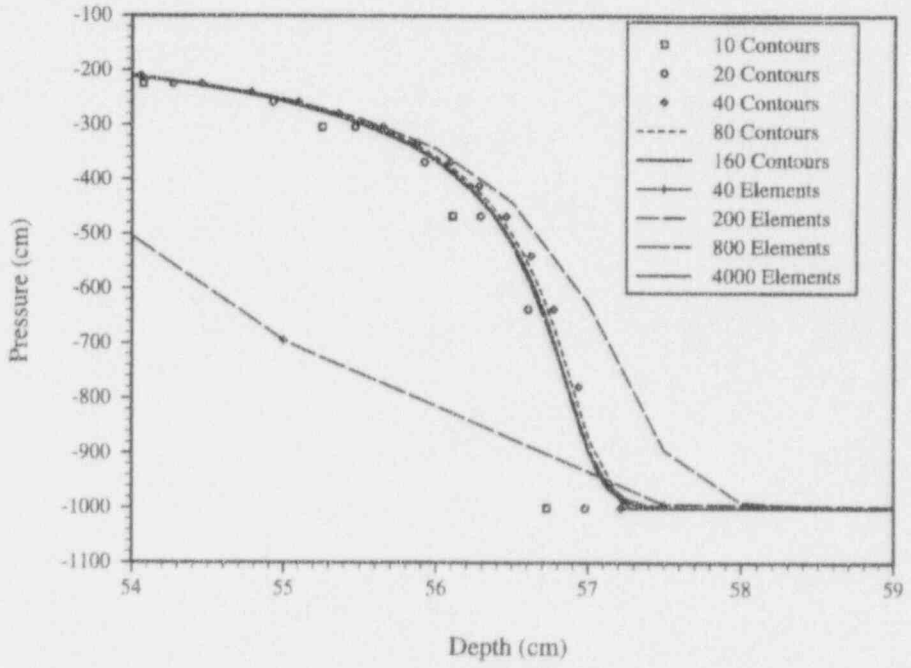

(b)

Figure 7-6. Comparison of moving-contour and UNSAT1D under refinement for homogeneous domain: (a) pressure solution over entire domain (0 to 100 cm), and (b) pressure solution near the front (55 to 59 cm)

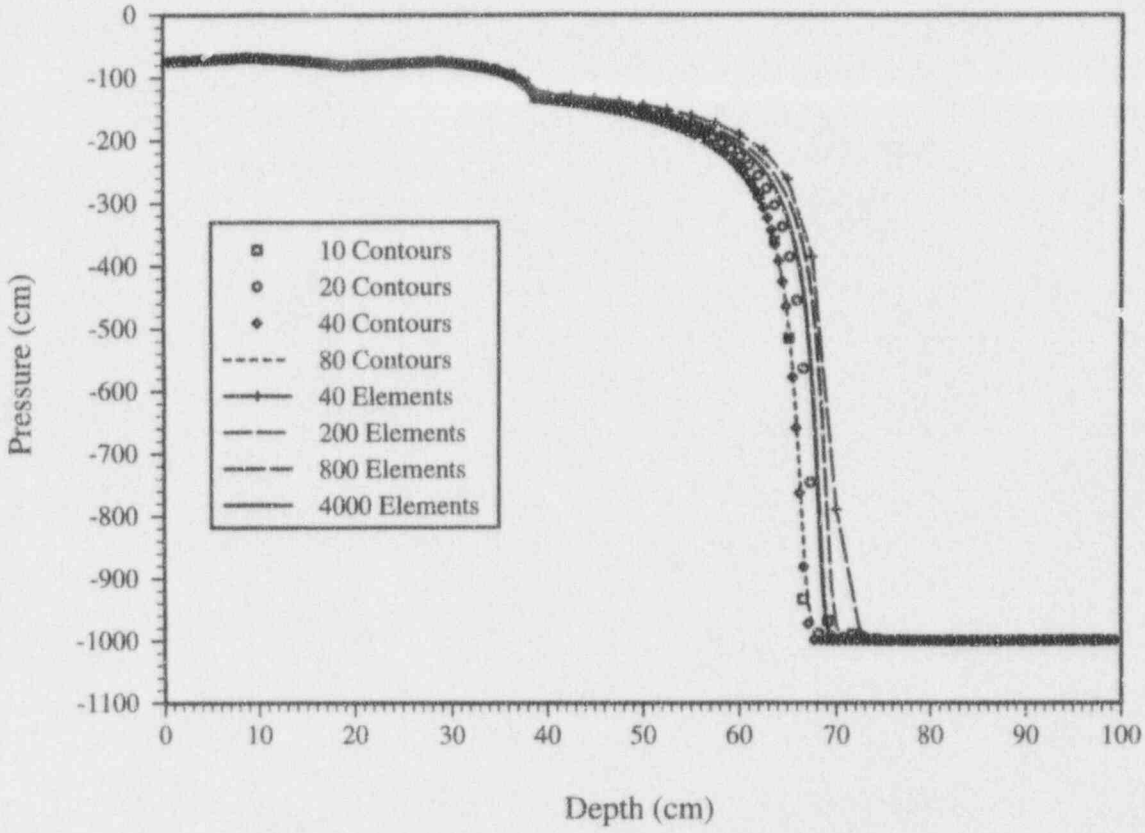

Figure 7-7. Comparison of moving-contour and UNSAT1D for five-layer domain

when material properties are rapidly varying, but not discontinuous, the true solution can develop low-gradient regions that are difficult to detect with the method of contours procedure.

The method of contours also has difficulty when different regions have strongly contrasting permeabilities. The region with the higher permeability determines the time-step size, even if this region is nearly at equilibrium. Small changes in the lower-permeability region are amplified, causing nodes to oscillate about the true solution in the high-permeability region. This oscillation often determines the time-step size for the problem, swamps the effects of the low-permeability region, drastically slows the solution, and can strongly impact the mass balance.

7.2.2.4 Summary and Results

A moving-contour approach, adapted to handle parabolic equations, was successfully applied to a number of test cases. The technique performs extremely well when simulating problems characterized by an invading front. On the other hand, the technique requires an inordinate number of time steps when the problem is characterized by large contrasts in time constant, such as arise in layered systems. From the previous computational tests, it does not appear that the method of contours is sufficiently robust and computationally efficient enough to replace more standard simulators. However, its capability to solve hyperbolic problems may make it very useful for benchmarking existing PA codes.

7.2.3 Task 3—Model Evaluation: Yucca Mountain INTRAVAL Test Case

The objective of this task is to develop practical quantitative and qualitative methods for determining the validity of flow and transport models applicable to unsaturated media. Considerable effort in this task has been devoted to participation in the international INTRAVAL project on the validation of geosphere models of flow and transport used to assess the safety of HLW repositories. The YM INTRAVAL test case was proposed by A. Flint, U.S. Geological Survey (USGS), at the February 1992 workshop in Sydney, Australia. Because of the obvious direct relevance of such a test case to NRC and CNWRA research efforts, and because INTRAVAL was scheduled to end in September 1993, it was decided that both the NRC and CNWRA teams would actively participate in this validation exercise.

As posed to the modelers, the problem was to use rock-hydraulic property data, detailed microstratigraphic data, and measured saturation profiles in near-surface boreholes provided by the DOE/USGS to construct a model and predict the water content profile at the then to-be-drilled USGS Well (USW) UZ-16 borehole (henceforth referred to as UZ-16). Upon completion of the modeling efforts and drilling of borehole UZ-16, measured water contents in UZ-16 were released so that direct comparisons of observations and predictions could be made.

7.2.3.1 Conceptual Model Development

Participants in the YM test case modeling exercise were provided with saturations, water contents, and porosity data, as well as lithologic descriptions of the core from three near-surface boreholes drilled in WT-2 wash on the eastern flank of YM. Measured saturation profiles in near-surface boreholes USW UZN-53, USW UZN-54, and USW UZN-55 were provided to the participants for calibrating the model used to predict the water content profile in UZ-16. UZN-54 and UZN-55, the two calibration boreholes considered in this study, lie some 60 m apart and are located just to the east-southeast of the perimeter of the proposed repository. UZN-54 lies directly in WT-2 wash and UZN-55 lies to the north, on the side slope of this wash. UZ-16 has been drilled 100 m downslope and to the east of UZN-55 and penetrates the entire 490-m thick unsaturated zone terminating just below the water table. In contrast, UZN-54 and UZN-55 are approximately 75 m deep and penetrate only the Tiva Canyon (TC) member and the upper portion of the Topopah Spring (TS) member.

The hydrostratigraphic column constructed for borehole UZ-16 consisted of 24 distinct layers that were delineated on the basis of detailed lithostratigraphic descriptions and measured values of porosity and bulk rock density. A description of the lithology of each of the 24 layers, the thickness of each layer, and the vertical distribution of porosity for UZ-16 are shown in Figure 7-8. For each layer, the fracture density was estimated from the information gathered from UZ-6. Water retention data were obtained from cores taken from surface outcrops of those units presumed to exist at UZ-16. These water retention data were plotted and then combined where similarity of the shape of the water retention curves and porosity values indicated that the samples were from the same hydrostratigraphic unit.

Unsaturated hydraulic conductivity and water release functions were assumed to be adequately described by the van Genuchten-Mualem model. For each set of water retention data, the van Genuchten model parameters α and n were determined using a standard Levenberg-Marquardt nonlinear least squares procedure. The saturated water content, θ_s, was set to the arithmetic mean of the measured porosity for all samples from the layer, and the residual water content θ_r was determined on the basis of the shape of the dry end of the retention curve. The van Genuchten model parameters were mapped

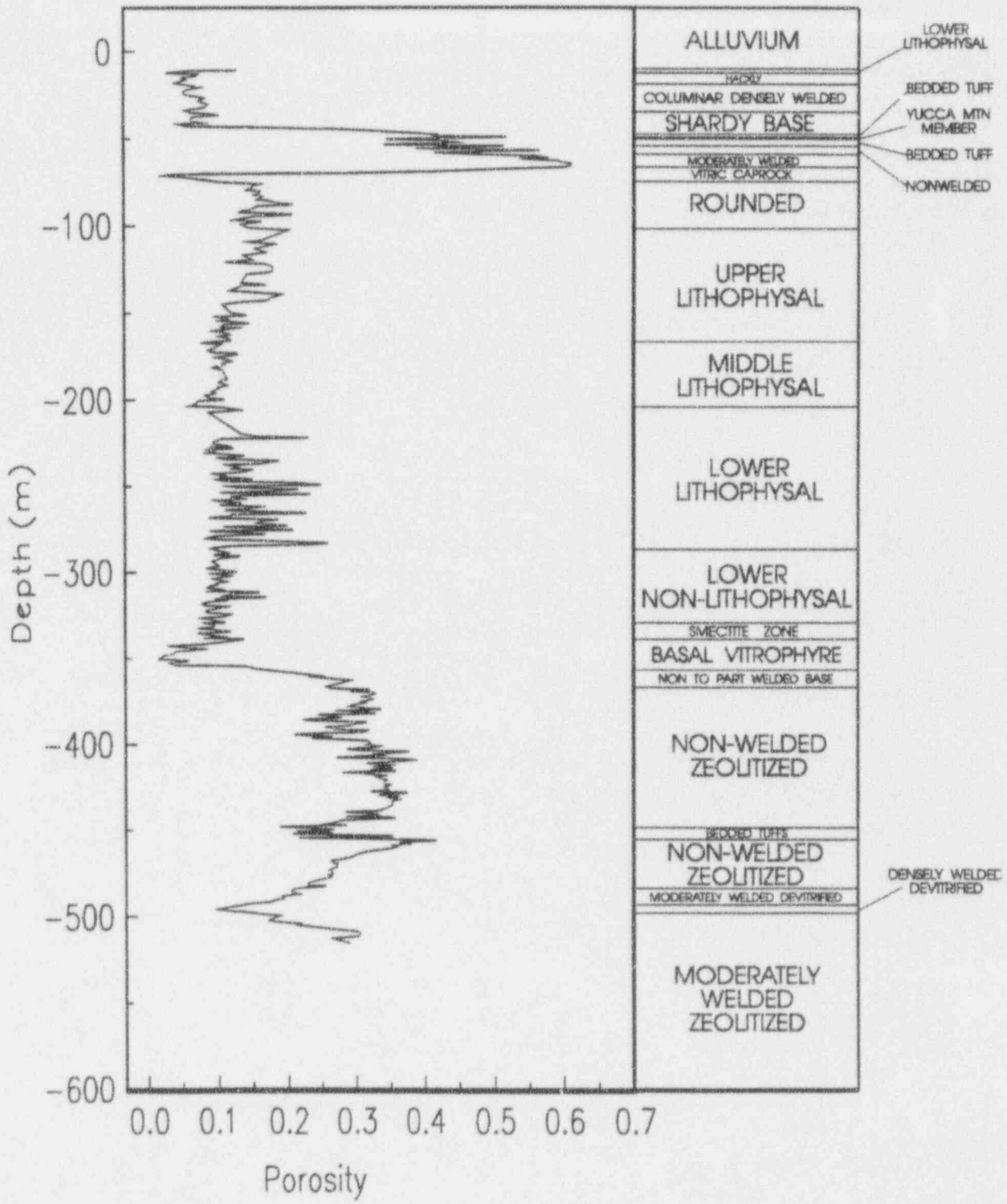

Figure 7-8. Stratigraphic column for UZ-16

to the 24-layer hydrostratigraphic description of UZ-16 by correlating the lithologic descriptions and porosity values of the outcrop samples to those from UZ-16. The van Genuchten parameters used for each of the 24 layers are shown in Table 7-2.

All modeling results described here were obtained from a simple 1D vertical, steady-state, isothermal model that employed the composite fracture-matrix continuum constitutive property model of Klavetter and Peters (1986), that assumes that pressure in the fracture and the immediately adjacent matrix are equal. This nonlinear, second-order ODE with specified flux condition at the upper boundary was analytically integrated to obtain a nonlinear, first-order initial value problem with specified pressure head at the lower boundary. The initial value problem is

$$\frac{d\psi}{dz} = -1 - \frac{q_0}{K(\psi)} \tag{7-16}$$

$$\psi(0) = \psi_0 \tag{7-17}$$

where ψ is the pressure head, $K(\psi)$ is the unsaturated hydraulic conductivity, z is the vertical coordinate, q_0 is the specified flux at the surface, and ψ_0 is the specified pressure head at the bottom of the borehole. This initial value problem was then solved using an adaptive, fourth-order Runge-Kutta procedure.

Measured saturations from near-surface boreholes USW UZN-54 and UZN-55 were used to estimate the flux at the surface. To determine the steady-state flux rates implied by the saturation profiles in UZN-54 and UZN-55, a simple inverse program was developed that minimized the sum of squared differences between measured and predicted saturations. This inverse program was constructed by embedding the Runge-Kutta solver for the initial value problem directly into a Levenberg-Marquardt nonlinear least squares routine. Parameters by van Genuchten were mapped to the hydrostratigraphic units defined for boreholes UZN-54 and UZN-55 by correlating lithologic descriptions and porosity measurements. Lower boundary conditions for UZN-54 and UZN-55 were determined by solving the van Genuchten model for pressure head given the parameters for the hydrostratigraphic unit and the measured value of saturation at the bottom of each borehole. Optimum vertical flux rates computed for boreholes UZN-54 and UZN-55 using the inverse procedure were -0.0086 mm/yr and -0.0135 mm/yr, respectively. Comparison of measured and computed saturation profiles for UZN-54 and UZN-55 are shown in Figures 7-9a and 7-9b, respectively.

The upper boundary conditions specified for the 1D model of UZ-16 were the fluxes determined for UZN-54 and UZN-55 using the inverse procedure, while the boundary condition imposed at the water table was a specified pressure head of zero. Measured water contents in UZ-16 and the predicted water content profile computed from the 1D model are shown in Figure 7-10. Considering the simplicity of the conceptual model, remarkably good agreement was obtained between the results from the simplified 1D steady-state model and the measured water content profile for both estimated vertical flux rates. However, the model failed to predict the higher water contents observed within the nonwelded units at the base of the TC member and overestimated the water content within the nonwelded, zeolitic unit of the Prow Pass. It should be noted that water retention data for the Prow Pass were not provided to the modelers, and estimates for Prow Pass hydraulic properties had to be gleaned from other published data.

Table 7-2. Matrix hydraulic parameters for 24-layer UZ-16 model

Top (m)	Bottom (m)	α (m^{-1})	n	K_s (m/s)	θ_s	θ_r	Lithology
0.00	−10.80	.1	1.3	1.0e−6	.098	.0001	Alluvium
−10.80	−17.80	.031	1.5	7.1e−13	.057	.003	TC Lower Lithophysal
−17.80	−34.10	.0024	1.82	7.8e−10	.071	.007	TC Hackly
−34.10	−42.60	.0024	1.82	3.9e−13	.072	.007	TC Colmn. Densely Welded
−42.60	−44.40	.86	1.3	5.8e−8	.28	.001	TC Colmn. Mod. Welded
−44.40	−48.40	.86	1.3	1.6e−6	.42	.001	TC Shardy Base
−48.40	−49.30	3.69	1.33	5.5e−5	.52	.01	TC Bedded Tuffs
−49.30	−52.30	1.40	1.28	4.3e−6	.41	.008	TC Yucca Mt. Member
−52.30	−58.00	.76	1.34	3.4e−6	.45	.009	TC Bedded Tuffs
−58.00	−66.30	.22	2.35	3.3e−6	.57	.011	TS nonwelded
−66.30	−69.60	.22	1.8	5.0e−7	.46	.01	TS Mod. Welded
−69.60	−71.90	.0076	1.8	3.7e−11	.042	.0004	TS Vitric Caprock
−71.90	−100.70	.14	1.42	1.8e−8	.16	.004	TS Rounded
−100.70	−165.60	.105	1.36	1.4e−11	.14	.004	TS Upper Lithophysal
−165.60	−203.30	.0074	1.64	4.5e−13	.10	.01	TS Middle nonLithophysal
−203.30	−285.80	.053	1.46	6.9e−12	.14	.008	TS Lower Lithophysal
−285.80	−328.30	.25	1.23	2.4e−12	.11	.01	TS Lower nonLithophysal
−328.30	−338.30	.25	1.23	7.0e−12	.096	.008	TS Smectite Zone
−338.30	−354.80	.0076	1.8	3.7e−11	.063	.006	TS Basal Vitrophyre
−354.80	−367.50	.021	2.65	2.0e−11	.24	.003	TS nonpart. Welded
−367.50	−446.80	.0051	1.68	3.0e−11	.32	.005	Calico Hills (CH) Nonwelded Zeolitic
−446.80	−454.80	.0026	1.4	2.5e−11	.24	.002	CH Bedded Tuff
−454.80	−482.20	.006	2.4	2.3e−12	.29	.003	Prow Pass (PP) Nonwelded Zeolitic
−482.20	−490.00	.004	1.46	6.5e−12	.20	.002	PP Mod. Welded Devit.

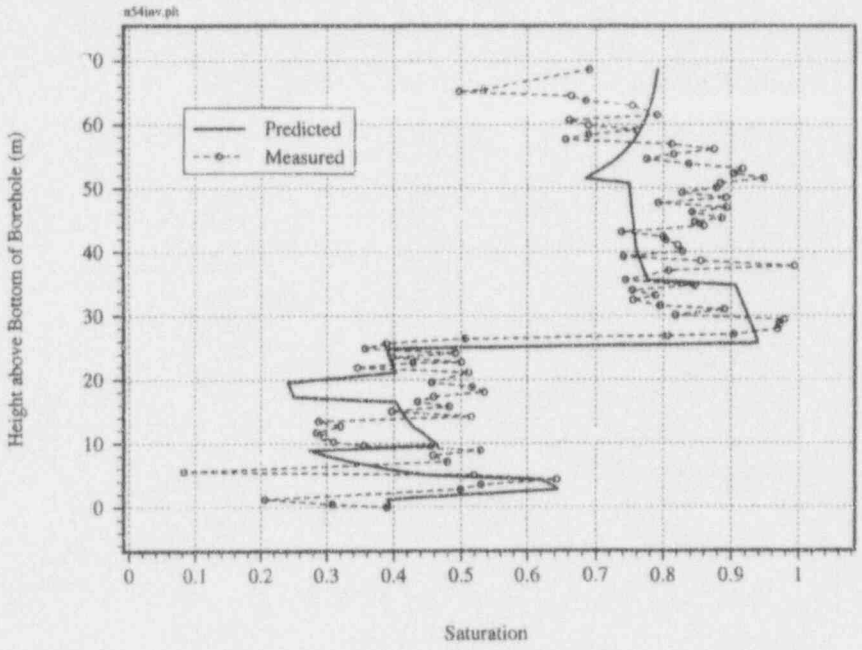

(a)

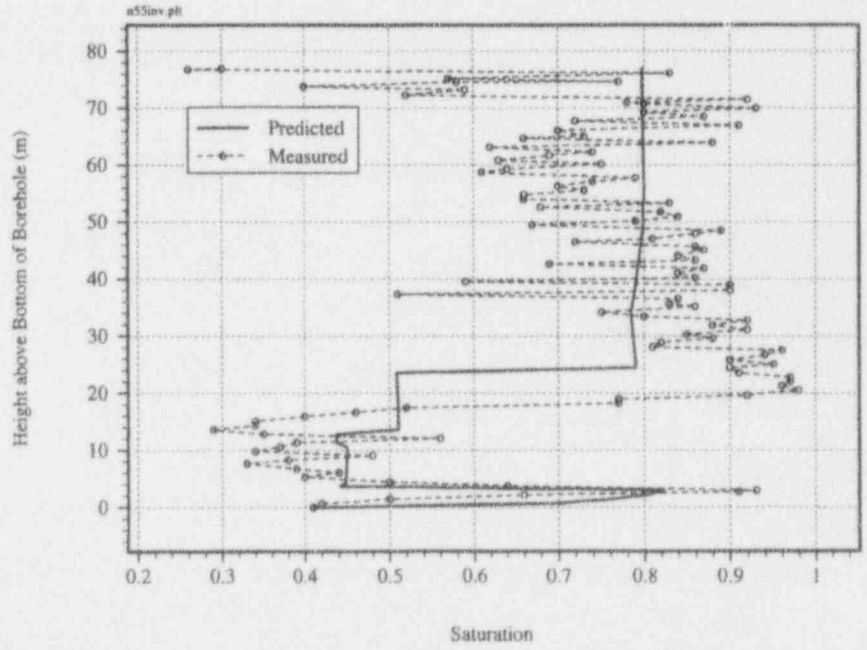

(b)

Figure 7-9. Comparison of measured and calibrated saturation profiles for (a) UZN-54, and (b) UZN-55

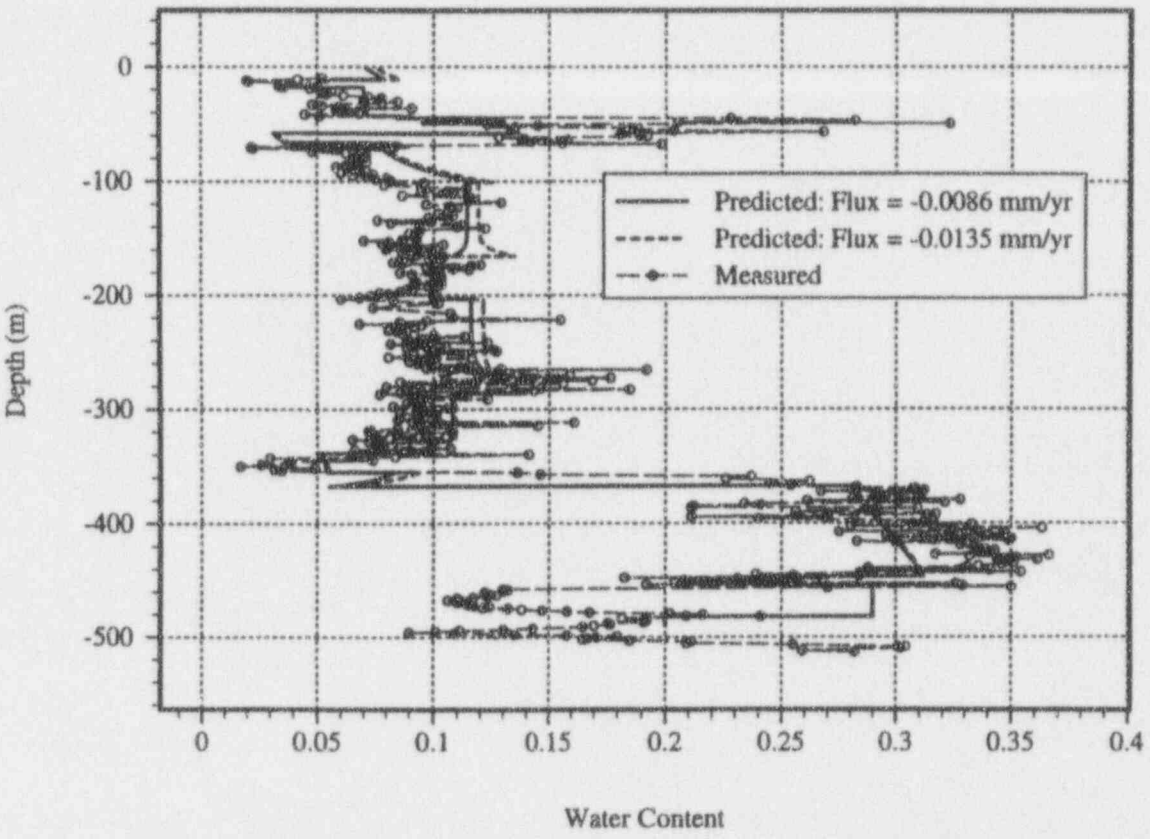

Figure 7-10. Comparison of measured and predicted water content profiles for UZ-16

7.2.3.2 Summary and Results

Other participants in the YM test case were also able to obtain good agreement between their model's predicted water contents and those observed in UZ-16. However, their results were achieved using different conceptual models of the flow regime and significantly different estimates of the vertical flux through YM. Indeed, estimates of vertical fluxes ranged from the −0.0086 mm/yr used in this study to −5 mm/yr for a more sophisticated two-dimensional (2D) model that explicitly incorporated the effects of fractures. The fact that vertical fluxes of greatly different magnitude all produce similar water content profiles suggests the observed water content profile reveals very little about the infiltration regime at YM.

It has been shown by Ross (1984) for 1D, nonisothermal, steady-state flow in a homogeneous stratigraphic column representing YM that, even under conditions of zero net infiltration, a downward vertical flux of liquid water of −0.03 mm/yr will occur to balance the upward diffusion of water vapor caused by the geothermal gradient. More detailed numerical models developed by Buscheck and Nitao (1993) and Pruess and Tsang (1993), which use several layers to account for the hydrostratigraphic detail at YM, also demonstrate that under nonisothermal conditions a vertical flux of liquid water of between −0.01 and −0.04 mm/yr can occur under conditions of zero net infiltration.

These results suggest measured water contents by themselves reveal little about the nature of infiltration at YM. Moreover, the fact that disparate conceptual models can produce very similar and very accurate water content profiles indicates the data provided for this test case are insufficient to demonstrate the validity of any one model. In order to discriminate between the models one must also have some method for bounding the magnitude of the vertical flux. Simple transport models may prove useful in estimating flux rates if environmental tracer data such as $\delta\,^{18}O$, δD, or tritium can be obtained from pore or fracture waters.

7.3 ASSESSMENT OF PROGRESS

In the current reporting period, strong emphasis was given to research under Task 1—Conceptual Model Development, that includes research on hydrologic conceptual models and disruptive event scenarios. Activities in Task 2—Computational Model Development were reduced as were those for Task 3—Model Evaluation.

Work on disruptive event scenarios (i.e., future system states) was given increased priority in accordance with technical direction from the NRC project officer. The topic of model validation (i.e., confidence building) was given the next level of priority because it is a KTU (Type 5) in CDS 6.1, Assessment of Compliance with the Requirement for Cumulative Releases of Radioactive Materials. As part of the continuing effort to address the IPA need for more robust, accurate, and efficient methods for modeling flow and transport, research was conducted on a new computational method. Improved computational methods will directly benefit the total-system code and auxiliary analysis codes. Significant improvements on this topic, in turn, will lessen constraints of simplifying assumptions that are part of the Mathematical Models KTU (Type 4). Research on conceptual models for flow and transport in fractured-porous tuff was continued as a joint effort with the Geochemical Analog of Contaminant Transport in Unsaturated Rock Research Project, but is not reported here because the analysis and interpretation of laboratory data are incomplete at this time.

Disruptive event scenarios are an important element of the NRC IPA exercises and provide the basis for estimating how well the geologic repository may perform under combinations of adverse events and processes. In this reporting period, the major portion of staff effort was devoted to two related activities: (i) an independent review and critique of the four IPA disruptive event scenario types, and (ii) a state-of-the-art review of the scenario-selection approaches. The first activity produced a detailed letter report containing recommendations for improvement of the current IPA scenario models and modules. These recommendations will be incorporated into the NRC/CNWRA plan for the IPA Phase 3 exercise. The second activity produced a technical report entitled Review of Scenario-Selection Approaches for Performance Assessment of High-Level Waste Repositories and Related Issues (Bonano and Baca, 1994). The report shows that many countries are using approaches very similar to the NRC/SNL scenario methodology used in IPA. Only the United Kingdom is utilizing a truly distinct approach that is based on environmental simulation. The report identifies a number of open generic issues in scenario analysis such as the validity of estimates of probability of occurrence, lack of uniqueness or completeness of scenarios, as well as the role of expert judgment in these issues. The subject document is expected to contribute to the formulation of guidance on disruptive scenarios. Both of the above documents represent significant progress toward the objectives of Task 1.

Research on conceptual models of flow and transport in fractured-porous tuff is being performed jointly with the Geochemical Analog of Contaminant Transport in Unsaturated Rock Research Project.

Although not reported here, progress was made on acquiring the unsaturated hydraulic conductivity properties of welded tuff (the laboratory analysis is being funded by the Geochemical Analog of Contaminant Transport in Unsaturated Rock Research Project). As these properties are compiled, they will be used to formulate conceptual and mathematical models of matrix-fracture interactions as part of this research project. Detailed discussion of progress will be included in the next reporting period.

A number of advanced computational techniques have been evaluated to find robust, accurate, and efficient techniques for solving the governing equations of flow and transport in unsaturated fractured-porous media. Several of these methods have been found to be very promising in this regard. One recent development, for example, indicates that the computational speed of auxiliary analysis codes, such as DCM3D (Updegraff et al., 1991), VTOUGH (Nitao, 1989), BIGFLOW (Ababou and Bagtzoglou, 1993), PORFLOW (Runchal and Sagar, 1992), and FLASH (Baca and Magnuson, 1992), may be improved by a factor of two or more. The approach for achieving this speed-up is being documented in a paper that will be submitted for journal publication. It is expected that research on this topic will yield significant benefits to the enhancement of the total-system and subsystem PA codes. The principal findings of this research will be reported in a topical report later in 1994. Very good progress has been made toward achieving the objectives of Task 2.

One popular view of model validation is that it is a scientific process for building confidence in models. However, many other views exist including that models cannot be validated. This multiplicity of views has resulted in a lack of consensus on the meaning and need for model validation. The investigators of this research project have been active participants in the international model validation project called INTRAVAL. Through the involvement in INTRAVAL, hydrologic models have been applied to experimental data sets from the Las Cruces Trench and, more recently, to field data from the YM site. This latest and final INTRAVAL validation exercise, which was completed in this reporting period, supports the conclusion that collection of adequate hydrologic field data for model validation exercises may be problematic because of the limitations of current measurement technology. For example, while measurements of moisture profiles are possible, their use in interpretation of moisture fluxes in the heterogeneous and fractured tuff is often nonunique and highly speculative. Adequate data sets for model validation exercises may not be available until new measurement techniques are available that can provide accurate measurements of: (i) pressure head profiles in the rock matrix and fractures (ii) surface boundary conditions, and (iii) estimates of flux rates.

7.4 PLANS FOR NEXT REPORTING PERIOD

In the next reporting period, high priority will continue to be placed on the Task 1 work. In particular, research activity will be focused on completing the work on near-field conceptual and mathematical models for flow; a technical report on this topic will be produced to fulfill an Intermediate Milestone. Work will continue on improvement of the IPA disruptive event scenario models and modules. This will include a closer examination of the environmental simulation approach. A parametric modeling study of fluid flow will be initiated using the hydraulic properties for tuff core samples from Peña Blanca.

The Task 2 work on advanced computational methods will primarily focus on incorporation of new developments in auxiliary analysis codes and documentation of principal findings. The documentation of results will include preparation of journal articles and a topical report.

The Task 3 activity on model validation is expected to pursue a new direction for consistency with the regulatory positions expressed in two key NRC documents: (i) NRC/Swedish Nuclear Power Inspectorate paper on model validation, and (ii) Performance Assessment Strategic Plan. In addition, the work will need to be coordinated with the hydrologic model testing planned between the CNWRA and the University of Arizona. The model testing will be performed under the new research project that is being planned to replace the Stochastic Unsaturated Flow and Transport Research Project. Current thinking is for the BIGFLOW code to be applied to data obtained from infiltration experiments at Queen Creek (in the vicinity of the Never Sweat Tunnel).

7.5 REFERENCES

Ababou, R., and A.C. Bagtzoglou. 1993. *BIGFLOW: A Numerical Code for Simulating Flow in Variably Saturated, Heterogeneous Geologic Media, Theory and User's Manual, Version 1.1.* NUREG/CR-6028, CNWRA 92-026. Washington, DC: U.S. Nuclear Regulatory Commission.

Baca, R.G., and S.O. Magnuson. 1992. *FLASH—A Finite Element Computer Code for Variably Saturated Flow.* EGG-GEO-10274. Idaho Falls, ID: EG&G Idaho, Inc.: Idaho National Engineering Laboratory.

Bear, J. 1972. *Dynamics of Fluids in Porous Media.* New York, NY: Elsevier.

Bonano, E.J., and R.G. Baca. 1994. *Review of Scenario Selection Approaches for Performance Assessment of High-Level Waste Repositories and Related Issues.* CNWRA 94-002. San Antonio, TX: Center for Nuclear Waste Regulatory Analyses.

Buckley, S.E., and M.C. Leverett. 1942. Mechanism of fluid displacement in sands. *Transcripts of the American Institute of Mining, Metallurgical, and Petroleum Engineers* 146: 107–116.

Buscheck, T.A., and J.J. Nitao. 1993. The analysis of repository-heat-driven hydrothermal flow at Yucca Mountain. *Proceedings of the Fourth International High-Level Radioactive Waste Conference.* La Grange Park, IL: American Nuclear Society: 847–867.

Celia, M.A. 1991. *The One-Dimensional Princeton Unsaturated Code.* Fundamentals of Unsaturated Zone Modeling Short Course. Princeton, NJ: Princeton University.

Connor, C.B., and E.B. Hill. 1993. Volcanism research. *NRC High-Level Radioactive Waste Research at CNWRA, January to June, 1993.* B. Sagar, ed. CNWRA 93-011S. San Antonio, TX: Center for Nuclear Waste Regulatory Analyses.

Dafermos, C. 1972. Polygonal approximations of solutions of the initial value problem for a conservation law. *Journal of Mathematical Analysis and Applications* 38: 33–41.

DeWispelare, A.R., L.T. Herren, M.P. Miklas, and R.T. Clemen. 1993. *Expert Elicitation of Future Climate in the Yucca Mountain Vicinity.* CNWRA 93-016. San Antonio, TX: Center for Nuclear Waste Regulatory Analyses.

Electric Power Research Institute. 1990. *Demonstration of a Risk-Based Approach to High-Level Waste Repository Evaluation.* EPRI NP-7057. Palo Alto, CA: Electric Power Research Institute.

Electric Power Research Institute. 1992. *Demonstration of a Risk-Based Approach to High-Level Waste Repository Evaluation: Phase 2.* EPRI TR-100384. Palo Alto, CA: Electric Power Research Institute.

Holden, H., L. Holden, and R. Hoegh-Krohn. 1988. A numerical method for first order nonlinear scalar conservation laws in one-dimension. *Computational and Mathematical Applications* 15(6–8): 595–602.

Klavetter, E., and R. Peters. 1986. *Fluid Flow in a Fractured Rock Mass.* SAND85-0855. Albuquerque, NM: Sandia National Laboratories.

Lucier, B. 1986. A moving mesh numerical method for hyperbolic conservation laws. *Mathematics of Computations* 146(173): 59–69.

Nitao, J.J. 1989. *V-TOUGH—An Enhanced Version of the TOUGH Code for the Thermal and Hydrologic Simulation of Large-Scale Problems in Nuclear Waste Isolation.* UCID-21954. Livermore, CA: Lawrence Livermore National Laboratory.

Pacific Northwest Laboratory. 1993. *Preliminary Total-System Analysis of a Potential High-Level Nuclear Waste Repository at Yucca Mountain.* PNL-8444. Richland, WA: Pacific Northwest Laboratory.

Pruess, K., and Y. Tsang. 1993. Modeling strongly heat-driven processes at a potential high-level nuclear waste repository at Yucca Mountain, Nevada. *Proceedings of the Fourth International High-Level Radioactive Waste Conference.* La Grange Park, IL: American Nuclear Society: 568–575.

Ross, B. 1984. A conceptual model of deep unsaturated zones with negligible recharge. *Water Resources Research* 20(11): 1,627–1,629.

Runchal, A., and B. Sagar. 1993. *PORFLOW: A Multifluid Multiphase Model for Simulating Flow, Heat Transfer, and Mass Transport in Fractured Porous Media, User's Manual, Version 2.41.* NUREG/CR-5991. CNWRA 92-003. Washington, DC: U.S. Nuclear Regulatory Commission.

Sagar, B., and R.W. Janetzke. 1993. *Total Performance Assessment (TPA) Computer Code: Description of Executive Module, Version 2.0.* CNWRA 93-017. San Antonio, TX: Center for Nuclear Waste Regulatory Analyses.

Sandia National Laboratories. 1992. *TSPA 1991: An Initial Total-System Performance Assessment for Yucca Mountain.* SAND91-2795. Albuquerque, NM: Sandia National Laboratories.

Stothoff, S. 1991. *A Boundary Integral Technique for Modelling Two-Phase Flow in Porous Media.* Ph.D. Dissertation. Princeton, NJ: Princeton University.

Stothoff, S. 1992. A semi-analytic solution technique for conservation equations. *Proceedings of the 7th International Mathematics And Computing Society Conference on Computer Methods for Partial*

Differential Equations. New Brunswick, NJ: International Mathematics and Computing Society: 123–129.

Stothoff, S., and G. Pinder. 1992. A boundary integral technique for multiple front simulation of incompressible, immiscible flow in porous media. *Water Resources Research* 28(8): 2,067–2,076.

Updegraff, C.D., D.E. Lee, and D.P. Gallegos. 1991. *DCM3D: A Dual Continuum, Three-Dimensional, Ground-Water Flow Code for Unsaturated, Fractured, Porous Media*. NUREG/CR-5536. Washington, DC: U.S. Nuclear Regulatory Commission.

U.S. Department of Energy. 1988. *Site Characterization Plan, Yucca Mountain Site, Nevada Research, and Development Area, Nevada*. DOE/RW-0199. Washington, DC: U.S. Department of Energy.

U.S. Nuclear Regulatory Commission. 1992. *Initial Demonstration of the NRC's Capability to Conduct a Performance Assessment for a High-Level Waste Repository*. NUREG-1327. Washington, DC: U.S. Nuclear Regulatory Commission.

U.S. Nuclear Regulatory Commission. 1994. *Phase 2 Demonstration of the NRC's Capability to Conduct a Performance Assessment for a High-Level Waste Repository*. NUREG-1464. Washington, DC: U.S. Nuclear Regulatory Commission.

Wang, J.S.Y., N.G.W. Cook, H.A. Wollenberg, C.L. Carnahan, I. Javandel, and C.F. Tsang. 1993. Geohydrologic data and models of Rainier Mesa and their implications to Yucca Mountain. *Proceedings of the Fourth International High-Level Radioactive Waste Conference*. La Grange Park, IL: American Nuclear Society: 675–681.

8 VOLCANISM RESEARCH

by Brittain E. Hill and Charles B. Connor

Investigators: Charles B. Connor, Brittain E. Hill, Kathy H. Spivey, Peggy Hunka (CNWRA)

NRC Project Officer: Linda A. Kovach

8.1 TECHNICAL OBJECTIVES

Characterization of the frequency and nature of past volcanic events in the Yucca Mountain region (YMR) and assessment of the probability and consequences of future volcanism are critical aspects of prelicensing scientific investigation. The technical objectives of the Volcanic Systems of the Basin and Range Research Project are to: (i) assess the probability of continued magmatic activity in the YMR, (ii) develop models that better predict the interaction between geologic structure and volcanism in this tectonic setting, and (iii) develop scenarios for the potential impact of volcanism on the candidate Yucca Mountain repository. Effective review of the U.S. Department of Energy (DOE) license application will require insight into volcanic processes operating in the YMR on several scales. These processes include assessment of: western Great Basin tectonic and structural controls on volcanism on local scales (10^2 to 10^3 km^2); the longevity of vent complexes and individual volcanoes in the western Great Basin; and the relationship between specific mappable faults, joints and fractures, and volcanic conduits such as dikes and dike swarms. The western Great Basin has been the site of recurring small-volume basaltic volcanism throughout the Quaternary. Modern analogs and theoretical studies have demonstrated convincingly that this activity encompasses a variety of eruption styles, from the gentle effusion of lavas to sub-Plinian and Plinian-style activity that has produced large and highly dispersive ash columns (e.g., Williams, 1950; McGetchin et al., 1974; Wilson et al., 1978; Wilson, 1980; Amos et al., 1983; Head and Wilson, 1989). The Volcanic Systems of the Basin and Range research project has been designed to assess the probability of future volcanism in the YMR, taking into account the range of activity and the structural controls on activity that are an inherent part of western Great Basin volcanism.

Insight gained through the Volcanic Systems of the Basin and Range Research Project will support the following sections of the License Application Review Plan (LARP): (i) Section 3.2.1.9; Evidence of Igneous Activity as a Potentially Adverse Condition, (ii) Section 3.2.2.7; Impact of Volcanism on Groundwater Movement, and (iii) Section 6.1; Assessment of Compliance with the Requirement for Cumulative Releases of Radioactive Materials. Research is necessary to develop these three sections of the LARP for the purpose of providing the U.S. Nuclear Regulatory Commission (NRC) with the methodology and acceptance criteria to determine DOE compliance with 10 CFR Part 60 requirements. Compliance Determination Methods (CDMs) for these LARP sections are currently under development. However, the Compliance Determination Strategies (CDSs) associated with evidence of Quaternary volcanism include Key Technical Uncertainties (KTUs) of Type 5, indicating that independent research by the NRC may be required to evaluate volcanism, and that volcanism poses a high risk of the NRC reaching unwarranted conclusions regarding compliance with 40 CFR Part 191 and 10 CFR Part 60.122(c)(15).

To date, three KTUs directly related to igneous activity have been identified as part of the CDS concerned with evidence of Quaternary igneous activity. These KTUs are:

- Low resolution of exploration techniques to detect and evaluate igneous features
- Inability to sample igneous features
- Development and use of conceptual tectonic models as related to igneous activity

In addition, five other KTUs have been identified that indirectly relate to igneous activity:

- Development of a conceptual groundwater flow model
- Prediction of future changes in the hydrologic system (due to tectonism)
- Conceptual model representation of the natural and engineered systems
- Variability in the model parametric values
- Prediction of future system states (disruptive scenarios)

Evaluation of these KTUs will require detailed safety review supported by analyses (Type 4), and detailed safety review supported by independent tests, analyses, and other investigations (Type 5). Specific tasks within the Volcanic Systems of the Basin and Range Research Project will address these KTUs. For example, development of a computerized database of volcanism in the western Great Basin will provide a basis for assessment of spatial and temporal patterns in volcanism in this region. This database, in conjunction with other ongoing research programs, will aid in the development of models describing the mechanisms that control the formation of igneous features. This investigation directly addresses KTUs related to development and use of conceptual tectonic models as related to igneous activity. In addition to evaluation of these KTUs, independent research in volcanism is needed to provide a basis to question how DOE research will address the potential consequences of igneous activity on repository performance, and to evaluate the DOE responses to these questions.

Successful completion of the Volcanic Systems of the Basin and Range Research Project and efficient integration with the LARP will require interaction with the Field Volcanism Research Project, an NRC research project that concentrates on eruption energetics, degassing, and controls on magma movement at shallow levels; the Tectonic Setting of the Central Basin and Range Research Project; and Geologic Setting Element Task 3 (Division of High-Level Waste Management) on faulting and dike interaction. The Volcanic Systems of the Basin and Range Research project, together with these associated investigations, will form the basis of volcanism models in Iterative Performance Assessment (IPA). The link between volcanism studies and IPA has been established, with preliminary probability models serving as the basis for IPA Phase 2 scenarios for volcanism. Volcanism research also provides support of NRC reactive work during the prelicensing stage. Results of the Volcanic Systems of the Basin and Range Research Project are utilized in reactive work, including at NRC–DOE Technical Exchanges and in the review of Topical Reports, Study Plans, and related reports.

Key elements of the Volcanic Systems of the Basin and Range Research Project are:

- Task 1: Literature review of Cenozoic volcanism and tectonism in the Basin and Range Province

- Task 2: Construction of a computerized database for Basin and Range volcanic and tectonic data
- Task 3: Critical review of Basin and Range volcanic and tectonic data, including an analysis of dating techniques for Cenozoic volcanic rocks
- Task 4: Analysis of database and volcano-tectonic model development
- Task 5: Semi-annual research reports

Research efforts in the Volcanic Systems of the Basin and Range Research Project have been initially directed toward the development of probability models of potential volcanic events in the YMR, based on geologic insight into tectonic processes operating in the western Great Basin and geologic controls on areal basaltic volcanism in general. Review of the regional tectonic setting of basaltic volcanism in the Great Basin, Task 1 of this project, is provided by Stirewalt et al. (1992). Connor and Hill (1993a, 1993b) discuss initial work on probability model development and the nature of basaltic volcanism in the YMR. This current report describes research activities since June 1993, that have focused on Tasks 2 and 3 of this research project.

8.2 SIGNIFICANT TECHNICAL ACCOMPLISHMENTS

Work during this reporting period has concentrated on a review and analysis of geochronological methods used to date Quaternary and Neogene basaltic rocks in the YMR. This study was initiated as part of Task 3 research because all of the KTUs directly related to igneous activity are dependent on understanding the sources of uncertainty in the precision and accuracy of volcano ages. The geochronology report presents an overview of the general principles for dating techniques used in the YMR, discussions on the limitations and uncertainties associated with these techniques, and an evaluation of dates produced by these techniques for basaltic rocks of the YMR. The details of this review are presented in Hill et al. (1993) and are summarized in the next subsection.

Data-gathering activities and probability model development also continued during this reporting period. Available geological, geochemical, and geochronological data have been compiled for the Cima Volcanic Field, California; the Coso Volcanic Field, California; the Lunar Crater-Pancake Range Volcanic Field, Nevada; and the Big Pine Volcanic Field, California. These volcanic fields are analogous to the YMR and have relatively large amounts of published data. The focus of Task 2 activities was to enter the available information into a computerized geographic information system (GIS), which then can be used to review the completeness of volcanism data for the Basin and Range Province (Task 3) and to develop and test volcano-tectonic models (Task 4). The volcanism database consolidates a large amount of information from a wide variety of data types into a consistent, readily accessible format. In addition to the specific tasks outlined in the Volcanic Systems of the Basin and Range Research Project, the Volcanism GIS will directly support Center for Nuclear Waste Regulatory Analyses (CNWRA) reactive work and will be used to evaluate volcanism models proposed by the DOE for the YMR. For example, the Volcanism GIS is used in this report to test the hypothesis of Crowe et al. (1993) that basaltic volcanoes of the Basin and Range province tend to form at low elevations in alluvial basins. Probability model development continued as part of Task 3 and 4 activities, and included incorporation and evaluation of volcano age uncertainties into models and publication of initial probability models by Connor and Hill (1993a). Uncertainty in the ages of Quaternary Crater Flat volcanoes (1.2 ± 0.4 Ma) affects all probability

calculations for direct disruption of the candidate repository at Yucca Mountain, and results in probabilities of 1×10^{-4} to 3×10^{-4} in 10,000 yr assuming spatially nonhomogeneous Poisson models. In contrast, uncertainty in the age of Lathrop Wells (about 0.1 ± 0.05 Ma) has little effect on probability predictions by the same model. A more detailed examination of spatially nonhomogeneous Poisson probability models for volcanic eruption is in final peer review for publication in Geophysical Research Letters.

8.2.1 Assessment of Geochronological Techniques

Assessing the limitations and uncertainties associated with volcanological data is an important goal of the Volcanic Systems of the Basin and Range Research Project. Because of the large apparent uncertainties in published dates of volcanic eruptions for the YMR, a critical review of geochronological methods and data was conducted as part of Task 3 activities. The details of this review were presented in Hill et al. (1993). In summary, the large uncertainties in many of the published dates for volcanic rocks in the YMR affect probability and consequence models of volcanism, especially models focusing on Quaternary volcanism. Dating techniques for post 10 Ma basaltic rocks in the YMR have inherent limitations and uncertainties which are rarely discussed in detail. Dates produced from the most widely available techniques have uncertainties that generally increase with decreasing age of the rock. Independent evaluation of most published dates is difficult due to a lack of documented information on analytical techniques, sample characteristics, and sources of error. Neogene (i.e., 1.6 to 23.7 Ma; Palmer 1983) basaltic volcanoes in the YMR have reported dates that generally reflect the precision and accuracy of the analytical technique, although the number of samples dated for each volcanic center only ranges from one to three. Dates for Quaternary (i.e., $\leq$1.6 Ma; Palmer 1983) volcanoes in the YMR have relatively large reported uncertainties and yield averages with large errors when reported uncertainty is propagated through statistical calculations. Using available data, estimates of the average ages of the Quaternary YMR volcanoes are 1.2 ± 0.4 Ma for Crater Flat, 0.3 ± 0.2 Ma for Sleeping Butte, and 0.1 ± 0.05 Ma for Lathrop Wells. These dates generally do not represent the most precise or accurate dates possible using currently available geochronological techniques. Uncertainty in the age of Lathrop Wells is relatively small and does not affect current probability models significantly. However, the relatively large uncertainties in the ages of Crater Flat volcanoes results in a range of probabilities between 1×10^{-4} to 3×10^{-4} in 10,000 yr assuming spatially nonhomogeneous Poisson models of direct repository disruption.

The calculation of uncertainty in ages of the YMR volcanoes requires that analytical error is propagated through statistical calculations. Too often, the uncertainty in a volcano age is reported as merely one standard deviation about the mean of available dates for the volcano, with no accounting of analytical error. This is significant because the analytical error associated with many dates is in excess of 50 percent, which should be reflected as the uncertainty associated with the age of the volcano. Calculations that use dates must preserve the associated uncertainty, and necessarily result in a product that also has uncertainty if the result is to be significant.

Dates reported by Turrin et al. (1991) provide a useful example of how uncertainty can be propagated through statistical calculations. These data are used as an example because Turrin et al. (1991) report sufficient analytical data to independently determine some aspects of analytical uncertainty, and these dates were produced at the internationally recognized Berkeley geochronology lab. A mean of 170 ± 114 ka is reported by Turrin et al. (1991) for eight $^{40}Ar/^{39}Ar$ dates from Lathrop Wells lava Ql_5 (Table 8-1). However, the reported uncertainty in the mean only represents one standard deviation of the

Table 8-1. $^{40}Ar/^{39}Ar$ dates for Lathrop Wells unit Ql_5 from Turrin et al. (1991).

Sample	Date (Ma)	$\pm 1\sigma$ Error (Ma)	$^{40}Ar_{rad}$ (%)	Error (%)
1555-1	0.168	0.318	0.6	189
1555-2	−0.020	0.263	−0.1	1315
1555-3	0.368	0.644	0.7	175
1555-4	0.164	0.089	0.9	54
1555-10	0.112	0.090	0.6	80
1555-11	0.107	0.155	0.4	145
1555-12	0.235	0.521	0.4	222
1555-13	0.228	0.200	1.2	88
Column Average	0.170	0.285	0.6	284
Column Std Dev	0.114	0.202	0.4	
Weighted Mean	0.138	0.054		39
Average Date	0.170	0.121		
Avg Std Dev	0.106	0.161		
Approximate Age	0.170	0.388		228

Column Average and Std Dev refer to the simple averages and standard deviations of the data columns. The weighted mean is calculated by weighting the individual dates with the inverse of the associated error squared (cf. Turrin et al., 1991). Average Date and Std Dev refer to statistics calculated by propagation of analytical error [Eqs. (8-1) and (8-2)] and are combined to give an approximate age of 0.170 ± 0.388 Ma (i.e., 0.2 ± 0.4 Ma) for this unit. Note that the 228-percent error associated with the approximate age is comparable to the average reported error of 284 percent for these dates.

population of estimated dates and does not reflect the large analytical errors (average of 284 percent) associated with these data. Using general rules for calculations involving numbers X_i with associated uncertainties x_i (e.g., Wang et al., 1975), propagation of reported errors through the calculation of a mean requires

$$\overline{X} \pm \bar{x} = \frac{\sum X_i}{n} \pm \frac{\sqrt{\left(\sum x_i^2\right)}}{n} \qquad (8\text{-}1)$$

when

$\overline{X}$ = Average date of n samples

$\bar{x}$ = Uncertainty in the average

and results in a mean of 170±121 ka for the Turrin et al. (1991) dates with reported 1 sigma errors (i.e., Average Date, Table 8-1). Note that the 121 ka uncertainty does not indicate 68 percent of the dates fall within 121 ka of the mean, but that the mean has an uncertainty of 121 ka. Calculation of the standard deviation for this date population requires

$$\text{Avg Std Dev} = \sqrt{\frac{\sum \left[\left(X_i \pm x_i\right) - \left(\overline{X} \pm \bar{x}\right) \right]^2}{n}} \qquad (8\text{-}2)$$

and results in one standard deviation of 106±161 ka (i.e., Avg Std Dev, Table 8-1). Thus, these dates fall within the range of 170±388 (i.e., 121+106+161) ka. Although this range is large, it accurately reflects a data set of eight samples that have an average reported analytical error of 284 percent. Raw (i.e., nonaveraged) data must be presented in order to adequately evaluate the precision of a series of dates, because reported averages and associated uncertainties in many radiometric dating reports (e.g., Turrin et al., 1991) do not necessarily reflect the large precision errors associated with the data.

8.2.1.1 Radiometric Dating Techniques

Radiometric dating techniques are based on the decay of naturally occurring radionuclides that are found in common rock-forming minerals. Assuming the chemical system has remained closed to gain or loss of the parent radionuclide and associated decay products, a date can be derived by determining the abundance of decay products relative to the initial abundance of parental isotopes. Radiometric dates can be both precise (i.e., low analytical errors) and accurate (i.e., dates represent the age of the unit), but there are fundamental limitations to these techniques. The uncertainties in radiometric dates are rarely discussed and generally focus on the partial determination of analytical error. Uncertainties in both precision and accuracy of radiometric dates in the YMR are poorly reported. Estimated uncertainties range from relatively small to large enough to affect probability models for future volcanism in the YMR (Hill et al., 1993).

The most common radiometric technique used to date basaltic rocks is based on the decay of ^{40}K to ^{40}Ar, a stable gas that is trapped in the mineral lattice. Heating the sample releases the ^{40}Ar which is collected and analyzed on a mass spectrometer. A date is calculated by comparing the ratio of

radiogenic ^{40}Ar to other stable isotopes of K and Ar and assuming that all K or Ar has remained trapped in the mineral since formation. A variation of the K-Ar technique involves irradiating the sample with neutrons and measuring only the artificial and naturally occurring isotopes of Ar (i.e., the $^{40}Ar/^{39}Ar$ technique). Both types of K-Ar dates are generally precise and accurate for nonaltered basaltic rocks older than about 1 Ma. Basaltic rocks as young as 50,000 yr also can be dated by the K-Ar techniques if special analytical procedures (i.e., $^{40}Ar/^{39}Ar$) are used (e.g., McDougall and Harrison, 1988).

Primary limitations to the K-Ar methods are loss of radiogenic ^{40}Ar from the sample, difficulties in accurate measurement of K content for older rocks, and low abundances of radiogenic ^{40}Ar in Quaternary rocks. Most basaltic rocks effectively retain Ar in the plagioclase crystal lattice, which is relatively insensitive to weak alteration and temperatures <200 °C (Dalrymple and Lanphere, 1969). Basaltic glass is unsuitable for K-Ar dating because it hydrates easily at surface conditions and is thus prone to Ar loss (Kaneoka, 1972). Incremental heating of the sample generally results in accurate dates for samples with minor amounts of low-temperature alteration (Dalrymple and Lanphere, 1974; Harrison, 1983), whereas total-fusion of the same sample commonly results in erroneously young dates (e.g., Fleck et al., 1977). For Quaternary rocks, uncertainties in resolving radiogenic ^{40}Ar from the nonradiogenic ^{40}Ar present in the earth's atmosphere generally result in large analytical errors (e.g., Dalrymple and Lanphere, 1969).

Most of the dates for YMR basaltic rocks were produced through K-Ar techniques, primarily by conventional K-Ar analysis (Table 8-2). For all volcanoes that have been dated at least twice, the standard deviation of the dates without incorporation of analytical error is significantly less than standard deviations calculated with reported analytical error. Two conventional K-Ar studies for Lathrop Wells (Figure 8-1) average 0.5 ± 0.5 Ma (Sinnock and Easterling, 1983) and 0.3 ± 0.2 Ma (Vaniman et al., 1982). A detailed $^{40}Ar/^{39}Ar$ study by Turrin et al. (1991) produced 36 noncontaminated dates for Lathrop Wells, which average 0.2 ± 0.3 Ma when analytical error is propagated. Dates for individual Lathrop Wells units studied by Turrin et al. (1991) are presented in Table 8-2. By using weighted-mean statistics, Turrin et al. (1991) reported average ages of 136 ± 8 ka and 141 ± 9 ka for Lathrop Wells units Ql_3 and Ql_5, which significantly underestimates the uncertainty associated with dates that average 200 percent analytical error. Average dates for these units calculated using Eqs. (8-1) and (8-2) are 0.2 ± 0.2 Ma and 0.2 ± 0.3 Ma, respectively (Table 8-2). The large uncertainties associated with these dates reflect the difficulty in dating young, low K basaltic rocks; other dating techniques yield an estimated age of 0.1 ± 0.05 Ma for Lathrop Wells.

The ages of the Sleeping Butte volcanoes (Table 8-2 and Figure 8-1) currently are indistinguishable from Lathrop Wells. Conventional K-Ar dates average 0.3 ± 0.2 Ma for Little Black Peak, and there is one date of 0.3 ± 0.2 Ma for Hidden Cone. K-Ar dates for the Quaternary volcanoes of Crater Flat range from 0.95 ± 0.08 Ma (Ho et al., 1991) to 1.9 ± 0.2 Ma (Sinnock and Easterling, 1983), and average 1.2 ± 0.4 Ma when analytical error is propagated through the calculations (Hill et al., 1993). Although the Crater Flat volcanoes cannot be distinguished by age due to these large uncertainties, soils on Red Cone are more developed relative to Black Cone and may indicate an age difference between these two volcanoes (Wells et al., 1990).

Most Neogene volcanic centers of the YMR only have one to three K-Ar dates, which at times date individual volcanoes that may have age differences of 0.1 to at least 1 Ma (e.g., Crowe et al., 1983). The exception to this generalization is the Pliocene Crater Flat volcanoes (Figure 8-1) which have 38 K-Ar dates (Table 8-2). These dates average 4.0 ± 0.5 Ma when analytical error is propagated through the calculations.

Table 8-2. Compilation of YMR basalt dates

Volcano	Unit	Technique	# Dates	Avg Date (Ma)	±Std Dev (Ma)	±Std Dev w/ Error	Source
Lathrop Wells	All	Ar-Ar	36	0.17	0.09	0.25	Turrin et al., 1991
Lathrop Wells	All	K-Ar	18	0.46	0.30	0.48	Sinnock & Easterling, 1983
Lathrop Wells	Main cone	^{36}Cl	2	0.076	0.002	0.02	Zreda et al., 1993
Lathrop Wells	Main cone	^{3}He	5	0.03	0.01	0.02	Crowe et al., 1992; Poths & Crowe, 1992
Lathrop Wells	Main cone	Ar-Ar	4	0.14	0.08	0.34	Turrin et al., 1991
Lathrop Wells	Ql_3	^{3}He	2	0.069	0.004	0.02	Poths & Crowe, 1992
Lathrop Wells	Ql_3	Ar-Ar	16	0.18	0.08	0.22	Turrin et al., 1991
Lathrop Wells	Ql_4	^{3}He	1	0.048	0.005	—	Crowe et al., 1992
Lathrop Wells	Ql_4	Ar-Ar	4	0.15	0.10	0.28	Turrin et al., 1991
Lathrop Wells	Ql_4	U/Th	1	0.15	0.04	—	Crowe et al., 1992
Lathrop Wells	Ql_5	^{3}He	2	0.062	0.002	0.01	Crowe et al., 1992; Poths & Crowe, 1992
Lathrop Wells	Ql_5	^{36}Cl	5	0.081	0.007	0.02	Zreda et al., 1993
Lathrop Wells	Ql_5	Ar-Ar	12	0.15	0.10	0.32	Turrin et al., 1991
Lathrop Wells	Ql_6	U/Th	1	0.14	0.04	—	Crowe et al., 1992
Lathrop Wells	Unkn	K-Ar	3	0.27	0.03	0.16	Vaniman & Crowe, 1981; Vaniman et al., 1982
Little Black Pk.	Sl. Butte	K-Ar	5	0.26	0.04	0.17	Crowe et al., 1982; Crowe & Perry, 1991
Hidden Cone	Sl. Butte	K-Ar	1	0.3	0.2	—	Crowe & Perry, 1991
Northern Cone		K-Ar	2	1.11	0.04	0.3	Vaniman et al., 1982
Red Cone		K-Ar	5	1.1	0.2	0.4	Vaniman et al., 1982; Ho et al., 1991
Red Cone		K-Ar	18	1.4	0.3	0.6	Sinnock & Easterling, 1983
Black Cone		K-Ar	2	1.08	0.01	0.3	Vaniman & Crowe, 1981
Little Cone SW	TSV-3	K-Ar	1	1.1	0.3	—	Vaniman & Crowe, 1981
Buckboard Mesa		K-Ar	2	2.81	0.02	0.1	Crowe et al., 1982
Pliocene Crater Flat		K-Ar	2	3.7	0.1	0.4	Vaniman & Crowe, 1981
Pliocene Crater Flat	Unit 1	K-Ar	18	4.0	0.3	0.7	Sinnock & Easterling, 1983
Pliocene Crater Flat	Unit 2	K-Ar	18	4.0	0.2	0.4	Sinnock & Easterling, 1983

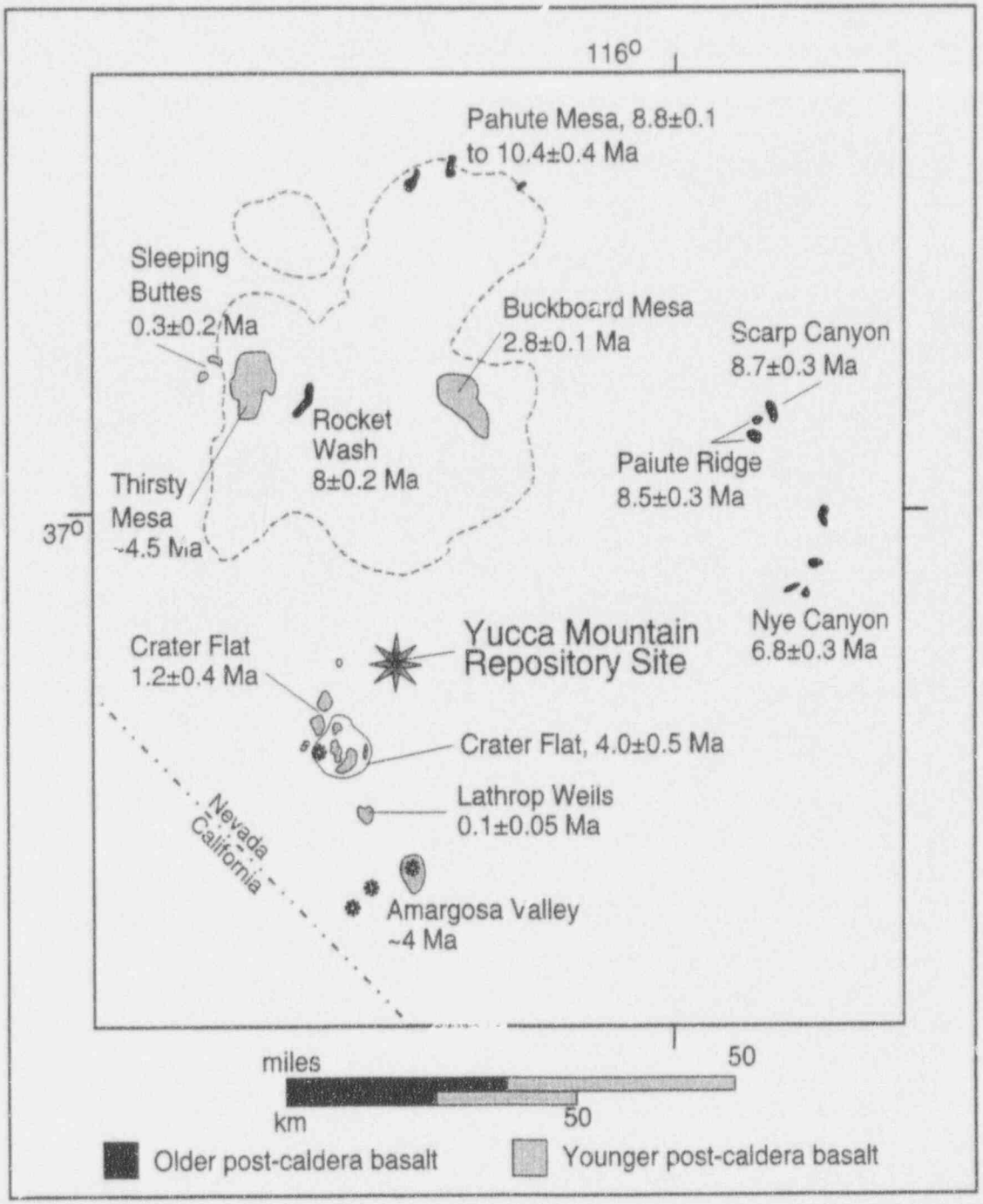

Figure 8-1. Post-caldera basaltic vent locations of the Yucca Mountain Region, modified from Crowe (1990). Basaltic units are shaded by relative age, and the average date is shown along with the estimated uncertainty calculated by propagation of analytical error [Eqs. (8-1) and (8-2)]. Miocene calderas of the Timber Mountain complex are outlined by the dashed lines. Asterisks denote aeromagnetic anomalies thought to represent buried basaltic volcanoes (Crowe, 1990), and the star indicates the location of the candidate repository site.

The only other radiometric technique that has been used to date YMR basaltic rocks is the U/Th method. The basis for this technique is similar to the K–Ar method, although the U/Th method has an upper age limit of about 350 ka (e.g., Gill et al., 1992). Minerals incorporate most isotopes of U and Th into the crystal lattice, and subsequent radioactive decay of ^{238}U produces ^{230}Th. Because the minerals incorporate some ^{230}Th upon formation, a correction is made for this initial activity by comparing ^{238}U and ^{232}Th abundances, which remains constant for at least 350 k.y. (Gill et al., 1992). The U/Th method also can be used to date carbonate deposits in soils (e.g., Luo and Ku, 1991).

For volcanic rocks of the YMR, U/Th dates have been determined only for Lathrop Wells units. Lavas Ql_4 and Ql_6 have dates of 0.15 ± 0.4 and 0.14 ± 0.4 Ma, respectively (Crowe et al., 1992). The U/Th method has been used to date carbonate deposits in soils beneath and above Lathrop Wells lavas (Szabo et al., 1981). Calcrete beneath Lathrop Wells lava has a U/Th date of 0.4 ± 0.2 Ma and caliche in soil overlying these lavas is 0.03 ± 0.01 Ma (Szabo et al., 1981). These soil dates are consistent with the U/Th and ^{3}He dates obtained on these lavas.

8.2.1.2 Radiation Interaction Techniques

Ionizing alpha, beta, gamma, and cosmic radiation can interact with minerals and change their physical and chemical properties. These changes can produce defects in a mineral's crystal lattice, create new elements through spallation or n-capture reactions, and excite electrons to unstable energy states. If the interaction effects are stable through time and the sample has been exposed to radiation at a constant rate, these effects can be used to date volcanic rocks. The radiation interaction techniques are sometimes viewed as experimental and do not always provide dates with the same precision and accuracy as some radiogenic isotope techniques. They can, however, provide dates for Quaternary deposits that cannot be analyzed by conventional radiogenic methods.

The thermoluminescence (TL) method is based on the interaction of ionizing radiation with electrons in a crystal lattice (e.g., Aitken, 1967). Defects within the crystal lattice result in "traps," which can accommodate electrons that have been excited to higher energy states through interaction with ionizing radiation. Although only some of these traps are stable, the number of occupied traps increases linearly with age if the radiation dose rate remains constant (Aitken, 1967). The stability of a trap increases with its excitation energy. Upon heating, electrons are released from the traps, and excess energy is emitted as light when the electron moves to a ground state (Aitken, 1967; 1978). The intensity of the emitted light is measured as a function of temperature to produce the TL signal used for dating.

The primary sources of error in the TL dating method are uncertainties in the external and internal radiation dose rates (e.g., Geyh and Schleicher, 1990). External dose rates are usually calculated based on an estimated composition of the material surrounding the sample, because *in situ* measurements are very time consuming. The moisture of the material surrounding the sample also will strongly affect the alpha dose rate to the sample. For 5-MeV alpha particles, which are produced by the U and Th decay series and have a range of about 3.5 cm in air, a layer of water about 40 μm thick will completely shield the sample from irradiation (Wang et al., 1975). Compaction of the sample retards the flow of soil-gas radon, which also affects the external dose rate to the sample (e.g., Berger, 1985). Thus, TL dates cannot be evaluated unless the methods used to determine external and internal dose rates are explicitly described. Assuming minimal errors in the estimate of these rates, TL dates of geologic materials commonly have uncertainties of around 25 percent, although more precise dates are possible if external dose rates are measured at the sample site (Geyh and Schleicher, 1990). The TL signal also is very sensitive to the grain size of the sample. In general, smaller sample sizes show a larger TL signal than

larger size fractions of the same sample (e.g., May, 1979). This effect may be due to both self-shielding and the larger activation area per unit volume of smaller grain sizes (e.g., Geyh and Schleicher, 1990). For these reasons, it is important to know what size fraction of a sample was used to produce a TL date. In addition, the TL growth curve may be nonlinear for samples older than about 50 ka (Forman, 1989). Failure to account for nonlinearity will underestimate the accumulated dose, and underestimate the age of the sample.

The TL dating method has had limited application to the Quaternary volcanic rocks of the YMR. Published data fail to report most of the details necessary to independently evaluate the precision and accuracy of the data, and many of the assumptions necessary in TL dating are not addressed. A TL date of 24.5±2.5 ka is reported in Crowe et al. (1992) for baked soil several decimeters under lava Ql_3 at the Lathrop Wells volcanic center. However, ^{3}He exposure dates for this and other temporally equivalent lavas (Crowe et al., 1992) are generally twice as old, which indicates there may be significant inaccuracies in this TL date.

Multiple analyses of three nonbaked soil samples from Lathrop Wells also were presented in Crowe et al. (1992). These soils are interbedded with primary fall deposits associated with the latest stage of activity at Lathrop Wells, which is called chronostratigraphic unit 1 by Crowe et al. (1992). Chronostratigraphic unit 1 has ^{3}He exposure dates up to 44±5 ka (Crowe et al., 1992). Soil 1, the oldest soil in the dated sequence, has TL dates of 8.9±0.7, 9.9±0.7, and 8.7±1.0 ka. Soil 2 has a date of 3.7±0.4 ka, and Soil 3, the youngest soil in the sequence, has dates of 3.7±0.4 and 4 5±0.4 ka. The reproducibility of the dates demonstrates the precision of the technique used to obtain these values. However, there is no way to evaluate the accuracy of these dates, nor is it at all clear how the TL signal was measured or acquired by the sample or even what material was dated. Although Crowe et al. (1992) state that the TL technique applied to these soils is preliminary, the large disparity between the ^{3}He exposure dates and the TL dates is difficult to reconcile. To further complicate this issue, Crowe et al. (1993) indicate that the ash beds in these soils may not be correlative with main-cone scoria. Clearly, these TL dates cannot be accurately evaluated until analytical procedures are reported and detailed stratigraphic relationships are presented for these Lathrop Wells deposits.

Cosmogenic nuclides including ^{3}He, ^{10}Be, ^{14}C, ^{21}Ne, ^{26}Al, and ^{36}Cl are produced by direct cosmic-ray irradiation of rocks at the surface of the earth (Lal, 1987; 1988); only the ^{3}He and ^{36}Cl dating techniques have been applied to YMR basaltic rocks. Cosmogenic nuclide dating methods are based upon the *in situ* accumulation of the cosmogenic nuclides in rocks exposed at the earth's surface (Dorn and Phillips, 1991). The rate of accumulation of the cosmogenic nuclides is dependent on altitude, geomagnetic latitude, rock chemistry, geometry of exposure to cosmic rays, and on the cosmic-ray flux. These factors can be measured to varying degrees of success (Zreda et al., 1991; Cerling, 1990; Kurz et al., 1990). The measurements of the cosmogenic nuclides in the exposed rocks allows the generation of an exposure age of the rock at the earth's surface. To assume that an exposure age of a rock is equivalent to the true age (i.e., eruption age) of the rock, the surface dated by cosmogenic nuclide techniques must have been continuously exposed since formation. Any erosion, cover, or disturbance of the surface will yield a minimum age for the surface and will not reflect the true age of the rock.

Accuracy for cosmogenic nuclide dates is dependent primarily on uncertainty in the production rates, which have been estimated to be less than 10 percent for ^{36}Cl to around 20 percent for ^{3}He (Zreda et al., 1991) for the Great Basin area. The precision of this technique is much better than those methods based on the K-Ar and U/Th system for very young volcanic rocks. Multiple analyses from the same surface by Zreda et al. (1993) indicate a precision of 10 percent or better for ^{36}Cl surface exposure dates

of young volcanic rocks. Comparison of dates derived from different samples of the same surface indicates the best estimate for precision of ^{3}He surface exposure ages is 14 percent (Anthony and Poths, 1992). Erosional removal of < 80 cm of soil since surface formation results in a small overestimation of the age, whereas removal of thicker material will have an opposite effect (Zreda et al., 1991; 1993).

Use of cosmogenic nuclide methods to determine the exposure ages of surfaces has been limited to ^{3}He and ^{36}Cl measurements of samples from the Lathrop Wells volcanic center (Poths and Crowe, 1992; Crowe et al., 1993; Zreda et al., 1993). As has been observed for most geochronological data in the YMR, details of the analytical methods used and the sample locations were not provided for the ^{3}He dates (Poths and Crowe, 1992; Crowe et al., 1993). As pointed out by Anthony and Poths (1992), the absolute accuracy for ^{3}He dates is probably only 30 percent. However, because the precision of the measurements is much less than 30 percent, this technique is applicable for relative dating of surfaces at a particular site. Within the resolution of this technique, the three lava units dated by Poths and Crowe (1992) apparently are the same age (Table 8-2). Only minimum ages are generated using the ^{3}He technique on samples that might have been wholly or partially covered by eolian or alluvial deposits during residence at the earth's surface. Using the 30 percent accuracy figure of Anthony and Poths (1992) and the oldest age generated (44 ka) for the Lathrop Wells scoria cone, a minimum exposure age of Lathrop Wells is thus 44 ± 13 ka.

Only the ^{36}Cl study by Zreda et al. (1993) provided sufficient analytical information to independently calculate the reported dates, determine that erosional modification and secondary mineralization had not occurred for each sample, and make the necessary correction for thermal-neutron leakage associated with the irregular geometry of pressure-ridge samples. As concluded by Zreda et al. (1993), the average ages for bombs from the summit of the main scoria cone (0.08 ± 0.02 Ma) and the stratigraphically older (Crowe et al., 1988) $Q1_5$ lava flow (0.08 ± 0.02) are indistinguishable.

8.2.1.3 Indirect Dating Techniques

A number of widely applied geochronology techniques utilize basic geological information to derive relative, and at times absolute, ages of volcanic units. These methods are based on correlating specific features of a sample, such as the orientation of remnant magnetization, with the same features on a unit of known age. Application of these methods requires that the ages of reference units are well-constrained through direct dating, and that specific geological features can be uniquely identified in the studied samples. Although these methods are generally incapable of producing absolute ages, they often provide useful age constraints and can be used to test the precision and accuracy of radiometric and radiation-interaction dates. Many of the indirect dating methods are based on stratigraphic relationships, which can be poorly developed in young volcanic terranes. Most flows and pyroclastic units have restricted occurrences due to pre-existing topography or prevailing winds. Determining these stratigraphic relationships usually requires detailed studies, including geochemical analyses, age determinations, and subsurface information. Regionally extensive marker beds generally occur in large depositional basins and are only rarely preserved in basaltic volcanic fields (e.g., Sarna-Wojcicki, 1976).

The orientation of a lava's magnetic field reflects the orientation of the earth's magnetic field at the time the lava cooled. When a lava cools below about 580 °C, magnetic minerals begin to acquire a remnant magnetization that is oriented in the same direction as the geomagnetic field. Because the orientation of the earth's magnetic field has changed markedly through time, remnant magnetization can be used to date or correlate basaltic rocks (e.g., Tarling, 1983). Changes in the intensity and directions of the nondipolar field occur over periods of 10^{0} to 10^{3} yr and are referred to as secular variations (e.g.,

Creer, 1981). For the western United States, the present drift of the nondipolar (i.e., secular) field is about 0.25 degree westward per year (Tarling, 1983). Secular variations of about 4.5 degrees per century also were determined by Holcomb et al. (1986) for the last 200 yr of volcanic activity on Hawaii. For sites at middle latitudes, secular variation over time can result in declination changes of about 20 degrees and inclination changes of about 25 degrees, relative to the average magnetic field direction (e.g., Champion, 1991).

Assuming that the lavas have not been rotated since cooling, statistically significant differences in paleomagnetic orientation clearly indicate that the lavas formed at different times. In addition, lavas with similar paleomagnetic orientations may be of similar age. However, the directions of the secular field have not been unique through time, and lavas with very similar paleomagnetic orientations may have significantly different ages (e.g., Champion, 1980). It is important to remember that resolvable differences in the nondipolar component of earth's magnetic field can develop in under 100 yr (e.g., Mankinen et al., 1986), which may not represent a significant interval of time in some geologic studies.

The most significant sources of error in paleomagnetic dating occur during sample selection and preparation. Lava flow interiors commonly yield more consistent paleomagnetic orientations than flow exteriors due to the mobility of large blocks along flow boundaries. Small degrees of tilting also may be difficult to detect in localized Quaternary deposits, which could affect correlations with secular variation curves. Weathering and alteration will commonly produce a large viscous remnant magnetization that may cause large systematic errors if uncorrected (e.g., Bogue and Coe, 1981). To avoid these problems, paleomagnetic sampling should be conducted only on fresh exposures of rock that have remained demonstrably stable since formation.

Paleomagnetic studies in the YMR have focused on the Lathrop Wells eruptive center (Champion, 1991; Turrin et al., 1991; Crowe et al., 1992, 1993). Much of the controversy surrounding Lathrop Wells focuses on the detection of multiple eruptions separated by some finite, but measurable, amount of time. Champion (1991) sampled 27 sites at Lathrop Wells in units Qs_5 (older flows and scoria), Ql_3 (younger flows), and the main cone. Although paleomagnetic orientation data and statistical parameters are not provided, Champion (1991) reports an angular difference of 4.7 degrees between units Qs_5 and Ql_3, which is interpreted to indicate that these units represent paleomagnetically distinct events at a 99.98 percent confidence level. Based on an historic secular variation of about 4.5 degrees per century (Champion, 1980; Holcomb et al., 1986), Champion (1991) concludes that only 100 yr separate units Qs_5 and Ql_3. Champion (1991) also reports that 40 samples from a site along the upper rim of the main Lathrop Wells scoria cone (Qs_1) are indistinguishable from his unit Qs_5, and concludes that Lathrop Wells is a simple monogenetic volcano. Crowe et al. (1992) do not present any paleomagnetic data, but state that units Ql_6 and Ql_5 have preliminary paleomagnetic orientations that do not differ significantly from unit Ql_5 (Champion, 1991). Crowe et al. (1992) are careful to note that their data are preliminary, and that detailed demagnetization studies still are required for these samples.

None of the paleomagnetic data presented to date disprove the polycyclic model proposed for Lathrop Wells by B.M. Crowe and coworkers (e.g., Crowe et al., 1992). Small differences in paleomagnetic orientation apparently occur between early lavas and scoria, and later deposits associated with the main cone. However, the length of time required to produce the angular differences is not well constrained. Historic secular variations of about 4.5 degrees per century (Holcomb et al., 1986; Champion, 1991) may not accurately represent Quaternary secular variations. For example, the rate of secular variation reported by Mankinen et al. (1986) for the last 2,000 yr varies considerably. Sizeable differences in the paleomagnetic field orientation can develop in tens of years, or the orientation may

remain relatively stable for hundreds of years (Mankinen et al., 1986). Holocene secular variations also are of smaller magnitude relative to the Quaternary (Mankinen et al., 1986). It is thus impossible to determine the length of time represented by the observed 4.7 degrees angular variation at Lathrop Wells (Champion, 1991; Crowe et al., 1993) without first determining, to within several hundred years, the absolute age of Lathrop Wells. Such an age resolution is impossible with currently available geochronological techniques. Thus, the paleomagnetic variations at Lathrop Wells do not refute the hypothesis of polycyclic volcanism (e.g., Crowe et al., 1992) and may have been produced over periods of time much longer than the 100 yr proposed by Champion (1991) and Turrin et al. (1991).

The relatively poorly consolidated character of basaltic cinder cones also provides a means to determine relative ages, based on increasing degrees of erosion with time (e.g., Scott and Trask, 1971; Wood, 1980). Geomorphic modifications associated with increasing age include decreases in cone slope and height, and increases in the thickness and length of the cone apron, crater diameter, cone diameter, and the number of gullies on the cone slope (e.g., Dohrenwend et al., 1984; Hasenaka and Carmichael, 1985). These geomorphic characteristics can be determined for cinder cones of known age and compared to cinder cones in similar climates to produce an age estimate.

Before geomorphic characteristics can be used as a dating technique, two important assumptions must be addressed. First, the paleoclimate for the known and unknown age volcanoes must be similar. Variations in the amount of rainfall, rates of precipitation, vegetation, and eolian conditions can strongly affect the geomorphic modification of volcanic features (e.g., Wells et al., 1985; McFadden et al., 1986). Second, the initial characteristics of the volcanic features must be similar (i.e., Porter, 1972; Wood, 1980). Although cinder cones generally have a similar initial morphology, variations in wind direction and eruption dynamics can strongly affect the form of a cinder cone (Porter, 1972; McGetchin et al., 1974; Gutmann, 1979; Settle, 1979). In addition, the degree of cinder annealing, presence of agglutinate layers, and initial breaching of the cone may strongly affect subsequent geomorphic modifications.

Wells et al. (1990) have compared the morphologies of the Lathrop Wells and Quaternary Crater Flat volcanoes with Quaternary volcanoes in the Cima Volcanic Field, California. In comparison with approximately 1-Ma Cima cinder cones, the Crater Flat volcanoes (Little, Black, and Red Cones) have morphological characteristics consistent with a 1-Ma age (Wells et al., 1990). The presented geomorphic parameters lack sufficient resolution to determine if any of the Crater Flat volcanoes have relatively different degrees of erosion, which would indicate significant differences in age. However, the variations in most geomorphic parameters apparently are incapable of resolving intervals of time roughly less than about 100 ka (Dohrenwend et al., 1986). Relative degrees of soil development may indicate that Black Cone is younger than Red Cone (Crowe et al., 1993), and Black Cone appears somewhat less deeply incised and eroded than Red Cone.

Wells et al. (1990) concluded that the geomorphic characteristics of the main Lathrop Wells cone are indistinguishable from those of the Black Tank Cone in the Cima Volcanic Field, which has an age of only about 20 to 30 ka. There are, however, several problems with this widely cited (Crowe et al., 1992; 1993) interpretation. Cinder cones associated with tephra rings (i.e., hydrovolcanic deposits) have different constructional forms than cones without tephra ring (Dohrenwend et al., 1986). The Lathrop Wells cone had hydrovolcanic eruptions prior to formation of the main cinder cone (e.g., Vaniman and Crowe, 1981; Crowe et al., 1988), whereas the Black Tank Cone lacks hydrovolcanic deposits (Dohrenwend et al., 1986). These two cinder cones thus have different original morphologies and cannot be directly compared for geomorphic dating. In addition, the Black Tank Cone has at least three relatively thick (2 to 3 m) agglutinate layers exposed in the crater walls and flanks. Lapilli and bombs at Black

Tank Cone are highly oxidized, commonly have aerodynamic deformation features such as spindles and ribbons, and form relatively cohesive deposits. Lathrop Wells lacks discernable, thick agglutinate layers, has relatively nonoxidized cinders, lacks abundant spindles and ribbons, and forms poorly consolidated deposits of loose, angular tephra. A logical conclusion would be that it is more difficult to erode Black Tank Cone than Lathrop Wells due to differences in the relative cohesiveness of these two cones. Thus, the age represented by the geomorphology of Black Tank Cone should overestimate the age of Lathrop Wells because it should take a shorter amount of time to erode a less cohesive cone. Lathrop Wells thus should be significantly younger than the 20 to 30 ka Black Tank Cone. However, ^{3}He exposure ages at the main cone of Lathrop Wells (Table 8-2) indicate a minimum age in excess of 40 ka (Crowe et al., 1992) and ^{36}Cl ages average 80 ± 20 ka (Zreda et al., 1993). Lathrop Wells is undoubtedly a young volcanic center and does not have the general geomorphic characteristics of a 200 ka Cima volcano or the roughly 1 Ma Crater Flat volcanoes. The absolute age of Lathrop Wells, however, cannot be determined robustly by geomorphic criteria. Direct dates of Lathrop Wells units indicate that the age of this volcano probably is between 50 and 150 ka.

8.2.2 Volcanism Geographic Information System

A computerized GIS provides the means necessary to construct models relating quantitative physical data to spatial data. In the Volcanism Research Project, a computerized GIS is being constructed to support conceptual, empirical, and theoretical models of volcanism and tectonism for the Basin and Range province. Most of the data compiled and manipulated in the Volcanism GIS originate in the published literature and include maps, data tables, digitized images, and complex binary geophysical data. In addition to model development, this GIS also will be useful in evaluating the DOE volcanism database used to demonstrate compliance with 10 CFR Part 60 requirements relating to igneous activity. The volcanism GIS will provide confirmatory data for addressing issues related to waste isolation and provide data that may be required to explore safety issues not adequately addressed by the DOE.

Arc/Info® is a series of computer programs designed to relate tabular and spatial data using real-world geographic coordinates. Arc/Info® also is used by both the NRC and DOE as primary GIS software for the Yucca Mountain Project and is used by the CNWRA for the Volcanism GIS. Available geological, geochemical, and geochronological data have been compiled and entered into the Volcanism GIS for the Cima Volcanic Field, California; the Coso Volcanic Field, California; the Lunar Crater-Pancake Range Volcanic Field, Nevada; and the Big Pine Volcanic Field, California (Figure 8-2). These volcanic fields have been the sites of numerous geologic studies in the past 25 yr and generally have readily available data. Basic geological and volcanological data exist for the other volcanic fields in Figure 8-2, but the data are less abundant and contained in less accessible formats such as theses and open-file reports. However, sufficient information exists for these fields to determine volcano distributions, bedrock and regional geology, distribution of major faults, and to characterize volcano ages and compositions. These data also will be entered into the Volcanism GIS.

The value of the Volcanism GIS extends well beyond the ability to rapidly access large amounts of complex data; conceptual, empirical and numerical models for igneous activity that combine both spatial and tabular data can be developed and rigorously tested. For example, Crowe et al. (1993) state ".. there is a common but not universal restriction of sites of Quaternary basaltic volcanic centers to alluvial basins of the basin-range province [p. 138] ... Because the Yucca Mountain site is located in a range interior, a [spatially] random model will overestimate the disruption probability [p. 283]." The hypothesis that basaltic volcanoes are restricted to low-elevation alluvial basins can be tested with the Volcanism GIS.

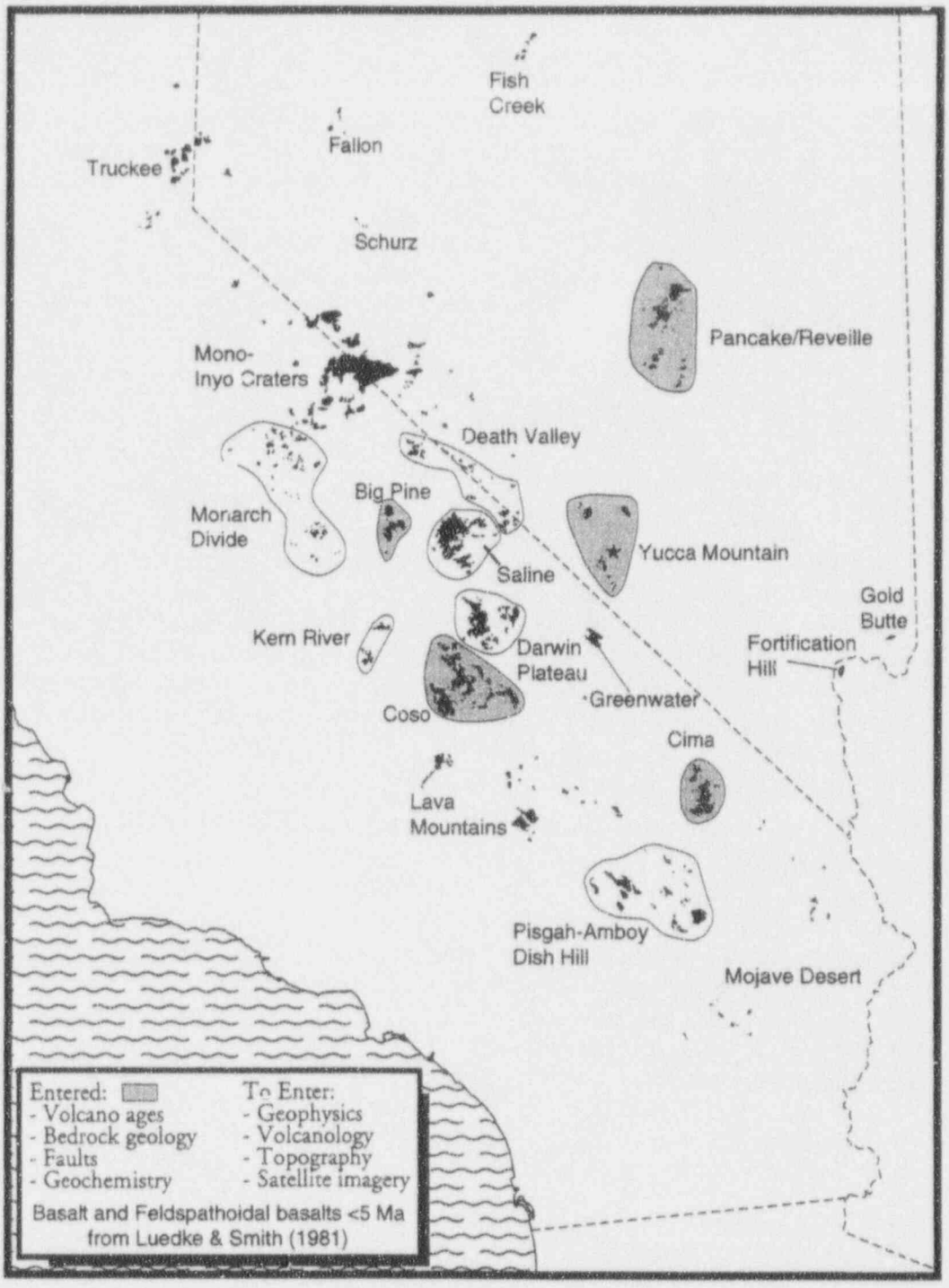

Figure 8-2. Distribution of basaltic volcanoes younger than 5 Ma, from Luedke and Smith (1981). Shaded areas represent volcanic fields that have volcanic geology, ages, geochemistry, faults, and basic geology entered into the Volcanism GIS. In addition, these fields have additional geophysical and volcanological data, and topography and satellite imagery available, which will be entered into the GIS. Other labeled volcanic fields will be added to the Volcanism GIS.

In the YMR, Quaternary basaltic volcanoes erupt between elevations of about 800 and 1500 m, whereas the maximum difference in elevation between Yucca Crest and the lowest elevation Quaternary volcano is only 670 m. A robust topographic barrier against volcanism thus would be >670 m. Figure 8-3 shows volcano distributions for the Cima Volcanic Field, California, produced with the Volcanism GIS. Cima volcanoes erupt over elevation differences of only around 450 m, indicating that a 500 m elevation difference may be significant in this volcanic field. It is, however, important to note that Cima volcanoes also are located on a broad topographic highland and did not erupt in nearby low-elevation basins. However, the volcanoes of the Big Pine field, California, are not restricted to either low elevations or alluvial basins (Figure 8-4). Although several Big Pine volcanoes did erupt within the Owens Valley, most volcanoes erupted at considerably higher elevations. Elevation differences range from about 800 m for the central part of the field, to over 1,000 m difference between the central and southern volcanoes (Figure 8-4).

The hypothesis that basaltic volcanoes are spatially restricted to low-elevation basins can be tested using the available data in the Volcanism GIS. A preliminary conclusion from analysis of these data is that the hypothesis is not valid. Thus, the elevation and location of the Yucca Mountain repository site does not present a significant topographic barrier to basaltic volcanoes. Once the Volcanism GIS is complete, the relationship between volcano distribution and topography can be accurately quantified. Other hypotheses, such as that certain basaltic compositions favor eruption at higher elevations, or that specific topographic gradients are effective barriers to basaltic volcanism, then can be tested robustly. It may be that certain types of basaltic volcanoes, which may be represented in the YMR, are not found when topographic gradients of more than 200 m/km occur. But until these apparent relationships are quantified, they cannot be incorporated into probability models for igneous activity in the YMR.

8.3 ASSESSMENT OF PROGRESS

Significant progress has been made in the last 6 mo toward understanding basic issues in basaltic volcanism for the YMR and western Great Basin. Volcanism probability and consequence models are critically dependent on geochronological data. However, the sources of uncertainty in these data are rarely discussed and a variety of geochronological methods are being used to study YMR volcanism. The review report undertaken as part of Task 3 activities represents a significant advancement in understanding both the convoluted origin of many YMR volcano ages and the limitations in the precision and accuracy of these data. Uncertainties in YMR volcano ages directly relate to identified igneous activity KTUs and to other KTUs related to conceptual model representation, variability in model parametric values, and the prediction of future system states for disruptive scenarios. Volcano age uncertainties can be propagated through existing probability model calculations (i.e., Connor and Hill, 1993a; 1993b) and result in probabilities of 1×10^{-4} to 3×10^{-4} in 10,000 yr for spatially nonhomogeneous Poisson models of direct repository disruption by basaltic volcanism (Connor and Hill, 1993a; Hill et al., 1993). Within the last 6 mo, the details of these probability models have been published in the proceedings of the *Focus '93* meeting (Connor and Hill, 1993b), and are in final review for *Geophysical Research Letters*.

Initial work on the Volcanism GIS has been completed, with spatial and tabular data from four volcanic fields entered into Arc/Info databases. The Volcanism GIS represents an important tool that will be used in volcanism model development and testing, and in evaluation of DOE volcanism hypotheses as part of prelicensing activities and the LARP. Development of the Volcanism GIS also directly relates to the evaluation of KTUs involving igneous activity, conceptual model representation, and prediction of future system states. The Volcanism GIS will be used to construct probability models that incorporate

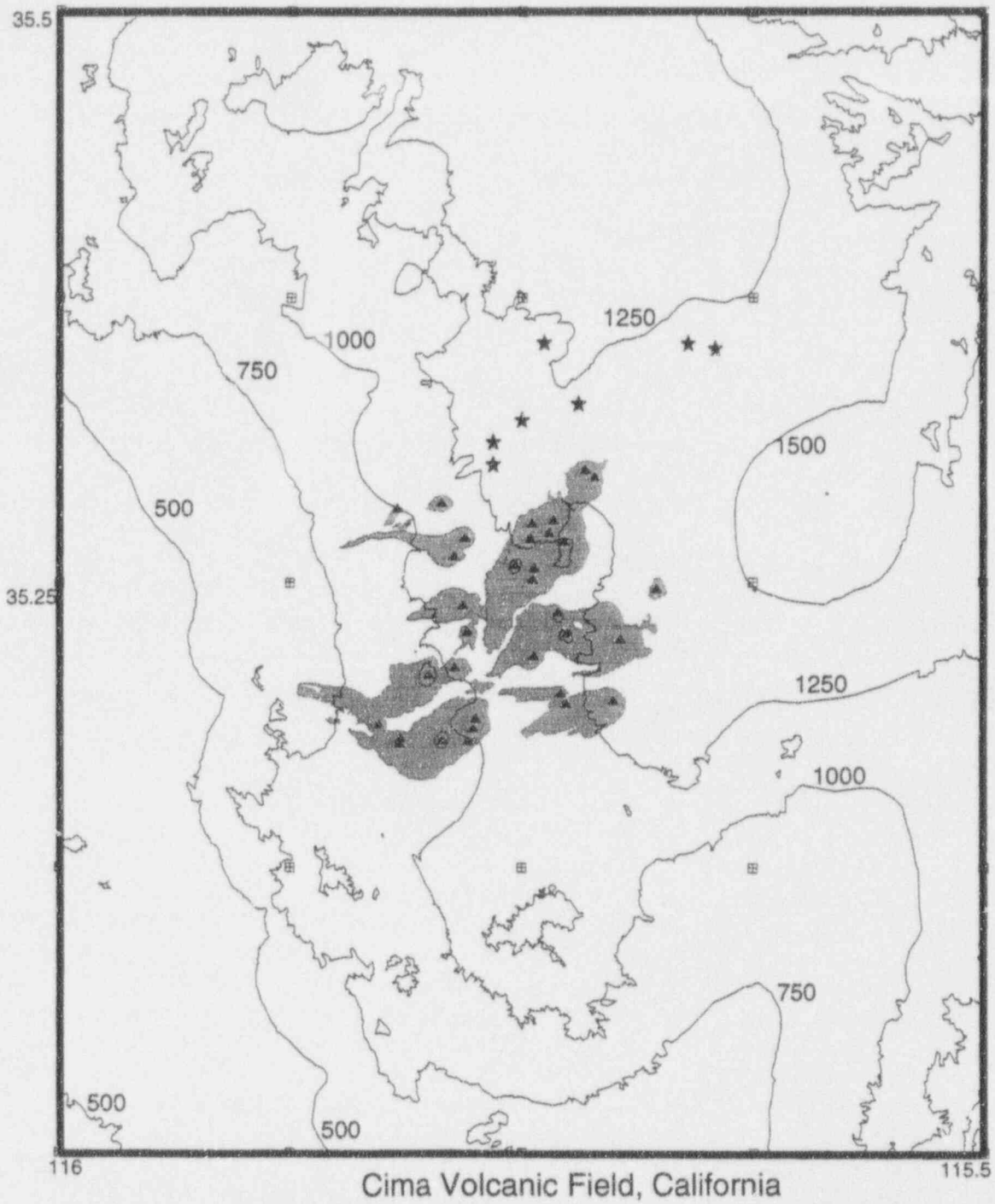

Figure 8-3. Distribution of Quaternary basaltic volcanoes of the Cima Volcanic Field, California. Volcano ages and flow distributions from Turrin et al. (1985) and Dohrenwend et al. (1986), topography from Ivanpah USGS 1:100,000 topographic map. Note that Quaternary volcanoes erupted on a topographic highland, and the volcanoes are distributed over 450 m of vertical relief.

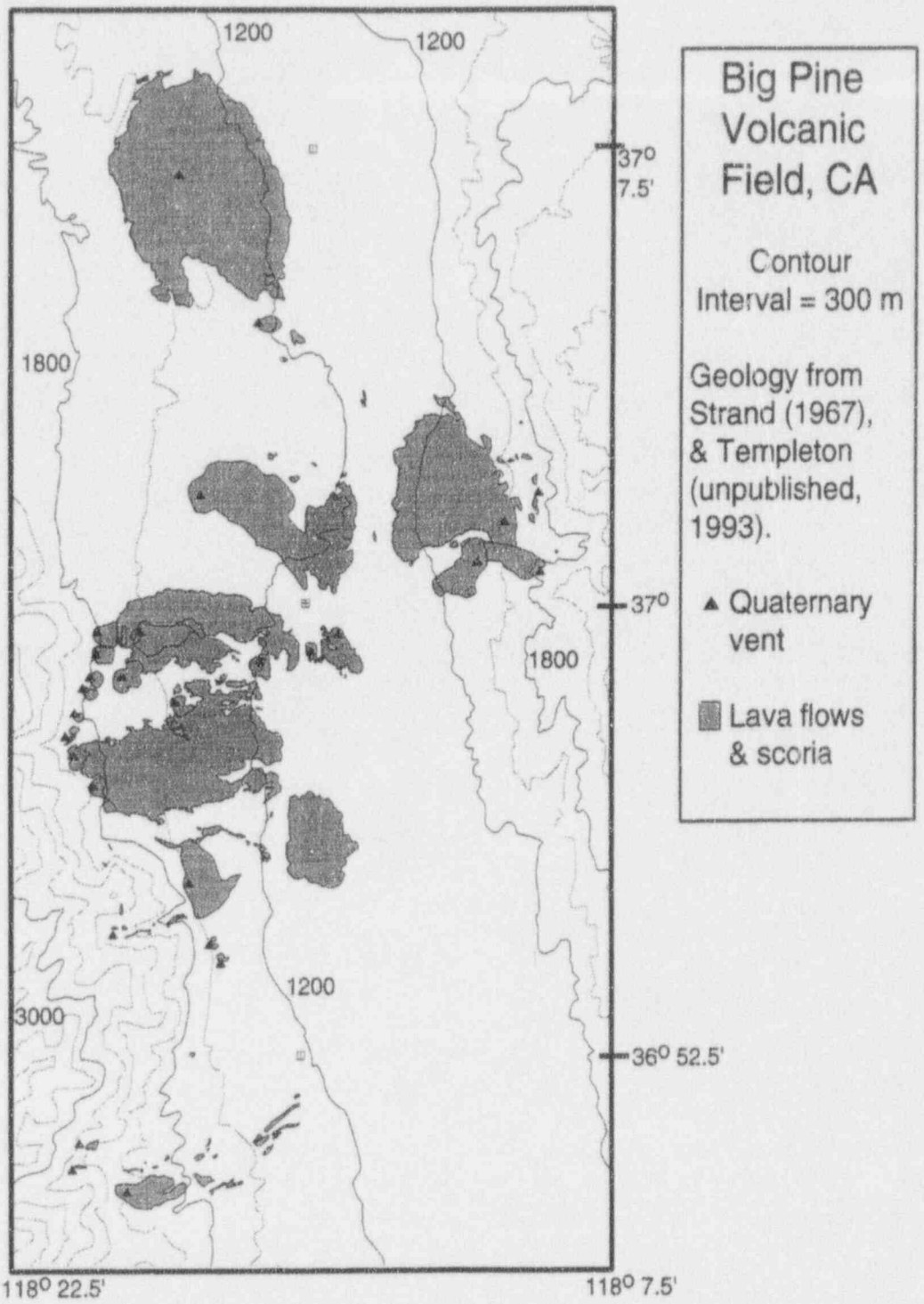

Figure 8-4. Distribution of Quaternary basaltic volcanoes of the Big Pine Volcanic Field, California. Flow distributions and topography from Moore (1963), Nelson (1966), and Strand (1967). Note that Quaternary volcanoes erupted from the Owens Valley floor up to the eastern slopes of the Sierra Nevada Mountains, which represents over 1 km of vertical relief.

geologic data and test these models at other volcanic fields in the western Great Basin. Although additional volcanic fields that are analogous to the YMR need to be entered into the Volcanism GIS, the initial database has been used to disprove the hypothesis that YMR-type volcanic fields are spatially restricted to low-elevation basins.

Results from the Volcanic Systems of the Basin and Range Research Project continue to support CNWRA and NRC reactive work, including DOE study plan reviews, technical exchanges, and document reviews. Regional volcanic data from this project are being integrated with the Field Volcanism and Tectonic Setting of the Basin and Range Research Projects to form the basis for volcanism models in IPA.

8.4 PLANNED PROGRESS IN THE NEXT SIX MONTHS

A major milestone will be delivered to the NRC during January 1994, which will discuss the Volcanism GIS. This report will present an overview of the Arc/Info® software and a discussion of the compiled data for volcanic fields of the Western Great Basin. The Volcanism GIS will be used to further test nonhomogeneous Poisson and similar models at analogous volcanic fields, and to further investigate relationships between tectonics and volcanism in the Western Great Basin. In addition, conceptual and empirical models of basaltic volcanism in the Basin and Range will be developed utilizing the Volcanism GIS.

A critical review of the compiled volcanic and tectonic data will be initiated during the next 6 mo, with a major milestone detailing the results of this review prepared for June 1994. This review will evaluate the completeness of the data used in the Volcanism GIS and assess the uncertainties associated with these data. This report also will address assumptions made in existing volcano-tectonic models for the Western Great Basin.

Probability model development will continue during the next 6 mo. Specific planned activities include development of a Markov point process model for the occurrence of volcanism in the YMR and analogous areas. This model and the nonhomogeneous Poisson model will be tested using data collected from the Springerville, San Francisco, and Pancake volcanic fields. In addition, an evaluation will be made of the best methods for incorporating structural data into probability models. As discussed in Chapter 10 of this volume, faults and related structural weaknesses in the crust act to focus ascending magmas. This has the net result of altering probability of scales of 5 to 10 km in regions of high fault density, such as the YMR. Preliminary data on magma transport along faults will be incorporated into probability models in order to assess the impact of this type of model on scenarios of volcanic disruption.

Extensive interaction with PA is planned for the next 6 mo. This interaction will include alteration of the IPA Phase 2 volcano module to include additional probability scenarios, based on results of the Volcanism of the Basin and Range Research Project.

8.5 REFERENCES

Aitken, M.J. 1967. Thermoluminescence. *Science Journal* 1: 32-38.

Aitken, M.J. 1978. Archaeological involvements of physics. *Physics Reports (Section C of Physics Letters)* 40-5: 277-351.

Amos, R.C., S. Self, and B.M. Crowe. 1983. Pyroclastic activity at Sunset Crater: Evidence of a large magnitude, high dispersal strombolian eruption. *EOS, Transactions of the American Geophysical Union* 62: 1085.

Anthony, E.Y., and J. Poths. 1992. ^{3}He surface exposure dating and its implication for magma evolution in the Potrillo Volcanic Field, Rio Grande Rift, New Mexico, USA. *Geochimica et Cosmochimica Acta* 56: 4,105–4,108.

Berger, G.W. 1985. Thermoluminescence dating of volcanic ash. *Journal of Volcanology and Geothermal Research* 25: 333-347.

Bogue, S.W., and R.S. Coe. 1981. Paleomagnetic correlation of Columbia River Basalt flows using secular variation. *Journal of Geophysical Research* 86: 11,883-11,897.

Cerling, T.E. 1990. Dating geomorphologic surfaces using cosmogenic ^{3}He. *Quaternary Research* 33: 148-156.

Champion, D.E. 1980. *Holocene Geomagnetic Secular Variation in the Western United States: Implications for the Global Geomagnetic Field*. U.S. Geological Survey Open-File Report 80-824. Washington, DC: U.S. Government Printing Office.

Champion, D.E. 1991. Volcanic episodes near Yucca Mountain as determined by paleomagnetic studies at Lathrop Wells, Crater Flat, and Sleeping Butte, Nevada. *Proceedings of the Second International High-Level Radioactive Waste Management Conference*. La Grange Park, IL: American Nuclear Society: 61-67.

Connor, C.B., and B.E. Hill. 1993a. Estimating the probability of volcanic disruption of the candidate Yucca Mountain repository using spatially and temporally nonhomogeneous poisson models. *Proceedings, American Nuclear Society Focus '93 Meeting*. La Grange Park, IL: American Nuclear Society.

Connor, C.B., and B.E. Hill. 1993b. Volcanism Research. *NRC High-Level Radioactive Waste Research at CNWRA, July 1 Through December 31, 1992*. San Antonio, TX: Center for Nuclear Waste Regulatory Analyses: 10-1-10-31.

Creer, K.M. 1981. Long-period geomagnetic secular variations since 12,000 yr BP. *Nature* 292: 208-212.

Crowe, B.M. 1990. Basaltic volcanic episodes of the Yucca Mountain region. *High Level Radioactive Waste Management, International Conference*. Las Vegas, NV. La Grange Park, IL. American Nuclear Society: 1: 65-73.

Crowe, B.M., and F.V. Perry. 1991. *Preliminary Geologic Map of the Sleeping Butte Volcanic Centers*. Los Alamos National Laboratory Report LA-12101-MS. Los Alamos, NM: Los Alamos National Laboratory.

Crowe, B.M., M.E. Johnson, and R.J. Beckman. 1982. Calculation of the probability of volcanic disruption of a high-level nuclear waste repository within southern Nevada, USA. *Radioactive Waste Management and the Nuclear Fuel Cycle* 3: 167-190.

Crowe, B.M., S. Self, D.T. Vaniman, R. Amos, and F.V. Perry. 1983. Aspects of potential magmatic disruption of a high-level nuclear waste repository in southern Nevada. *Journal of Geology* 91: 259-276.

Crowe, B.M., C. Harrington, L. McFadden, F.V. Perry, S. Wells, B. Turrin, and D. Champion. 1988. *Preliminary Geologic Map of the Lathrop Wells Volcanic Center*. Los Alamos National Laboratory Report LA-UR-88-4155. Los Alamos, NM: Los Alamos National Laboratory.

Crowe, B.M., R. Morley, S. Wells, J. Geissman, E. McDonald, L. McFadden, F.V. Perry, M. Murrell, J. Poths, and S. Forman. 1992. The Lathrop Wells volcanic center: Status of field and geochronology studies. *Proceedings of the Third International High Level Radioactive Waste Management Conference*. La Grange Park, IL: American Nuclear Society. 1,997-2,013.

Crowe, B.M., F.V. Perry, and G.A. Valentine. 1993. *Preliminary Draft: Status of Volcanic Hazard Studies for the Yucca Mountain Site Characterization Project*. Los Alamos National Laboratory Report: Los Alamos, NM: Los Alamos National Laboratory.

Dalrymple, G.B., and M.A. Lanphere. 1969. *Potassium-argon dating*. San Francisco, CA: W.H. Freeman and Co.

Dalrymple, G.B., and M.A. Lanphere. 1974. $^{40}Ar/^{39}Ar$ age spectra of some undisturbed terrestrial samples. *Geochimica et Cosmochimica Acta* 38: 715-738.

Dohrenwend, J.C., L.D. McFadden, B.D. Turrin, and S.G. Wells. 1984. K-Ar dating of the Cima Volcanic Field, eastern Mojave Desert, California: Late Cenozoic volcanic history and landscape evolution. *Geology* 12: 163-167.

Dohrenwend, J.C., S.G. Wells, and B.D. Turrin. 1986. Degradation of Quaternary cinder cones in the Cima Volcanic Field, Mojave Desert, California. *Geological Society of America Bulletin* 97: 421-427.

Dorn, R. I., and F. M. Phillips. 1991. Surface exposure dating: review and critical evaluation. *Physical Geography* 12: 303-333.

Fleck, R.J., J.F. Sutter, and D.H. Elliot. 1977. Interpretation of discordant $^{40}Ar/^{39}Ar$ age-spectra of Mesozoic tholeiites from Antarctica. *Geochimica et Cosmochimica Acta* 41: 15–32.

Forman, S.L. 1989. Applications and limitations of thermoluminescence to date Quaternary sediments. *Quaternary International* 1: 47–59.

Geyh, M.A., and H. Schleicher. 1990. *Absolute Age Determination*. New York, NY: Springer Verlag.

Gill, J.B., D.M. Pyle, and R.W. Williams. 1992. Igneous rocks. *Uranium Series Disequilibrium: Applications to Earth, Marine, and Environmental Sciences*. M. Ivanovich, and R.S. Harmon, eds. Oxford: Clarendon Press: 207–258.

Gutmann, J.T. 1979. Structure and eruptive cycle of cinder cones in the Pinacate Volcanic Field and the controls of strombolian activity. *Journal of Geology* 87: 448-454.

Harrison, T.M. 1983. Some observations on the interpretation of $^{40}Ar/^{39}Ar$ age spectra. *Isotope Geoscience* 1: 319–338.

Hasenaka, T., and I.S.E. Carmichael. 1985. The cinder cones of Michoacán-Guanajuato, central Mexico, their age, volume, distribution, and recharge rate. *Journal of Volcanology and Geothermal Research* 25: 195–204.

Head, J.W., III, and L. Wilson. 1989. Basaltic pyroclastic eruptions: Influence of gas-release patterns and volume fluxes on fountain structure, and the formation of cinder cones, spatter cones, rootless flows, lava ponds and lava flows. *Journal of Volcanology and Geothermal Research* 37: 261–271.

Hill, B.E., B.W. Leslie, and C.B. Connor. 1993. *A Review and Analysis of Dating Techniques for Neogene and Quaternary Volcanic Rocks*. CNWRA 93-018. San Antonio, TX: Center for Nuclear Waste Regulatory Analyses.

Ho, C.-H., E.I. Smith, D.L. Feurbach, and T.R. Naumann. 1991. Eruptive probability calculation for the Yucca Mountain site, USA: Statistical estimation of recurrence rates. *Bulletin of Volcanology* 54: 50–56.

Holcomb, R., D. Champion, and M. McWilliams. 1986. Dating recent Hawaiian lava flows using paleomagnetic secular variation. *Geological Society of America Bulletin* 97: 829–839.

Kaneoka, I. 1972. The effect of hydration on the K/Ar ages of volcanic rocks. *Earth and Planetary Science Letters* 14: 216–220.

Kurz, M.D., D. Colodner, T.W. Trull, R.B. Moore, and K. O'Brien. 1990. Cosmic ray exposure dating with *in situ* produced cosmogenic ^{3}He: results from young Hawaiian lava flows. *Earth and Planetary Science Letters* 97: 177–189.

Lal, D. 1987. Cosmogenic nuclides produced *in situ* in terrestrial solids. *Nuclear Instruments and Methods in Physics Research* B29: 238–243.

Lal, D. 1988. *In situ*-produced cosmogenic isotopes in terrestrial rocks. *Annual Review of Earth and Planetary Science* 16: 355-388.

Luedke, R.G., and R.L. Smith. 1981. Map showing distribution, composition, and age of Late Cenozoic volcanic centers in California and Nevada. *USGS Misc. Inv. Ser. Map I-1091-C.* 1:1,000,000.

Luo, S., and T.-L. Ku. 1991. U-series isochron dating: a generalized method employing total-sample dissolution. *Geochimica et Cosmochimica Acta* 55: 555-564.

Mankinen, E.A., C.S. Grommé, G.B. Dalrymple, M.A. Lanphere, and R.A. Bailey. 1986. Paleomagnetism and K-Ar ages of volcanic rocks from Long Valley Caldera, California. *Journal of Geophysical Research* 91: 633-652.

May, R. J. 1979. *Thermoluminescence Dating of Hawaiian basalt.* U.S. Geological Survey Professional Paper 1095. Washington, DC: U.S. Government Printing Office.

McDougall, I., and T.M. Harrison. 1988. *Geochronology and Thermochronology by the $^{40}Ar/^{39}Ar$ Method.* New York, NY: Oxford University Press.

McFadden, L.D., S.G. Wells, and J.C. Dohrenwend. 1986. Influences of Quaternary climatic changes on processes of soil development on desert loess deposits of the Cima Volcanic Field, California. *Catena* 13: 361-389.

McGetchin, T.R., M. Settle, and B.A. Chouet. 1974. Cinder cone growth modeled after Northeast Crater, Mount Etna, Sicily. *Journal of Geophysical Research* 79: 3,257-3,272.

Moore, J.G. 1963. *Geology of the Mount Pinchot Quadrangle, Southern Sierra Nevada, California.* U.S. Geological Survey Bulletin 1130. Washington, DC: U.S. Government Printing Office.

Nelson, C.A. 1966. *Geologic Map of the Waucoba Mountain Quadrangle, Inyo County, California.* U.S. Geological Survey Map GQ-528. Washington, DC: U.S. Government Printing Office.

Palmer, A.R. 1983. The Decade of North American Geology 1983 Geologic Time Scale. *Geology* 11: 503-504.

Porter, S.C. 1972. Distribution, morphology, and size frequency of cinder cones on Mauna Kea Volcano, Hawaii. *Geological Society of America Bulletin* 83: 3,607-3,612.

Poths, J., and B.M. Crowe. 1992. Surface exposure ages and noble gas components of volcanic units at the Lathrop Wells volcanic center, Nevada. *EOS, Transactions of the American Geophysical Union* 73-43: 610.

Sarna-Wojcicki, A.M. 1976. *Correlation of Late Cenozoic Tuffs in the Central Coast Ranges of California by Means of Trace- and Minor-Element Chemistry.* U.S. Geological Survey Professional Paper 972. Washington, DC: U.S. Government Printing Office.

Scott, D.H., and N.J. Trask. 1971. *Geology of the Lunar Crater Volcanic Field, Nye County, Nevada.* U.S. Geological Survey Professional Paper 599-I. Washington, DC: U.S. Government Printing Office.

Settle, M. 1979. The structure and emplacement of cinder cone fields. *American Journal of Science* 279: 1,089-1,107.

Sinnock, S., and R.G. Easterling. 1983. *Empirically Determined Uncertainty in Potassium-Argon Ages for Plio-Pleistocene Basalts from Crater Flat, Nye County, Nevada.* Sandia National Laboratory Report SAND 82-2441. Albuquerque, NM: Sandia National Laboratory.

Stirewalt, G.L., S.R. Young, and K.D. Mahrer. 1992. *A review of pertinent literature on volcanic-magmatic and tectonic history of the Basin and Range.* CNWRA 92-[illegible]5. San Antonio, TX: Center for Nuclear Waste Regulatory Analyses.

Strand, R.G. 1967. *Geologic Map of California, Mariposa Sheet.* Mariposa Sheet, Scale 1:250,000. Sacramento, California: California Division of Mines and Geology.

Szabo, B.J., W.J. Carr, and W.C. Gottschall. 1981. *Uranium-Thorium Dating of Quaternary Carbonate Accumulations in the Nevada Test Site Region, Southern Nevada.* U.S. Geological Survey Open-File Report. 81-19. Washington, DC: U.S. Government Printing Office.

Tarling, D.H. 1983. *Paleomagnetism—Principles and Application in Geology, Geophysics, and Archaeology.* New York, NY: Chapman and Hall.

Turrin, B.D., D.E. Champion, and R.J. Fleck. 1991. $^{40}Ar/^{39}Ar$ age of the Lathrop Wells Volcanic Center, Yucca Mountain, Nevada. *Science* 253: 654–657.

Turrin, B.D., J.C. Dohrenwend, R.E. Drake, and G.H. Curtis. 1985. K–Ar ages from the Cima Volcanic Field, eastern Mojave Desert, California. *Isochron/West* 44: 9–16.

Vaniman, D.T., and B.M. Crowe. 1981. *Geology and Petrology of the Basalts of Crater Flat: Applications to Volcanic Risk Assessment for the Nuclear Waste Storage Investigations.* Los Alamos National Laboratory Report LA-8845-MS. Los Alamos, NM: Los Alamos National Laboratory.

Vaniman, D.T., B.M. Crowe, and E.S. Gladney. 1982. Petrology and geochemistry of Hawaiite lavas from Crater Flat, Nevada. *Contributions to Mineralogy and Petrology* 80: 341–357.

Wang, C.H., D.L. Willis, and W.D. Loveland. 1975. *Radiotracer Methodology in the Biological, Environmental, and Physical Sciences.* Englewood Cliffs, NJ: Prentice-Hall, Inc.

Wells, S.G., J.C. Dohrenwend, L.D. McFadden, B.D. Turrin, and K.D. Mahrer. 1985. Late Cenozoic landscape evolution on lava flow surfaces of the Cima volcanic field, Mojave Desert, California. *Geological Society of America Bulletin* 96: 1,518-1,529.

Wells, S.G., L.D. McFadden, C.E. Renault, and B.M. Crowe. 1990. Geomorphic assessment of late Quaternary volcanism in the Yucca Mountain area, southern Nevada: Implications for the proposed high-level radioactive waste repository. *Geology* 18: 549–553.

Williams, H. 1950. *Volcanoes of the Parícutin region.* U.S. Geological Survey Bulletin 965B. Reston, VA: U.S. Geological Survey: 165–275.

Wilson, L. 1980. Relationships between pressure, volatile content, and ejecta velocity in three types of volcanic explosion. *Journal of Volcanology and Geothermal Research* 8: 297–313.

Wilson, L., R.S.J. Sparks, T.C. Huang, and N.D. Watkins. 1978. The control of volcanic column heights by eruption energetics and dynamics. *Journal of Geophysical Research* 83(b4): 1,829.

Wood, C.A. 1980. Morphometric evolution of cinder cones. *Journal of Volcanology and Geothermal Research* 7: 387–413.

Zreda, M.G., F.M. Phillips, D. Elmore, P.W. Kubik, P. Sharma, and R.I. Dorn. 1991. Cosmogenic chlorine-36 production rates in terrestrial rocks. *Earth and Planetary Science Letters* 105: 94-109.

Zreda, M.G., F.M. Phillips, P.W. Kubik, P. Sharma, and D. Elmore. 1993. Cosmogenic ^{36}Cl dating of a young basaltic eruption complex, Lathrop Wells, NV *Geology* 21: 57–60.

9 TECTONICS

by Stephen R. Young and Gerry L. Stirewalt

Investigators: Stephen R. Young, Gerry L. Stirewalt, Ronald H. Martin, Richard Klar (CNWRA); and Brent Henderson (SwRI)

NRC Project Officer: George F. Birchard

9.1 TECHNICAL OBJECTIVES

The objectives of the Tectonics Research Project are: (i) to compile and integrate tectonic data for the central Basin and Range and Yucca Mountain (YM) regions, and (ii) to develop and assess models of tectonic processes. The purpose of the project is to evaluate the adequacy of existing data, methods, and models for demonstrating and determining compliance with regulatory requirements. Of particular concern is the adequacy of existing and anticipated data for meeting quantitative waste-isolation performance objectives. A Geographic Information System (GIS) is being used to compile data from disparate sources into an integrated management, review, and analysis environment. Significant technical accomplishments to date consist of: (i) development of digital terrain models of the YM and central Basin and Range regions; (ii) production of integrated maps of Quaternary faults, Quaternary basaltic volcanic fields, and historic earthquake seismicity; and (iii) compilation of an initial database of geodetically measured regional strain and geologically determined slip rates for individual fault systems. Data and references compiled by Tectonics Research project staff have been used to develop Compliance Determination Strategies (CDSs) on Structural Deformation [License Application Review Plan (LARP) No. 3.2.1.5], Evidence of Igneous Activity (LARP No. 3.2.1.9), and Structural Deformation and Groundwater (LARP No. 3.2.2.8). Digital terrain and boundary data, and visualization methods developed for tectonics research are also being used in the Regional Hydrogeology Research Project.

Important goals of this project include development and analyses of alternative tectonic models and evaluation of potential hazards due to fault displacement and seismic shaking. Thus, it is necessary to consider contemporary strain, partitioning of neotectonic strain as reflected by Quaternary faulting and paleoseismicity, and correlations with modern seismicity. Paleoseismology, identification, and study of prehistoric earthquakes (Wallace, 1981) relies largely on the stratigraphic record to decipher timing and recurrence of Quaternary faulting and related prehistoric earthquakes (Crone 1987a). Dependable age estimates are critical for assessing history of faulting and paleoseismicity. Analysis techniques appropriate for Quaternary nonmarine sedimentary rocks are used for estimating ages and slip history of prehistoric faulting and associated paleoseismic events (Crone, 1987a; Wallace, 1987a). Assessments of the utility and reliability of methods used to determine Quaternary slip history of faulting, to recognize paleoseismic events in the nonmarine rock record, and to estimate ages of fault displacements are, thus, very important to quantification of uncertainty in paleoseismology.

The purpose of the Global Positioning Satellite (GPS) surveys are to directly measure contemporary strain (patterns and rates) in the YM region. The GPS surveys are expected to provide reliable displacement vectors in less than a decade, with detection limits for horizontal motion in the range of millimeters. The general procedure involves periodic measurement of the survey stations to determine precise positions using satellite signals. Consequently, contemporary tectonic movement can be detected and rates and patterns of strain can be calculated. This information will provide important

constraints on alternative tectonic models of the YM region, and for prelicensing and license review of potential hazards due to fault rupture, earthquakes, and igneous activity.

9.2 SIGNIFICANT TECHNICAL ACCOMPLISHMENTS

Significant accomplishments since the last report include: (i) development of an improved Quaternary fault coverage in the Tectonics Research Geographic Information System (TecResGIS), (ii) field work to assist in conducting a U.S. Nuclear Regulatory Commission (NRC)/CalTech GPS survey in the YM region, and (iii) completion of a literature review on geochronological methods used to determine slip history of faulting.

9.2.1 Correlation of Large Earthquakes with Quaternary Faults

Coverage of Quaternary and Holocene fault traces in the TecResGIS has been considerably enhanced by incorporation of new data sets (Figure 9-1). Detailed fault traces have been added from Jennings (1992) in California, and from Dohrenwend (1982), Dohrenwend and Moring (1991 a,b,c; 1993), and Dohrenwend et al. (1991 a-f, 1992 a,b) in Nevada. These types of regional maps of earthquakes, Quaternary faults, Holocene faults, and historical ground rupture readily show which fault systems are seismically active and are required to determine more precisely the earthquake return period for discrete fault segments. Comprehensive regional compilations are also needed to determine if existing data are sufficient to describe temporal and geographic patterns of seismicity and faulting. At this time, it is not clear that existing data are sufficient to characterize these patterns.

Tne tectonic framework of earthquake seismicity in the central Basin and Range region is not well understood. Considerable evidence exists that slip rates on discrete fault segments are not uniform in space or time. In essence, recurrence frequency predictions (estimated return period) of large earthquakes from localized measurements are very uncertain. In general, estimates of recurrence of large ($>$ M6.0) earthquakes depend almost exclusively on: (i) extrapolation of historic rate of occurrence of large earthquakes, (ii) extrapolation of historic rate of occurrence of smaller earthquakes, and (iii) geological studies of prehistoric coseismic faulting events preserved in the layered rock record. Even for regions within which somewhat longer historical records and paleoseismological data are available (e.g., southern California), estimates of recurrence frequency remain uncertain. The central Basin and Range region is particularly problematic because of the relatively short historical record (60 to 100 yr) and because few detailed paleoseismological studies have been conducted. There is substantial inconsistency between recurrence estimates based on the different approaches mentioned above (Rogers et al., 1991), which indicates a lack of fundamental understanding or a lack of data, or both.

Since about 1852 (initial historical observation), earthquakes in Nevada of M7.0 and greater have occurred on average every 27 yr, and have been generally restricted to within the central Nevada seismic belt (CNSB) (Rogers et al., 1991). The CNSB is marked by the cluster of earthquakes in the west-central part of the state (Figure 9-1). However, geological estimates (e.g., trench studies, fault-scarp geomorphology) of the average return period for large earthquakes on individual Quaternary fault segments within the Basin and Range region (including parts of the Wasatch fault zone) range from less than 1,000 to 3,000 yr (for a review of recent work see Young et al., 1993). Thus, rates of earthquakes and coseismic faulting appear to be nonuniform in time and space. Faults within a particular region (e.g., the CNSB) may be active at a high rate over a certain period of time, and then remain quiet over an equal or greater period. Wallace (1987b) and Rogers et al. (1991) have suggested that the average duration of

Figure 9-1. Correlation of large earthquakes with Quaternary faults. Fault traces are from Jennings (1992) in California; Dohrenwend (1982), Dohrenwend and Moring (1991 a,b,c), and Dohrenwend et al. (1991 a–f, 1992 a,b) in Nevada; Nakata et al. (1982) in Nevada (bold trace); and Frizzell and Shulters (1990) in the Yucca Mountain area (nine-square grid in center of image). Earthquakes M 6.0–7.0 are indicated by the six pointed star (asterisk). Earthquakes > M 7.0 are indicated by five pointed star.

an active episode for a discrete fault segment is between 5,000 and 10,000 yr, and that the duration of the combined active and quiescent episodes is between 15,000 and 30,000 yr. Because fault activity apparently migrates in space and time, the slip rate of discrete fault segments or groups of segments can change significantly with time. Slip rates during the active episodes may be significantly higher than the long-term average rate estimated from the total displacement of a fault system. Return periods estimated from active-episode slip rates would overestimate long-term risk. Return periods estimated from average slip rates, or quiescent-episode rates, would underestimate long-term risk.

9.2.2 Global Positioning Satellite Measurements

To measure and analyze contemporary strain in the region around YM and to better understand its role in distribution and timing of faulting, earthquake seismicity, and volcanism GPS survey stations have been established throughout the YM region (Figure 9-2). The GPS is comprised of a constellation of satellites used to determine the position of a single radio receiver, or network of receivers (Leick 1990). Survey stations were first selected and data collection begun by Brian Wernicke (CalTech) and his team in October, 1991. Stations utilized either previously surveyed U.S Geological Survey (USGS) benchmarks, or newly surveyed points placed by CalTech staff in 1991 under the direction and supervision of Wernicke. The stations occupied during this survey campaign (1993), which are the same as those occupied in 1991, are shown in Figure 9-2. Latitudes, longitudes, and particularly elevations used to post the stations are approximate values read from the receiver in the field. These values will be refined upon final processing of data by J. Davis at the Smithsonian Institution Astrophysical Observatory (SIAO) in Cambridge, Massachusetts.

The GPS surveys are being conducted within a region which includes YM, the Northern Death Valley (NDV) fault zone, and the Hunter Mountain (HM) fault zone. The northwest-southeast-trending NDV Furnace Creek fault zone lies northeast of the Cottonwood Mountains, and the subparallel HM fault zone bounds the Cottonwoods on the southwest (Snow and White, 1991). Both fault zones exhibit large right-lateral strike-slip displacements. The Death Valley region is the most strongly extended sector of the Cordillera and is characterized by a complex combination of right-lateral shearing, crustal thinning, and vertical-axis rotation of major crustal blocks like the Black Mountains (Holm et al., 1993), and possibly Bare Mountain (Snow and Wernicke, 1989; Holm et al., 1993). The YM region survey is designed to detect displacements that would indicate the rate and amount of strain accumulating across the network. The survey is structured to detect discrete slip across the NDV and HM fault zones, and to detect distributed strain across the Wahomie-Claim baseline at YM. Because strain accumulation is a necessary condition for earthquake rupture, direct measurement of displacements and crustal strain will contribute substantially to estimates of earthquake frequency and magnitude, especially in the absence of appropriate historical and paleoseismological data. A preliminary comparison of the Wahomie-Mile baseline (Figure 9-2) with previous geodimeter (optical geodetic distance meter) surveys conducted by the USGS in 1984 did not indicate significant relative motion. However, comparison of the Wahomie-Mile GPS baseline (1991) with a subsequent USGS survey of the line conducted after the 1992 Little Skull Mountain earthquake indicates a significant (approximately 1 cm) lengthening of the baseline, probably as a result of the earthquake. These results are preliminary and will be reevaluated in detail following final processing of the recent GPS positions.

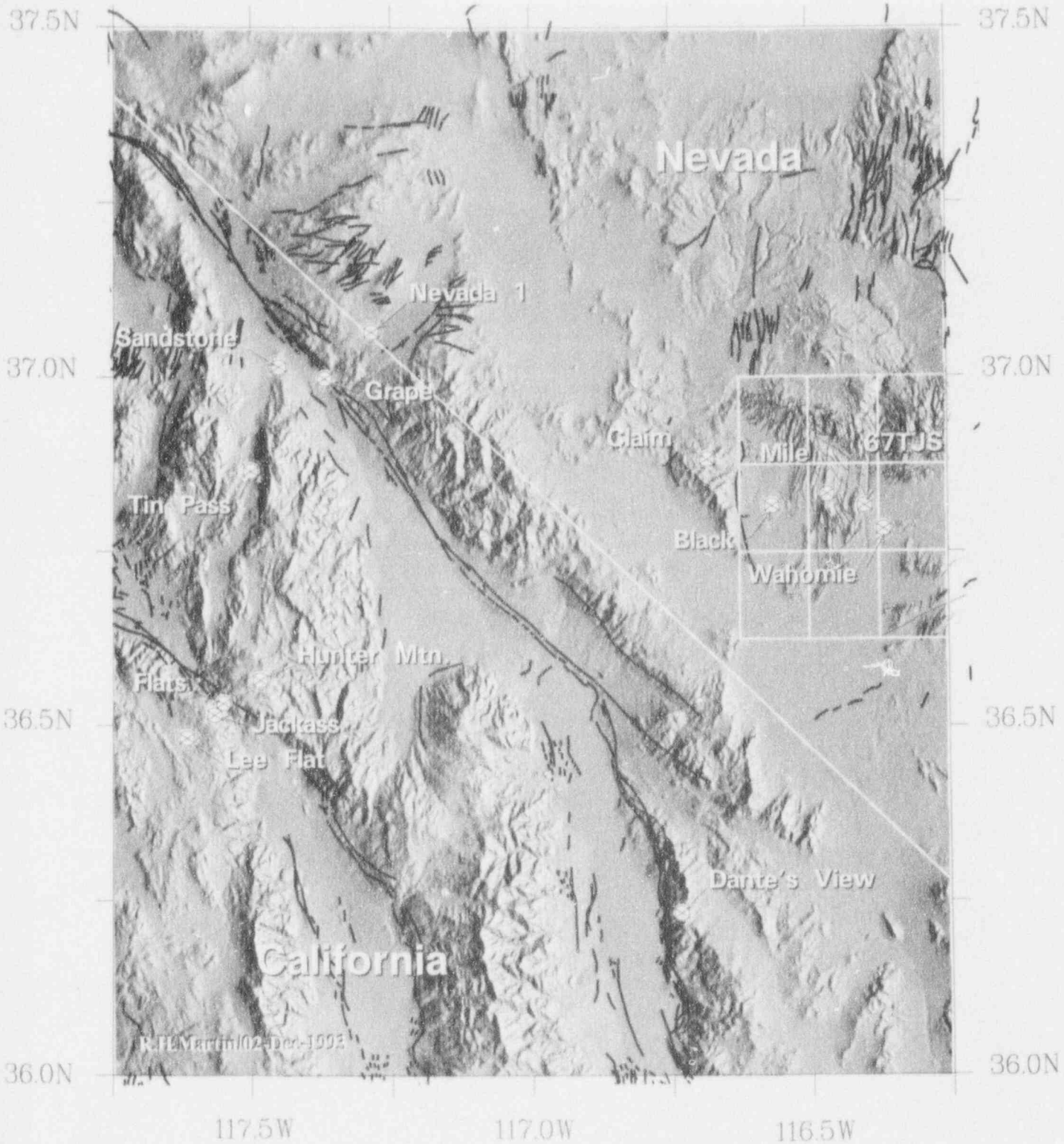

Figure 9-2. Global positioning system (GPS) stations. Faults are from sources noted in Figure 9-1. Yucca Mountain is located at the center of the nine-square grid. Map projection is Universal Transverse Mercator.

9.2.3 Review of Literature on Paleoseismology and Geochronology of Faulting

Recognition of paleoseismic events preserved in the Quaternary rock record and methods used to date these events are substantial sources of uncertainty in assessments of hazards due to earthquakes and fault rupture. Preservation of geological evidence of prehistoric earthquakes and coseismic fault rupture is dependent upon a somewhat fortuitous balance between tectonic, erosional, and depositional processes. Nevertheless, good age estimates of these events are unequivocally recognized as essential for credible risk assessments (Allen, 1986; Crone, 1987b).

In addition to potential preservation problems, characteristics of deposits preserved have been observed to vary with type of tectonic environment (i.e., extensional, compressional, or strike-slip) existing at the time of faulting (Crone, 1987b; McCalpin, 1987; Carver, 1987; and Rockwell, 1987). In extensional environments, geologic criteria for recognition of paleoseismic events fit broadly into one of three categories: (i) relationships between geomorphic surfaces and fault scarps, (ii) multiple-event fault-scarp morphology, and (iii) fault-scarp-derived stratigraphy (McCalpin, 1987). The most detailed information on number of faulting events, fault displacement, and recurrence rates of faulting is derived from stratigraphy in fault-scarp-derived colluvial wedges at the base of the scarp, either naturally exposed or in excavated trenches (McCalpin, 1987; Nelson, 1987).

An early example of the use of scarp-derived colluvial wedge stratigraphy for analysis of faulting history is shown by investigations of the Wasatch fault zone in Utah by Swan et al. (1980). They were able to deduce that repeated surface faulting along the same trace of the fault produced a complex stack of wedges of fault-scarp-derived colluvium with each wedge representing an individual faulting and paleoseismic event. Subsequent workers have commonly used fault-scarp-derived colluvium and associated soil horizons (in connection with determination of age estimates for faulting) to successfully analyze fault slip history and paleoseismicity (e.g., Schwartz and Coppersmith, 1984; Machette and Lund, 1987; Schwartz et al., 1988; Forman et al., 1989. 1991; Berry, 1990; and Machette et al., 1992).

Although the theory behind determining the number and timing of faulting events using fault-scarp-derived stratigraphy is clear (i.e., count the number of individual colluvial wedges to tally the events and determine ages of appropriate materials within individual wedges to bracket the ages of faulting), tectonic, erosional, and depositional modification of the wedges commonly introduce complexities which must be taken into account at specific study locations. Repeated faulting along the same fault trace (e.g., Swan et al., 1980) is an example of complexities introduced by local tectonic modification of existing scarps and scarp-derived colluvium. It most often disrupts earlier colluvial wedges by displacement or rotation, altering the initial shape of the wedge and possibly juxtaposing colluvial blocks produced by different faulting events (McCalpin, 1987). This disruption leads to difficulty in definition and description of individual faulting events.

From analyses of historical surface faulting in the Basin and Range region, DePolo et al. (1991) determined that surface ruptures from seismic events of M7 or greater involved failure on multiple segments. Temporal and spatial segmentation of fault systems results in variation of slip along a fault trace so that maximum slip may not have occurred at the location being analyzed (Menges, 1987). Hence, if segmentation is not recognized, slip amount and slip rates can be incorrectly determined.

Nonuniformity of slip rates, evidenced in temporal clustering of fault movement (Wallace, 1987b) and in consecutive rupture of a single fault or fault zone preferentially over adjacent faults

(Machette, 1987), is a tectonic complexity which may lead to incorrect determination of slip rates and faulting recurrence rates. For example, Machette (1987) notes a 5- to 10-fold increase in average slip rate for the Wasatch fault zone over a shorter time frame (15 ka) compared to a longer one (150 ka) because of temporal clustering. More recent studies along the Wasatch fault have corroborated the concept of Holocene temporal clustering of slip on this fault (Machette et al., 1991). Preliminary results from studies of excavated trenches suggest that temporal clustering may characterize late Quaternary movement history of the Paintbrush Canyon and Solitario Canyon faults at YM (J. Whitney and A. Ramelli, personal communication, 1993).

Erosion of colluvial wedges and capping soil horizons can produce fragmentary stratigraphic records (Nelson, 1987) resulting in an incomplete stratigraphic sequence for bracketing ages of faulting. Complex lithofacies which may be caused by a variety of factors (e.g., climatic change; magnitude, extent, and recurrence interval of events producing surface ruptures; surface rupture patterns; local geomorphology; type of sediment; and mode of deposition) influence sediment transport and deposition patterns near fault scarps (Nelson, 1987). This complexity leads to difficulty in determining clear-cut stratigraphic relationships for age estimates of faulting.

In general, Quaternary age determination methods have been classified according to type of method and anticipated results (Colman et al., 1987). However, not all of these methods are useful for estimating age of Quaternary faulting. The same is true for techniques which have generally been used for estimating age of faulting at nuclear power sites (Murphy et al., 1979). Estimating ages of stratigraphic units and horizons which are either offset by or overlie a fault without displacement provide maximum or minimum ages for faulting, respectively, regardless of the method used. (That is, an age for a unit offset by a fault gives a maximum age for the fault because it must be younger than the unit cut; a date on an overlying unit that is not displaced gives a minimum age for fault displacement because the fault must be older than that unit. Age determinations on secondary minerals in the fault plane which have not been disrupted by faulting also give minimum ages for fault movement since the fault must predate formation of those minerals.) Ideally, the ages more closely approximate the age of faulting if fault-scarp-derived colluvial wedge materials or associated soil horizons can be analyzed, particularly if the time for deposition or development of these units is relatively short as workers have suggested from field evidence at certain locations in the Basin and Range (e.g., Forman et al., 1989, 1991). Analyses of degradation of historic fault scarps in the Basin and Range region indicate that colluvium shed from the free face of the scarps covers soils on the surface of the downthrown block within 5 to 10 m of the fault zone in about 10–100 yr after faulting has occurred (Wallace, 1977; Crone et al., 1987; Bell and Katzer, 1987; and Lubetkin and Clark, 1988).

Determining the age of scarp-derived colluvium and associated soils is the common approach used for analysis of Quaternary fault history and paleoseismicity, with both standard methods (e.g., use of Carbon-14 by Schwartz and Coppersmith, 1984; Machette and Lund, 1987; Schwartz et al., 1988) and less standard techniques [e.g., application of thermoluminescence (TL) by Jackson et al., 1987; Forman et al., 1988a; 1989; McCalpin and Forman, 1991] being applied. The recommended approach is to use multiple methods on different types of samples from the same stratigraphic sequence as a cross-check on age estimates of faulting (Forman et al., 1991). Berry and Birkeland (1988) and Berry (1990) combined Carbon-14 with TL in analysis of late Quaternary faulting in the Sierra Nevada, stressing the potential problems with relying on a single method for ascertaining the age of fault-scarp-derived surficial materials. Uranium-series (U/Th) may have applicability for age estimates on carbonate vein material and caliche (Geyh and Schleicher, 1990) seen to occur associated with fault zones at YM. Electron spin resonance (ESR) is an experimental method which may prove useful to directly estimate the age of last

fault movement by determining the age of quartz in fault gouge, since the fault movement itself resets the "time clock" in the quartz to time zero under the proper depth conditions (Grun, 1991, 1992). Table 9-1 indicates ideal age ranges over which these methods can be used and the materials for which they may be applicable at YM.

9.2.3.1 Carbon-14

Radiocarbon dating (Faure, 1986) is the standard method for obtaining ages on organic material (Geyh and Schleicher, 1990), usually for materials less than about 40 ka in age (Hill et al., 1993). The technique is applicable for determining ages of organic materials in sediments which have been offset by a fault (maximum age for faulting) or overlie a fault (minimum age for faulting), including sediments developed as fault-scarp-derived colluvium and associated soils. The largest source of error from this method originates in contamination of the sample by younger carbon (Geyh and Schleicher, 1990) as may occur by root growth into fault-scarp-derived colluvium or associated soils. This error is separate and distinct from the problems which may develop in selection of materials to be analyzed because of effects of tectonic, erosional, and depositional processes on colluvium and associated soils. Careful sampling and removal of contaminants are necessary to avoid contamination problems. Conservative researchers consider conventional Carbon-14 age estimates to have an analytical precision around ±60–80 yr (Stenhouse and Baxter, 1983). For sediments and soils with carbon content varying between 0.2 to 5 percent, 50 to 1500 g of material may be required to obtain enough for a reliable age estimate (Geyh and Schleicher, 1990). Among other factors, sample size is determined by carbon content of the material being collected. It may need to be increased as much as tenfold if the material is highly contaminated with organic residues from roots or humic acids or has a high detrital mineral content (Geyh and Schleicher, 1990). The sample should not be so large that the time span of its formation, or the sample time-width, is as great or greater than the confidence interval of the Carbon-14 age (Mook, 1983).

Carbon-14 age analysis should have application at YM for investigating Holocene faulting if carbonaceous materials exist in the fault scarp-derived colluvium or associated soils. Carbon-14 has been successfully used for soils formed on fault-scarp-derived colluvium to provide age estimates for late Quaternary fault history of segments of the Wasatch fault zone (Schwartz and Coppersmith, 1984; Machette and Lund, 1987; Schwartz et al., 1988). It has also been used with TL to estimate timing of faulting and paleoseismic history along the Wasatch fault (Machette et al., 1992). As previously discussed, estimated ages may more closely approximate age of faulting when fault-scarp-derived colluvium and associated soils are analyzed (Forman et al., 1989; 1991).

9.2.3.2 Uranium-Series

Use of Uranium-234/Thorium-230 for determining ages based on radioactive disequilibrium can provide age estimates on carbonate deposits, usually for materials greater than several thousand years to about 350-ka in age (Geyh and Schleicher, 1990). The technique is applicable to estimating ages of terrestrial carbonate materials, including caliche and secondary calcite in fault zones (Geyh and Schleicher, 1990) and pebbles of pedogenic carbonate which occur in arid regions (Schlesinger, 1985). The application of the U/Th method to carbonate deposits is possible because they are usually free of initial Thorium-230, but coprecipitate dissolved uranium. Therefore, calculation of time elapsed since deposition is possible if these deposits have remained a closed system with respect to uranium isotopes and Thorium-230 (Szabo and O'Malley, 1985). Consequently, one potential problem is recognized to be the existence of open systems wherein uranium may be partially mobilized by leaching, accumulation, or precipitation of secondary carbonate (Geyh and Schliecher, 1990). Thiel et al. (1983) have discussed

Table 9-1. Methods potentially applicable for estimating age of Quaternary faulting at Yucca Mountain

Method [a]	Ideal Effective Age Range [b]	Applicable Materials [c]
Carbon-14	less than/equal to 40 ka [1]	Organic Carbon [c]
U/Th	several ka to 350 ka [2]	Organic and inorganic carbonates (including secondary calcite and caliche) [c]
TL	75-100 ka [3]	Sediments (including fault-scarp) derived colluvium and associated soils) [c]
ESR	1 ka to 1-2 my [4]	Quartz in fault gouge [d] and secondary silica and calcite [c]

[a] Carbon-14 and U/Th are standard methods; TL is considered less standard; ESR is most experimental of the four (Colman et al., 1987)

[b] 1 ka=a thousand years; 1 my=a million years (Colman et al., 1987)

[c] Provides maximum or minimum age estimates for faulting

[d] Provides direct age estimate for last fault movement

References for age ranges shown:

[1] Hill et al., 1993

[2] Geyh and Schleicher, 1990

[3] Forman, 1989

[4] Grun, 1992

procedures for detection of mobilization of uranium, however. Another potential problem, detrital contamination containing allochthonous Thorium-230, can often be recognized by the presence of clay (Geyh and Schliecher, 1990). Precision of the method decreases with increasing age and decreasing uranium content of the sample (Geyh and Schleicher, 1990). Up to about 250 ka, a standard deviation of ± 1 to 10 ka may be expected, and a standard deviation of ± 50 ka is expected for material in excess of 250 ka in age (Schwartz and Gascoyne, 1984). Several hundred grams of sample are needed for uranium concentrations below 1 ppm (Geyh and Schleicher, 1990).

Unsheared calcite veins in fault zones will give minimum ages for faulting. Age estimates on caliche horizons will be maximum or minimum depending on whether the horizons are offset by or overlie the fault. U/Th dating has been done on calcite vein fillings at Devil's Hole in Nevada by Ludwig et al. (1992). Thorium-230 ages were determined with precision ranging from less than 1 ka for samples younger than about 140 ka to less than 50 ka for the oldest samples (about 566 ka), indicating long-term calcite precipitation of calcite from about 566-60 ka (Ludwig et al., 1992). This study was in connection

with determination of long-term climatic history rather than history of faulting, but does show the utility of the method. Szabo and O'Malley (1985) have analyzed secondary carbonate samples (vein fillings in fault zones and caliche horizons above the faults) from the vicinity of faults west of YM, apparently including the Solitario Canyon fault. A minimum age of 70 $\pm$5 ka was obtained for the Solitario from their work, with associated faults ranging from 27$\pm$3 to 33$\pm$4 ka. They also reported U/Th ages of greater than 350 ka on opaline carbonate samples from Trench 14 along the Bow Ridge fault (Szabo and O'Malley, 1985).

9.2.3.3 Thermoluminescence

The TL method can be used for determination of age estimates on sediments. This method is based on the fact that, for certain minerals (e.g., quartz and feldspar), metastable electrons, detached from atoms of the material by ionizing radiation and subsequently trapped in defects of the crystal lattice, recombine when heated, accompanied by the emission of light referred to as TL (Aitken, 1967; Wintle and Huntley, 1982; Geyh and Schleicher, 1990; and Hill et al., 1993). The intensity of the emitted light is measured to provide the TL signal used for age determinations. Sediments lose primary TL energy by exposure to sunlight (Wintle and Huntley, 1982). This loss provides the basis for TL age analysis of sediments that are exposed to sunlight during transportation for a period long enough to fade out the inherited (primary) TL signal and then buried to induce development of a nuclear radiation TL signal once again. Hence, time since depositional burial-the time the materials were last exposed to sunlight—is recorded by the TL signal. That is, sediment grains are long-term radiation dosimeters and the TL signal is ideally a measure of radiation exposure accumulated since burial of the grain (Forman, 1989). Forman et al. (1989) consider that exposure of sediments to sunlight for a period of only 8 hr will bleach the inherited TL signal and reset the TL clock to time zero. However, Geyh and Schleicher (1990) point out that the rate at which the inherited TL signal is bleached away is a function of the type of mineral as well as the duration of its exposure to sunlight. References wherein principles and analytical methodology involved in the TL method are discussed in detail include Aitken (1985), Geyh and Schleicher (1990), and Hill et al. (1993).

For use in eolian sediments, as may be found in sequences of fault-scarp-derived materials, it is thought possible to use TL up to ages of at least 200 ka, with a precision of about $\pm$10 percent (Wintle, 1982). However, Geyh and Schleicher (1990) indicate geological samples are datable with precision of only about $\pm$25 percent. Based on the time required for common detrital minerals to reach a saturation dose, Forman (1989) suggested an applicable age range of 75–100 ka for use of this method on sediments. Forman et al. (1988b) have used the TL method for fine-grained distal colluvium associated with late Holocene movement of the Wasatch Fault which produced age estimates in agreement with radiocarbon ages, stating that the TL technique probably has a maximum resolution of about 500 yr for Holocene deposits along the Wasatch. Forman (1989) reported coarse-grained proximal colluvium from that fault yielded spurious TL age estimates because of inadequate sunlight-bleaching of these coarser materials. Buried A horizons in loess gave TL ages in approximate agreement with radiocarbon control (Wintle and Catt, 1985). Samples of eolian sediments, commonly several tens of grams in size, must be taken at least several centimeters below the surface and not exposed to direct sunlight for even a brief period (Geyh and Schleicher, 1990) since exposure to UV light sources during sample collection or preparation produces anomalous fading of the TL signal and erroneously young ages (Hill et al., 1993). Laboratory preparation of samples is done under darkroom conditions with red light. Forman (1989) indicates approximately 30 g of sample should be collected for sediments. One common source of potential error in the TL method is related to uncertainties in determining the external (i.e., irradiation of a sample by its environment) and internal (i.e., self-radiation) radiation dose rates affecting the sample

(Geyh and Schleicher, 1990). Errors of up to 15 percent have been reported when uranium or thorium has been gained or lost by the sample while buried (Hille, 1979; Ikeya, 1982). Lack of exact knowledge about the degree of bleaching during transportation is also a potential problem for this method (Mejdahl, 1985), and uncertainty about water content of the sediment during burial can be a large source of error (Forman et al., 1989). Forman et al. (1989) point out that little is known about the effects of pedogenesis on stability of the TL signal.

9.2.3.4 Electron Spin Resonance

Although the ESR method is generally considered experimental and presently lacks a routine set of procedures for its use (Hennig and Grun, 1983; Colman et al., 1987; Geyh and Schleicher, 1990; and Grun, 1991), there are two reasons it should not be dismissed for potential use at YM. First, the age range covered by this method is considered to be the entire Quaternary (Hennig and Grun, 1983). Grun (1992) indicates the range may be from 1 ka to 1-2 my. Second, ESR is possibly the only technique with potential for providing the age of last fault movement directly by analyzing samples of quartz in fault gouge (Grun, 1991; 1992).

Just as for the TL method, the ESR technique is based on the detection of metastable electrons trapped in the crystal lattice which have been exposed to ionizing radiation (Faure, 1986). For ESR, the fact that these trapped electrons form paramagnetic centers is used, and the ESR method is based on the direct, nondestructive measurement of the number of radiation-induced paramagnetic electrons trapped in crystal defects-the number of which increases constantly with time (Hennig and Grun, 1983). Using an ESR spectrometer which contains a microwave unit for generation of microwave radiation and detection of the radiation absorption signal, the ESR signal can be recorded (Hennig and Grun, 1983). Intensity of the signal is proportional to the number of radiation-induced paramagnetic defects and to the age of the sample (Hennig and Grun, 1983). That is, the mineral sample acts as a dosimeter to record doses from radioactive sources in its environment up to about 30 cm radial distance away (Grun, 1989). The ESR signal is ideally a measure of radiation exposure since the mineral time clock was reset to zero by erasing the inherited ESR signal with fault movement. Material collected should yield at least 5 g of quartz for analysis (Grun, 1992). References in which principles and analytical methodology of the ESR method are discussed include Hennig and Grun (1983) and Geyh and Schleicher (1990).

The premise for use of ESR in directly determining the age of last fault movement is related to the principle that the inherited ESR signal in quartz contained in fault gouge is reset to zero by fault movement itself (Grun, 1992). Fukuchi (1992) suggests the resetting is a result of shear heating during faulting—a concept suggested earlier by Ikeya et al. (1982). It should be noted, however, that Buhay et al. (1988) consider degree of resetting to be dependent on grain size, with the smaller grains totally reset, and propose that heating alone is not the cause. Their analysis was conducted in quartz contained in fault gouge from the San Jacinto fault zone in southern California where the sample fraction less than 2 mm in size was analyzed. A most important limitation for using ESR to determine age of surface faulting and related paleoseismicity, derived from computer simulation by Fukuchi (1992), suggests resetting will not occur if the samples collected were initially at depths less than about 200 m below the surface when fault movement occurred. Ito and Sawada (1985) concluded minimum depths for effective zeroing of the inherited ESR signal was greater than 20 m for reverse faults, greater than 70 m for strike-slip faults, and greater than 100 m for normal faults. Most recently, Grun (1992) suggested samples collected for ESR dating should have been at depths of at least 250 m during the last fault movement to assure erasure of the inherited ESR signal indicating acceptable samples can only be taken from cores or tunnels. This statement addresses the concept that determining if a sample were completely reset by the

last fault episode is a major concern for this method, a point raised earlier by many workers (e.g., Fukuchi, 1988). It also indicates determination of ages for Quaternary displacements cannot be accomplished using ESR on samples from surface outcrops. In a study of Holocene faulting in Scotland, Grun and Fenton (1990) found no evidence of resetting in 17 samples collected from surface exposures of the fault. If the ESR signal is not completely reset by fault movement, it is recognized that the method then fails to provide a reasonable age estimate for last fault movement (Fukuchi, 1992).

In general, ESR ages have not been carefully confirmed by independent means, a factor which proponent Grun (1992) considers to be a basic weakness of the method. He indicates that investigators should focus on areas where geologic evidence or other age determination methods prove recency of fault movements. Just as for the TL method, errors in ages will occur if the system is open and uranium or thorium is lost or gained from the sample. Also, uncertainty about initial water content may produce uncertainties in the ESR age estimate (Geyh and Schleicher, 1990). Determination of accumulated dose and dose rate, essential components of the age determination equation, may be complex and introduce errors in age estimates also (Grun, 1991).

9.3 ASSESSMENT OF PROGRESS TOWARD MEETING PROJECT OBJECTIVES

Compilation of data on tectonic processes and critical review of the data are on schedule. In particular, the database on age of faulting and average slip rates for specific fault systems has improved due to inclusion of very recent and ongoing work. However, assessment and development of alternative tectonic models is somewhat behind schedule. Work on models is expected to increase during the next year. Still, the modeling task may need to be extended.

Development of Compliance Determination Methods (CDMs) for the primary regulatory requirements related to tectonics has not yet started. The Tectonics Research Project is expected to contribute to CDM development for the following LARP sections: 3.2.1.5 Structural Deformation; 3.2.1.6 Historic Earthquakes; 3.2.1.7 Correlation of Earthquakes with Tectonic Processes; 3.2.1.8 Increasing Earthquake Frequency/Magnitude; 3.2.1.9 Evidence of Igneous Activity; and 3.2.2.8 Structural Deformation and Groundwater. At this time, input to Iterative Performance Assessment (IPA) is expected to consist mainly of uncertainty estimates for seismic and fault rupture risk analysis. For IPA input, the current emphasis is on compilation of slip-rate estimates for Quaternary and Holocene faults, and correlation of slip rate to earthquake recurrence and magnitude.

The focus of the project has been mainly on data compilation. Therefore, modeling results with direct implications to specific Key Technical Uncertainties (KTUs) have not yet been produced. However, significant progress has been made with respect to correlation of earthquakes with tectonic processes (LARP 3.2.1.7). At this time, the TecResGIS provides capabilities to correlate historical earthquakes with Quaternary faults throughout the central Basin and Range region and within the YM area. Of particular importance, published data from trench studies have been used to assign estimated ages to slip events on selected individual fault segments. Thus, for the selected fault segments, modern earthquakes can be quickly correlated with prehistoric slip history (frequency), and age of latest slip (whether the fault is considered active or not). Ongoing critical review of the database and development of alternative tectonic models is expected to contribute particularly to reduction of the KTU related to poor resolution of critical exploration methods (LARP 3.2.1.5), and to resolution of KTUs in development and use of conceptual tectonic models related to structural deformation (LARP 3.2.1.5) and igneous activity (LARP 3.2.1.9).

9.4 PLANS FOR NEXT REPORTING PERIOD

Work on data compilation will decrease over the next year. The research focus will shift more to critical review of the data and to assessment and development of alternative tectonic models. Field work will focus on direct support of alternative tectonic models and on interaction of faulting and igneous intrusive processes. Specifically, work is planned to determine the feasibility of fission track thermochronology at Bare Mountain. This work may clarify the role of the Bare Mountain fault in the tectonic evolution of YM, and subsequently in earthquake risk assessment. Work in the Reveille Range (Nevada) and perhaps at the San Francisco volcanic field (Arizona) is planned to investigate relationships between Quaternary faulting and intrusion of mafic dikes. This work will be accomplished in concert with the field volcanism research project. Reconnaissance field work may be conducted in the Landers area to investigate associated ground rupture effects. The Center for Nuclear Waste Regulatory Analyses will become more actively involved in the GPS effort beyond FY94, at least by providing assistance for annual data collection and possibly by placement of additional stations which would be linked to the existing network of B. Wernicke. Location of any new stations would be done in concert with NRC Research (G. Birchard) and B. Wernicke after additional planning discussions.

9.5 REFERENCES

Aitken, M.J. 1967. Thermoluminescense. *Science Journal* 1: 32-38.

Aitken, M.J. 1985. *Thermoluminescence Dating*. New York, NY: Academic Press: 291.

Allen, C.A. 1986. Seismological and paleoseismological techniques of research in active tectonics. *Active Tectonics*. National Research Council/Geophysics Study Committee, eds. Washington, DC: National Academy Press: 148-154.

Bell, J.W., and T. Katzer. 1987. Surficial geology, hydrology, and Late Quaternary tectonics of the IXL Canyon area, Nevada. *Bulletin of Nevada Bureau of Mines and Geology* 102: 52.

Berry, M.E. 1990. *Soil-Geomorphic Analysis of Late Quaternary Glaciation and Faulting, Eastern Escarpment of the Central Sierra Nevada, CA*. Unpublished Ph.D. Thesis. University of Colorado, Denver, CO. Department of Geological Sciences: 365.

Berry, M.E., and P.W. Birkeland. 1988. Comparison of TL and 14C dates for late Quaternary movement on the Hilton Creek Fault, eastern Sierra Nevada, CA (abs). *Abstracts with Programs*. Geological Society of America: 20(7): A54.

Buhay, W.M., H.P. Schwartz, and R. Grun. 1988. ESR dating of fault gouge — The effect of grain size. *Quaternary Science Reviews* (7): 515-522.

Carver, G.A. 1987. Geologic criteria for recognition of individual paleoseismic events in compressional tectonic environments. *Directions in Paleoseismology*. A.J. Crone and E.M. Omdahl, eds. USGS Open-File Report 87-673. Reston, VA: U.S. Geological Survey: 115-128.

Colman, S.M., K.L. Pierce, and P.W. Birkeland. 1987. Suggested terminology for Quaternary dating methods. *Quaternary Research* 28(2): 314-319.

Crone, A.J. 1987a. Introduction to directions in paleoseismology. *Directions in Paleoseismology*. A.J. Crone and E.M. Omdahl, eds. USGS Open-File Report 87-673. Reston, VA: U.S. Geological Survey: 1-6.

Crone, A.J. 1987b. Summary of discussion section—recognition of paleoseismic events in the geologic record. *Directions in Paleoseismology*. A.J. Crone and E.M. Omdahl, eds. USGS Open-File Report 87-673. Reston, VA: U.S. Geological Survey: 186-189.

Crone, A.J., M.N. Machette, M.G. Bonilla, J.J. Lienkaemper, K.L. Pierce, W.E. Scott, and R.C. Bucknam. 1987. Surface faulting accompanying the Borah Peak earthquake and segmentation of the Lost River Fault, central Idaho. *Bulletin of the Seismological Society of America* 77: 739-770.

DePolo, C.M., D.C. Clark, D.B. Slemmons, and A.R. Ramelli. 1991. Historical surface faulting in the Basin and Range Province, western North America—Implications for fault segmentation. *Journal of Structural Geology* 13(2): 123-136.

Dohrenwend, J.C. 1982. *Surficial Geologic Map of the Walker Lake 1° by 2° Quadrangle, Nevada—California. Scale 1:250,000.* U.S. Geological Survey Miscellaneous Field Studies Map MF-1382-C. Reston, VA: U.S. Geological Survey.

Dohrenwend, J.C., and B.C. Moring. 1991a. *Reconnaissance Photogeologic Map of Young Faults in the Vya 1° by 2° Quadrangle, Nevada, Oregon, and California. Scale 1:250,000.* U.S. Geological Survey Miscellaneous Field Studies Map MF-2174. Reston, VA: U.S. Geological Survey.

Dohrenwend, J.C., and B.C. Moring. 1991b. *Reconnaissance Photogeologic Map of Young Faults in the Winnemucca 1° by 2° Quadrangle, Nevada. Scale 1:250,000.* U.S. Geological Survey Miscellaneous Field Studies Map MF-2175. Reston, VA: U.S. Geological Survey.

Dohrenwend, J.C., and B.C. Moring. 1991c. *Reconnaissance Photogeologic Map of Young Faults in the McDermitt 1° by 2° Quadrangle, Nevada, Oregon, and Idaho. Scale 1:250,000.* U.S. Geological Survey Miscellaneous Field Studies Map MF-2177. Reston, VA: U.S. Geological Survey.

Dohrenwend, J.C., and B. Moring. 1993. Reconnaissance photogeologic map of late tertiary and quaternary faults in Nevada. Abstracts with Programs. *Cordilleran and Rocky Mountain Section Meeting, Geological Society of America, May 19-21.* Reno, NV: Geological Society of America, 25(5): 31.

Dohrenwend, J.C., M.A. McKittrick, and B.C. Moring. 1991a. *Reconnaissance Photogeologic Map of Young Faults in the Lovelock 1° by 2° Quadrangle, Nevada and California. Scale 1:250,000.* U.S. Geological Survey Miscellaneous Field Studies Map MF-2178. Reston, VA: U.S. Geological Survey.

Dohrenwend, J.C., M.A. McKittrick, and B.C. Moring. 1991b. *Reconnaissance Photogeologic Map of Young Faults in the Wells 1° by 2° Quadrangle, Nevada, Utah, and Idaho. Scale 1:250,000.* U.S. Geological Survey Miscellaneous Field Studies Map MF-2184. Reston, VA: U.S. Geological Survey.

Dohrenwend, J.C., C.M. Menges, B.A. Schell, and B.C. Moring. 1991c. *Reconnaissance Photogeologic Map of Young Faults in the Las Vegas 1° by 2° Quadrangle, Nevada, California, and Arizona. Scale 1:250,000.* U.S. Geological Survey Miscellaneous Field Studies Map MF-2182. Reston, VA: U.S. Geological Survey.

Dohrenwend, J.C., B.A. Schell, and B.C. Moring. 1991d. *Reconnaissance Photogeologic Map of Young Faults in the Elko 1° by 2° Quadrangle, Nevada and Utah. Scale 1:250,000.* U.S. Geological Survey Miscellaneous Field Studies Map MF-2179. Reston, VA: U.S. Geological Survey.

Dohrenwend, J.C., B.A. Schell, and B.C. Moring. 1991e. *Reconnaissance Photogeologic Map of Young Faults in the Lund 1° by 2° Quadrangle, Nevada and Utah. Scale 1:250,000.* U.S. Geological Survey Miscellaneous Field Studies Map MF-2180. Reston, VA: U.S. Geological Survey.

Dohrenwend, J.C., B.A. Schell, and B.C. Moring. 1991f. *Reconnaissance Photogeologic Map of Young Faults in the Ely 1° by 2° Quadrangle, Nevada and Utah. Scale 1:250,000.* U.S. Geological Survey Miscellaneous Field Studies Map MF-2181. Reston, VA: U.S. Geological Survey.

Dohrenwend, J.C., B.A. Schell, M.A. McKittrick, and B.C. Moring. 1992a. *Reconnaissance Photogeologic Map of Young Faults in the Goldfield 1° by 2° Quadrangle, Nevada and California. Scale 1:250,000.* U.S. Geological Survey Miscellaneous Field Studies Map MF-2183. Reston, VA: U.S. Geological Survey.

Dohrenwend, J.C., B.A. Schell, and B. C. Moring. 1992b. *Reconnaissance Photogeologic Map of Young Faults in the Millett 1° by 2° Quadrangle, Nevada. Scale 1:250,000.* U.S. Geological Survey Miscellaneous Field Studies Map MF-2176. Reston, VA: U.S. Geological Survey.

Faure, G. 1986. *Principles of Isotope Geology.* New York, NY: John Wiley and Sons.

Forman, S.L. 1989. Applications and limitations of thermoluminescence to date Quaternary sediments. *Quaternary International* (1): 47–59.

Forman, S.L., P. Maat, and M.E. Jackson. 1988a. TL dating of paleoearthquakes—Recent results and future prospects. *Cordilleran Section Abstracts.* Reno, NV: Geological Society of America: 20(3): 161.

Forman, S.L., P. Maat, and M.E. Jackson. 1988b. TL dating of fault generated slope deposits—A new tool for deciphering the timing of paleoearthquakes. *Abstracts with Programs.* Denver, CO: Geological Society of America: 20: A345.

Forman, S.L., M.N. Machette, M.E. Jackson, and P. Maat. 1989. An evaluation of TL dating of paleoearthquakes of the American Fork segment, Wasatch fault zone, Utah. *Journal of Geophysical Research* 94(B2): 1,622–1,630.

Forman, S.L., A.R. Nelson, and J.P. McCalpin. 1991. TL dating of fault-scarp derived colluvium—Deciphering timing of paleoearthquakes on Weber segment of the Wasatch fault zone, north-central Utah. *Journal of Geophysical Research* 96(B1): 595-605.

Frizzel, V.A., Jr, and J. Shulters. 1990. *Geologic Map of the Nevada Test Site, Southern Nevada. 1: 100,000.* U.S. Geological Survey Miscellaneous Investigations Series Map I-2046.

Fukuchi, T. 1988. Applicability of ESR dating using multiple centers in quartz—The case of the Itoigawa-Shizuoka tectonic line, a major fault in Japan. *Quaternary Science Reviews* (7): 265-314.

Fukuchi, T. 1992. ESR studies for absolute dating of fault movements. *Journal of the Geological Society of London* 149: 265-272.

Geyh, M.A., and H. Schleicher. 1990. *Absolute Age Determinations.* New York, NY: Springer-Verlag: 503.

Grun, R. 1989. Electron Spin Resonance (ESR) dating. *Quaternary International* 1: 65-109.

Grun, R. 1991. Potential and problems of ESR dating. *International Journal of Radiation and Applied Instrumentation* Part D 18(1/2): 143-153.

Grun, R. 1992. Remarks on ESR dating of fault movements. *Journal of the Geological Society of London* (149): 261-264.

Grun, R. and C. Fenton. 1990. An ESR study of fault gouge from Holocene fault systems in Scotland. *6th International Specialist Seminar on TL and ESR Dating.* Abstract 129. Clermont-Ferrand, France:

Hennig, G.J., and R. Grun. 1983. ESR dating in Quaternary geology. *Quaternary Science Reviews* 2: 157-238.

Hill, B.E., B.W. Leslie, and C.B. Connor. 1993. *A Review and Analysis of Dating Techniques for Neogene and Quaternary Volcanic Rocks.* CNWRA 93-018. San Antonio, TX: Center for Nuclear Waste Regulatory Analyses.

Hille, P. 1979. An open system model for uranium series dating. *Earth and Planetary Science Letters* 42: 138-142.

Holm, D.K., J.W. Geissman, and B. Wernicke. 1993. Tilt and rotation of the footwall of a major normal fault system—Paleomagnetism of the Black Mountains, Death Valley extended terrane, California. *Geological Society of America Bulletin* 105(10): 1,373-1,387.

Ikeya, M. 1982. A model of linear uranium accumulation for ESR age of Heidelberg (Mauer) and Tautavel bones. *Journal of Applied Physics* 21: 690-692.

Ikeya, M., T. Miki, and K. Tanaka. 1982. Dating of a fault by ESR on intrafault materials. *Science* 215: 1,392-1,393.

Ito, T., and S. Sawada. 1985. Reliable criteria for selection of sampling points for ESR dating in M. Ikeya and T. Miki, eds. ESR Dating and Dosimetry. *IONICS*, Tokyo, Japan: 536.

Jackson, M.E., S.L. Forman, and M.N. Machette. 1987. Dating of paleoseismic events using the TL dating method—Preliminary results (abs). American Geophysical Union Abstracts. *EOS* 68(44): 1,287.

Jennings, C.W. 1992. *Preliminary Fault Activity Map of California.* DMG Open-File Report 92-03. The Resources Agency, California Department of Conservation, Division of Mines and Geology: 76. Replaces the 1:750,000 scale Fault Map of California, Bulletin 201, California Department of Conservation, Division of Mines and Geology, and the Fault Map of California with location of volcanoes, thermal springs, and thermal wells (Jennings 1975).

Leick, A. 1990. *GPS Satellite Surveying.* New York, NY: John Wiley & Sons: 352.

Lubetkin, L.K.C., and M.M. Clark. 1988. Late Quaternary activity along the Lone Pine fault, eastern California. *Geological Society of America Bulletin* 100(5): 755-766.

Ludwig, K.R., K.R. Simmons, B.J. Szabo, I.J. Winograd, J.K.M. Landwehr, A.C. Riggs, and R.J. Hoffman. 1992. Mass-spectrometric Th-230/U-234/U-238 dating of Devils Hole calcite vein. *Science* 258: 284-287.

Machette, M.N. 1987. Changes in long-term versus short-term slip rates in an extensional environment in *Directions in Paleoseismology*. A.J. Crone and E.M.Omdahl, eds. USGS Open-File Report 87-673. Reston, VA: U.S. Geological Survey: 228-238.

Machette, M.N., and W.R. Lund. 1987. Late Quaternary history of the American Fork segment of the Wasatch Fault Zone, Utah. GSA Abstracts for Rocky Mountain Section. *Geological Society of America Bulletin* 19(5): 317.

Machette, M.N., S.F. Personius, A.R. Nelson, D.P. Schwartz, and W.R. Lund. 1991. The Wasatch fault zone, Utah-Segmentation and history of Holocene earthquakes. *Journal of Structural Geology* 13(2): 137-149.

Machette, M.N., S.F. Personius, and A.R. Nelson. 1992. Paleoseismology of the Wasatch fault zone—A summary of recent investigations, interpretations, conclusions in P.L. Gori and W.W. Hays, eds., *Assessment of Regional Earthquake Hazards and Risk Along the Wasatch Front, Utah.* Prof. Paper 1500-A-J. Reston, VA: U.S. Geological Survey. A1–A71.

McCalpin, J. 1987. Geologic criteria for recognition of individual paleoseismic events in extensional environments. *Directions in Paleoseismology*. A.J. Crone and E.M.Omdahl, eds. USGS Open-File Report 87-673. Reston, VA: U.S. Geological Survey: 102-114.

McCalpin, J., and S.L. Forman. 1991. Late Quaternary faulting and TL dating of the East Cache fault zone, north-central Utah. *Bulletin of Seismological Society of America* 81(1): 139-161.

Mejdahl, V. 1985. Thermoluminescence dating of partially bleached sediments. *Nuclear Tracks* 10(4-6): 711-715.

Menges, C.M. 1987. Temporal and spatial segmentation of Pliocene-Quaternary fault rupture along the western Sangre de Cristo mountain front, northern New Mexico, in *Directions in Paleoseismology.* A.J. Crone and E.M. Omdahl, eds. USGS Open-File Report 87-673. Reston, VA: U.S. Geological Survey: 203–222.

Mook, W.G. 1983. Carbon-14 calibration curves depending on sample time-width. W.G. Mook and H.T. Waterbolk, eds. *Carbon-14 and Archaeology* 8: 517–525.

Murphy, P.J., J. Briedis, and J.H. Peck. 1979. Dating techniques in fault investigations in geology in the siting of nuclear power plants. A. Hatheway and C. McClure, eds. *Reviews in Engineering Geology (IV).* Geological Society of America: 153–168.

Nakata, J.K., C.M. Wentworth, and M.N. Machette. 1982. *Quaternary Fault Map of the Basin and Range and Rio Grande Rift Provinces, Western United States.* U.S. Geological Survey Open-File Report 82-579.

Nelson, A.R. 1987. A facies model of colluvial sedimentation adjacent to a single-event normal-fault scarp, Basin and Range Province, western United States. *Directions in Paleoseismology.* A.J. Crone and E.M. Omdahl, eds. USGS Open-File Report 87-673. Reston, VA: U.S. Geological Survey: 136–145.

Rockwell, T. 1987. Recognition of individual paleoseismic events in strike-slip environments, in *Directions in Paleoseismology.* A.J. Crone and E.M. Omdahl, eds. USGS Open-File Report 87-673. Reston, VA: U.S. Geological Survey: 129–135.

Rogers, A.M., S.C. Harmson, E.J. Corbett, K. Priestley, and D. dePolo. 1991. The seismicity of Nevada and some adjacent parts of the Great Basin. *Neotectonics of North America.* D.B. Slemmons, E.R. Engdahl, M.D. Zoback, and D.D. Blackwell, eds. Boulder, CO, Geological Society of America: Decade Map Volume.

Schlesinger W.H. 1985. The formation of caliche in soils of the Mojave Desert, California. *Geochimica Cosmochemica Acta* 49: 57-66.

Schwartz, H., and M. Gascoyne. 1984. Uranium-series dating of Quaternary deposits. *Quaternary Dating Methods.* W.C. Mahaney, ed. Amsterdam, Elsevier: 33–51.

Schwartz, D.P., and K.J. Coppersmith. 1984. Fault behavior and characteristic earthquakes—Examples from the Wasatch and San Andreas fault zones. *Journal of Geophysical Research* 89(B7): 5,681–5,698.

Schwartz, D.P., W.R. Lund, W.E. Mulvey, and K.E. Budding. 1988. New paleoseismicity data and implications for space-time clustering of large earthquakes on the Wasatch Fault Zone, Utah. *Seismological Research Letters* 59(1): 5.

Snow, J.K., and B. Wernicke. 1989. Uniqueness of geological correlations—An example from the Death Valley extended terrain. *Geological Society of American Bulletin* 101: 1,351-1,362.

Snow, J.K., and C. White. 1991. Listric normal faulting and synorogenic sedimentation, northern Cottonwood Mountains, Death Valley region, California. *Basin and Range Extensional Tectonics Near the Latitude of Las Vegas, Nevada*. B.P. Wernicke, ed. GSA Memoir 176, Geological Society of America: 413-445.

Stenhouse, M.J., and M.S. Baxter. 1983. Carbon-14 dating reproducibility—Evidence from routine dating of archaeological samples. *Carbon-14 and Archaeology*. W.G. Mook and H.T. Waterbolk, eds. PACT 8: 147-161.

Swan, F.H., III, D.P. Schwartz, and L.S. Cluff. 1980. Recurrence of moderate-to-large magnitude earthquakes produced by surface faulting on the Wasatch fault zone, Utah. *Bulletin of Seismological Society of America* 70(5): 1,431-1,462.

Szabo, B.J., and P.A. O'Malley. 1985. *Uranium-series Dating of Secondary Carbonate and Silica Precipitates Relating to Fault Movements in the Nevada Test Site Region and of Caliche and Travertine Samples from the Amargosa Desert.* USGS Open-File Report 85-47. Reston, VA: U.S. Geological Survey: 12.

Thiel, K., R. Vorwerk, R. Saager, and H.D. Stupp. 1983. Uranium-235 fission tracks and uranium-238 series disequilibrium as a means to study recent mobilization of uranium in Archaean pyritic conglomerates. *Earth and Planetary Science Letters* 65: 249-262.

Wallace, R.E. 1977. Profiles and ages of young fault scarps, north-central Nevada. *Geological Society of America Bulletin* 88: 1,267-1,281.

Wallace, R.E. 1981. Paleoseismology. *Abstracts with Programs*. Geological Society of America: 13(7): 575.

Wallace, R.E. 1987a. A perspective of paleoseismology. *Directions in Paleoseismology*, A.J. Crone and E.M. Omdahl, eds. USGS Open-File Report 87-673. Reston, VA: U.S. Geological Survey: 7-15.

Wallace, R.E. 1987b. Grouping and migration of surface faulting and variations in slip rates on faults in the Great Basin Province. *Bulletin of Seismological Society of America* 77(3): 868-876.

Wintle, A.G. 1982. Thermoluminescence properties of fine-grained minerals in loess. *Journal of Soil Science* 134: 164-170.

Wintle, A.G., and J.A. Catt. 1985. Thermoluminescence dating of soils developed in Late Devensian Loess at Pegwell Bay, Kent. *Journal of Soil Science* 36: 293-298.

Wintle, A.G., and D.J. Huntley. 1982. Thermoluminescence dating of sediments. *Quaternary Science Reviews* 1: 31-53.

Young, S.R., and G.L. Stirewalt. 1993. *Project Plan for Research on Tectonic Processes in the Central Basin and Range Region.* CNWRA Research Project Plan, Rev 0, Change 4. San Antonio, TX: Center for Nuclear Waste Regulatory Analyses.

Young, S.R., R. Martin, and B. Henderson. 1993. Tectonic processes in the central Basin and Range region. B. Sagar, ed. *NRC High-Level Radioactive Waste Research at CNWRA January–June 1993.* CNWRA 93-01S. San Antonio, TX: Center for Nuclear Waste Regulatory Analyses.

10 FIELD VOLCANISM RESEARCH

by Charles B. Connor, Steven McDuffie, and Brittain E. Hill

Investigators: Charles B. Connor, Brittain E. Hill, Jeffrey Templeton, and Ronald W. Janetzke (CNWRA); Steven McDuffie (NRC); Kenneth D. Mahrer and Jorge Parra (SwRI)

NRC Project Officer: Linda A. Kovach

10.1 OBJECTIVES

The Yucca Mountain region (YMR) has been the site of recurring small volume basaltic eruptions during the last 10 m.y. (Crowe et al., 1983; Smith et al., 1990). This volcanic activity has led to the formation of numerous cinder cones, eight of which are less than 1.6 Ma. These volcanoes likely represent a range of eruptive activity from extremely explosive eruptions to comparatively gentle effusive volcanic eruptions (Valentine et al., 1992; Amos et al., 1983; Walker, 1991, 1993). The technical objectives of the Field Volcanism Research Project are to better characterize the effect of this type of volcanic activity on repository performance and, as a result, to better constrain probability models of disruption of the repository. This improved characterization will be possible through investigation of the: (i) mechanics of mafic cinder cone eruptions, (ii) extent and characteristics of shallow hydrothermal systems and diffuse degassing associated with small volume mafic eruptions, and (iii) nature of mafic intrusive geometries at repository depths. Successful completion of the Field Volcanism Research Project, which began in April 1993, will require study of Plio-Quaternary cinder cones in the western Great Basin and comparison with modern, recently active cinder cones located elsewhere.

Results of the Field Volcanism Research Project will be used to support specific sections of the License Application Review Plan (LARP). Insight into the possible magnitude of volcanic processes likely to occur in the YMR in the event of further volcanic activity, the areas probably affected, and the likely duration of volcanic activity form an integral part of site characterization activities (Evidence of igneous activity as a potentially adverse condition, Section 3.2.1.9; and Impact of volcanism on groundwater movement, Section 3.2.2.7) and the description of overall system performance (Assessment of compliance with the requirement for cumulative releases of radioactive materials, Section 6.1). Compliance Determination Strategies (CDSs) for these LARP sections are currently under development. The CDSs associated with evidence of Quaternary volcanism are of Type 5, indicating that independent research must be conducted to evaluate Key Technical Uncertainties (KTUs) associated with volcanism and that volcanism poses a high risk to the U.S. Nuclear Regulatory Commission (NRC) of reaching unwarranted conclusions regarding compliance with 40 CFR Part 191 and 10 CFR Part 60.122(c)(15). For example, until acceptable methods for the characterization of the likely magnitude and duration of eruptive activity and the determination of the impact of this activity on groundwater and geochemical transport are found, it will be difficult to ascertain compliance with 40 CFR Part 191.

To date, three KTUs related to igneous activity have been identified as part of the CDSs concerned with evidence of Quaternary igneous activity. These KTUs are:

- Low resolution of exploration techniques to detect and evaluate igneous features (Type 4)
- Inability to sample igneous features (Type 5)
- Development and use of conceptual tectonic models as related to igneous activity (Type 5)

Evaluation of these KTUs will require a detailed safety review supported by analyses (Type 4) and a detailed safety review supported by independent tests, analyses, and other investigations (Type 5). Additional KTUs related to igneous activity will likely be identified in a forthcoming CDS on rates of tectonic activity. The Field Volcanism Research Project will address each of these KTUs. For example, Task 4 investigations into geophysical techniques for identifying anomalies related to subsurface igneous dikes will address uncertainties resulting from the low resolution of exploration techniques, a Type 4 KTU. Many problems in eruption dynamics and the extent of volatile degassing following eruptive activity can only be addressed by comparison of past eruptions at recently active cinder cones with those of the YMR. Tasks 2 and 3 in the Field Volcanism Research Project are designed to investigate eruptive activity and degassing, providing independent testing, analysis, and investigation addressing the inability to sample igneous features, a Type 5 KTU.

Successful completion of the Field Volcanism Research Project and efficient integration with the LARP will require interaction with the Volcanic Systems of the Basin and Range research project. This project concentrates on probability model development and the structural setting of volcanism in the Basin and Range, the Tectonic Setting of the central Basin and Range project, Geologic Setting Task 3 Nuclear Material Safety and Safeguards (NMSS) on faulting and dike interaction, and performance assessment (PA) projects. For example, the Field Volcanism Research Project will provide data that are critical for review of alternate probability models. In addition, results of the Task 3 (NMSS) work on dike-fault interaction will be important to modeling mechanisms of dike emplacement in Task 4 of the Field Volcanism Research Project. The Field Volcanism Research Project, together with these associated investigations, will form an integral part of volcanism models in Iterative Performance Assessment (IPA). For example, the effects of development of a shallow diffuse degassing system about a cooling cinder cone, and estimates of the area likely to be influenced by such a system, are not currently part of IPA models. This type of geological detail will be critical to the development of more comprehensive IPA models. In addition, understanding the range of possible consequences of direct disruption of the repository will have an important effect on probability calculations.

The interdependence of probability and consequences of volcanism in IPA studies is illustrated by calculating a complementary cumulative distribution function (CCDF) for volcanism, utilizing different consequence models. Figure 10-1 illustrates a CCDF assuming that the probability of volcanism within a 12×12 km region about the candidate repository block is unity. Other disruptive scenarios, such as human intrusion or climate change, are not considered. Varying the probability of volcanism, through construction of a range of probability models, decreases the exceedence probability of a given normalized release by varying amounts. The goal of continued probability model development and the incorporation of geologic data into probability models is to determine the conservative position probability for reasonable geologic scenarios. Varying the type of volcanic activity from the gentle effusion of basaltic lavas [a scenario most often invoked in IPA models to date (e.g., Barr et al., 1993)] to one of normal explosive cinder cone activity (Connor et al., 1993a; Walker, 1993) has a substantial impact on the CCDF as well. Specifically, the exceedence probability at a given normalized release is as much as one order of magnitude higher when explosive rather than effuse igneous scenarios are considered. Therefore, it is critical to constrain both the probability of igneous activity occurring at or near the candidate repository site and the likely nature of this igneous activity in order to fully incorporate geologically reasonable models of volcanism into IPA studies.

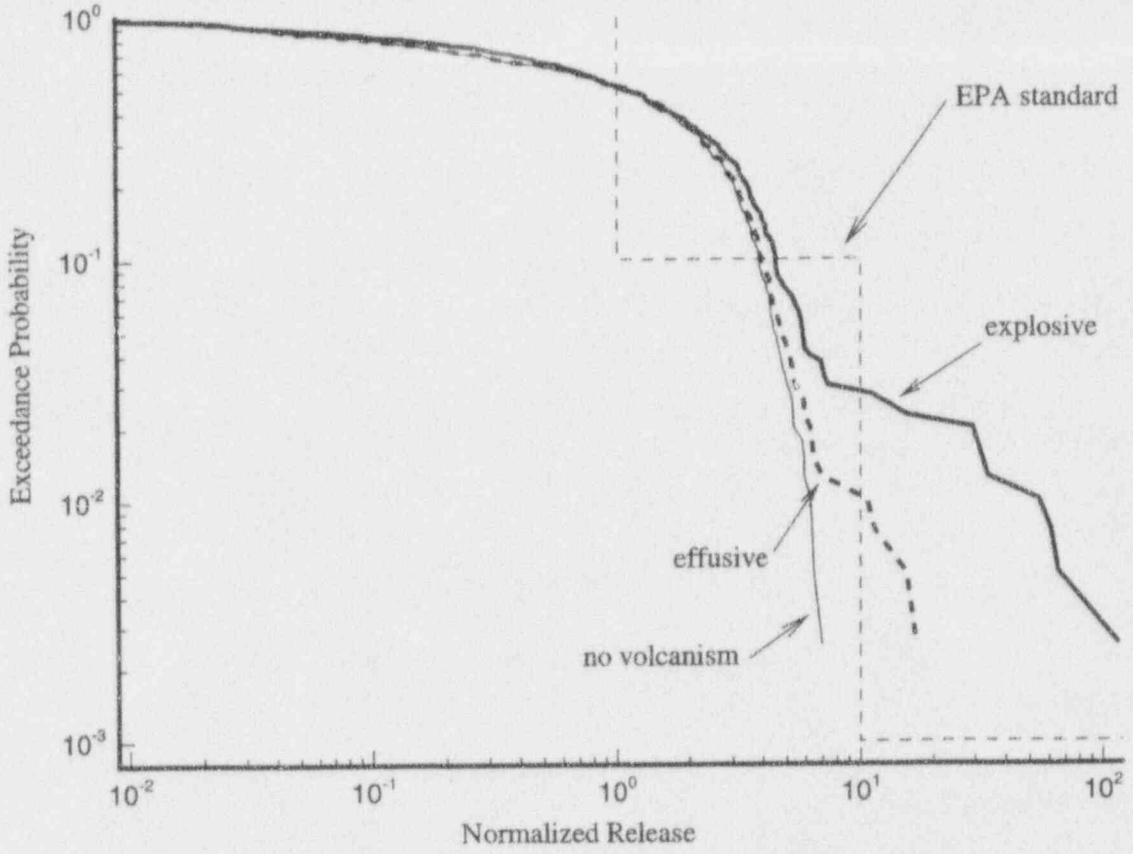

Figure 10-1. CCDF calculated assuming that the probability of volcanic eruption in a 12×12-km area about the candidate repository during the next 10,000 yr is unity. Different models of volcanism, explosive or effusive, produce substantially different CCDFs.

10.2 SIGNIFICANT TECHNICAL ACCOMPLISHMENTS

Several specific research activities were initiated during the last six months. These activities are designed to address issues related to the probability and consequences of igneous activity in the YMR. These activities include:

- Collection and analysis of basalt samples for petrogenetic studies
- Review of the seismic tomographic method and its application to the study of small volume basaltic cinder cone fields
- Analysis of magnetic field anomalies associated with shallow intrusions
- Mapping of shallow dikes associated with Neogene volcanism in the Basin and Range

- Review of literature on dike-fault interaction and development of analytical models to describe this interaction

- Preliminary study of diffuse degassing at Cerro Negro volcano, Nicaragua

- Study of eruption energetics of the 1992 eruption of Cerro Negro

These activities resulted in an Intermediate Milestone (IM) (Technical and Regulatory Basis for the Study of Recently Active Cinder Cones) (Connor, 1993) and an abstract (The 1992 eruption of Cerro Negro, Nicaragua, an example of Plinian-style activity at a small basaltic cinder cone) presented at the Fall Meeting of the American Geophysical Union (Connor et al., 1993a).

The findings on two technical topics are summarized. These topics include an analysis of fault dike interaction and a preliminary study of diffuse volcanic degassing at Cerro Negro cinder cone, Nicaragua. These topics of investigation are critical to the resolution of probability models and consequence models, respectively.

10.2.1 Crustal Structure as a Means of Focusing Magmas

Current probability models rely on the distribution and timing of cinder cone eruptions in the YMR in order to estimate the probability of volcanic disruption (Ho, 1992; Connor and Hill, 1993). One way in which these models need to be improved is through the incorporation of additional geologic data (Trapp and Justus, 1992). Geologic factors may play a role in altering current probability estimates of volcanic disruption of the candidate repository through dike interaction with pre-existing structural features, such as joints or fault zones. This interaction could result in lateral transport of magma during the emplacement of cinder cones, and a focusing of magma along or near fault traces at the surface. Such a process, if significant, would increase the probability of volcanic eruptions in faults zones, such as along the Solitario Canyon fault. Little is known, however, about the mechanisms by which structures redirect magmas as they ascend, the circumstances under which this type of dike capture might occur, and the magnitude of lateral transport of magma that can occur once the dike has been captured by a fault zone.

Numerous examples of dike-fault interaction have been discussed in the literature (e.g., Parsons and Thompson, 1991, Figure 8-4). However, several factors complicate models of dike-fault interaction. First, current models of dike propagation indicate that the properties of rock surrounding the dike have relatively little or no control on ascent rate or related dike properties. Second, Parsons and Thompson (1991) have noted that the intrusion of dikes into extending lithosphere creates strain in a manner quite similar to faulting. As a result, faulting and related topography are suppressed in regions of active dike intrusion. As a result of this suppression, it is difficult to determine if a relationship between faults and dikes exist in many active fields.

In order to resolve this issue, the Field Volcanism Research Project has been structured to: (i) provide field data on dike and fault interactions at varying stratigraphic levels and (ii) provide insight into the likely relationship between faults and dikes through the development of analytical and numerical models. Here, the literature on dike propagation is reviewed and a simple analytical model is proposed to illustrate the nature of dike-fault interaction and its implications for igneous activity in the YMR. Future research activities will be directed toward further refinement of this model and gathering of field

data for the purpose of determining the adequacy of this approach. Finite element models of dike-fault interaction are also being developed as part of the Geologic Setting (GS) Tectonics Research Project, and these models will be compared with field and analytical data.

10.2.1.1 Fundamentals of Dike Propagation

Igneous dikes transport molten material from a magma reservoir in the crust or upper mantle to some higher level in the crust. Dikes propagate upward in the same manner as a hydrofracture: as magma pushes upward, more stress is exerted on the walls near the crack tip, causing tensile stress amplification at the crack tip, resulting in fracture and advancement of the dike. If the crack reaches the surface, magma discharges as a volcanic eruption. The fundamental driving force behind this process is the excess fluid pressure (i.e., pressure in excess of the least principal *in situ* stress) that forces magma into the advancing crack tip. The source of this pressure is normally attributed to buoyancy forces (Lister, 1990a,b; Lister and Kerr, 1991; Pollard and Muller, 1976; Spence et al., 1987). Such forces result from the density contrast between host rock and the less dense magma. There is some debate as to what enables basaltic magmas, such as those that formed the cinder cones of the YMR, with greater density than the upper crustal rock to erupt at the surface. Lister and Kerr (1991) believe dikes can advance through less dense material as long as there is a positive hydrostatic pressure gradient averaged over the entire dike length. However, the fluid pressure may be induced by a process other than buoyancy. Volatile exsolution (Reches and Fink, 1988; Rubin and Pollard, 1987) and pressure on the magma chamber from the weight of overlying rock (Pollard, 1987) are other possible sources of fluid pressure. The precise cause of the magma pressure is of minor importance in controlling the propagation path of a dike; some authors simply assume a magma pressure exists (e.g., Delaney and Pollard, 1982; Emerman et al., 1986).

Magma pushing into a fracture tip exerts stress on the fracture walls, that works to advance the fracture. It is well established from fracture mechanics (e.g., Irwin, 1957) that stress concentrates at the crack tip in such situations, and the magnitude of the crack tip stress field is represented by K, the stress intensity factor (Atkinson, 1987). The stress intensity factor increases as the square root of fracture length (Lister and Kerr, 1991; Pollard and Holzhausen, 1979; Rubin and Pollard, 1987). As a propagation criterion, K must reach a value K_c, the critical stress intensity factor, also known as the fracture toughness (Emerman et al., 1986; Lister and Kerr, 1991; Rubin and Pollard, 1987; Pollard, 1987; Spence et al., 1987). Similar to tensile strength, K_c is a material property of the host rock that is affected by host rock pressure and temperature, among other things (Pollard, 1987). Since K increases with fracture length, $K=K_c$ is an increasingly easy condition to meet as a dike lengthens. A longer dike requires less stress against its walls to achieve $K=K_c$ at the crack tip, so less driving pressure is needed to propagate the crack. Lister and Kerr (1991) believe that once a dike driven by buoyancy exceeds a critical length, approximately 100 m, it will continue propagating toward the surface until it either freezes or reaches its level of neutral buoyancy. The level of neutral buoyancy is the depth at which the magma density equals that of the host rock. Rubin (1993) prefers to cast the problem in terms of fracture energy, rather than fracture toughness, at high confining pressures.

In addition to K achieving the K_c value, two other criteria are necessary to create and advance a magma fracture. First, the crack pressure must overcome the *in situ* stress in the rock due to overburden and any tectonic forces. The state of stress can be resolved into principal components (i.e., normal stresses with no accompanying shear stress components) along three perpendicular axes. Given no intervening factors, dikes, like hydraulic fractures, open against the smallest or least principal stress (σ_3). A fracture with this orientation requires the least amount of magma pressure to open; it is the path of least resistance. This basic finding was first made in the early part of this century (Stevens, 1911;

Anderson, 1938) and has since been confirmed repeatedly. Since overburden stress decreases with decreasing depth, overcoming *in situ* stress is, like the critical stress intensity, easier to achieve (requires less fluid pressure) as a dike lengthens.

Finally, if a fracture is to open there must be sufficient fluid pressure to deform the host rock. The walls must be separated to make space for the magma to flow. The amount of stress needed to deform the wall rock depends on the material properties (e.g., shear modulus and Poisson's ratio) of the host rock. As with the requirement of $K=K_c$ at the tip, less pressure is needed to create a given dike aperture as dike length increases. Lister and Kerr (1991) demonstrate that dike width is proportional to pressure times length, so longer dikes require less fluid pressure to maintain a given aperture. Pollard (1987) quantified the relationship, finding that the aspect ratio of a dike, thickness over length, is approximately equal to the ratio of driving pressure to host rock stiffness. Driving pressure is the effective pressure (i.e., fluid pressure minus the least principal stress, $P-\sigma_3$), or the pressure available to deform the wall rock. Pollard (1987) estimates that the driving pressure for a typical dike, about 1 to 10 m wide with an aspect ratio around 10^{-3}, is in the range of 1 [illegible] MPa for a rock with shear modulus on the order of 10^3 MPa.

Because fluid pressure is a fundamental driving force, it is the lack of pressure that prevents many dikes from reaching the surface. The criteria of meeting critical stress intensity and ambient stress require less pressure as a dike extends to shallower levels, so these factors are not likely to be major causes of dike arrest. Propagation may be hindered by viscous dissipation that reduces fluid pressure and slows the upward flow of magma. In addition, fluid pressure begins to drop after a dike surpasses its level of neutral buoyancy (Lister and Kerr, 1991). As magma loses heat to the cool wall rock, it becomes more viscous and its pressure is not sufficient for its motion to continue. Thermal losses are greater closer to the surface where the wall rock is cooler. Because of viscous dissipation, it is quite common for a dike to lose its driving energy and solidify without reaching the surface. However, volatiles are more likely to exsolve from a magma as it approaches the surface, leading to lower magma density and an increase in buoyancy-induced pressure gradient. The relationships between dike geometry, magma flow rate, and solidification time are discussed by Delaney and Pollard (1982). Their results suggest that a 2 m thick dike flowing through cool upper crust with an initial velocity of 1 m/s will solidify in a matter of hours.

Lister and Kerr (1991) provide a detailed analysis of the energy necessary to propagate a dike: energy for fracture, elastic deformation of the walls, and overcoming viscous dissipation. They conclude that for a dike of any reasonable length (i.e., over 100 m), the energy needed for fracture and elastic deformation of the host rock is trivial compared to the energy necessary to overcome viscous losses. Lister and Kerr (1991) see dike propagation as a simple balance between fluid pressure (buoyancy forces) and viscous drag. Many other studies have reached this same conclusion regarding the unimportance of fracture energy in propagating a dike, (e.g., Emerman et al., 1986; Lister, 1990a; Spence and Turcotte, 1985; Turcotte et al., 1987). Settari (1988) states that fracture toughness is an important control on dike propagation, but only with low-viscosity fluids. Lower viscosity fluids have less viscous dissipation, so fracture toughness represents a greater percentage of the energy required for propagation.

The relatively high viscosity of magma causes an interesting situation at the tip of an advancing fracture. Analytical solutions of fluid-filled crack propagation (Lister, 1990b; Lister and Kerr, 1991) indicate fluid pressure goes to zero where the crack width goes to zero, leading to a very large pressure gradient near the tip. This large gradient is necessary to drive viscous fluid into a narrow gap. The low pressure at the tip allows volatile exsolution from the magma, so small volumes of low-viscosity volatiles should be present in the tips of extending cracks (Lister, 1990b; Lister and Kerr, 1991; Carrigan

et al., 1992). Some experimental hydrofractures show the fracturing fluid lagging so far behind the advancing tip that only 60 to 70 percent of the fracture length is occupied by fluid (Daneshy, 1978). Nonetheless, Emerman et al. (1986) express skepticism about the presence of low-viscosity precursors in dike tips. This doubt is based on their analytical model that shows that crack parameters are quite insensitive to fluid viscosity.

Dike propagation can be represented by a number of analytical models. The models generally assume that a two-dimensional (2D) dike filled with incompressible viscous fluid propagates upward through a homogeneous, impermeable elastic-brittle medium. The influence of the earth surface is rarely taken into account. Several of the models developed in recent years are discussed. Pollard and Muller (1976) have one of the earliest models of dike propagation. They develop relationships between dike geometry and gradients in stress and pressure, and they support their findings with field data from two large igneous intrusions. In addition to deriving expressions for dike length, width, and driving pressure, the model of Spence and Turcotte (1985) demonstrates minimal importance of fracture toughness on dike parameters. A competing model (Spence et al., 1987) suggests that dike width and propagation speed do depend on the fracture toughness of the host material. However, these conclusions seem to be an isolated view in the dike propagation literature. Emerman et al. (1986) generally concur with Spence and Turcotte (1985), but they go a step further by addressing turbulent flow in a dike. Lister (1990a), Lister and Kerr (1991), and Turcotte et al. (1987) also address turbulent flow, and their general finding is that turbulence leads to slightly wider dikes. In most situations, however, magma flow in a dike is likely to be laminar (Delaney and Pollard, 1982; Emerman et al., 1986). Most recent and comprehensive is the model of Lister and Kerr (1991). They present analytical solutions of dike length, width, breadth, propagation velocity, and pressures for several situations, including a linear magma source, a point source, and a bladed dike propagating horizontally at the level of neutral buoyancy. This model, which builds on earlier work by Lister (1990a,b), is used by the U.S. Department of Energy (DOE) in its analyses of dike-repository interaction (Crowe et al., 1983; Pacific Northwest Laboratory, 1993). In addition to these studies, other worthwhile analytical models of dike parameters have been presented by Weertman (1971), Secor and Pollard (1975), Delaney and Pollard (1982), Gudmundsson (1983), Rubin and Pollard (1987), Pollard (1987), and Settari (1988).

10.2.1.2 Interaction Between a Dike and a Pre-existing Weakness

Most analytical models of dike propagation assume an elastically continuous, homogeneous host rock. However, faults and joints are ubiquitous in the crust. It is these weaknesses that can lead to structural control of dike orientation and/or trajectory. The key to understanding structural control is quantifying the conditions under which a dike will deviate to follow a plane of weakness rather than continue a vertical course perpendicular to the least principal stress. Some effort (e.g., Daneshy, 1974, 1978; Weertman, 1980; Abé et al., 1985; Warpinski and Teufel, 1987) has been devoted to understanding the interaction between a propagating crack and a pre-existing weakness, but the work has been largely concerned with a water-filled crack intersecting a joint. Fortunately, many aspects of a magma-filled crack are analogous. One aspect that is not analogous is the concern with fluid leak-off into permeable wall rock. Due to the higher viscosity of magma, fluid leak-off is not an issue with dikes. However, if segregation of volatiles occurs from the magma then leak-off may become important. (Carrigan et al., 1992).

There are a variety of scenarios for hydrofractures that encounter a joint or fault in the crust. A crack can be arrested at a joint, it can exploit a joint as a preferred pathway, it can cross a joint with no deviation, or it can follow a joint a short distance before returning to its original or an alternate

trajectory. Daneshy (1974) spelled out the three most important factors that influence the behavior of a fracture when it meets a joint: the coefficient of friction across the joint, the angle of the joint relative to the fracture, and the difference between the maximum (σ_1) and minimum principal stresses in the host rock (differential stress). Of less importance is the length of the joint encountered by the fracture (Abé et al., 1985). If a joint has a low coefficient of friction, meaning the two faces could slide easily, a crack can be arrested where it meets the joint (Weertman, 1980). A critical amount of stress must be transmitted in advance of the crack tip to keep it propagating. If the stress transmitted across the joint causes failure (slippage) of the joint before it reaches the level necessary to advance the crack across the joint, fracture growth is arrested by the joint. If a fracture intersects a joint with a similar orientation, that is, the joint is nearly normal to σ_3, the joint is much more likely to be exploited by the fracture than a joint parallel to σ_3 (Warpinski and Teufel, 1987). This likelihood is because the pressure needed to dilate a joint increases as its angle relative to σ_3 decreases. The differential stress comes into play here as well. In a setting with low differential stress, the normal-to-σ_3 direction represents a relatively small advantage (in terms of driving pressure requirements) over crack propagation in other directions. Hence, low differential stress allows fractures to reorient themselves along joints with a broader range of attitudes. These qualitative relationships for hydrofracture-joint interactions have been verified by extensive theoretical and experimental work (e.g., Daneshy 1974, 1978; Weertman, 1980; Abé et al., 1985; Warpinski and Teufel, 1987).

As for interactions between a magma-filled fracture and a plane of weakness, Delaney et al. (1986) represent pioneering work. They combine field evidence and theory in a study of several dikes on the Colorado Plateau. Delaney et al. (1986) formulate a ratio of relevant stresses, σ_1, σ_3, and fluid pressure, and tie this ratio to the angle (α) of the joint plane relative to σ_3. Given the three stresses and α, their solution determines whether the fluid pressure within the dike is sufficient to overcome the ambient stresses across the joint, that is, whether the joint can be dilated by the magma and serve as a conduit. Reches and Fink (1988) also use this approach in their study of the Inyo Dike in California. In both studies, planes of weakness are assumed vertical, or parallel to σ_1. As with hydrofractures, the differential stress ($\sigma_1 - \sigma_3$) and α are the key variables in dike-joint interaction. Dike arrest because of joint slippage is an unlikely scenario considering the dimensions ($\sim$1 m versus $\sim$1 cm wide) and the flow properties of dikes compared to hydrofractures. Joint slippage may perturb the course of a dike, but it will be able to cross the joint plane.

10.2.1.3 Interaction Between a Dike and a Stress-Free Surface

The Yucca Mountain repository, as currently envisioned, will consist of a series of tunnels at near atmospheric pressure. For all practical purposes, these tunnels will have stress-free surfaces. A free surface certainly has an effect on the propagation of a dike, although there is not complete agreement on the nature of the effect. Experience and models show that a stress-free surface (e.g., the earth's surface) attracts fractures. Analytical models by Pollard and Holzhausen (1979) and Rubin and Pollard (1987) indicate that a free surface accelerates fracture propagation. For a finite, vertical crack in the earth, both models demonstrate that the stress intensity at the crack tip increases with decreasing distance to the surface. Therefore, propagation is favored in the upward direction regardless of the upward pressure from fluid within the dike. The Pollard and Holzhausen (1979) theory predicts that a free surface begins to influence a dike when the ratio of depth below the surface to total dike length is less than about three. Thus, a dike 3 km long will begin to feel the surface at a depth of 9 km. Dike width is not a factor in the Pollard and Holzhausen (1979) model. This issue is discussed further in the results of our numerical models. Reches and Fink (1988) view dike-surface interaction differently. They believe the upward

decrease in rock tensile strength and the corresponding reduction in tensile stress magnitude make the propagation of dikes increasingly difficult as they near the earth's surface.

10.2.2 Analytical Model Results

Analytical models have been adapted for the purpose of better understanding the parameters that are most important in dike-fault interactions. In particular, these models address the roles of rock properties, depth, regional deviatoric stress state, and fault zone geometry in influencing the paths followed by upwardly propagating dikes. Three analytical models are calculated in the following. The first is a simple model of elliptical dikes, used to illustrate the tensile stresses produced at the dike tip during propagation. The second analytical model uses a static, elastic approach in which the stress state of a vertical dike propagating by fracturing rock is compared with the stress state of a nonvertical dike that is propagating by opening a pre-existing fault plane. This model addresses the conditions under which dikes are likely to be redirected as they ascend from depth. The third model calculates the free surface effects as an edge dislocation, and is used to illustrate the depth ranges over which free surface effects are likely to be important.

10.2.2.1 Elliptical Model of a Dike

Pollard (1973) developed closed form analytical solutions for the stress fields around a pressurized, 2D elliptical hole in a stressed elastic solid. The model assumes uniform pressure applied to the face of the hole, analogous to the fluid pressure within a dike, and assumes the edges of the infinite solid are loaded by principal stresses acting at any angle to the hole, analogous to *in situ* stresses. Given the pressure, loads, and initial shape of the ellipse, the model returns the equilibrium stresses and displacements at any point within the solid. This crack model is an excellent analog for a dike, and is used to calculate stresses around the tip of the dike (end of the ellipse). The elliptical model allows one to avoid the singularity encountered at the crack tip in many fracture mechanics models of crack tip stresses.

Pollard's (1973) solutions were programmed using the following input parameters: the shear modulus and Poisson's ratio of the host material; maximum and minimum *in situ* stresses, σ_1 and σ_3, respectively; the angle between σ_1 and the long axis of the ellipse; and the initial length, width, and internal pressure of the ellipse. First, a parametric study was made to determine input values that result in displacements that correspond to a realistic dike profile. Then these values were used to calculate stresses around the tip of the dike. The primary goal of these calculations was to determine if the state of stress around the crack tip is such that pre-existing weaknesses of varying orientations can be exploited by a propagating fracture. The results of the parametric study are displayed in Figure 10-2. For the purpose of this study, initial crack width (0.01-m), Poisson's ratio (ν=0.25), shear modulus ($\mu=2\times10^4$ MPa), σ_1 (25 MPa), and σ_3 [8.333 MPa, or $\sigma_1\times\nu/(1-\nu)$] were held constant. Fluid pressure (P) was varied from σ_3+1 MPa to σ_3+15 MPa, and length from 100 to 10,000 m. Results indicate direct relationships between wall displacement (crack half-width), driving pressure ($P-\sigma_3$), and crack length. Since an elliptical model was used, wall displacement varies from zero at the ends to a maximum at the midpoint of the major axis. The value we used is the average displacement over the central 70 percent of the ellipse major axis. The requisite driving pressure to achieve a given displacement decreases as crack length increases, a result that agrees with previous work (cf. Lister and Kerr, 1991; Pollard, 1987). The parametric study also revealed an inverse relationship between displacement, μ and ν; the more rigid the material, the lower the displacement given a constant pressure. Initial crack width has a negligible

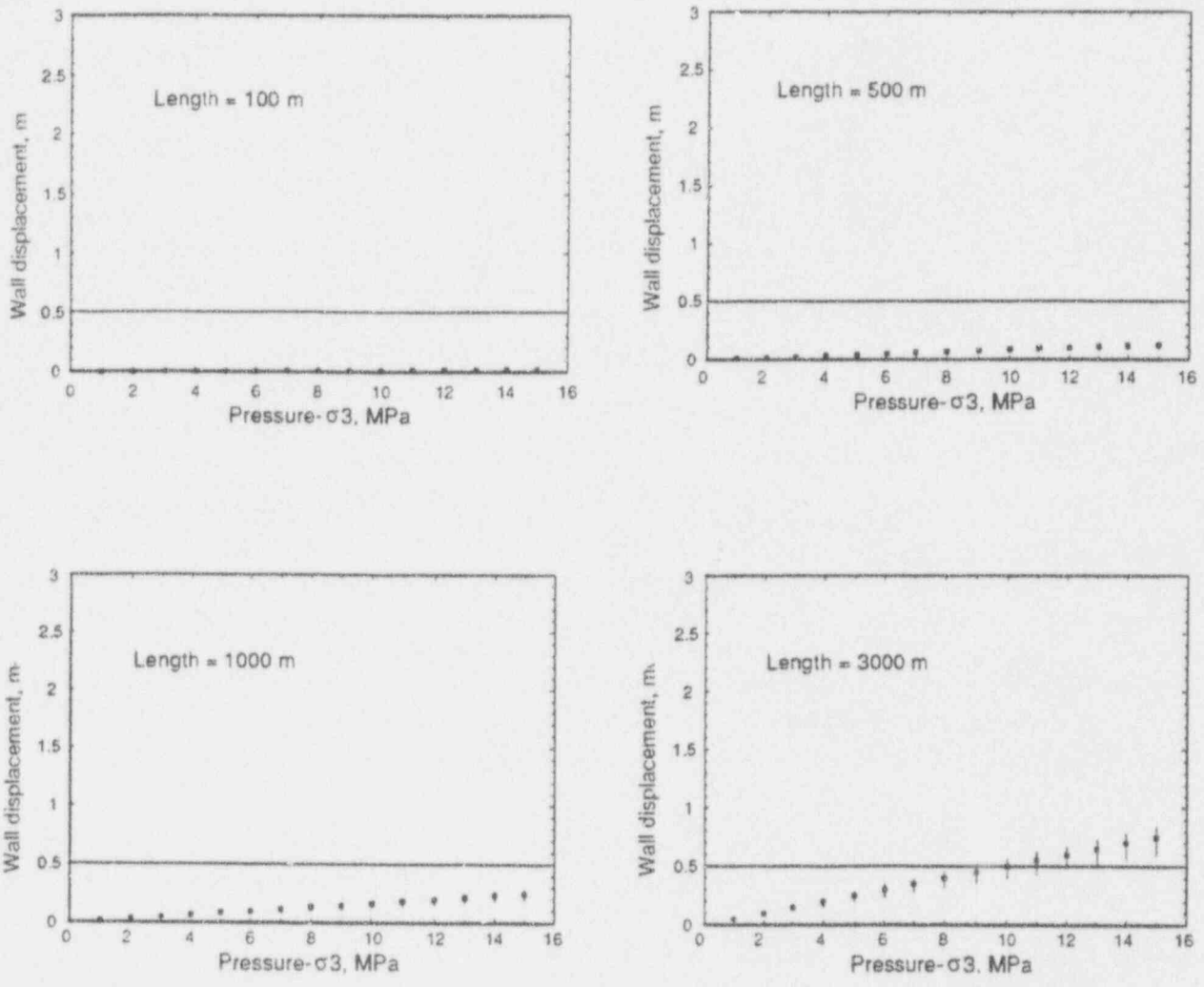

Figure 10-2. Results of the parametric study to find realistic input values for the elliptical crack model of Pollard (1973). Each plot represents a different major axis length of an elliptical crack. The horizontal lines at 0.5-m displacement represent a realistic aperture for a dike. The x-axes are fluid pressure available for elastic deformation ($P-\sigma_3$), and the y-axes are the equilibrium displacement of each wall over the central 70 percent of the ellipse major axis. The data points represent the average aperture over the central 70 percent of the ellipse, and the bars show the maximum and minimum widths. The maximum is at the midpoint of the major axis, and the minimum is at the end of the 70-percent range, toward the crack tip. These results have constant Poisson's ratio = 0.25, shear modulus = 2×10^4 MPa, σ_1 = 25 MPa, and σ_3 = 8.333 MPa. Crack fluid pressure varies from 9.3333 to 23.3333 MPa. Unless fluid pressure is extremely high, crack length must be on the order of kilometers to have a realistic wall displacement.

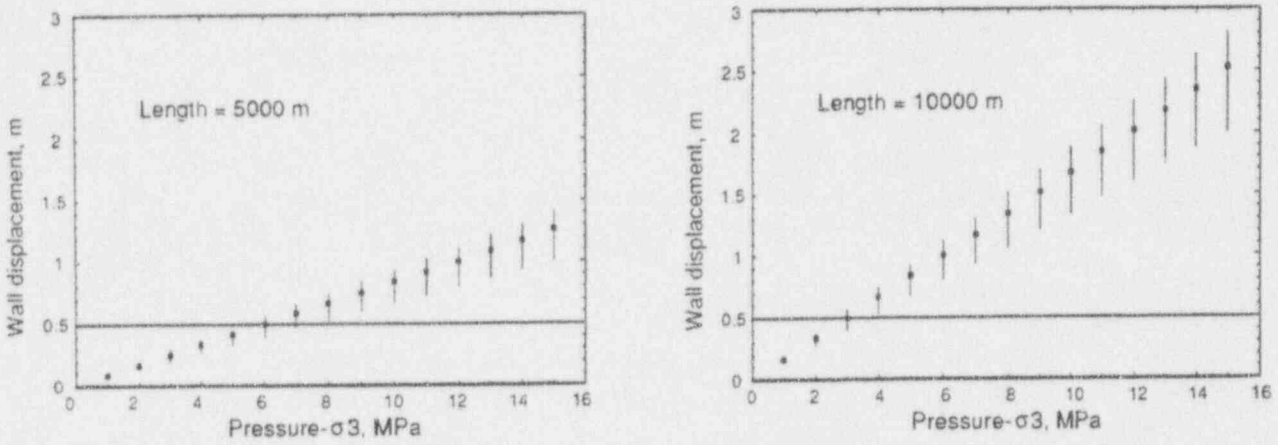

Figure 10-2 (Cont'd). Results of the parametric study to find realistic input values for the elliptical crack model of Pollard (1973). Each plot represents a different major axis length of an elliptical crack. The horizontal lines at 0.5-m displacement represent a realistic aperture for a dike. The x-axes are fluid pressure available for elastic deformation ($P-\sigma_3$), and the y-axes are the equilibrium displacement of each wall over the central 70 percent of the ellipse major axis. The data points represent the average aperture over the central 70 percent of the ellipse, and the bars show the maximum and minimum widths. The maximum is at the midpoint of the major axis, and the minimum is at the end of the 70-percent range, toward the crack tip. These results have constant Poisson's ratio=0.25, shear modulus=2×10^4 MPa, σ_1=25 MPa, and σ_3=8.333 MPa. Crack fluid pressure varies from 9.3333 to 23.3333 MPa. Unless fluid pressure is extremely high, crack length must be on the order of kilometers to have a realistic wall displacement.

effect on wall displacement; the equilibrium crack width is the same regardless. Maximum principal stress also has a minimal influence as σ_1 significantly affects wall displacement only to the extent that it affects σ_3 and the $P-\sigma_3$ value.

Realistic input values that give a displacement of approximately 0.5 m (i.e., a dike width of 1 m) are $\mu=2\times10^4$ MPa, $\nu=0.25$, length=4,000-m, σ_1=25 MPa, σ_3=8.333 MPa, and fluid pressure=16 MPa ($P-\sigma_3$=7.666 MPa). These numbers were used to calculate the stress field around the tip of an elliptical crack. Pollard's (1987) calculations suggest that a dike 1,000 m long with $P-\sigma_3\approx3$ MPa is capable of opening to an average width of 1 m. However, Pollard (1987) uses a shear modulus an order of magnitude lower than values used in this study that were obtained through laboratory measurements (Birch, 1966).

The results of our stress calculations indicate that sufficient tensile stress occurs around the tip of a 4,000-m long elliptical crack to open a pre-existing fracture of nearly any orientation (Figure 10-3). Fractures intersecting the crack tip with dips as shallow as a fraction of a degree have tensional stress across them, so theoretically the crack tip could open such fractures, and magma could flow into them. As Figure 10-3 indicates, most of the curvature in the ellipse, representative of the crack tip, takes place over a very small region. An ellipse with an aspect ratio of 4,000:1 resembles two nearly parallel lines with very tight curves connecting them at the ends. Tensional tangential stress, that can open fractures, occurs only at the tips of the ellipse. Approximately 1.5 mm from the crack tip, the tangential stress is compressional and thus unfavorable for fracture dilation. The significance of these findings is that there is sufficient stress at the dike tip to open any plane of weakness. However, whether a dike continues to propagate vertically or follows a pre-existing weakness, such as a dipping fault plane, depends on additional criteria.

10.2.2.2 Modeling Dike-Fault Interaction

One criterion for the dilation of a pre-existing structure by magma is that a dike must have adequate driving pressure relative to the *in situ* stress across a joint (Delaney et al., 1986). Delaney et al. (1986) give the range of joint orientations that can be dilated by a dike, but do not address whether a dike will actually exploit such features. Assuming a dike will choose only one path, admittedly a tenuous assumption close to the earth's surface, it will choose the path of least resistance. The direction normal to σ_3 requires the least pressure to overcome the *in situ* stress, but the dike must create a new fracture in undeformed rock. A pre-existing joint or fault plane, oriented in a direction not normal to σ_3, requires no fracture creation, but greater *in situ* stress must be overcome for the joint to be dilated. Presumably, if the difference in *in situ* stress exceeds the stress necessary for fracture, the dike continues to propagate normal to σ_3. Conversely, the dike follows the structural weakness if the fracture stress is greater than the *in situ* stress necessary for dilation of the structure.

Based on these assumptions, a simple method of addressing these issues is to develop a static, elastic approach in which the stress state of a vertical dike propagating by fracturing rock is compared with the stress state of a nonvertical dike that is propagating by opening a pre-existing fault plane. The undeformed rock is assumed to be uniform and homogeneous. Linear elastic-brittle behavior is also assumed, implying that at a fixed tensile stress level an unconfined sample of rock will fracture. This stress level corresponds to the uniaxial tensile strength, S_o, of the rock. It is assumed that fluid pore pressure in the undeformed rock is not a significant factor. The shear stress and associated displacements that may occur across an intruded fault are a function of *in situ* conditions and are not part of the energy budget of the dike.

Assuming tensile fracturing, the normal stress needed to open a dike to some arbitrary aperture, σ_{dike}, is the sum of the uniaxial tensile strength, S_o, the *in situ* stress normal to the dike, σ_3, and the additional normal stress required to displace the wall of the dike to create the aperture, σ_d.

$$\sigma_{dike} = S_o + \sigma_3 + \sigma_d \qquad (10\text{-}1)$$

A similar expression can be derived to estimate the stress necessary to separate the walls of a fault. The fault is simply modeled as a plane of weakness dipping at some angle, θ. The fault plane may have experienced some recrystallization or cementation creating tensile strength along the fault plane. This tensile strength is modeled as some fraction of the rock tensile strength, αS_o, where $0 \leq \alpha \leq 1$.

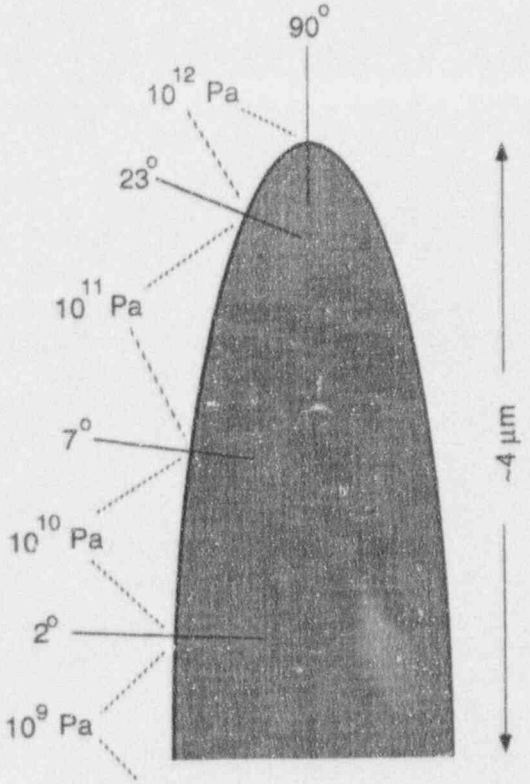

Figure 10-3. The tensional stresses around the tip of an elliptical crack. The parameters are those listed in the text as realistic for a dike. The stress decreases away from the tip, but is still tensional at locations where normal planes have dips less than 1 degree. Beyond 1.5 mm from the tip, the stresses become compressional. Any joint normal to the ellipse with tensional stress across it is capable of being opened and injected with fluid, but this by no means assures that it will be opened.

Parenthetically, if the fault plane has annealed to the extent that it has greater strength than the tensile strength of undeformed rock, the propagating dike will never follow this fault plane, and this case is not considered further. The *in situ* stress acting across the fault is $\sigma_3 \sin^2\theta + \sigma_1 \cos^2\theta$, where σ_1 is lithostatic pressure. Assuming that only vertical strain exists in the *in situ* stress field:

$$\sigma_3 = [\nu/(1-\nu)]\ \sigma_1 \qquad (10\text{-}2)$$

where ν is Poisson's ratio.

Therefore, the total stress needed to open a fault or joint plane to the same aperture as the dike described above is

$$\sigma_f = \sigma_3 \sin^2\theta + \sigma_1 \cos^2\theta + \alpha S_o + \sigma_d \qquad (10\text{-}3)$$

Based on these assumptions, the stress required for a dike to follow a dipping fault zone, rather than continue to propagate vertically is

$$\sigma_f \leq \sigma_{dike} \tag{10-4}$$

Defining

$$h_o = \frac{S_0 (1-\alpha)(1-\nu)}{\rho g (1-2\nu)} \tag{10-5}$$

then

$$\theta \geq \cos^{-1}\left[\left(\frac{h_o}{h}\right)^{1/2}\right] \tag{10-6}$$

Faults with dips greater than or equal to θ provide a lower energy path to the surface for a propagating dike than does continued vertical propagation. Under these circumstances, the fault will redirect the ascending magma. As a result, lateral transport as it ascends and focusing of this magma at the surface near fault traces become possible.

Using these expressions for θ and h_o, it is possible to examine the behavior of dikes intersecting fault zones at varying depths and fault dip angles. In order to bound the problem, h_o is calculated using a relatively weak rock and a relatively strong rock (Table 10-1). Figure 10-4 plots the dependence of minimum fault dip, θ, on depth for these two rock types, given that the fault strength is negligible, $\alpha=0$. The effect of varying fault strength for a given rock strength is shown in Figure 10-5. Clearly, the analytical results suggest that the ability of a fault or fault zone to redirect ascending magmas is highly dependent on the depth at which the fault zone is intersected by the dike and the dip of the fault zone.

Table 10-1. Theoretical data for weak (Example 1) and strong (Example 2) rock where S_o is uniaxial tensile strength, ν is Poisson's ratio, g is the acceleration of gravity, and h_o is calculated using Eq. (10-5)

Example	S_o, MPa	ρ, kg/m^3	ν	g, m/s^2	h_o, m
1	1.0	2700	0.2	9.8	50.4
2	10.0	3300	0.33	0.8	609.0

10.2.2.3 Free Surface Effects

In addition to simple dike-fault interactions, understanding the interaction between a dike and a free surface is important for modeling repository disruption. Here, a numerical model is used to quantify the effects of a free surface on a 1-m wide dike. The dike is modeled as a single vertical edge dislocation in a homogeneous half-space. The 2D analytical solution to this problem is taken from Head (1953) for the stress surrounding such a dislocation. The requisite input parameters for this model are crack aperture (1 m), shear modulus (2.1×10^4 MPa), Poisson's ratio (0.25), and the distance from the crack tip to the free surface. The Head (1953) solutions give two principal stress and shear stress values

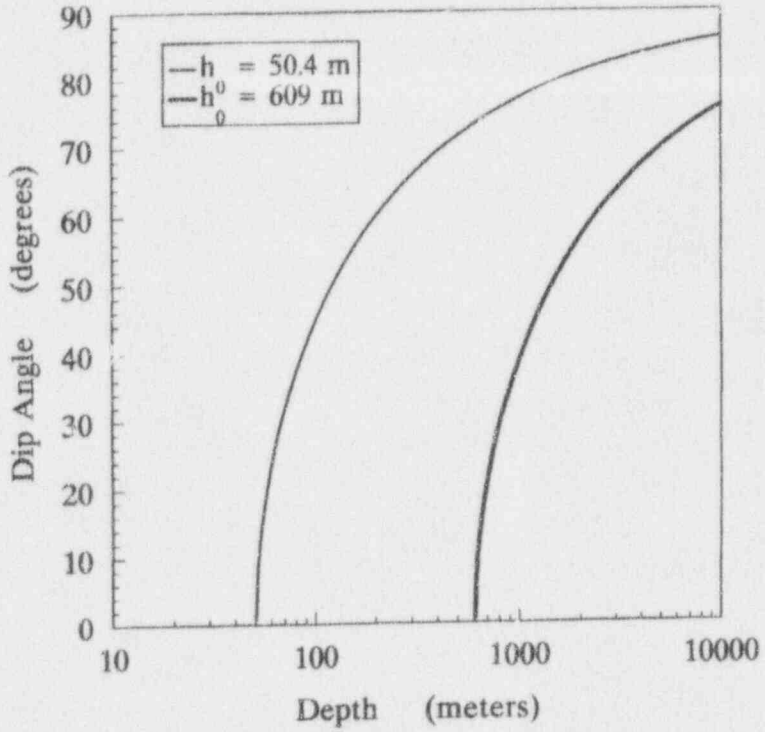

Figure 10-4. Plot of stresses versus depth for a 1-m wide dislocation. The image plus residual stress, or free surface contribution, decreases as the inverse of depth. Vertical and horizontal *in situ* stresses increase linearly with depth. A good rule of thumb is that free surface effects on the stress field surrounding a dislocation approximate those of the minimum *in situ* stress at a depth 500 times the dislocation width.

at any point in the half-space except for the crack tip, where high stress gradients create a singularity. The solution requires that the in-plane stresses at the free surface are always zero, a proper constraint.

Calculation of free-surface effects is accomplished by adding to the dislocation self stress, an image dislocation at an equal distance above the surface, in addition to a term to remove any residual stress in the plane of the free surface. These two terms represent the free surface contribution to the stress at any point, so the modeled stress accounts for free surface effects. Comparing the free surface component to other stress values allows quantification of the free surface influence. For a 1-m wide dike, this influence was determined for distances from the surface to the dike tip varying between 10 and 1,000 m. The free surface contribution is plotted in Figure 10-6, along with the approximate *in situ* stress components (i.e., lithostatic stresses) for comparison. The free surface effects decrease as the inverse of depth, while the vertical (σ_1) and horizontal (σ_3) stresses increase linearly with depth. Vertical stress is assumed to be equal to $\rho g d$, where ρ is about 2,600 kg/m^3, g is gravity, and d is depth in meters. At approximately 500 m, the free surface effects are comparable to the minimum *in situ* stress in terms of influence on the state of stress. Keep in mind these results are for a 1-m wide dike; the image plus residual term increases linearly with crack aperture. For a 5-m wide dike, free surface effects would be significant to a depth of about 2,500 m, again 500 times the width. These results suggest that the depth at which a dike feels the free surface is a linear function of dike width rather than dike length as Pollard and Holzhausen (1979) have suggested. Host rock elastic properties also affect the curve in Figure 10-6.

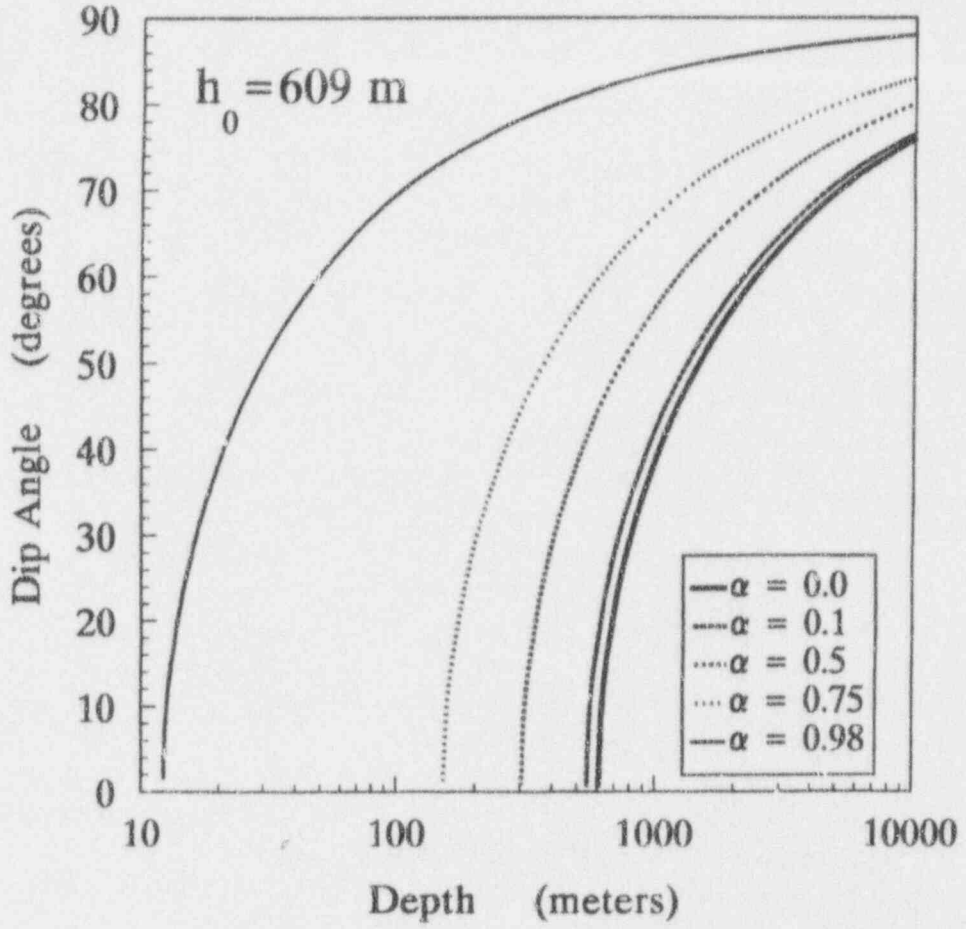

Figure 10-5. The minimum dip angle of a fault that will redirect an upwardly propagating dike are a function of depth and rock properties (h_o). Rock properties for h_o are shown in Table 10-1.

For lower values of shear modulus or Poisson's ratio, the image plus residual stress term decreases, hence, the free surface is influential to a lesser depth.

10.2.3 Summary and Implications for the Yucca Mountain Region

Given a pressurized, fluid-filled crack in a homogeneous elastic medium, the crack advances such that it opens in the direction of the least principal stress. The balance between fluid pressure and viscous drag controls the flow of fluid into the crack tip, thus propagation of the crack. The fracture resistance and elastic strength of the host rock influence fracture advance only in the early stages during when the crack length is small. As a crack lengthens, the fluid pressure necessary to maintain a given aperture decreases. The key to understanding structural control of dike orientation and trajectory is to constrain the conditions under which a dike changes course to follow a pre-existing weakness in the crust. Our analytical model of the stress around a crack tip confirms that crack tip stress does not influence dike trajectory, as tensile stress at the tip is capable of opening a joint of any orientation. Dike trajectory is largely determined by a balance between the stress necessary to create and dilate a new fracture perpendicular to σ_3, and the stress needed to dilate a pre-existing weakness at some angle oblique to σ_3.

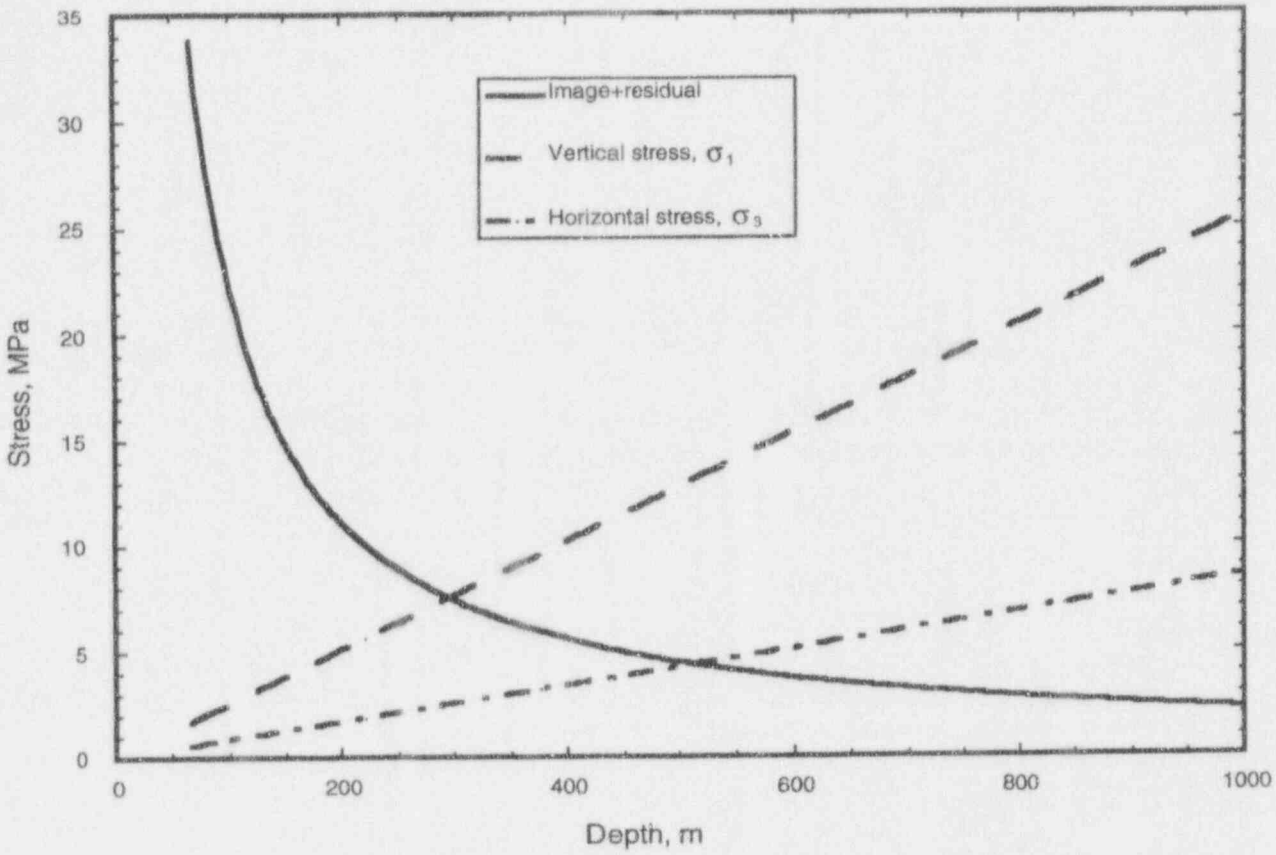

Figure 10-6. For a given rock strength, the cohesive strength of the fault zone (α) plays an important role in determining the minimum dip angle of a fault that will redirect an upwardly propagating dike.

Factors that affect this balance include differential stress, dip angle of the fault or joint plane, fluid pressure in the dike, depth below the surface, and host rock material properties. Moreover, stresses due to the free surface, proportional to dike width, can affect the balance. These free surface effects are the most important, given normal dike widths, at depths of less than about 1 km. This range is the same one at which faults of shallow dips begin to provide low-energy pathways to the surface. Therefore, it seems reasonable to conclude that large-scale lateral migration of magmas is likely to occur only if these magmas intersect relatively steeply dipping faults at relatively great depths.

This model suggests an upper bound on the ability of regional crustal structures to focus magmatism. At greater depths, more than about 1 km, only high-angle faults can capture and redirect magmas ascending in dikes. At shallow depths, less than 1 km, low-angle faults can redirect magmas. However, at these shallow depths, there is very little opportunity for large lateral transport of these magmas, especially because free surface effects will act on magmas ascending in fault planes at shallow depths. Based on the calculations presented here, there is little opportunity for fault planes to capture and transport magmas for map distances of greater than 2 km and never greater than 5 km. This theoretical result would suggest that (i) knowledge of fault geometry as a function of depth could provide important

insight into the likelihood that given faults will focus magma should it ascend through crust in the YMR; and (ii) probability models of volcanic disruption of the candidate repository (e.g., Connor and Hill, 1993) may be affected by structural controls on magmatism, but only on local, rather than regional scales. Finally, it is emphasized that these models are preliminary, and will be tested using field data, where direct comparisons of dike and fault interaction can be made, and through the study of cinder cone alignment development.

10.3 VOLCANOLOGICAL BASIS FOR INVESTIGATION OF DEGASSING FROM COOLING, SMALL-VOLUME BASALTIC SYSTEMS

Volatile concentration in magmas and interaction with shallow groundwater is one of the most important parameters driving eruption energetics. After the cessation of eruptive activity, heat and mass transfer to the surface and through the rock surrounding the volcano continues through convective degassing and heat conduction. This type of degassing activity may have an important impact on repository performance in several ways. Direct effects of volcano degassing include the movement of gas through the repository block itself that may lead to accelerated rates of container corrosion and deterioration of the waste package. Direct effects of volcano degassing would likely accompany direct magmatic disruption of the repository, and could also occur if magma intruded rocks near the repository, without actually intersecting the repository. Indirect effects of degassing may include geochemical effects on the partitioning of radionuclides between aqueous and solid phases and sorption. Movement of aqueous and gas phases in the geologic environment and changes in the mechanical properties of the rock may also result from degassing and thermal loading of rock by degassing. The effects of volcanic degassing are different than those associated with eruptive activity for several reasons

(i) Volcanic degassing is a long-term process. Vigorous, high-temperature degassing persists at some cinder cones for decades. Low-temperature and less vigorous degassing may continue for more than 100 yr. As a result, a broad range of time scales must be considered in developing models of how volcanic degassing influences repository performance.

(ii) Volcanic degassing is capable of influencing an area much greater than is disrupted by eruptive activity. This wide area of influence is important because most probability models for volcanic activity are area dependent; the probability of volcanic gases interacting with the repository and surrounding geological environment is much higher than the probability of direct disruption by magma transport. The areal extent of degassing and the nature of variation in degassing is uncertain and will need to be assessed through field investigation.

(iii) Volcanic degassing does not result in the fragmentation, transport, and dispersion of rock and repository waste as would result in direct disruption by magma. Instead, volcanic degassing has long-term effects on the geochemistry of the repository and surrounding rock. Volcanic gases are generally acid solutions, with pH in the range of 0.1 to 2. Dominant species in the gases are water, carbon dioxide, sulfur dioxide, hydrogen chloride, and trace compounds, including trace metals like mercury and noble gases. Because of their composition, volcanic gases can accelerate corrosion of waste containers, alter transport in the geologic environment, and alter the mechanical strength of the rocks in and around the repository block. Transport might also be altered in the repository

block as a result of volcanic degassing. These effects are different than simple thermal loading, such as that resulting from the repository itself, because, in addition to thermal effects, mass flow through the geologic environment will increase.

10.3.1 Conceptual Models For Heat and Mass Transfer in Cooling Small-Volume Basaltic Systems

Data gathered at cooling cinder cones will be useful in the development of numerical models for changes in heat and mass flow associated with potential intrusive and extrusive activity in the YMR. Numerical models will be developed that explore the relationship between heat and mass transfer around dikes and cinder cones as they cool through time.

By knowing rock and gas properties and measuring mass and heat transfer at the surface, it is possible to gain insight into heat and mass transfer at depth (Connor et al., 1993b). A simplified conceptual model is illustrated in Figure 10-7. Heat is lost from a cooling dike by conduction and convection. Mass is also lost from the cooling dike by advection. Because of vaporization, the dike acts as a groundwater sink, and there is a net movement of groundwater toward the dike. Above the dike, flow is by free convection in the rock (or alluvium) and by forced convection through fractures. At cinder cones, fractures often concentrate around the crater rim, and these fractures are the location of fumaroles. Further factors, such as condensation zones in the rock surrounding the cooling system, will be incorporated in future numerical models.

10.3.2 Preliminary Results from Cerro Negro, Nicaragua

Soil mercury (Hg) concentrations are an excellent indicator of convective upwelling of gases related to the cooling and crystallization of magmas at shallow depths. The spatial distribution of anomalous Hg concentrations serves to give an idea of the areal extent of convective upwelling (Varekamp and Buseck, 1983; Williams, 1985) and the presence of fracture zones both within the cone itself and in areas extending from the base of the cone (Connor, 1989). Soil Hg is used extensively in geothermal exploration because there is little chance for lateral transport of Hg away from zones of convective upwelling. A preliminary soil Hg survey was conducted at Cerro Negro, Nicaragua, during September 1993, for the purpose of better constraining the areal extent of degassing at this cone. As described elsewhere (Connor, 1993), Cerro Negro is in many respects analogous to cinder cones in the YMR. An important difference is that Cerro Negro has been historically active, first forming in 1850, and last erupting in April 1992.

A total of 35 samples were collected for soil Hg analysis at Cerro Negro. These samples were collected from soil depths of 25 to 30 cm and stored in glass vials. During analysis, ampules were sieved using a No. 80 (180-mm diameter) sieve, and 0.5 g of the sieved fraction were placed in 10-mL glass ampules. The sample then digested using a 1-mL 5-percent HCl and 2-mL concentrated nitric acid solution. Following digestion, 0.5 ml of digested material added to 20 mL of 1-percent HCl solution and analyzed by atomic fluorescence spectrometry. In the case of high concentration samples, further dissolution was necessary. Analysis of soil standards indicate that this procedure is accurate to ± 4 ppb (1 part in 10^9) at 60-ppb Hg concentrations.

The highest soil Hg concentrations were found on the north crater rim of Cerro Negro, about 75 m from the 1992 vent (Figure 10-8). Samples in this region were as high as 4,813 ppb and were quite

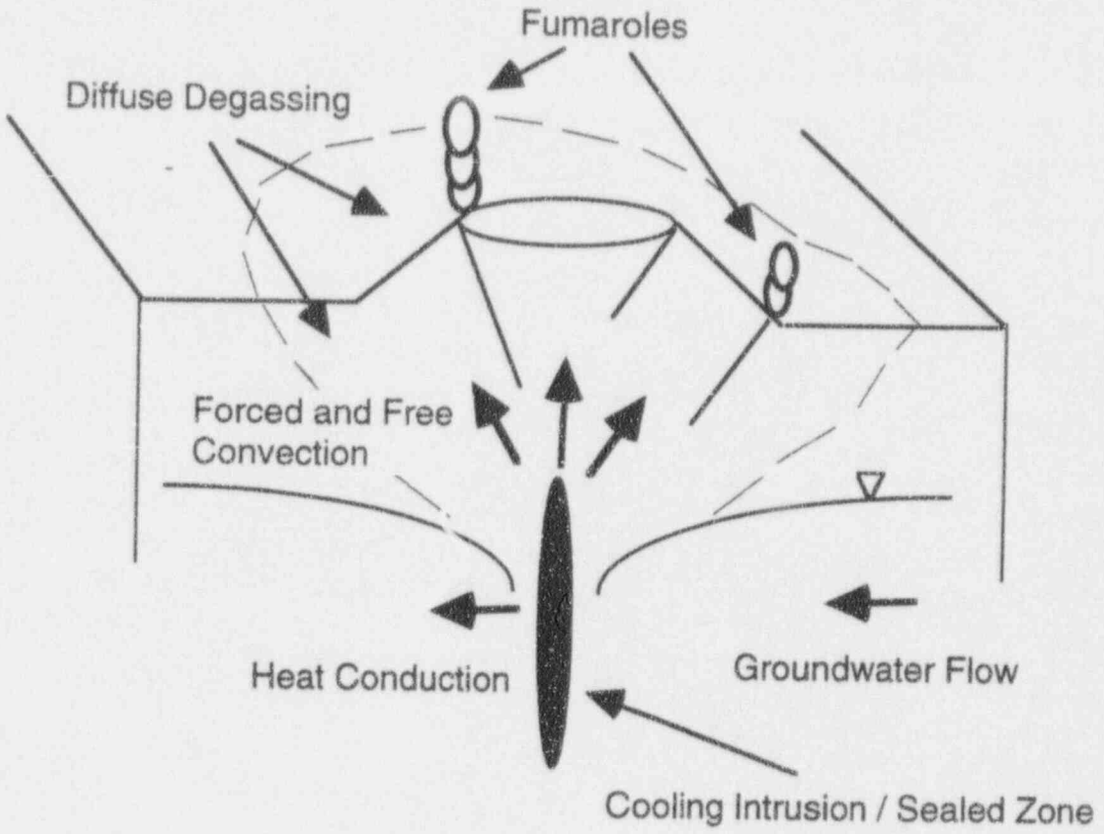

Figure 10-7. Schematic diagram illustrating one conceptual model of heat and mass transfer in a cooling cinder cone.

variable. This was an area of active gas flux along fractures at the time these samples were collected. High concentrations adjacent to low concentrations are quite common in these areas because often the soil is too hot for Hg adsorption to occur. This zone of high Hg flux is at least 250 m long, but its total areal extent was not determined by the survey. Other than those samples collected on the crater rim, the highest Hg concentrations were found approximately 700 m from the 1992 vent, 100 m from the base of the cone. Hg concentrations in this area were as high as 910 ppb, and six samples had concentrations in excess of 100 ppb. On the east flank of the volcano, normal background soil Hg concentrations were found (< 10 ppb).

10.3.3 Implications for Volcanism Consequence Models

Based on the results of this preliminary soil Hg survey, it is clear that degassing is taking place over a broad zone at Cerro Negro volcano. Anomalous soil gas flux has been identified at distances of up to 700 m from the most recently active vent and 17 months after the most recent volcanic activity. A more extensive survey, and measurement of other gas components, including CO_2, He, and ^{222}Rn, and their fluxes, should provide a complete picture of diffuse degassing at Cerro Negro. These data have important implications for assessing indirect consequences of volcanism in the YMR because they provide insight into the area likely to be influenced by the flux of magmatic and related volatiles.

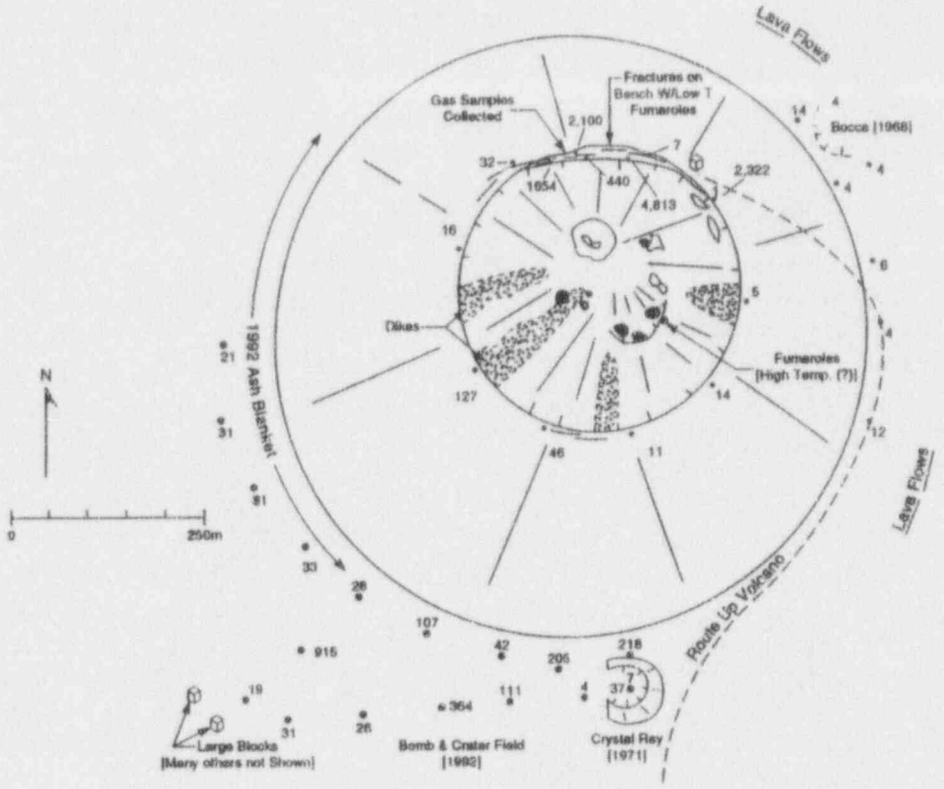

Figure 10-8. Soil Hg distribution at Cerro Negro, Nicaragua. Sampling points, solid dots, are shown relative to the central cone, crater, and related features. Adventive cones, at the Bocca and Crystal Rey, formed during 1968 and 1971 activity, are also shown. Hg concentrations are posted adjacent to sample locations.

10.4 ASSESSMENT OF PROGRESS

The models of dike-fault interaction developed at the Center for Nuclear Waste Regulatory Analyses (CNWRA) over the last 6 mo are the first of their kind to address basic questions about the degree to which pre-existing crustal structures can result in the lateral transport and focusing of magmas. The results of this investigation are preliminary and will need to (i) be tested using a variety of field observations, (ii) be tested for a greater range of rock and dike properties, (iii) be compared with finite element methods under development in the CNWRA Tectonics Research Project, and (iv) receive peer review, before the results are incorporated into probability models and IPA phase III. Nonetheless, the preliminary results reported here indicate that geologic data on dike-fault interaction and geophysical models of these processes can provide defensible constraints on probability models of volcanic disruption of the repository. This step is an important one toward the incorporation of geologic insight into probability model development.

Studies of volatile flux from cooling cinder cones have rarely been conducted in the past. The survey conducted at Cerro Negro volcano, Nicaragua, during September 1993 indicates that it is important to understand this process because it continues for much longer periods of time than does

eruptive activity and effects a broader region about the cone. Although these data do not, in and of themselves, provide a basis for the modification of PA models of the consequences of igneous activity, they do indicate that
these models are inadequate because they do not reflect the true spectrum of adverse conditions resulting from volcanic activity.

10.5 PLANNED PROGRESS IN THE NEXT SIX MONTHS

The Field Volcanism Research Project utilizes a dual approach to the evaluation of the consequences of potential volcanic activity in the YMR. Clearly, the range of volcanic activity in the western Great Basin, the duration of this activity, and geology of near-surface structures must be evaluated using detailed field studies of specific sites in the region. Much can also be learned from the study of historically active cinder cones, especially those in which eruptions have been rigorously monitored. As described previously, recent work indicates that many physical and conceptual models of cinder cone volcanism do not encompass the range of activity in modern cinder cones. Therefore, the dynamics of cinder cone eruptions in the western Great Basin cannot be truly assessed without thorough comparison to monitored cinder cone eruptions. One simple approach adopted in the Field Volcanism Research Project is to compare near-vent deposits at YMR volcanoes with those at Parícutin, Tolbachik, and Cerro Negro, volcanoes with well known eruption histories. Furthermore, processes such as diffuse degassing and thermal loading operate on geologically limited time scales, but could have important impact on repository performance. These processes can be studied most directly at recently active cinder cones. This integrated approach, the study of western Great Basin cinder cones and recently active cones, will provide the most comprehensive and defensible basis for evaluation of compliance with 40 CFR Part 191 and 10 CFR Part 60.122(c)(15). As such, results of the Field Volcanism Research Project will directly support the LARP. Without this type of integration, consequence studies and their utility in probability model development will become unnecessarily tenuous.

Field work will begin at Parícutin volcano during the next 6 mo. This field work will include sampling of the deposits of the 1943–1952 eruptions for the purpose of characterizing variation in vesiculation and volatile content during the eruption, and sampling of gases and soils for the purpose of characterizing current degassing at this cooling cinder cone. Planning will continue for field work at the Tolbachik cinder cones during July 1994.

A Major Milestone (MM) will be transmitted during the next 6 mo. This MM will provide a review of geophysical studies for the characterization of magnetic field anomalies associated with cinder cones and dikes. This MM will include a review of the aeromagnetic data available for the YMR, ground magnetic data collected in the YMR and similar volcanic fields, and an analytical review of the utility of this type of data in the identification and mapping of shallow dikes and buried volcanic centers. In addition, a systematic review of seismic tomographic methods and their application to study of the structure and activity of volcanic fields will be included as part of this MM. This MM will also include a detailed review of the seismic tomographic method, its application to the study of basaltic fields, and a synthetic seismic tomographic survey of the YMR for the purpose of illustrating the resolution of the seismic tomographic method.

Work will continue on the characterization of dike-fault interactions. This characterization will include continued model development and refinement, and field mapping in volcanic fields and in older, more dissected regions to better identify dike-fault interactions.

All these activities will be important contributions to the LARP and to CDS development. In addition, these activities will be coordinated with Volcanic Systems of the Basin and Range research in order to refine probability models on a continuing basis.

10.6 REFERENCES

Abé, H., K. Hayashi, and S. Arima. 1985. Theoretical study on the stability of a reservoir created by the intersection of a fluid-filled crack with an oblique joint for the extraction of geothermal heat. *International Journal for Numerical and Analytical Methods in Geomechanics* 9: 15–27.

Amos, R.C., S. Self, and B.M. Crowe. 1983. Pyroclastic activity at Sunset Crater: Evidence of a large magnitude, high dispersal strombolian eruption. *EOS, Transactions of the American Geophysical Union* 62: 1,085.

Anderson, E.M. 1938. The dynamics of sheet intrusion. *Proceedings of the Royal Society of Edinburgh* 58: 242–251.

Atkinson, B.K. 1987. Introduction to fracture mechanics and its geophysical applications. B.K. Atkinson, ed. *Fracture Mechanics of Rock.* New York: Academic Press: 1–26.

Barr, G.E., E. Dunn, H. Dockery, R. Barnard, G. Valentine, and B. Crowe. 1993. *Scenarios Constructed for Basaltic Activity at Yucca Mountain and Vicinity.* SAND-91-1653. Albuquerque, NM: Sandia National Laboratories.

Birch, F. 1966. Compressibility; Elastic constants. Handbook of physical constants. S.P. Clark, ed. *Geological Society of America Memoir* 97: 95–173.

Carrigan, C.R., G. Schubert, and J.C. Eichelberger. 1992. Thermal and dynamical regimes of single- and two-phase magmatic flow in dikes. *Journal of Geophysical Research* 97B: 17,377–17,392.

Connor, C.B. 1989. Anomalous soil Hg concentrations at Parícutin volcano, Michoacán-Guanajuato volcanic field, Mexico. *Geofisica Internacional* 28: 1,029–1,042.

Connor, C.B. 1993. *Technical and Regulatory Basis for the Study of Recently Active Cinder Cones.* Letter Report to the U.S. Nuclear Regulatory Commission, Center for Nuclear Waste Regulatory Analyses, San Antonio, TX.

Connor, C.B., and B.E. Hill. 1993. *NRC High-Level Radioactive Waste Research at CNWRA, July 1 Through December 31, 1992. Chapter 10: Volcanism Research.* NRC–02W.G. Mook and H.T. Waterbolk, eds, 88–005. Washington, DC: U.S. Nuclear Regulatory Commission: 10-1 to 10-31.

Connor, C.B., L. Powell, W. Strauch, M. Navarro, O. Urbina, and W.I. Rose. 1993a. The 1992 eruption of Cerro Negro, Nicaragua: An example of Plinian-style activity at a small basaltic cinder cone. *EOS, Transactions of the American Geophysical Union* 74: 640.

Connor, C.B., B.M. Clement, X. Song, S.B. Lane, and J. West-Thomas. 1993b. Continuous monitoring of high-temperature fumaroles on an active lava dome, Volcán Colima, Mexico: Evidence of mass flow variation in response to atmospheric forcing. *Journal of Geophysical Research* 98: 19,713–19,722.

Crowe, B.M., S. Self, D. Vaniman, R. Amos, and F. Perry. 1983. Aspects of potential magmatic disruption of a high-level waste repository in southern Nevada. *Journal of Geology* 91: 259-276.

Daneshy, A.A. 1974. Hydraulic fracture propagation in the presence of planes of weakness. *Society of Petroleum Engineers Paper Number 4852*. Amsterdam, The Netherlands: Society of Petroleum Engineers.

Daneshy, A.A. 1978. Hydraulic fracture propagation in layered formations. *Society of Petroleum Engineers Journal* 18: 33–41.

Delaney, P.T., and D.D. Pollard. 1982. Solidification of basaltic magma during flow in a dike. *American Journal of Science* 282: 856–885.

Delaney, P.T., D.D. Pollard, J.I. Ziony, and E.H. McKee. 1986. Field relations between dikes and joints: Emplacement processes and paleostress analysis. *Journal of Geophysical Research* 91B: 4,920–4,938.

Emerman, S.H., D.L. Turcotte, and D.A. Spence. 1986. Transport of magma and hydrothermal solutions by laminar and turbulent fluid fracture. *Physics of the Earth and Planetary Interiors* 41: 249–259.

Gudmundsson, A. 1983. Form and dimensions of dykes in eastern Iceland. *Tectonophysics* 95: 295–307.

Head, A.K. 1953. Edge dislocation in inhomogeneous media. *Proceedings of the Physical Society of London* B66: 793–801.

Ho, C.-H. 1992. Risk assessment for the Yucca Mountain high-level nuclear waste repository site: Estimation of volcanic disruption. *Mathematical Geology* 24: 347–364.

Irwin, G.R. 1957. Analysis of stresses and strains near the end of a crack traversing a plate. *Journal of Applied Mechanics* 24: 361–364.

Lister, J.R. 1990a. Buoyancy-driven fluid fracture: Similarity solutions for the horizontal and vertical propagation of fluid-filled cracks. *Journal of Fluid Mechanics* 217: 213–239.

Lister, J.R. 1990b. Buoyancy-driven fluid fracture: The effects of material toughness and of low-viscosity precursors. *Journal of Fluid Mechanics* 210: 263–280.

Lister, J.R., and R.C. Kerr. 1991. Fluid-mechanical models of crack propagation and their application to magma transport in dykes. *Journal of Geophysical Research* 96B: 10,049–10,077.

Pacific Northwest Laboratory. 1993. *Preliminary Total-System Analysis of a Potential High-Level Nuclear Waste Repository at Yucca Mountain*. PNL-8444. Richland, WA: Pacific Northwest Laboratory.

Parsons, T., and G.A. Thompson. 1991. The role of magma overpressure in suppressing earthquakes and topography: Worldwide examples. *Science* 253: 1,399–1,402.

Pollard, D.D. 1973. Equations for stress and displacement fields around pressurized elliptical holes in elastic solids. *Mathematical Geology* 5: 11–25.

Pollard, D.D. 1987. Elementary fracture mechanics applied to the structural interpretation of dykes; Mafic dyke swarms. H.C. Halls and W.F. Fahrig, eds. *Geological Association of Canada Special Paper 34*: 5–24.

Pollard, D.D., and G. Holzhausen. 1979. On the mechanical interaction between a fluid-filled fracture and the earth's surface. *Tectonophysics* 53: 27–57.

Pollard, D.D., and O.H. Muller. 1976. The effect of gradients in regional stress and magma pressure on the form of sheet intrusions in cross section. *Journal of Geophysical Research* 81: 975–984.

Reches, Z., and K. Fink. 1988. The mechanism of intrusion of the Inyo Dike, Long Valley Caldera, California. *Journal of Geophysical Research* 93B: 4,321–4,334.

Rubin, A.M. 1993. Tensile fracture of rock at high confining pressure: Implications for dike propagation. *Journal of Geophysical Research* 98: 15,919–15,935.

Rubin, A.M., and D.D. Pollard. 1987. Origins of blade-like dikes in volcanic rift zones. *U.S. Geological Survey Professional Paper 1350*: 1,449–1,470.

Secor, D.T., and D.D. Pollard. 1975. On the stability of open hydraulic fractures in the earth's crust. *Geophysical Research Letters* 2: 510–513.

Settari, A. 1988. Quantitative analysis of factors influencing vertical and lateral fracture growth. *SPE Production Engineering* 3: 310–322.

Smith, E.I., D.L. Feuerbach, T.R. Naumann, and J.E. Faulds. 1990. The area of most recent volcanism near Yucca Mountain, Nevada: Implications for volcanic risk assessment. *First Annual International High-Level Radioactive Waste Management Conference Proceedings*: La Grange IL: High-Level Radioactive Waste Management, International Conference, April 8-12, 1990, Las Vegas, Nevada. American Nuclear Society 1: 81–90.

Spence, D.A., and D.L. Turcotte. 1985. Magma-Driven propagation of cracks. *Journal of Geophysical Research* 90B: 575–580.

Spence, D.A., P.W. Sharp, and D.L. Turcotte. 1987. Buoyancy-driven crack propagation: A mechanism for magma migration. *Journal of Fluid Mechanics* 174: 135–153.

Stevens, B. 1911. The laws of intrusion. *Transactions of the American Institute of Mining Engineers* 41: 650–672.

Trapp, J.S., and P.S. Justus. 1992. Regulatory requirements to address issues related to volcanism and magmatism: Code of federal regulations, title 10, part 60, disposal of high-level radioactive waste in geologic repositories. *Third International Proceedings High-Level Radioactive Waste Management Conference*. La Grange Park, IL: American Nuclear Society and American Society of Civil Engineers: 2,039–2,046.

Turcotte, D.L., S.H. Emerman, and D.A. Spence. 1987. Mechanics of dyke injection; Mafic dyke swarms. H.C. Halls and W.F. Fahrig, eds. *Geological Association of Canada Special Paper* 34: 25–29.

Valentine, G.A., B.M. Crowe, and F.V. Perry. 1992. Physical processes and effects of magmatism in the Yucca Mountain Region. *Third International Proceedings High-Level Radioactive Waste Management Conference*. La Grange Park, IL: American Nuclear Society and American Society of Civil Engineers: 2,014–2,024.

Varekamp, J.C., and P.R. Buseck. 1983. Hg anomalies in soils: A geochemical exploration method in geothermal areas. *Geology* 12: 283–286.

Walker, G.P.L. 1991. Origin of vesicle types and distribution patterns in the Xitle pahoehoe basalt, in Mexico City. *EOS, Transactions of the American Geophysical Union* 72: 766.

Walker, G.P.L. 1993. The pyroclastic deposits of El Paricutin. *50 Años Del Volcán Parícutin, Reunión Internacional Conmemorativa, Programa y Resumenes*. Mexico City: Instituto de Geofísica.

Warpinski, N.R., and L.W. Teufel. 1987. Influence of Geologic Discontinuities on Hydraulic Fracture Propagation. *Journal of Petroleum Technology* 39: 209–220.

Weertman, J. 1971. Velocity at which liquid-filled cracks move in the earth's crust or in glaciers. *Journal of Geophysical Research* 76: 8,544–8,553.

Weertman, J. 1980. The stopping of a rising, liquid-filled crack in the earth's crust by a freely slipping horizontal joint. *Journal of Geophysical Research* 85B: 967–976.

Williams, S.N. 1985. Soil radon and mercury distribution in relation to magmatic resurgence at Long Valley caldera. *Science* 229: 551–553.

11 REGIONAL HYDROGEOLOGIC PROCESSES OF THE DEATH VALLEY REGION

by Gordon Wittmeyer, William M. Murphy, and Vivek Kapoor

Investigators: Vivek Kapoor, H. Lawrence McKague, William M. Murphy, and Gordon Wittmeyer (CNWRA), Brent Henderson and Sandy Nguyen (SwRI)

NRC Project Officer: Thomas J. Nicholson

11.1 TECHNICAL OBJECTIVES

Yucca Mountain (YM) has been proposed as a potential high-level nuclear waste (HLW) repository in part because of the favorable geochemical and hydrologic environment provided by its 700-m thick unsaturated zone. Siting the repository in the unsaturated zone may significantly reduce the potential for waste canister corrosion and subsequent dissolution of the waste form. Moreover, the low water flux rates that are presumed to exist in the unsaturated zone reduce the likelihood that radionuclides that are dissolved will be rapidly transported to the accessible environment. Mechanisms that may saturate the repository horizon, and thus compromise favorable conditions provided by the YM site, include rapid infiltration of water from the surface through highly conductive fracture networks and an increase in the elevation of the regional water table. The first mechanism is a site-scale or subregional issue and is not addressed by this research project. Elevation of the water table may occur due to increased recharge to the regional carbonate system along stream channels and mountain fronts in topographically closed basins 100 km to the north and northeast of YM. Even if elevation of the regional water table does not saturate the repository block, the reduced thickness of the unsaturated zone has the potential to significantly diminish travel times within the vadose zone. The primary objectives of this research project are to: (i) analyze existing conceptual models and develop new conceptual models of the regional hydrogeologic flow regime in the Death Valley region that contains YM; and (ii) construct numerical models of regional flow that may be used to assess the potential for the water table beneath YM to rise in response to wetter climatic conditions.

Predictions made with numerical models will be used by the U.S. Department of Energy (DOE) in their license application to demonstrate that the YM site meets the overall performance standards outlined in 10 CFR 60.112 and the geologic subsystem performance standard defined in 10 CFR 60.113(a)(2). In addition, the DOE may choose to use numerical models to demonstrate the absence of potentially adverse conditions including: The effects of future pumping on the regional flow system [10 CFR 60.122(c)(2)]; The potential for deleterious changes to the hydrologic system [10 CFR 60.122(c)(5)]; The potential for changes to the hydrologic conditions resulting from climate change [10 CFR 60.122(c)(6)]; the potential for water table rise [10 CFR 60.122(c)(22)]; and the presence of favorable conditions, including the clear absence of fully saturated pathways connecting the repository to the water table [10 CFR 60.122(b)(8)(ii)]. Understanding of the regional hydrogeologic system developed from this project will be used to guide the review of the DOE license application and to assess the adequacy of the models used by the DOE to demonstrate compliance with the regulatory requirements and environmental standards.

Understanding of the regional hydrogeologic system gained from this research project will be used to construct specific Compliance Determination Methods (CDMs) outlined in the License Application Review Plan (LARP). Literature reviews and hydrogeologic data gathered in Task 1 of the project will

provide information that may be directly used to assess the Description of individual systems and characteristics of the site (Section 3.1) and in particular the Description of the hydrologic and geochemical systems (Sections 3.1.2 and 3.1.3, respectively). Evidence gleaned from literature reviews and data analysis in conjunction with conceptual and numerical models of the regional flow regime developed in this research project will be directly used to determine if the applicant has provided convincing evidence of the presence or absence of favorable hydrogeologic conditions and potentially adverse hydrogeologic conditions (Sections 3.2.1.1, 3.2.2.1, 3.2.2.3, 3.2.2.6, 3.2.2.8, 3.2.2.9, 3.2.2.11, and 3.2.4.2). Flow models developed in this project will also be used to confirm that velocity fields and travel times within the saturated zone estimated by the DOE are accurate enough to demonstrate compliance with the Groundwater travel time performance objective (Section 3.3).

Compliance Determination Strategies (CDSs) for the LARP sections listed previously have been developed but will not be finalized until a thorough review of the LARP has been conducted. However, the Regional Hydrogeology Research Project will be instrumental in resolving specific technical uncertainties identified during the CDS development process. Key Technical Uncertainties (KTUs) that pose a high risk of noncompliance with the total-system or subsystem performance requirements may require that the U.S. Nuclear Regulatory Commission (NRC) conduct independent research to resolve the issue. Development of a conceptual groundwater flow model that is representative of the YM site groundwater system has been identified as a KTU that must be addressed in LARP Sections 3.2.2.1, 3.2.2.9, and 3.3.

The Regional Hydrogeology Research Project has been divided into five tasks: Task 1—Collect and analyze data and existing models; Task 2—Construct alternative conceptual models of key hydrogeologic processes in the Death Valley region of the western Great Basin; Task 3—Construct and calibrate mathematical and numerical models of subsurface flow at local, basin, and regional scales; Task 4—Use geochemical data to evaluate and refine regional flow models; and Task 5—Apply models to analyze problems critical to repository performance. Current plans call for completion of Tasks 1 and 2 during the first 2 yr of the project with the remaining tasks to be initiated in the third year and completed by the fourth and final year of the project. To date, efforts have focused solely on Task 1. The primary technical objectives of Task 1 are: (i) To conduct literature reviews to assess the current understanding of the regional flow regime; (ii) Perform an inventory of hydrogeologic data collected from the immediate vicinity of YM and the Death Valley region; and (iii) Compile relevant hydrogeological, hydrochemical, and mineralogical data into an integrated geographic information system (GIS) database.

11.2 SIGNIFICANT TECHNICAL ACCOMPLISHMENTS

Progress toward achieving the technical objectives outlined in Section 11.1 has been made in Task 1 on the collection and analysis of data and existing models. Work has commenced on three activities: (i) review of the extensive body of literature characterizing the hydrogeology and hydrogeochemistry of subbasins within the Death Valley region, (ii) collection of hydraulic, geologic, and geochemical data, and (iii) integration of data into the GIS database. For the first activity, efforts have been concentrated on summarizing estimates of water budgets for subbasins and on an evaluation of recent investigations of the hydrochemical facies of waters from the Death Valley region. For the second activity, hydraulic and water chemistry data have been obtained from the Carson City and Las Vegas offices of the U.S. Geological Survey (USGS) and are being entered into the Center for Nuclear Waste Regulatory Analyses (CNWRA) ARC/INFO GIS. Only results for the first activity and

a brief description of a regional field trip conducted to enhance understanding of reviewed material are reported.

11.2.1 Overview of Death Valley Region Physiography and Hydrogeology

The proposed HLW repository at YM in southern Nevada lies within the Great Basin subprovince that is situated in the northern portion of the Basin and Range physiographic province. The Great Basin subprovince is characterized by north-trending mountain ranges separated by alluviated valleys that are topographically closed and internally drained except for the northeastern and southern portions of the subprovince where watersheds are tributary to the Snake and Colorado Rivers, respectively. Yucca Mountain lies in the southwestern portion of the Great Basin in a topographically distinct region known as the Walker Lane where mountain ranges trend northwest, roughly parallel to the Nevada-California border. According to Mifflin (1988), the Great Basin is divided into two hydrogeologically distinct provinces based on the permeability of the underlying consolidated rocks. The western half of the Great Basin is underlain by low-permeability rocks that constrain the groundwater flow regime to intra-basin flow within inter-montane valleys. The eastern and southwestern portions of the Great Basin, including the Death Valley region, are underlain by thick sequences of Paleozoic carbonates that in many areas provide hydraulic connection between structural basins. The Death Valley region as identified in Bedinger et al. (1989) covers an area of about 80,200 km^2 in southern Nevada and southeastern California.

As described by Bedinger et al. (1989), the major hydrogeologic units within the Death Valley region consist of Quaternary and late Tertiary basin fill deposits, tuff units, and lava flows of Tertiary age, and thick Paleozoic sedimentary rocks. The basin fill, which ranges in thickness from 1,300 to 2,000 m, consists of alluvial sediments including Paleozoic, Tertiary, and Quaternary detritus, and volcanic material of Tertiary age; volcanic flows and ash falls from the Tertiary and Quaternary Periods; and evaporites and lacustrine deposits. The volcanic units, which have a composite thickness of over 4,000 m, can be subdivided on the basis of their hydrologic characteristics into ash-flow tuffs, lava flows, and undifferentiated volcanic rocks (Bedinger et al., 1989). The upper Precambrian and Paleozoic sedimentary rocks, which are over 8,000 m thick, have been differentiated by Winograd and Thordarson (1975) from bottom to top into a lower clastic aquitard, a lower carbonate aquifer, an upper clastic aquitard, and an upper carbonate aquifer. According to Bedinger et al. (1989), the lower carbonate aquifer is much more areally extensive than the upper carbonate aquifer, and forms the primary hydraulic connection between topographically closed basins.

Many of the mountain ranges and valleys that characterize the western portion of the Basin and Range define closed topographic basins that are coincident with closed groundwater flow systems. However, the Death Valley region lies in the carbonate rock province where many of the topographically closed basins are hydraulically connected. Bedinger et al. (1989) divided the Death Valley region into nine hydrogeologic subbasins or groundwater units (Figure 11-1). The presence of wet, discharging playas indicate that three of these units, DV-02, which contains the Mesquite Valley at the southern end of Pahrump Valley, DV-04, which contains Panamint Valley, and DV-09, which contains the southern end of Big Smoky Valley, are closed groundwater basins coincident with topographically closed basins. The presence of regional springs, absence of discharging playas, and great depths to water indicate that the remaining six groundwater units are composed of two or more hydraulically connected, closed topographic basins. The largest of these six units is DV-03, which lies in the central portion of the Death Valley region containing YM. Waddell et al. (1984) subdivided a region approximately coincident with

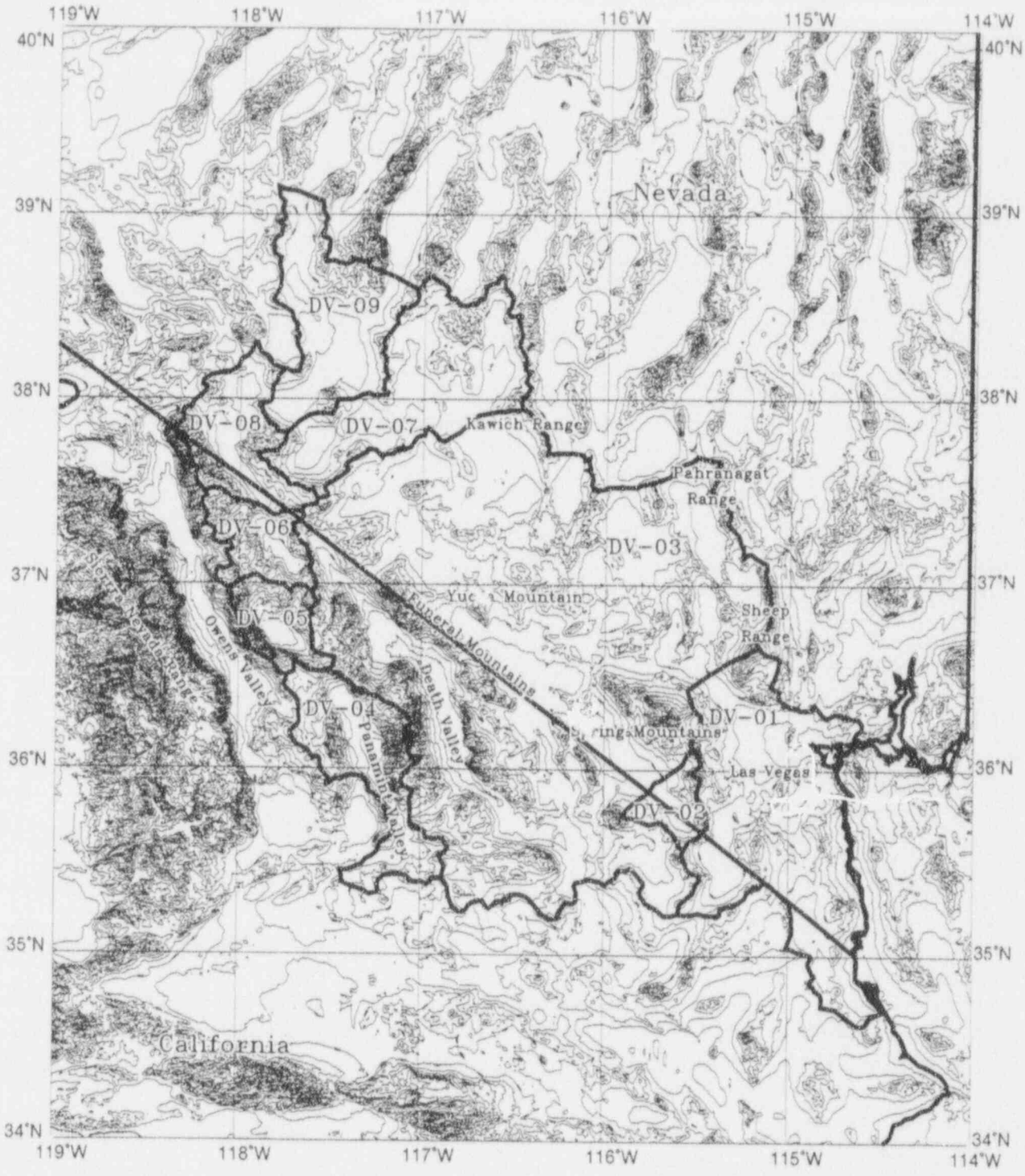

Figure 11-1. Death Valley region location map

the middle one-third of unit DV-03 into the Oasis Valley subbasin, the Ash Meadows subbasin, and the Alkali Flat-Furnace Creek subbasin, each of which is defined on the basis of a readily identifiable recharge area connected by flow paths to a discharge area. The Oasis Valley and Ash Meadows subbasins are tributary to the Alkali Flat-Furnace Creek subbasin, which in turn discharges into Death Valley.

Interbasin movement of groundwater is largely controlled by the complex deformed structure of the lower carbonate aquifer system and the lower clastic aquitard. Winograd and Thordarson (1968) suggest that while the faults and folds that typify the Death Valley region tend to fracture the lower carbonate unit and greatly increase its transmissivity, the juxtaposition of the low-permeability clastic units against the carbonate unit caused by faulting and folding may effect extensive flow barriers. These hydraulic barriers cause water levels in adjacent valleys to differ by as much as 600 m and in the carbonate units within a valley by as much as 150 m (Winograd and Thordarson, 1975). Near the Nevada Test Site (NTS) transmissivities in the fractured carbonate aquifer range from 1.5×10^{-5} to 0.15 m^2/s, while the transmissivity of the fractured clastic unit is generally less than 1.5×10^{-5} m^2/s (Winograd and Thordarson, 1968). Low transmissivity of the deformed clastic units is attributed to the tendency of the argillaceous rocks to deform plastically rather than fracture. In addition, clastic units that fracture when deformed are resistant to chemical dissolution that would enhance fracture permeability. Additional evidence for the low transmissivity of the clastic unit is the absence of high-yield springs where the unit crops out in the northwestern Spring Mountains (Winograd and Thordarson, 1968).

11.2.2 Literature Review of Basin Hydrologic Studies

The inability of hydrologists to balance measured discharge with reasonable estimates of recharge within topographically closed structural basins in the southern and southeastern portion of the Great Basin lead them to conclude that the basins discharge water to the underlying Paleozoic carbonate aquifer (Mifflin, 1988). Indirect evidence for the drainage of water from the alluvial fill to the Paleozoic carbonate aquifer, that hydraulically connects the basins, is the great depths to water measured in certain topographically closed basins. This establishes a need to consider the fluxes of water in a larger region, a region that can be considered hydrologically closed for both surface and subsurface fluxes. For regional water budgets, positive and negative fluxes are referred to as recharge and discharge, respectively, and the hydraulic conduits that connect recharge and discharge areas are referred to as flow paths.

11.2.2.1 Recharge Estimates

The climate of the Death Valley region is arid to semiarid with average annual precipitation ranging from 50 mm at Furnace Creek, to 500 to 700 mm in the Sheep and Spring Mountains. Estimates of annual potential evaporation range from 600 mm in the higher mountain terrain (Mifflin, 1988) to over 2,500 mm in Death Valley (Bedinger et al., 1989). Due to this large moisture deficit, little recharge by direct infiltration of precipitation is believed to occur in the lower valley floors. Because annual precipitation in the region generally increases with altitude, altitude may be expected to control the spatial variation of recharge in the Death Valley region. Walker and Eakin (1963) and Eakin (1966) postulated that the percentage of precipitation that recharges the groundwater system also increases with altitude, and formulated a simple relationship to estimate this percentage. Malmberg (1967) employed this approach to estimate recharge to Pahrump Valley. However, Mifflin (1968) rejected this approach and concluded for the development of groundwater budgets that "annual precipitation ... in some areas may have no relationship to recharge." Mifflin argues that the presence of exposed fractures or thin alluvial cover may enable water to bypass the root zone. Regions where the alluvial cover is uniformly thick may

limit recharge by preventing rapid downward water movement through highly-conductive pathways. As potential evapotranspiration in the region greatly exceeds precipitation, water prevented from deep percolation can generally be expected to evaporate. If recharge is indeed dependent on altitude, it may be due to the decreased thickness or absence of soils and alluvial cover on steep slopes at higher elevations. The effect of local vegetal cover on evapotranspiration also strongly affects recharge. Such local controls on recharge need not be precipitation- or altitude-dependent in the simple way postulated by Eakin (1966).

The absence of hydraulic data that may be used to directly estimate recharge or to clearly establish a relationship between precipitation and recharge makes the use of geochemical information indispensable. Feeney et al. (1987) calibrated a discrete state compartmental model of the western NTS and vicinity using measured deuterium data, and inferred that Fortymile Canyon wash and Pahute Mesa were major recharge areas. Sadler et al. (1992) used a discrete state compartmental model that had been calibrated to deuterium data to infer that Stockade Wash, which drains the southern flank of Rainier Mesa and the southeastern portion of Pahute Mesa, is an important recharge area. Using techniques similar to Feeney et al. (1987), Kirk and Campana (1988) inferred recharge from the Sheep Range to Coyote Spring Valley.

In order to model the recharge process, it is necessary to account for the saturated and unsaturated hydraulic properties of alluvial cover, the rock matrix and fractures, as well as the magnitude of near-surface sources and sinks. Once the upper surface has been partially wetted by infiltrating rain or melt water, gravity becomes the primary force that drives water down to the saturated zone. The unit magnitude of the vertical hydraulic gradient, along with the moisture dependence of hydraulic conductivity, exacerbates the effects of soil and rock heterogeneity, and may cause water to infiltrate rapidly through highly conductive pathways. If rapid infiltration through preferential pathways prevents water from being evaporated and thus controls recharge, flux boundary conditions imposed in a saturated zone regional model to account for areal recharge must incorporate the effects of the alluvial cover and rock fractures. Focused recharge to the local water table aquifer may also occur when storm runoff is captured by large fissures in playa lakes.

11.2.2.2 Discharge Estimates

Discharge in the Death Valley region occurs by evaporation from springs and shallow water tables and by phreatophyte transpiration. To estimate the response of the water table to changes in recharge, discharge locations and rates and their relationship to hydrogeologic and climatic controls must be determined. The presence of fossil spring deposits located above the present water table suggests that discharge has exceeded recharge since the disappearance of the pluvial lakes at the end of the late Wisconsin stade. Unlike recharge that may be readily, if crudely, estimated using the Eakin (1966) formula, discharge is best obtained by direct measurement.

Discharge rates as high as 36 to 110 cm/yr have been measured by Czarnecki (1990) at Franklin Lake Playa, that was found to control the water table depth beneath YM in a modeling study by Czarnecki and Waddell (1984). By comparison, the mean annual precipitation at YM is less than 20 cm, and estimates of unsaturated zone vertical fluxes through YM are on the order of 0.1 cm/yr (Montazer and Wilson, 1984). Because the potential evapotranspiration is so great, the quantity of discharged water that is either evaporated or transpired is wholly controlled by the capacity of the aquifer to supply water.

Increased precipitation resulting in increased recharge would tend to force the water table up. However, if discharge is directly controlled by the amount of water the system can supply to springs and shallow water tables, increased discharge resulting from increased recharge may counteract any major rise in the water table. Changes in precipitation also can be expected to be accompanied by inverse changes in potential evapotranspiration, and would have an effect on water table depth. The inverse relationship between discharge and water table depth postulated by Czarnecki (1990) may provide a mechanism that dampens the amplitude of water table movement from fluctuations in rainfall. The speed at which water can move from recharge locations to discharge locations and the nature of discharge are the key elements in the response of the water table to changes in recharge.

The energy-budget eddy-correlation technique (Campbell, 1977) was used by Czarnecki (1990) to estimate evapotranspiration rates at Franklin Lake Playa. Empirical relations for estimating evapotranspiration are unreliable unless they are developed specifically for the regions in which they are to be used. Empirical formulae developed by Ivanov (1954), Papadakis (1966), Doorenbos and Pruitt (1974), Turc (1961), Behnke and Maxey (1969) and Linacre (1969) were found by Czarnecki (1990) to overestimate evapotranspiration by more than 100 percent at Franklin Lake playa. Development of empirical relations for the Death Valley region will require additional studies like that by Czarnecki (1990) be conducted at discharge locations throughout the region. Extrapolation of the empirical relations to infer discharge in a possibly different climate may be supported by an understanding of their physical basis.

Using deuterium data to calibrate a discrete state compartmental model, Feeney et al. (1987) found Oasis Valley and Amargosa Desert to be major discharge areas. Young (1972) inferred the Amargosa Valley in California (to the southwest of YM) to be a major discharge area. Sarcobatus Flat to the northwest of YM and Pahrump Valley, which is southwest of the Spring Mountains, are the other major discharge areas. The ultimate discharge point for most of the region lies within Death Valley where numerous seeps and springs discharge along a line that parallels the Amargosa River in Badwater Basin.

11.2.2.3 Regional Flow Paths

Regional groundwater flow paths are defined by hydraulic connections between recharge and discharge areas. The elevation of the Death Valley region decreases from the northeast to the southwest and appears to control the regional flow direction. Local structural and topographic features may induce complex circulation patterns that are superimposed on the regional flow regime within the areally extensive Paleozoic carbonate aquifer. Regional flow paths inferred from various sources referenced here are shown in Figure 11-2.

If the carbonate aquifer provides an important conduit for water from recharge to discharge zones, then the impact of increased recharge on the water table depth will be determined by the transmissivity of the carbonate. However, the paucity of deep hydraulic conductivity or head data makes these determinations difficult. Near-surface movements of groundwater can be relatively easily related to the nature of recharge and discharge. However, its linkage with the deep Paleozoic carbonate may be difficult to explore because so few boreholes penetrate the carbonate system.

Evaluation of the chemistry of water provides an invaluable tool in assessing directions of groundwater movement. Mifflin (1968) interprets groundwater temperature to infer depth of circulation and recognize interbasin flow. The water chemistry, water temperature, variation in discharge, tritium concentrations, and ^{14}C measurements of springs in the carbonate rock province of Nevada are used to

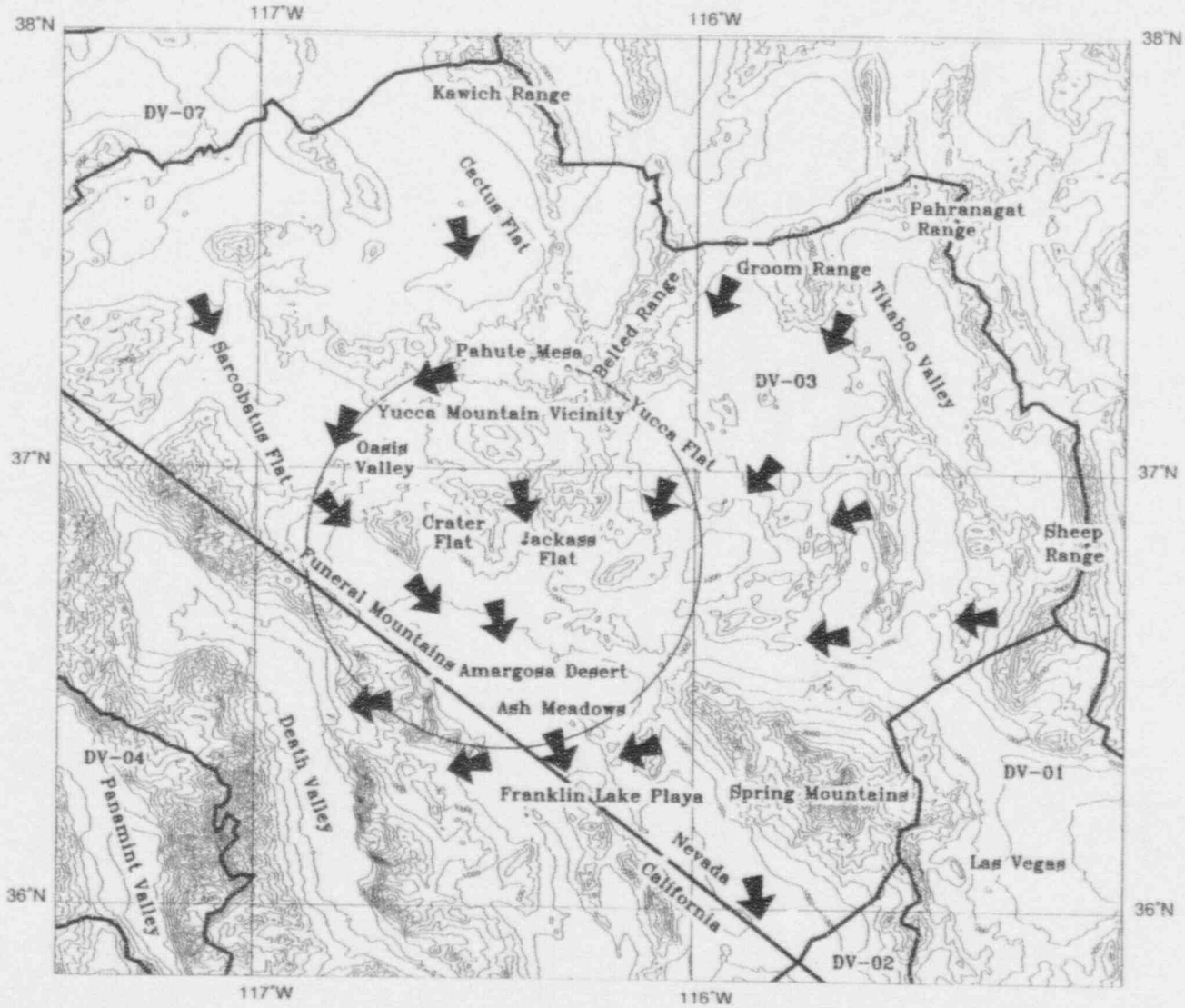

Figure 11-2. Regional flow of groundwater in the Death Valley system. Arrows indicate general direction of regional flow. Circle centered on Yucca Mountain has a radius of 50 km. Heavy black lines indicate boundaries of Death Valley subbasins (i.e., DV-01) identified by Bedinger et al. (1989). Contour interval is 200 m.

delineate flow systems by Mifflin. Kirk and Campana (1988) infer westward underflow along the Pahranagat shear zone by analyzing deuterium isotope data. They also estimate the storage in the carbonate portion of the White River flow system, a regional carbonate/alluvial groundwater system in southeastern Nevada. Lyles and Hess (1988) used stable isotope measurements and major ion chemistry to infer mixing of water from the Spring Mountains with the regional carbonate groundwater along the Las Vegas shear zone.

Although the regional hydrogeology of this region has been extensively studied, the regional flow patterns are still not well understood and no single conceptual model of the flow system has been universally accepted. Czarnecki (1989) has suggested that the apparent hydraulic connection between the Amargosa Desert and Furnace Creek identified by Winograd and Thordarson (1975) may be through a deep, confined portion of the Paleozoic carbonate aquifer beneath the Funeral Mountains. However, based on an inferred potentiometric high in the Greenwater Range, Czarnecki (1989) also postulates that no such hydraulic connection exists and discharge at Furnace Creek may be solely derived from local recharge in the Greenwater Range and possibly the Funeral Mountains. Czarnecki (1989) argues that if Furnace Creek Wash–Nevares Springs is a discharge point of the regional flow system containing YM, then flow of groundwater beneath YM may be quite large.

11.2.3 A Summary of Chemical Constraints on Regional Hydrology

Hydrologists studying groundwater flow in the region around YM have used chemical characteristics of the water in four general applications. First, hydrochemical facies have been identified to categorize waters according to major chemical composition. Waters of the same facies generally have similar origins and histories in terms of flow and water-rock interactions. Second, chemical and isotopic mass balance relations have been used to identify mixtures of waters from different sources. Third, relations between recharge areas, flow paths, and discharge areas have been identified on the basis of chemical and isotopic similarities and systematic variations in water chemistry combined with analyses of water potential gradients. And fourth, the ages of groundwaters have been evaluated using radioisotope techniques and temporal variations in the isotopic composition of rainfall. Chemical analyses of minerals precipitated from groundwater also provide important constraints on groundwater flow. In this section, a summary is given of major findings reported in selected publications concerning chemical constraints on the hydrology of the YM region.

11.2.3.1 Hydrochemical Facies

Winograd and Thordarson (1975) defined five hydrochemical facies in the south-central Great Basin and presented summaries of their major component chemistry and their regional distributions (Table 11-1). Groundwater chemistry in the region is primarily controlled by interactions with one or both of the two dominant rock types. Interactions with marine carbonate rocks generate waters characterized by calcium and magnesium bicarbonate (and aqueous silica). Interactions with silicic volcanic rocks produce waters dominated by sodium and potassium bicarbonate. A mixed facies results from commingling of waters from these two primary facies or by interactions of water with both rock types either sequentially along flow paths or where the rock types coexist in alluvium. In areas where water discharges and there is extensive evaporation (e.g., playas), water chemistry becomes relatively concentrated in sodium, potassium, bicarbonate, and chloride. The fifth facies is dominated by sodium, sulfate, and bicarbonate.

Table 11-1. Hydrochemical facies of the Yucca Mountain region (Winograd and Thordarson, 1975)

Facies	Main Occurrences	Associated Rock Types
Calcium magnesium bicarbonate	Southern Indian Springs Valley Southern Three Lakes Valley Northwestern Las Vegas Valley Pahrump Valley Spring Mountains Pahranagat Valley Springs	Lower carbonate aquifer Carbonate-rock valley fill Carbonate-rock springs
Sodium potassium bicarbonate	Western Emigrant Valley Yucca Flat Frenchman Flat Jackass Flats Pahute Mesa Oasis Valley	Tuff Rhyolite Volcanic-rock valley fill
Calcium magnesium Sodium bicarbonate	Ash Meadows Eastern NTS	Mixed carbonates and volcanics
Playa	Wet (discharging) playas	—
Sodium sulfate bicarbonate	Furnace Creek Wash Nevares Springs	—

11.2.3.2 Flow Paths and Groundwater Mixing

Qualitative identification (or speculation) of mixing of waters from different facies is commonly based on occurrences of characteristic chemical species. For example, in the YM region Winograd and Thordarson (1975) postulate that excess sodium and sulfate in the calcium magnesium sodium bicarbonate facies is derived from Tertiary tuff aquifers and aquitards. Excess sodium within the lower carbonate aquifer water beneath the NTS has been interpreted to be a consequence of cross flow through tuffaceous rocks, or importation from the northeast, for example, from Pahranagat Valley. Speculative quantitative mass balance relations for this system, mixing a hypothetical water from the tuff aquitard with characteristic carbonate aquifer water, indicate that leakage from the tuff may account for only a few percent to perhaps 20 percent of the discharge at Ash Meadows (Winograd and Thordarson, 1975).

Waters from Pahrump Valley originate from recharge into carbonate rocks that crop out in the Spring Mountains and are typical of the calcium magnesium bicarbonate facies (Winograd and Thordarson, 1975). Pahrump Valley waters contain less sodium and sulfate than waters discharging at Ash Meadows, so significant flow from Pahrump Valley north to springs in Ash Meadows is unlikely (Winograd and Thordarson, 1975). Water from Indian Springs Valley, Three Lakes Valley, and northwest

Las Vegas Valley has lower sodium, potassium, sulfate, and chloride concentrations than water from the NTS and Ash Meadows, indicating that water does not flow eastward from the NTS (Winograd and Thordarson, 1975).

Diverse water chemistries in the valley fill of the Amargosa Desert indicate diverse sources (Winograd and Thordarson, 1975). Calcium magnesium sodium bicarbonate water probably leaks from the east through the hydrologic barrier responsible for springs in Ash Meadows. Sodium potassium bicarbonate facies waters are probably derived from tuffaceous aquifers in western Jackass Flats. Low dissolved salt contents of waters in Fortymile Wash may reflect local infiltration along the arroyo bed and little westward flow in the vicinity of Lathrop Wells (Winograd and Thordarson, 1975).

Claassen (1985) has also used water chemistry data to evaluate the hydrologic system of the southern Amargosa Desert area with an emphasis on flow in the valley fill aquifers. In the valley fill, a positive correlation exists between coarse grained, permeable material, and low-dissolved solids. Major dissolved species concentrations follow a pattern of low values in a trough that generally parallels the eastern distributary of Fortymile Canyon in the area west and south of Lathrop Wells. Water in this low-salinity trough is concluded to be derived from recharge along surface drainages (Winograd and Thordarson, 1975; Claassen, 1985).

Heterogeneity in water chemistry and one high ^{14}C value suggest that water east of the intersection of the Gravity Fault and the Specter Range Thrust Fault is a variable mixture of upwelling carbonate aquifer water and recharging valley fill water (Claassen, 1985). Aspects of water chemistry that characterize the recharge component include elevated sodium, potassium, chloride, and sulfate. A potentiometric high west of the fault intersection is interpreted to be due to upward leakage from the carbonate aquifer. Temperature in the carbonate aquifer and in wells in the area of suspected upwelling is about 30 °C. In contrast, temperature in the valley fill aquifer at about the same depth, but remote from the site of postulated upwelling, is about 20 °C, which is a further indication of upwelling (Claassen, 1985).

Chemical and isotopic data have been used by Claassen (1985) to derive major conclusions regarding the amount and mechanisms of recharge to the Amargosa Valley and Fortymile Canyon alluvial aquifers. The chloride and sulfate content of Fortymile Canyon valley-fill aquifer water correspond to the concentrations in precipitation increased by a factor of about 25. In contrast, in the Amargosa River drainage, the concentration factor is about 100 in the lower valley and 200 in the upper valley. These data suggest that a significantly greater fraction of precipitation recharges in Fortymile Canyon than in the Amargosa River Valley. This result is consistent with the more confined channel and coarser, more permeable sediments in Fortymile Canyon (Claassen, 1985).

Claassen (1985) further elucidated recharge mechanisms through an examination of stable hydrogen and oxygen isotope data. A linear positive correlation exists between δD and $\delta^{18}O$ for precipitation in Colorado and Nevada that corresponds closely to the global meteoric relation. Valley fill groundwaters from Amargosa River, Fortymile Canyon, and Oasis Valley have heavier oxygen than water of the meteoric trend. Heavier oxygen suggests that recharging water underwent evaporative isotopic fractionation (Claassen, 1985) or recharge under different paleoclimatic conditions (White and Chuma, 1987). The general oxygen and hydrogen isotopic similarity of the Amargosa River and Fortymile Canyon valley-fill aquifer waters [$\delta D = -97$ to -108 and $\delta^{18}O = -12$ to -14 per mil relative to Standard Mean Ocean Water (SMOW)] indicates similar recharge mechanisms. However, the salinity differences noted above indicate much more evaporation of the Amargosa Valley water. A resolution of this apparent

paradox suggested by Claassen (1985) is that the increased salinity in the Amargosa Valley waters is due to complete evaporation of most precipitation, and then intermittent redissolution of residual salts in water that recharges following limited evaporation. Complete evaporation of precipitation would convey an insignificant oxygen and hydrogen isotope effect to the recharging water.

White and Chuma (1987) and Stuckless and Whelan (1991) summarize and interpret pCO_2, ^{14}C, and stable hydrogen, oxygen, and carbon isotope data for water from the Oasis Valley and Fortymile Canyon groundwater basins. The isotopically lightest hydrogen and oxygen occur in waters from Pahute Mesa and at the head of Oasis Valley indicating flow from under Pahute Mesa to Oasis Valley. For example, Pahute Mesa water has $\delta^{18}O$ from -14.05 to -14.75, whereas Fortymile Canyon and upper Amargosa Desert area waters range from -12.8 to -13.4 relative to SMOW (White and Chuma, 1987). These data indicate the waters in Fortymile Canyon and upper Amargosa Desert are not derived from recharge at Pahute Mesa under climatic conditions similar to those at the time Pahute Mesa groundwaters were recharged (White and Chuma, 1987). Similarly, δD values for Pahute Mesa waters range from -109.5 to -114.0 (White and Chuma, 1987), and are lighter than waters from underneath YM, that range from -99.5 to -104.0 (Stuckless and Whelan, 1991). Going down the water potential gradient in the alluvial aquifer in Oasis Valley, the oxygen and hydrogen become isotopically heavier indicating mixing of heavier waters from the Bullfrog Hills to the west or evaporation (White and Chuma, 1987).

Carbon is a ubiquitous component of groundwater in this region and the complex controls on its abundance, oxidation state, and isotopic composition make it particularly valuable in interpreting groundwater flow. For example, generally lighter carbon (lower $\delta^{13}C$) to the north of YM and heavier carbon to the south could be a manifestation of increasing upward leakage from the carbonate aquifer toward the south (Stuckless and Whelan, 1991). Enhanced leakage could be due to structural or stratigraphic breaching of the confining basal unit of the volcanic rocks. Reaction of the tuffaceous aquifer waters with uplifted carbonate rocks or with calcite previously precipitated from carbonate aquifer water could also hypothetically account for the pattern of $\delta^{13}C$ values (Stuckless and Whelan, 1991).

Three features of the local geology could contribute to the observed variations in the carbon isotopic composition of the groundwater. First, the offset on north-south trending normal faults in this area increases markedly from north to south (Scott, 1990), which could increasingly juxtapose carbonate and tuffaceous rocks in the south leading to increased groundwater mixing. Second, the projected southern limit of the Paleozoic clastic aquitard formed by the Eleana Formation also forms an east-west transect underneath YM (Scott, 1990). South of this limit increasing upward flow from the carbonate aquifer may account for the heavier carbon isotopic composition. Third, YM is near the southern limit of volcanic rocks and their influence on water chemistry must diminish south of U.S. Highway 95.

Mass balance relations among carbon isotopes have been used by Stuckless and Whelan (1991) to speculate that waters from Fortymile Wash could be generated by mixing water from the UE29a#2 well in northern Fortymile Wash and Paleozoic aquifer water represented by UE25p#1. Other waters from the tuffaceous aquifer in the vicinity of YM have older ^{14}C apparent ages and may represent recharge of mixed ages (Stuckless and Whelan, 1991).

In the shallow alluvial aquifer in Oasis Valley the waters evolve along their flow path toward higher ^{14}C and pCO_2 and lower $\delta^{13}C$, and toward carbon system chemistry that is characteristic of soil water in Oasis Valley (White and Chuma, 1987). This evolution indicates progressive incorporation of modern ^{14}C, organically controlled isotopically light carbon, and CO_2 from the soil zone, that is, "open system soil CO_2 input" (White and Chuma, 1987). In contrast, in the tuffaceous aquifer of upper

Fortymile Canyon, ^{14}C and pCO_2 are higher and ^{13}C is lower than in down-gradient alluvial material. The interpretation of White and Chuma (1987) for the relations in Fortymile Canyon is that "the soil component is being depleted in the alluvium under closed system conditions."

11.2.3.3 Groundwater Ages

Uncorrected ^{14}C ages for water in tuff and tuffaceous valley fill indicate recharge between 10,000 and 15,000 yr ago, which corresponds to the cool period that ended at the start of the Holocene (Claassen, 1985). Waters are younger near modern drainage paths. No dates exceed 17,000 yr indicating either no recharge prior to that time, subsequent flow out of the system, or failure to sample the older water. Groundwaters may be significantly younger than indicated by uncorrected ^{14}C ages because of the introduction of old (^{14}C depleted) carbon, particularly through water-rock interactions.

Chemical data presented by Winograd and Pearson (1976) for springs and wells in the Ash Meadows Basin have been interpreted to indicate regional flow mechanisms and to suggest separate periods of recharge. Waters discharging along the Ash Meadows spring line have nearly identical bulk chemistries. They are interpreted to be composed of calcium magnesium bicarbonate waters from recharge areas in the Spring Mountains mixed with leakage of sodium bicarbonate (sulfate) waters from tuffaceous rocks overlying the carbonate aquifer. However, Crystal Pool has an anomalously high ^{14}C content (11.1 percent modern) relative to all others (average 2.35 percent modern). Following an examination of several hypotheses for the anomaly, the authors conclude that large-scale (e.g., greater than tens of km) lateral channeling of water to Crystal Pool is likely, and distinct ^{14}C contents may represent recharge during separate pluvial periods. A younger water following the large-scale channel path to Crystal Pool has flushed out older water that still discharges from other springs in Ash Meadows.

Hydrogen and oxygen isotope values from Oasis Valley and Fortymile Canyon waters fall on a trend parallel to the present meteoric water line (White and Chuma, 1987), that corresponds closely to the global meteoric line (Claassen, 1985). The parallel trend is unlikely to result from vadose zone evaporation and suggests recharge under cooler paleoclimatic conditions rather than under present conditions (White and Chuma, 1987).

11.2.3.4 Mineral Precipitates

Paces et al. (1993) present uranium and thorium isotopic data for two of three carbonate rich spring deposits in southern Crater Flat. These sites were interpreted to record discharge from an ancient regional groundwater flow system. Initial $^{234}U/^{238}U$ activity ratios near 3.0 indicate precipitation of the deposits from regional groundwater rather than a pedogenic origin (Paces et al., 1993). Three rhizoliths from the Crater Flat deposit were dated by the uranium series method at about 18.5 ± 1.4 ka. Carbonate nodules from progressively deeper portions of the Crater Flat deposit were dated at 30.0 ± 2.7 and 45.3 ± 3.6 ka. A poorly resolved but probably older date was obtained from a sample taken yet deeper in the Crater Flat deposit. A date from the Horse Tooth Deposit that lies to the south of the Crater Flat deposit yields a date of 45.7 ± 4.9 ka. This date is indistinguishable from one from the Crater Flat deposit and indicates simultaneous discharge at the two springs. The ages of the spring deposits correlate well with ages of high water stands in Browns Room of Devils Hole in Ash Meadows. The two dated spring deposits in lower Crater Flat are 79 to 85 m and 98 to 116 m above the present water table and indicate repeated groundwater table fluctuations to this level during the late Quaternary (Paces et al., 1993).

Winograd et al. (1992) present oxygen isotopic data for a 36-in core of calcite from Devils Hole that constitute a continuous record of climatic variation. Lower values of $\delta^{18}O$ in the precipitated calcite indicate lower temperatures of water at the time of recharge, and vice versa. Uranium series dating establishes that precipitation of the calcite was continuous from 560,000 to 60,000 yr bp at an average rate of 0.7 mm/1,000 yr. A major thrust of the paper is to note small discrepancies between the timing of temperature variations recorded at Devils Hole and the temporal pattern of glacial and interglacial stages derived from Milankovitch orbital oscillations. An auxiliary conclusion is that groundwater travel time to Devils Hole must be a fraction of 10,000 yr. Oxygen-18 fluctuations in the calcite on this time scale record variations in recharge temperatures that correspond closely to other paleoclimatic records. If groundwater travel times were greater than a few thousand years, then multiple recharge areas at variable distances, heterogeneity of the aquifer, and mixing and dispersion would have blurred this signal.

11.2.4 Overview of Death Valley Region Field Trip

The CNWRA and NRC technical staff conducted a three-day trip to the NTS, Oasis Valley, Amargosa Desert, and Death Valley to examine first-hand some of the major recharge and discharge areas in the region. Recharge areas examined during this trip were on the upland plateaus at NTS, Rainier Mesa, and Pahute Mesa. Discharge areas examined were at Ash Meadows, Death Valley, and Oasis Valley. In addition, paleo-discharge sites at the Horse Tooth Spring deposits and near Travertine Point in Furnace Creek Wash, Death Valley National Monument, were visited.

11.2.4.1 Recharge Areas

Rainier Mesa and Pahute Mesa are remnants of an eroded volcanic plateau that ranges in altitude from 1,800 to 2,300 m and receives over 32 cm/yr of precipitation (Jacobson et al., 1986). Rainier Mesa is composed of a series of welded, zeolitized, and friable tuffs of Miocene age that dip 10 to 25 degrees to the west and south (Russell et al., 1987). Water that infiltrates Rainier Mesa is presumed to travel through networks of fractures within the tuff units until it reaches the regional water table located in the Paleozoic carbonate aquifer 1070 m below the summit (Jacobson et al., 1986). An extensive network of tunnels and adits has been bored into the southeast side of Rainier Mesa at depths ranging from 240 to 700 m below the surface for underground nuclear testing. Water encountered during mining of the tunnels is derived from perched water zones that develop where fractures in the tuffaceous materials are poorly connected. When perched water zones are first encountered, flow rates into the tunnels may be quite large but usually decrease rapidly with time, suggesting that flow is initially derived directly from storage. Participants of the field trip were escorted by representatives of the Defense Nuclear Agency (DNA) into a section of N-tunnel in Rainier Mesa that intersects a fault zone discharging water at a rate of 4 to 10 l/m. Based on comparison of the δD and $\delta^{18}O$ composition of N-tunnel water with local precipitation, Russell et al. (1987) infer that the perched water body is of meteoric origin and receives recharge primarily during winter. According to Russell et al. (1987), "the groundwater regime in Rainier Mesa is characterized by rapid fracture flow in the upper welded formations, slower interstitial flow through the [underlying] friable tuffs...and slow fracture flow through the aquitard created by the highly zeolitized [tuffs]." White et al. (1980) have shown that fracture water and interstitial (pore) water above the water table at Rainier Mesa have different chemistries indicating separate although related origins.

Pahute Mesa constitutes the primary watershed for Fortymile Canyon Wash, Stockade Wash, and the Amargosa River, and lies to the north and northwest of Rainier Mesa. As part of the

environmental restoration program conducted at NTS, the Desert Research Institute (DRI) has developed an experimental recharge facility at Dead Horse Flat in the north central portion of Pahute Mesa. Field trip participants were given a briefing on the automated meteorologic station and soil moisture measuring equipment installed to correlate precipitation events with infiltration. Soil moisture measuring equipment consist of a vertical array of horizontally emplaced time-domain reflectrometry probes installed at depths up to 90 cm. As noted in Section 11.2.3.2, oxygen and hydrogen isotope data indicate that groundwater underneath Pahute Mesa flows toward Oasis Valley rather than toward YM and Fortymile Canyon.

11.2.4.2 Discharge Areas

Discharge along the Ash Meadows Spring line is conveyed from the Paleozoic carbonate aquifer to the surface along a buried fault. Total spring discharge at Ash Meadows exceeds 0.63 m^3/s, 72 percent of which is derived from Crystal Pool, Fairbanks Spring, Big Spring, Longstreet Spring, and Rogers Spring that discharge through the valley fill aquifer (Winograd and Thordarson, 1975). Point of Rocks Spring and Devils Hole, which discharge directly from the lower carbonate aquifer, were also inspected during the field trip.

According to Winograd and Thordarson (1975), groundwater from Pahute Mesa and Timber Mountain predominantly moves southwestward through Tertiary tuff units to discharge areas in Oasis Valley. Waddell et al. (1984) state that spring discharge at Oasis Valley is controlled by the presence of low-permeability rocks down the hydrologic gradient from Beatty, Nevada. Although total spring discharge throughout Oasis Valley is estimated to be only 0.078 m^3/s (Malmberg and Eakin, 1962), field trip participants were readily able to identify discharge areas by the presence of phreatophytes.

Waddell et al. (1984) suggest that Franklin Lake Playa (Alkali Flat) and Death Valley are the primary discharge points for the Alkali Flat–Furnace Creek Ranch subbasin. Water discharges near Furnace Creek Ranch in Death Valley through springs located several hundred meters above the valley floor (Waddell et al., 1984). The major springs in the Furnace Creek area, Travertine Spring, Texas Spring, and Nevares Spring, discharge approximately 0.16 m^3/s from the lower carbonate aquifer through overlying Quaternary gravel deposits. This discharge is sufficient to supply irrigation water to orchards of date palms at Furnace Creek.

The Horse Tooth paleo-spring deposits are located south of Crater Flat approximately 5 km east of the intersection of Steve's Pass road and U.S. Highway 95 at an approximate elevation of 800 m. According to Paces et al. (1993), these deposits are composed of "[w]ell-cemented, fine-grained nodular carbonate with, porous vuggy structure," and "[contain] only a small ... amount of fine-grained, well-sorted detritus." Age dating of these spring deposits and implications for the height of past water table fluctuations are discussed in Section 11.2.3.4.

Travertine Point is located approximately 25 km west of Death Valley Junction on California State Route 190 that follows the valley between the Funeral Mountains and the Greenwater Range and the westward reach of Furnace Creek Wash. Several hundred meters above the road, on the north wall of the canyon, there are vertical fracture zones tens of meters in length that have been infilled with mineral deposits believed to be derived from upwelling waters from the carbonate units in the Funeral Mountains. An easily accessible set of vertical fracture zones several meters in length, filled with travertine composed of calcite with thin bands of hematite, is located within 50 m of the road. Presence of these deposits indicates that water levels within the carbonate units in the Funeral Mountains were either much higher in the past or that significant uplift of the Funeral Mountain has occurred.

11.2.4.3 Summary of Field Trip

The knowledge of the regional physiographic, topographic, geologic, and hydrologic setting gained during this field trip has proved invaluable in reviewing existing flow models and in developing alternative conceptual flow models of the hydrogeologic regime. Although the major recharge areas in the Kawich, Groom, Pahranagat, Sheep, and Spring ranges were not visited, the nature of recharge at Rainier Mesa and Pahute Mesa is readily examined due to the extensive network of tunnels and boreholes constructed for weapons testing. Except for Franklin Lake Playa, all of the primary regional discharge areas for the Death Valley region were examined. Future field trips are planned to increase understanding of the relationship between local and regional flow systems.

11.3 SUMMARY AND ASSESSMENT OF PROGRESS

Review of the extensive body of technical literature outlining the hydraulic and hydrochemical information that has been used to construct conceptual models of the hydrogeology of the Death Valley region is progressing well. However, in order to concentrate on determining forces external to the flow system that may induce the water table to rise beneath YM, the current review has focused on defining recharge areas, discharge areas, and connecting flow paths. Literature surveys of geologic structures that control local and regional hydraulic gradients, such as the steep gradients north of YM and between Emigrant Valley and Yucca Flat, will be emphasized in future work. Isotopic data from spring deposits indicate that the water table in the past has fluctuated above current levels. It is hypothesized that water table fluctuations due to changes in recharge may be buffered by discharge at Franklin Lake Playa and/or Crater Flat. Whether or not this postulated buffering action is sufficient to preclude the water table from rising as high as the repository block during an extended period of substantially increased recharge will be addressed with predictive models to be developed.

11.4 PLANS FOR NEXT REPORTING PERIOD

During the next reporting period, the literature review will continue with increased focus on stratigraphic and structural control of the regional flow regime. Water level, hydrochemical facies, and hydrogeologic data are being entered into the ARC/INFO database and maps will be prepared to assist in the development of alternative conceptual models. Development of a three-dimensional hydrostratigraphic description of the Death Valley region will also be initiated. These alternative conceptual models of the hydrogeology will be designed to address key technical questions affecting the proposed repository such as: (i) structural features that may explain steep groundwater gradients, (ii) the effect of discharge zones such as Franklin Lake Playa on moderating the fluctuations of the water table due to increased recharge, and (iii) groundwater travel time.

11.5 REFERENCES

Bedinger, M.S., K.A. Sargent, and W.H. Langer. 1989. *Studies of Geology and Hydrology in the Basin and Range Province, Southwestern United States, for Isolation of High-Level Radioactive Waste—Characterization of the Death Valley Region, Nevada, and California*. U.S. Geological Survey Professional Paper 1370-F. Washington, DC: U.S. Geological Survey.

Behnke, J.J. and G.B. Maxey. 1969. An empirical formula for estimating monthly potential evapotranspiration in Nevada. *Journal of Hydrology* 8(4): 418–430.

Campbell, G.S. 1977. *An Introduction to Environmental Biophysics*. New York, NY: Springer Verlag.

Claassen, H.C. 1985. *Sources and Mechanisms of Recharge for Ground Water in the West-Central Amargosa Desert, Nevada—A Geochemical Interpretation*. U.S. Geological Survey Professional Paper 712-F. Washington, DC: U.S. Geological Survey.

Czarnecki, J.B. 1989. Characterization of the subregional ground-water flow system at Yucca Mountain and vicinity, Nevada-California. *Radioactive Waste Management and the Nuclear Fuel Cycle*. Harwood Academic Publishers 13(1-4): 51–61.

Czarnecki, J.B. 1990. *Geohydrology and Evapotranspiration at Franklin Lake Playa, Inyo County, California*. Open File Report 90-356. Washington, DC: U.S. Geological Survey.

Czarnecki, J.B., and R.K. Waddell. 1984. *Finite Element Simulation of Groundwater Flow in the Vicinity of Yucca Mountain, Nevada-California*. U.S. Geological Survey Water-Resources Investigations report 84-4349. Washington, DC: U.S. Geological Survey.

Doorenbos, J., and W.O. Pruitt. 1974. *Guidelines for Prediction of Crop Water Requirements*. Irrigation and Drainage Paper No. 4. Rome, Italy: Food and Agriculture Organization of the United Nations.

Eakin, T.E. 1966. A regional interbasin groundwater system in the White River area, Southeastern Nevada. *Water Resources Research* 2(2): 251–271.

Feeney, T.A., M.E. Campana, and R.L. Jacobson. 1987. *A Deuterium-Calibrated Groundwater Flow Model of the Western Nevada Test Site and Vicinity*. Publication #45057. Reno, NV: Desert Research Institute.

Hess, J.W., and M.D. Mifflin. 1978. *A Feasibility Study of Water Production from Deep Carbonate Aquifers in Nevada*. Publication 41054. Reno, NV: Desert Research Institute.

Hunt, C.B., T.W. Robinson, W.A. Bowles, and A.L. Washburn. 1966. *Hydrologic Basin Death Valley California*. Geological Survey Professional Paper 494-B. Washington, DC: U.S. Government Printing Office.

Ivanov, N.N. 1954. The determination of potential evapotranspiration. *Izvestiia Vsesoiuznogo Geograficheskogo Obschestva* 86(2).

Jacobson, R.L., M.S. Henne, and J.W. Hess. 1986. *A Reconnaissance Investigation of Hydrogeochemistry and Hydrology of Rainier Mesa*. DRI Publication No. 45046. Reno, NV: Desert Research Institute.

Kirk, S.T., and M.E. Campana. 1988. *Simulation of Groundwater Flow in a Regional Carbonate-Alluvial System with Sparse Data: The White River Flow System, Southeastern Nevada*. Publication 51115. Reno, NV: Desert Research Institute.

Linacre, E.T. 1969. Climate and evaporation from crops. *Journal of the Irrigation and Drainage Division, American Society of Civil Engineers* 95: 348–352.

Lyles, F.B., and J.W. Hess. 1988. *Isotope and Ion Geochemistry in the Vicinity of the Las Vegas Valley Shear Zone*. Publication 41111. Reno, NV: Desert Research Institute.

Malmberg, G.T. 1967. *Hydrology of the Valley-Fill and Carbonate-Rock reservoirs, Pahrump Valley Nevada-California*. Geological Survey Water-Supply Paper 1832. Washington, DC: U.S. Geological Survey.

Malmberg, G.T., and T.E. Eakin. 1962. Ground-water appraisal of Sarcobatus Flat and Oasis Valley, Nye and Esmeralda Counties, Nevada. *Ground-Water Resources Reconnaissance Series Report*. Carson City, NV: Nevada Department of Conservation and Natural Resources: 10.

Mifflin, M.D. 1968. *Delineation of Groundwater Flow Systems in Nevada*. Publication 42004. Reno, NV: Desert Research Institute.

Mifflin, M.D. 1988. *Region 5, Great Basin. Hydrogeology*. Boulder, CO: The Geological Society of America, Inc. O-2: 69–78.

Montazer, P., and W.E. Wilson. 1984. *Conceptual Hydrologic Model of Flow in the Unsaturated Zone, Yucca Mountain, Nevada*. Water Resources Investigations Report 84-4345. Denver, CO: U.S. Geological Survey.

Paces, J.B., E.M. Taylor, and C. Bush. 1993. Late Quaternary history and uranium isotopic compositions of ground water discharge deposits, Crater Flat, Nevada. *Proceedings Fourth International High-Level Radioactive Waste Management Conference*. LaGrange Park, IL: American Nuclear Society: 1,573–1,580.

Papadakis, J. 1966. *Climates of the World and their Agricultural Potentialities*. Buenos Aires, Argentina.

Russell, C.E., J.W. Hess, and S.W. Tyler. 1987. *Hydrogeologic Investigations of Flow in Fractured Tuffs, Rainier Mesa, Nevada Test Site: Flow and Transport Through Unsaturated Fractured Rock*. Geophysical Monograph 42. Washington, DC: American Geophysical Union: 43–50.

Sadler, W.R., M.E. Campana, R.L. Jacobson, and N.L. Ingraham. 1992. *A Deuterium-Calibrated Discrete-State Compartment Model of Regional Groundwater Flow, Nevada Test Site and Vicinity*. Publication 45088. Reno, NV: Desert Research Institute.

Scott, R.B. 1990. *Tectonic Setting of Yucca Mountain, Southwest Nevada. Basin and Range Extensional Tectonics Near the Latitude of Las Vegas, Nevada*. B.P. Wernicke, ed. Geological Society of America Memoir 176. Boulder, CO: Geological Society of America.

Stuckless, J.S., and J.F. Whelan. 1991. Isotopic discontinuities in ground water beneath Yucca Mountain, Nevada. *Proceedings of Second International High-Level Radioactive Waste Conference*. La Grange Park, IL: American Nuclear Society: 1,410–1,415.

Turc, L. 1961. Evaluation des besoins en eau d'irrigation, evapotranspiration potentielle, formule climatique simplifice et mise a jour. *Annales Agronomique* 12(1): 13–49.

Waddell, R.K., J.H. Robison, and R.K. Blankenagel. 1984. *Hydrology of Yucca Mountain and Vicinity, Nevada-California, Investigative Results through Mid-1983*. Water Resources Investigations Report 84-4267. Denver, CO: U.S. Geological Survey.

Walker, G.E., and T.E. Eakin. 1963. *Geology and Groundwater of Amargosa Desert, Nevada-California*. Carson City, NV: State of Nevada Department of Conservation and Natural Resources.

White, A.F., and N.J. Chuma. 1987. Carbon and isotopic mass balance models of Oasis Valley-Forty Mile Canyon groundwater basin, Southern Nevada. *Water Resources Research* 23: 571–582.

White, A.F., H.C. Claassen, and L.V. Benson. 1980. *The Effect of Dissolution of Volcanic Glass on the Water Chemistry in a Tuffaceous Aquifer, Rainier Mesa, Nevada*. Geological Survey Water-Supply Paper 1535-Q. Washington, DC: U.S. Government Printing Office.

Winograd, I.J., and F.J. Pearson, Jr. 1976. Major carbon 14 anomaly in a regional carbonate aquifer: Possible evidence for megascale channeling, South Central Great Basin. *Water Resources Research* 12: 1125–1143.

Winograd, I.J., and W. Thordarson. 1968. *Structural Control of Ground-Water Movement in Miogeosynclinal Rocks of South-Central Nevada. Studies of Geology and Hydrology*. E.B. Eckel, ed. Geological Society of America Memoir 110. Boulder, CO: Geological Society of America.

Winograd, I.J., and I. Friedman. 1972. *Deuterium as a Tracer of Regional Ground-Water Flow, Southern Great Basin, Nevada and California*. Geological Society of America Bulletin 83(2). Boulder, CO: Geological Society of America.

Winograd, I.J., and W. Thordarson. 1975. *Hydrogeologic and Hydrochemical Framework, South-Central Great Basin, Nevada-California, with Special Reference to the Nevada Test Site*. Geological Survey Professional Paper 712-C. Washington, DC: U.S. Government Printing Office.

Winograd, I.J., T.B. Coplen, J.M. Landwehr, A.C. Riggs, K.R. Ludwig, B.J. Szabo, P.T. Kolesar, and K.M. Revesz. 1992. Continuous 500,000-year climate record from vein calcite in Devils Hole, Nevada. *Science* 258: 255–260.

Young, R.A. 1972. *Water Supply for the Nuclear Rocket Development Station at the U.S. Atomic Energy Commission's Nevada Test Site*. Geological Survey Water-Supply Paper 1938. Washington, DC: U.S. Government Printing Office.